



University of Strathclyde

Department of Electronic & Electrical Engineering

# **FDTD Modelling of Partial Discharge in High Voltage Cables**

Xiao Hu

A thesis submitted for the degree of

*Doctor of Philosophy*

2014

*This thesis is the result of the authors original research. It has been composed by the author and has not been previously submitted for examination which has led to the award of a degree.*

*The copyright of this thesis belongs to the author under the terms of the United Kingdom Copyright Acts as qualified by University of Strathclyde Regulation 3.50. Due acknowledgement must always be made of the use of any material contained in, or derived from, this thesis.*

Signed:

Date:

## Acknowledgements

I would like to acknowledge my supervisor Prof Martin D. Judd and Dr W. H. Siew. Thanks for their kindness to provide me with the opportunity to pursue a PhD degree in the University of Strathclyde and moreover always being supportive and patient in supervision of my study. One of my former colleagues also under Prof Judd ever said that Martin is the best supervisor you can ever have! I can't agree more.

Many thanks to my colleague Dr Alistair Reid who provided invaluable experiment results to assist with my part of work in the project.

Special thanks to Mr Frank Cox and those colleagues in the workshop based in the high voltage technologies group. Without their kind help in lab experiments involving electronic and mechanical work, finishing the experiments required by the thesis would be impossible.

Thanks to my colleagues in the high voltage technologies group for providing a convenient working environment.

Thanks to all of my families, especially my mother who has always been trying to support my life and study.

Finally, I would like to give my most sincere thanks to God who has been accompanying and strengthening me in daily life throughout of the study.

## Abstract

Partial discharge (PD) is recognized as an effective insulation diagnostic tool. PD measurement on high voltage (HV) cables is performed to evaluate the cable insulation conditions and high frequency current transformers (HFCTs) are widely used as the PD sensor. Detected PD signals can be subject to significant attenuation caused by propagation in the cables. How to relate the detected signals to the PDs actually occurring at PD-producing defects and moreover find out the nature of the defects is a problem. To investigate this problem experimentally is both difficult and limited since some defect types cannot be easily reproduced. Exploring this problem through modelling can potentially provide useful insights. A hybrid modelling framework is proposed to simulate HFCT-based PD detection in HV cables regarding PD excitation and propagation in the cables and PD detection using HFCTs. The finite-difference time-domain (FDTD) technique is used to simulate PD in the cables and transfer function theory is used to consider effects of HFCTs on the PD signals. The framework can be used to excite a PD pulse anywhere in a cable model and predict the output from HFCTs some distance away. Implementing the framework requires parameters such as cable material/propagation properties, currents flowing on conductors in FDTD models and HFCT transfer functions. Based on available cable samples and HFCTs, methods to obtain these parameters were described or developed and implementation of the framework was demonstrated. Although only cable modelling was carried out, the framework is expected applicable to modelling of PD detection in cable accessories. Furthermore, some experience gained in implementing FDTD modelling of the cables was summarised to facilitate future applications.



# Contents

<b>Contents</b>	<b>iv</b>
<b>1 Introduction</b>	<b>1</b>
1.1 Power Cables . . . . .	1
1.1.1 Power Distribution Cables . . . . .	2
1.2 Partial Discharge as a Diagnostic Tool . . . . .	4
1.3 Motivation for the Present Study . . . . .	4
1.4 Thesis Outline . . . . .	6
<b>2 Partial Discharge in HV Cables</b>	<b>8</b>
2.1 Introduction . . . . .	8
2.2 Partial Discharge Phenomena . . . . .	9
2.2.1 Partial Discharges . . . . .	9
2.2.2 Generation of Partial Discharge Signals . . . . .	11
2.2.3 Partial Discharges in Solid Dielectrics . . . . .	13
2.3 Partial Discharges in HV Cables . . . . .	16
2.3.1 Partial Discharge in Paper-insulated Cables . . . . .	16
2.3.2 Partial Discharge in Polymeric-insulated Cables . . . . .	17
2.4 Partial Discharge Measurement for HV Cables . . . . .	20
2.4.1 PD Pulse Representation and Propagation . . . . .	20
2.4.2 High Frequency Losses in HV Cables . . . . .	22
2.4.3 PD Detection in HV Cables . . . . .	24
2.4.4 PD Detection using a Current Transformer . . . . .	29
2.5 Conclusions . . . . .	31
<b>3 FDTD Methodology and its Application in PD Modelling</b>	<b>33</b>
3.1 Introduction . . . . .	33
3.2 Review of FDTD Applications in Power Industry . . . . .	34

---

3.2.1	FDTD Modelling of PD in GIS . . . . .	35
3.2.2	FDTD Modelling of PD in Transformers . . . . .	37
3.2.3	FDTD Modelling of PD in HV Cables . . . . .	39
3.2.4	Other Applications in Power Industry . . . . .	43
3.3	Electromagnetic FDTD Technique . . . . .	45
3.3.1	Development of the FDTD Technique . . . . .	45
3.3.2	Basic Algorithm of the FDTD Technique . . . . .	49
3.4	FDTD Modelling of PD Location in GIS . . . . .	53
3.4.1	Simulation of PD Within a GIS Tee Section . . . . .	55
3.4.2	PD Location for the Tee Section . . . . .	58
3.4.3	Discussion . . . . .	61
3.5	Implementing FDTD Modelling of PD in HV Cables . . . . .	65
3.5.1	Creating FDTD Models of HV Cables . . . . .	65
3.5.2	Choosing Appropriate FDTD Cell Sizes . . . . .	74
3.5.3	Setting Boundary Conditions . . . . .	78
3.5.4	Creating PD Source and Modelling of TDR measurement . . . . .	80
3.5.4.1	Evaluation of Excitation Sources in XFDTD . . . . .	80
3.5.4.2	FDTD Modelling of TDR Measurement on Cables . . . . .	82
3.6	Conclusions . . . . .	85
<b>4</b>	<b>Characterisation of Cable Semicon Properties</b>	<b>88</b>
4.1	Introduction . . . . .	88
4.2	Definition of Dielectric Properties . . . . .	89
4.3	Lumped Element Equivalent Circuits . . . . .	91
4.4	Review of Dielectric Measurement Techniques . . . . .	94
4.4.1	Frequency Domain and Time Domain Methods . . . . .	94
4.4.2	Implementation of Frequency Domain Method . . . . .	95
4.5	Review of Dielectric Measurements on Cable Semicon . . . . .	98
4.6	Measurement Result and Fit Using Dielectric Models . . . . .	101
4.7	Conclusions . . . . .	107
<b>5</b>	<b>Measurement of Cable Responses</b>	<b>108</b>
5.1	Introduction . . . . .	108
5.2	Cable Sample Details . . . . .	109
5.3	Cable Transmission Line Model . . . . .	111
5.4	Cable Frequency Response . . . . .	114

---

5.4.1	Transmission Measurement . . . . .	114
5.4.2	Reflection Measurement . . . . .	117
5.5	Characterisation of Cable Propagation Properties . . . . .	123
5.5.1	Using TDR Measurement . . . . .	123
5.5.2	Using Analytical Method . . . . .	126
5.6	Conclusions . . . . .	131
<b>6</b>	<b>Measurement of HFCT Transfer Functions</b>	<b>133</b>
6.1	Introduction . . . . .	133
6.2	HFCT Specifications and Transfer Function Measurement Methods	136
6.3	Time Domain Measurement . . . . .	138
6.3.1	Measurement Setup . . . . .	138
6.3.2	Pulse and Step Sources . . . . .	140
6.3.3	Measurement Procedures . . . . .	142
6.3.4	Measurement Results and Discussion . . . . .	143
6.4	Frequency Domain Measurement . . . . .	149
6.5	Conclusions . . . . .	151
<b>7</b>	<b>FDTD Modelling of HFCT-based PD Detection in Cables</b>	<b>152</b>
7.1	Introduction . . . . .	152
7.2	Measuring Currents in XFDTD . . . . .	153
7.2.1	Method Evaluation with a Basic Circuit Model . . . . .	153
7.2.2	Application to a Basic Cable Model . . . . .	157
7.3	Working out an HFCT's Voltage Output . . . . .	160
7.3.1	Application of FFT and Transfer Function Methods . . . . .	160
7.3.2	Applying HFCT Transfer Functions to Gaussian Pulses . . . . .	167
7.4	Framework for Modelling of HFCT-based PD Detection in Cables	174
7.5	Conclusions . . . . .	181
<b>8</b>	<b>Parametric Study of PD Measurement for 11 kV Cables</b>	<b>183</b>
8.1	Overview of the Study . . . . .	183
8.2	Modelling of TDR Measurement . . . . .	184
8.3	Parametric Study on both 11 kV Cables . . . . .	191
8.3.1	Effect of PD Size on PD Signal . . . . .	191
8.3.2	Effect of PD Cross-sectional Position on PD Signal . . . . .	195
8.4	Conclusions . . . . .	198

---

<b>9</b>	<b>Conclusions</b>	<b>200</b>
9.1	The Modelling Framework . . . . .	200
9.1.1	Advantages of the Modelling Framework . . . . .	200
9.1.2	Challenges . . . . .	201
9.2	HFCT Transfer Function Measurement . . . . .	202
9.3	Modelling Using Published Semicon Data . . . . .	202
9.4	Implementing FDTD Modelling of PD in Cables . . . . .	203
9.5	Applications of the Technique . . . . .	203
9.6	Recommendations for Future Work . . . . .	204
9.6.1	Parallel Experiments and FDTD Modelling . . . . .	204
9.6.2	Converse of the Modelling Framework . . . . .	205
	<b>References</b>	<b>206</b>
	<b>Appendix A</b>	<b>223</b>
	<b>Appendix B</b>	<b>226</b>
	<b>Appendix C</b>	<b>231</b>

# Chapter 1

## Introduction

### 1.1 Power Cables

Power cables are those cables used for the transmission, distribution and utilization of electrical power. Overhead lines serve the same purpose and are used extensively in rural areas for economic reasons, while in urban areas, power cables buried underground are more usual because of environmental considerations. Power cables are also widely used in factories, domestic premises and other locations (e.g., coal mines, oil refineries and shipboard) as the most practical means of conveying electrical power to equipment, tools and appliances of all types [1]. In order to meet diverse requirements, power cable designs vary enormously but there are some components common to all [1]. Two essential features are a low resistance conductor for carrying the current and insulation to isolate the conductor from other conductors and surrounding environment. The design generally becomes more complex with the increasing voltage. For example, screening to control the radial electric field in the insulation; an outer sheath, either made of metals or plastics, to prevent moisture ingress, protect metallic components from corrosion and keep the components tightened up with each other; and armoring for mechanical protection etc. In addition, modern polymeric-insulated cables always have semi-conductive layers on the inner and outer surfaces of the insulation, which is to provide smooth interfaces between the conductor structure and the dielectric.

Power cables are rated in British Standards by designating the nominal power frequency voltages for which they are designed. The design voltages are expressed in the form of  $U_0/U(U_m)$ .  $U_0$  is the nominal voltage between conductor and

earth.  $U$  and  $U_m$  represent respectively the nominal voltage and the maximum sustained voltage between phase conductors [2]. For example, 6.35/11 (12) kV and 12.7/22 (24) kV. For cables rated at transmission voltages, usually only the value of  $U$  is quoted, for example, 132 kV and 275 kV. Sometimes power cables are described as low voltage (LV), medium voltage (MV), high voltage (HV) and extra/ultra high voltage (EHV/UHV). However, apart from low voltage (LV), which is defined internationally as maximum 1 kV, the other terms do not have generally accepted precise meanings [1]. On the other hand, from a user's point of view, cables can be referred to based on their applications. For example, in a power distribution system, cables are described according to their positions in the chain of transferring electrical power from the generation to the user [3], i.e., customer cables, distribution cables and transmission cables. The positions in the transfer chain determine the voltage levels of the cables, since the generation produced voltage is increased to high voltage for transmission and the high voltage will be gradually decreased before the electrical power reaches the customer. In the British standard, distribution cables are associated with voltage levels from 0.6/1 (1.2) kV up to 19/33 (36) kV.

### 1.1.1 Power Distribution Cables

Power distribution cables generally have two types of insulation. One is lapped cellular paper insulation. The corresponding cable is often called the paper-insulated lead covered (PILC) cable. The other type uses an extruded polymer such as polyethylene (PE), cross-linked polyethylene (XLPE) or ethylene propylene rubber (EPR). Paper insulation was introduced at the turn of the last century and has been used for both distribution and transmission purposes. Paper insulated cables have proved impressively reliable. In the UK supply industry, such distribution cables have already demonstrated an operational life of over 40 years [1]. Extruded polymer insulation suitable for high voltage cables was introduced at the beginning of 1960s and began to gain popularity worldwide since 1970s. In the UK, the swing from paper-insulated cables to polymeric-insulated cables was slower and started in 1980s. To date, regional electricity companies have had good operational experience with 11 kV polymeric cables [1]. Both XLPE and EPR insulation are designed to have an expected service life of 40 years, but whether these polymeric-insulated cables can really have an ultimate life matching that of paper-insulated cables remains to be confirmed over time.

However, since polymeric-insulated cables are easier to install and maintain and are more environmentally friendly, more widespread use to replace traditional paper-insulated cables is the future trend. Amongst the dielectrics of PE, XLPE and EPR, continued increasing demand for XLPE is likely as it has lower capital cost and higher productivity processes [1].

Figure 1.1 shows the construction of a typical polymeric-insulated distribution cable. Primary distribution cables normally have aluminium conductors. The conductors can be solid or stranded. The strand shield (inner semi-conductive layer), the polymer insulation and the insulation shield (outer semi-conductive layer) are co-extruded through a triple extrusion process [4]. The metallic shield (outer conductor) is usually constructed of copper wires or tapes applied helically. The jacket (outer sheath) is frequently made from polyvinyl chloride (PVC).

In this research, cable samples under investigation were polymeric-insulated distribution cables, due to their availability. At the same time, the term of high voltage (HV) cables are used throughout the discussion to represent cables rated above 1 kV.

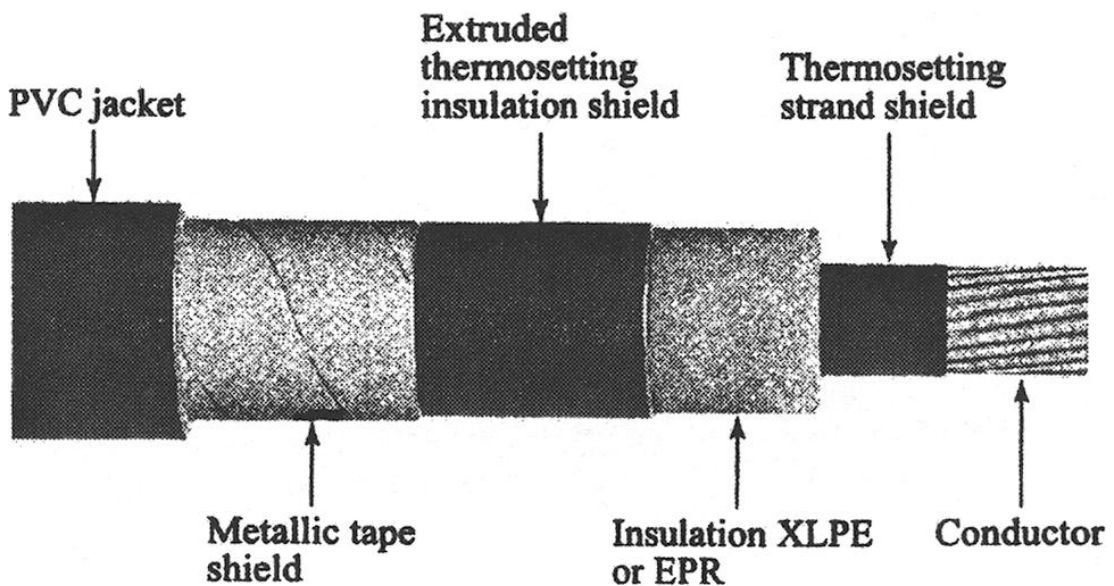


Figure 1.1: Polymeric-insulated power distribution cable [4].

## 1.2 Partial Discharge as a Diagnostic Tool

Partial discharge (PD) measurement for an insulation system is carried out for design or quality assurance purposes to make sure that no PD (or only PD below some threshold level) occurs under normal operation or no defect was introduced during manufacturing/processing of the insulation system [5]. Long time operation involving electrical, thermal, mechanical and environmental aging processes may still produce defects in the insulation system. PD can occur at these defects under electrical stress, which will eventually cause breakdown of the insulation system. Therefore, PD measurement is also useful as a diagnostic tool to assess the insulation condition. Location of the discharge site is particularly meaningful in insulation diagnostic of HV cables and their accessories as this will allow a problem cable section to be pinpointed and fixed as soon as possible.

PD measurement has been recommended as an effective method to establish the baseline condition for newly installed cable systems and diagnose the condition of aged systems [6; 7]. Both off-line and on-line testing can be carried out. Off-line testing will allow applying elevated voltages so that those PDs that will not occur under normal working voltages can be found. On-line testing is carried out while a cable is in service and may allow detection of PDs that are active while the cable is under normal operating condition. PD measurement is regarded as especially useful in detecting problems in cable joints and terminations [5]. Continuous PD monitoring is suggested particularly for polymeric-insulated cables where PD, once detected, is likely to cause breakdown of the insulation in a short time, e.g., within a few days or less [5].

Measured PD signal characteristics are found to depend strongly on the type, size and location of defects, type of insulation (PILC, EPR, XLPE, etc.), applied voltage, cable operation conditions and environmental noise [8]. The damage caused by PD can vary significantly ranging from negligible to causing failure after times from days to years [9]. Therefore, proper interpretation of the measured PD signals is essential to achieve an effective condition assessment of the cable insulation.

## 1.3 Motivation for the Present Study

There are currently three types of strategy to perform maintenance for HV cables. They are *corrective maintenance* which is to repair or to replace broken compo-



nents, *time-based maintenance/preventive maintenance* which is to perform maintenance on a predetermined schedule, and *condition-based maintenance/predictive maintenance* which is to perform maintenance based on the results of condition assessment of the component. Although corrective maintenance and time-based maintenance are mostly adopted by cable owners, trends are moving in the direction of condition-based maintenance [10]. In the UK, installation of distribution cables was at its peak rate in the 1950s and 1960s [11]. Since typical design life of these cables are said to range from 60 to 70 years, many of them are approaching their life expectancy. The situation drives the need for a condition-based approach to manage these aged cables. Condition assessment of cable insulation can include both off-line and on-line PD testing. It was reported that one of the UK utilities has deployed on-line PD monitoring to over 600 of its distribution cables [11]. Considerable increase in PD testing and monitoring for power cables in the UK can be expected.

PD testing for cables and cable accessories has been implemented predominantly using high frequency current transformers (HFCTs) as PD sensors [5]. High frequency current transformers (HFCTs) are usually installed at cable terminations where cable conductors or earth connections are accessible. PD currents initiating at PD sources are coupled onto the cable conductors and travel away from the PD sources and will be detected by HFCTs. The processes of coupling, propagation and detection can cause significant changes to the PD signals, which makes it difficult to interpret the measurement results. Investigating the relationship between the PD current pulses excited at PD sources and the measured PD signals from HFCTs in laboratory is limited by the fact that some defect types cannot easily be reproduced experimentally. Exploring this problem through modelling is more versatile and can potentially provide useful insight. In this study, a hybrid framework based on the finite-difference time-domain (FDTD) technique and transfer function theories is proposed to address the three stages of HFCT-based PD measurement for cables:

1. PD excitation in cables.
2. Propagation along the cables.
3. Detection of PD current signals using HFCTs.

The principles of this approach could also be used in modelling PD-like transients in other high voltage and power devices.

## 1.4 Thesis Outline

This thesis is focused on realizing modelling of the practice of HFCT-based PD measurement for cables. The thesis is subdivided into:

- Review of PD in HV cables.
- Review of the finite-difference time-domain (FDTD) technique and its applications to power industry.
- Summary of experience in FDTD modelling of PD in cables.
- Characterising modelling required cable properties and HFCT transfer functions.
- Principle of a hybrid modelling framework and demonstration of the framework.

A more detailed summary of the thesis content is as follows.

In Chapter 2, basic background of PD and generation of an externally measurable PD signal are reviewed. Typical PD defects in HV cables are summarised. The analytical representation of a PD pulse and attenuation to the pulse as a function of distance propagated are presented. Explanations of the causes of the attenuation are reviewed and some typical PD detection methods for cables are discussed.

In Chapter 3, applications of the FDTD technique to power industry are firstly reviewed, followed by an introduction to the basic concept of the FDTD technique. An example of using the commercial FDTD package to investigate optimal PD sensor installation positions for PD detection in GIS is presented. A summary of experience gained from working on modelling of PD detection in cables is given to facilitate future research on similar topics.

In Chapter 4, relevant dielectric physics basics are introduced. Some techniques for broadband measurement of the complex permittivity are reviewed, with a focus on applying those techniques particularly developed to measure the complex permittivity of the semi-conductive (semicon) layers of cables. The obtained cable semicon properties are fitted by certain dielectric models of which parameters are required in creating FDTD cable models.

In Chapter 5, details of the 11 kV cable samples investigated in this study are presented. By considering the cables as two-port networks, transmission and

reflection responses were measured using a network analyzer. Dielectric constants of the cable insulation were derived from the reflection responses. By time domain reflectometry (TDR) measurement, attenuation constants of the cables were obtained and used as a reference to improve the accuracy of the analytical model. Results from the analytical model will be used to improve the accuracy of the FDTD cable models.

In Chapter 6, specifications of the HFCTs used in this study are presented. A time domain method combining the step response and the pulse response of an HFCT was proposed to obtain the complex transfer function of the HFCT. Measurement results from the time domain method were found to agree with those from the frequency domain method. The measured HFCT transfer functions were combined with spectra of PD currents to work out the HFCTs' voltage output.

In Chapter 7, a method to derive currents flowing on conductors within FDTD models is described and the accuracy of the method is evaluated. Two methods of applying the measured HFCT transfer functions to PD currents to produce the HFCTs' voltage output are explained and demonstrated through applications to Gaussian pulses. A hybrid framework for modelling of HFCT-based PD detection in cables is proposed and illustrated step-by-step using an FDTD cable model.

In Chapter 8, FDTD modelling of TDR measurement is demonstrated and used to evaluate the accuracy of the created FDTD cable models. Using the FDTD cable models and considering two scenarios to vary PD source specifications in the models, a parametric study was carried out to investigate, in each case, the PD-induced current on the cable earth conductor. The parametric study shows a possibility to determine the coupling sensitivity between PD source currents and the PD-induced currents on the cable earth conductor, which is an example of how the FDTD cable models can be used to study PD in the cables.

In conclusion, Chapter 9 summarises the main contributions of this work. Potential applications of the proposed modelling framework are suggested and possible future research directions are discussed.

# Chapter 2

## Partial Discharge in HV Cables

### 2.1 Introduction

Partial discharge (PD) is indicative of local defects within electrical insulation. Although the discharge magnitude is usually small, leaving it to develop can result in complete electrical breakdown of the insulation system, which can in turn lead to disruption of power supply and economic losses. Therefore, detection as well as location of partial discharge (PD) in high voltage equipment is of interest in terms of realizing effective maintenance of these equipment and ultimately improving reliability of the equipment operation. PD measurement for high voltage (HV) cables has been widely carried out by utility operators in order to monitor and diagnose insulation conditions of the cables. There are various PD measurement methods. Generally, they can be divided into off-line PD detection (during service outages) and on-line PD detection (during service). In this chapter, some fundamentals of PD phenomena are firstly reviewed. After that, typical PD defects in paper-insulated cables and polymeric-insulated cables are summarised. PD pulses propagating along the cables are subject to attenuation and dispersion, so state of art understanding of these effects are reviewed. Finally, PD measurement methods are discussed in terms of off-line and on-line detection with relevant PD sensors being employed. A special address is given to the current transformer (CT) type of PD sensor which, due to its essentially non-intrusive property, has been widely adopted in practices of PD detection in cables.

## 2.2 Partial Discharge Phenomena

### 2.2.1 Partial Discharges

Partial discharge (PD) is a localized electrical discharge that only bridges part of the insulation between conductors and which can or cannot occur adjacent to a conductor [12]. PD is essentially a result of local electric field concentrations. Subject to whether the concentrations occur in the insulation or on the surface of the insulation, PD can be classified into internal discharges and surface discharges (Figures 2.1a and 2.1b). More specifically, internal discharges occur in inclusions being embedded in a more dense dielectric system. These inclusions can be gas-filled cavities, oil-filled cavities and impurities like dirt, conducting particles, textile fibres and so on [13]. Surface discharges may occur when there is a stress component in parallel to a dielectric surface. For example, at ends of cables, ends of generator windings, bushings etc. [13]. Corona discharges (Figure 2.1c) form a third PD category. They typically occur in gaseous media and around

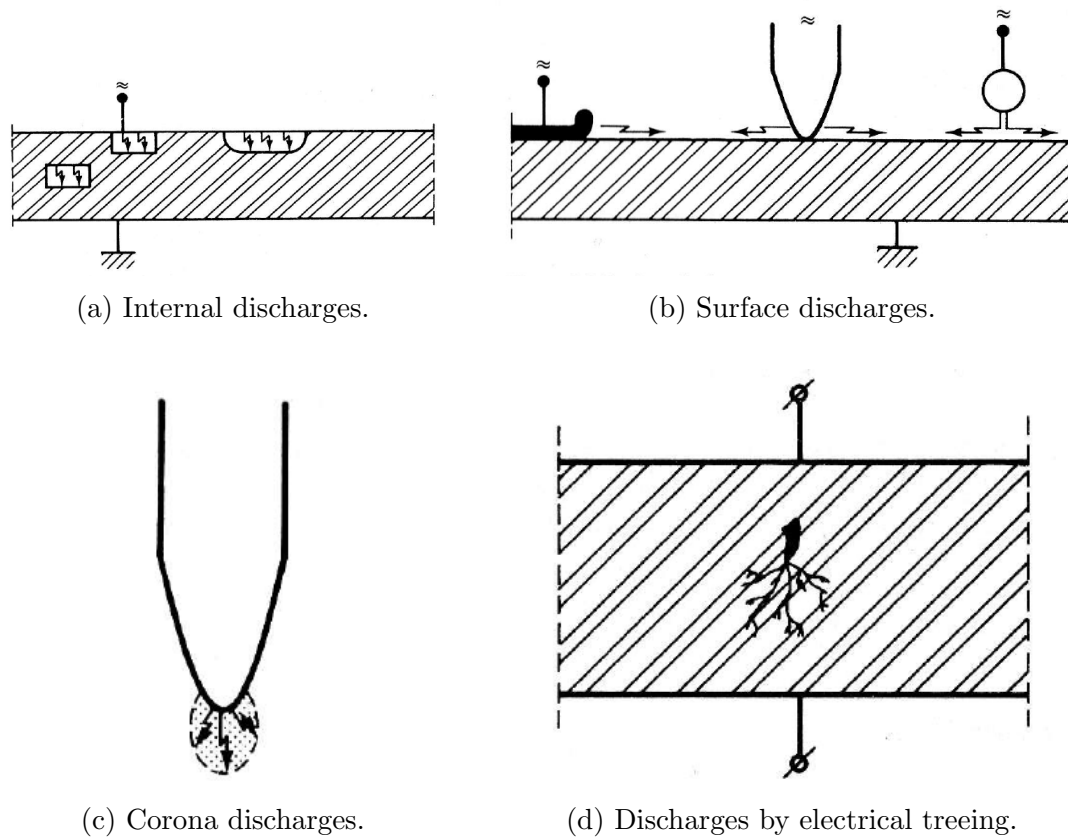


Figure 2.1: Classification of partial discharges [13].

conductors remote from solid or liquid dielectrics. The conductors are usually at high voltages, but sharp edges and protrusions at earth potential can also cause corona discharges. Finally, a special case of PD is discharges by electrical treeing (Figure 2.1d) which may be classified as internal discharges of specific origin [13]. Electrical treeing starts from defects in a dielectric. The treeing process can gradually develop branch like hollows in the dielectric and discharges occur in them. However, the process may take hours to years before considerable PD can take place and be measured externally. Comparing to other PD categories, PD by electrical treeing can be very unstable. The discharges in the hollows also contribute to further growth of the hollow branches and can at some stage result in rapid breakdown of the whole dielectric system.

Although PD is observed in gas, liquid and solid dielectrics, PD itself is most commonly regarded as a phenomenon taking place in gases [14]. This is obvious for corona, voids and floating components where the gas is a natural part of the system. In other cases like oil-filled cavities and impurities within oils and extruded polymers, it is believed that after initial breakdown, gas-filled cavities and hollows will be formed and afterwards gaseous discharges will occur. Initiating requirements of gas discharges can be investigated based on the well known Paschen's curve. Figure 2.2 shows the Paschen's curve of air. According to a cer-

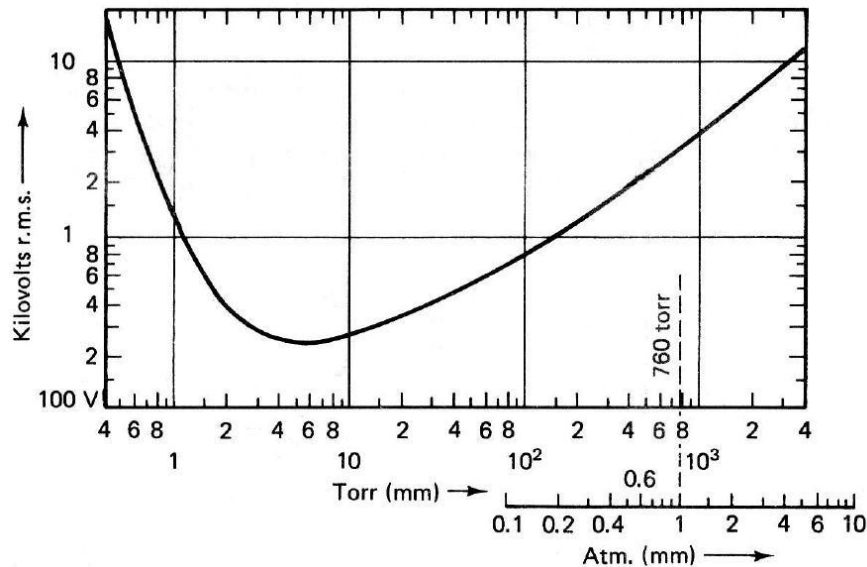


Figure 2.2: Paschen's curve. Breakdown voltage of air as a function of the product of gas pressure and electrode spacing [13].

tain gas type, gas pressure and distance between electrodes, breakdown voltage of the gas can be found using the Paschen's curve of the gas. For those electrode arrangements other than plate capacitors, some approximations can be made for relating to the Paschen's curve to have an estimate of the breakdown voltage.

Apart from the breakdown voltage of the gas, another main cause of PD is the relatively low dielectric constant of the gas compared to those media around it. For example, Figure 2.3 shows a gas-filled cavity incorporated in another dielectric. The cavity is flat in a direction perpendicular to the direction of the

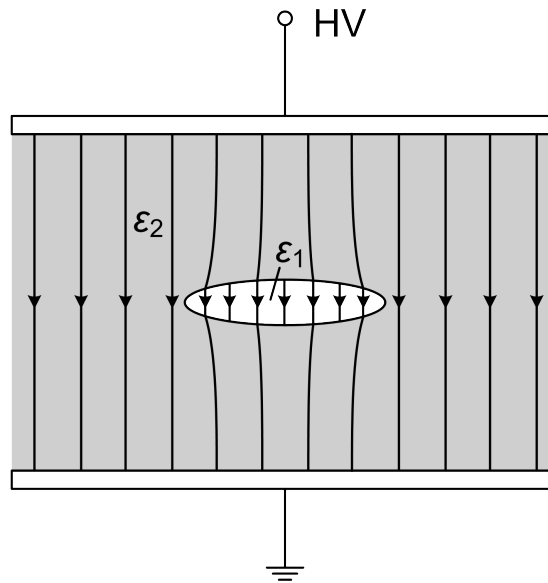


Figure 2.3: Diagram of the electric field in a dielectric with a gas-filled cavity.

electric field. In this case, the electric field stress in the cavity will be  $\epsilon_2/\epsilon_1$  times higher than the stress in the dielectric, where  $\epsilon_1$  and  $\epsilon_2$  are the dielectric constant of the gas and the dielectric respectively and with  $\epsilon_2 > \epsilon_1$  [13]. Furthermore, since a liquid/solid dielectric usually has a much higher dielectric strength than a gas dielectric does, it is often used for purposes of withstanding high electrical stress. Consequently, a gas-filled cavity within the liquid/solid dielectric is very likely to develop PD.

### 2.2.2 Generation of Partial Discharge Signals

A PD is essentially a flow of electrons and ions in a gas over a small volume of the total insulation [15]. The PD event causes both electrical and nonelectrical

phenomena. The nonelectrical phenomena can include chemical transformation, gas pressure, heat, sound and light [13]. Although mentioned here, this discussion is limited to the electrical phenomena which are radio frequency current and voltage pulses emitted by the PD event. A PD pulse is often measured by the total charge within the current pulse. The apparent charge in picocoulombs (pC) is the charge which, when injected at the measurement terminals, produces the same amplitude pulse as the PD produces at the measurement terminals [12]. This is the “effective PD magnitude” that can be measured externally. It is different from the “true” PD charge which is the actual charge transfer taking place at the PD source. How the “true” charge is related to the measured PD magnitude or how the externally measurable PD signal is generated following a PD event, detailed processes can vary from PD type to PD type. However, some most important aspects regarding basic PD analysis are similar.

Using a floating component as an example, the process of PD signal generation was illustrated by Boggs [14]. Figure 2.4 shows an arrangement that could cause a floating component-type PD. It is a gas insulated substation (GIS) spacer used to

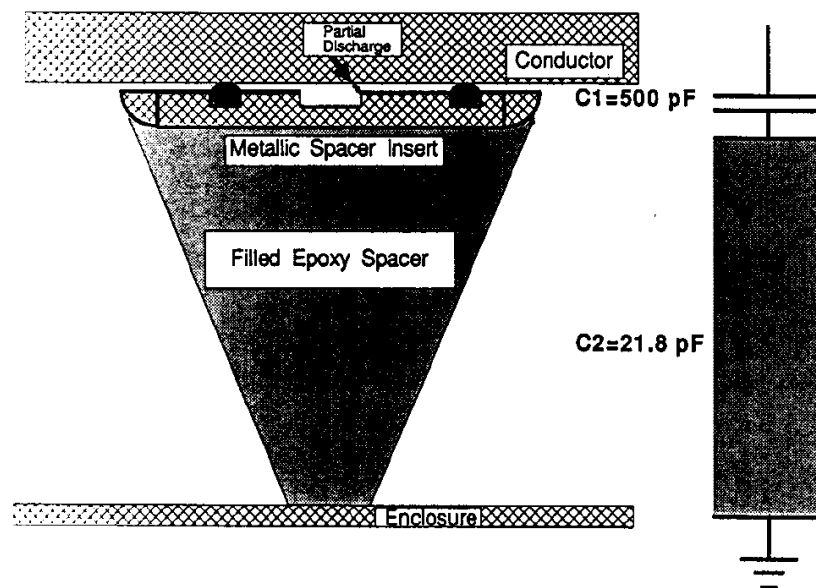


Figure 2.4: Axial cross section of a disc-shaped epoxy spacer supporting the GIS conductor. The metallic spacer insert and the conductor are supposed to be connected. PD is possible in the gas gap between the insert and the conductor if the connection between them is ineffective. In that case, the lumped circuit of the system is two capacitors in series as shown on the right [14].



isolate a phase bus in the GIS. Assuming no effective connection between the GIS conductor and the spacer insert, the electric potential of the spacer insert will be floating. Consequently, when the voltage difference between the conductor and the spacer insert becomes higher than the breakdown voltage of the gap between them, the breakdown is caused in the gap to eliminate the voltage difference. Typically, the epoxy spacer has a dielectric constant  $> 3$ . Therefore, electric field stress in the gap is several times higher than that in the epoxy spacer. As the voltage on the conductor is increased the voltage over the gap builds up and, when it exceeds the breakdown voltage of the gap, a discharge takes place and causes charge transfer between the conductor and the spacer insert to bring the voltage on the spacer insert to approximately the same as that on the conductor, i.e., short-circuiting the capacitor C1 in Figure 2.4. As a result, the total capacitance of C1 and C2 in series is replaced by only C2 during the discharge and thus an increase in the total capacitance between the conductor and the enclosure (connected to the ground). The capacitance increase will result in the voltage on the conductor being momentarily lower than that of the voltage supply. The voltage supply then provides a current to compensate the voltage drop. This current pulse will flow through the whole system and go into the ground. It is this current that enables the PD signal to be measured by an external circuit. Since not all charge that actually goes on in the discharge will flow through the system into the ground, the measured PD signal is some kind of “effective” PD magnitude that is not directly related to the total charge transfer in the discharge. Actually, it has been suggested that the measured PD magnitude may only represent a very small part of the total charge. Generally, the PD magnitude measured outside is inversely proportional to the size (or insulation thickness) of a system under investigation [13; 14].

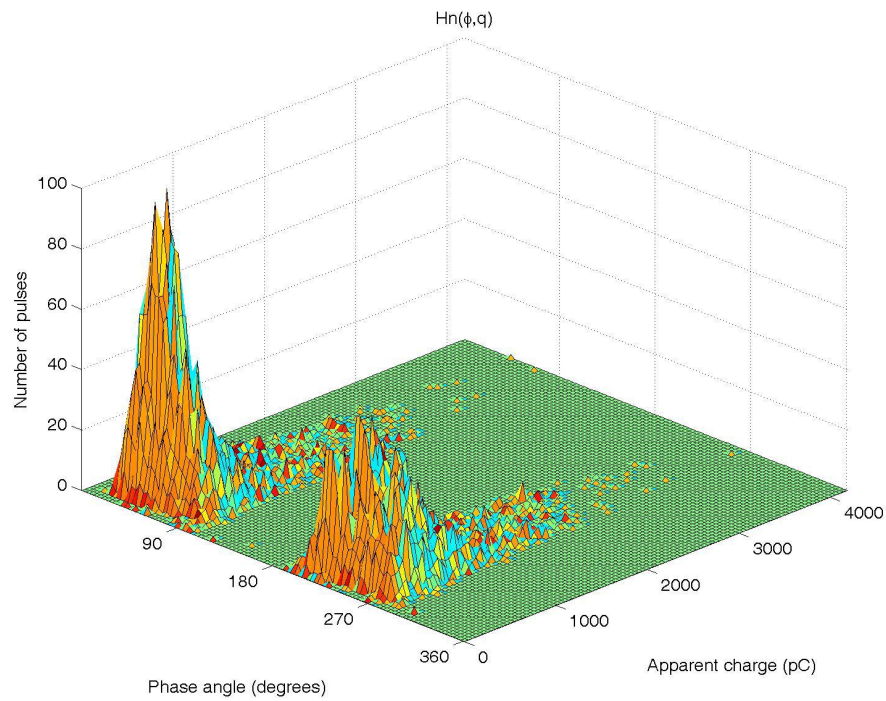
### 2.2.3 Partial Discharges in Solid Dielectrics

Among the four PD categories, internal discharges, surface discharges and discharges by electrical treeing all usually involve solid dielectrics. Internal discharges are thought to be the most harmful to the insulation while surface discharges are less dangerous since they are less concentrated and thus even a relatively large magnitude may be tolerated [13]. Internal discharges in solid dielectrics can occur in gas/oil filled cavities, around foreign inclusions and during an electrical treeing process. Basic mechanisms of the internal discharges

in cavities (and by electrical treeing) and their implications for PD detection are reviewed as follows. For internal discharges around foreign inclusions, it is considered that after the initial breakdown caused by the stress enhancement around the inclusions, gas is generated and gas-filled cavity is formed to allow gas discharges [13].

PD in a cavity is said to be the most technologically important PD source, since detection of such defects is frequently the main objective of carrying out PD measurement [16]. Initialization of PD in the cavity has to satisfy two conditions: (a) the electric field within the cavity must exceed the minimum field that will allow a streamer discharge to develop (where the minimum field is determined by the gas type and pressure and cavity size); (b) there has to be a first electron to initiate the streamer discharge. The free electron can result from many effects such as cosmic radiation, a previous discharge's remnant ionisation or emission from a metallic surface. Provided the minimum field condition is met, depending on if there are sufficient electrons within the cavity, the waiting time before a discharge initiates varies and, subsequently, PD patterns being produced will vary. A cavity with sufficient electrons will have PD occurring at regular phase positions, i.e., generating a well-defined phased-resolved PD pattern (see Figure 2.5a). However, a cavity with scarce electrons will have PD occurring at electric fields well above the minimum field and at random phase positions. Therefore, there will be no obvious phase-resolved PD pattern (e.g., Figure 2.5b). Instead, the ratio between the maximum and minimum apparent PD magnitudes and the envelop of the PD magnitudes serve as the PD patterns. The identified PD patterns can be used in determining defect types and characteristics. The phase-resolved pattern is called "regular" patterns while the other patterns are called "statistical" patterns. Generally, the "regular" patterns may result from a large cavity (e.g.,  $> 1$  mm), a delamination cavity adjacent to a metallic electrode and a floating component. The "statistical" patterns may result from less frequently occurring discharges and thus the involved defects are less important in terms of insulation aging.

PD takes place in branched channels developed by the electrical treeing process. The original defects in the insulation, being the stem of the branched channels, may be metallic protrusions (e.g., on an electrode, at a point from the semi-conductive layer protruding into the dielectric, etc.) or a void within the dielectric [14; 18]. Given a defect, (for example, a metallic protrusion), the de-



(a) Void in resin.

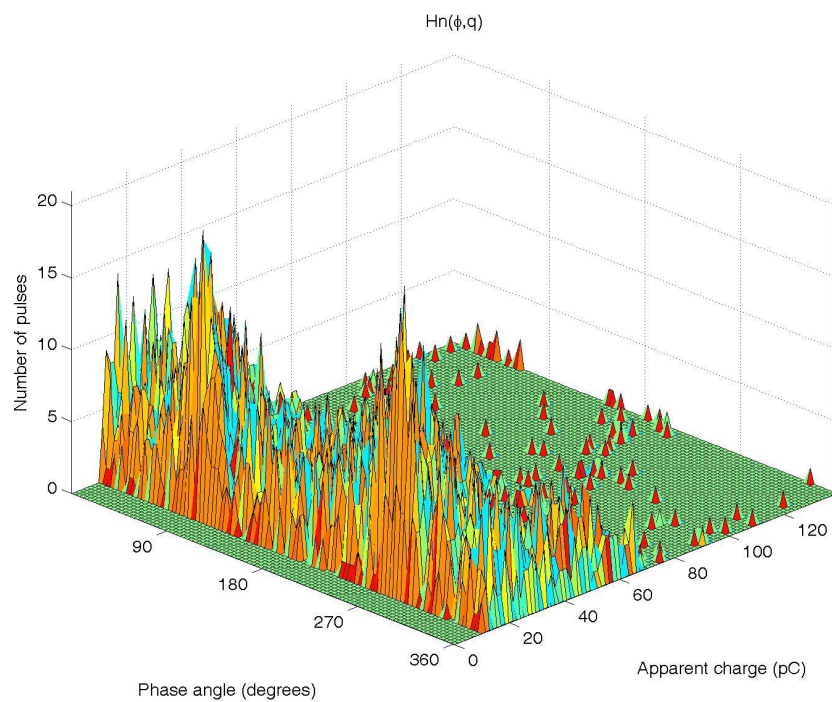
(b) Free aluminium particle in  $SF_6$ .

Figure 2.5: PD testing results showing well-defined and no obvious phase resolved PD patterns respectively [17].

velopment process of electrical treeing can be divided into three steps which are the charge injection stage, the micro PD stage and the tree growth stage [19]. In the charge injection stage, if the stress enhancement around the protrusion can result in an electric field higher than a certain threshold field (e.g., in the range of MV/cm), it will cause sufficient charge injection to degrade the dielectric around the protrusion through electrochemical processes. At this stage, no detectable PD is normally involved. The degradation following the charge injections eventually causes a cavity to form around the protrusion. PD will first initiate in this cavity, which is the micro PD stage where the PD magnitude is normally too small (e.g.,  $< 0.1$  pC) to be detected. Continued PD in the cavity can trigger branched channels to grow from the cavity, and PD moves on to take place in the grown channels and cause further growth of the channels. The PD magnitude during the initial growth of the branched channels is still very small. Generally, larger PD pulses only occur seconds to minutes before the ultimate failure. It is for this reason, using PD measurement to detect the defects leading to electrical treeing is more of interest to researchers than to utility operators [14].

## 2.3 Partial Discharges in HV Cables

### 2.3.1 Partial Discharge in Paper-insulated Cables

For PILC cables, thermal ageing is the main ageing mechanism, and electrical stress is thought to have little effect on the thermal ageing process in absence of PD [20]. The insulation of the PILC cables consists of helically applied paper tapes with a small gap between turns and an impregnating compound such as oil. The paper tapes are impregnated by the compound, and any gaps are filled with the compound. While in service, most distribution cables are subject to cyclic loading, thus heating and cooling, predominantly on a daily basis [1]. Heating causes expansion of the impregnating compound, but the compound does not always flow back between the paper layers. In that case, voids are formed and PD can take place. Prolonged PD activities can cause carbonized, tree-like tracks to develop across the paper layers and finally result in breakdown of the insulation. Figure 2.6 shows the development of carbonized tracking in a PILC cable's insulation. Nevertheless, it is recognized that, compared with polymeric insulations, paper insulations are highly resistive to PD. Hundreds of picocoulombs PD is not uncommon for the PILC cables [20]. Electrical failures are rare for the paper/oil

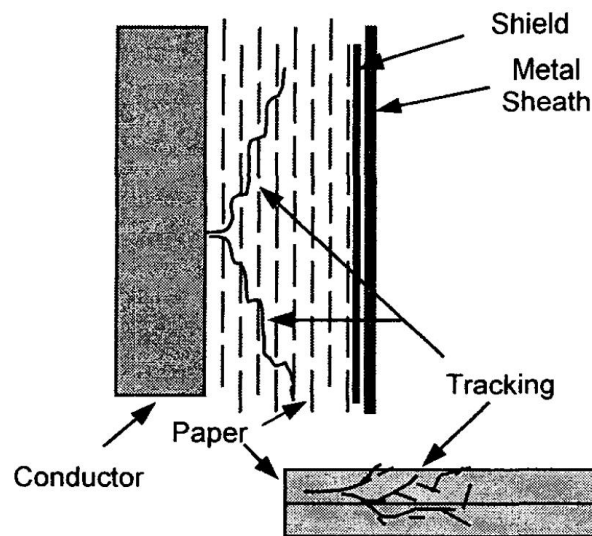


Figure 2.6: Illustration of the PD produced tracking in a PILC cable [21].

insulation up to 6 kV. It is at 11 kV and above that the kind of failure caused by the PD-produced tracking is more likely to happen [1].

### 2.3.2 Partial Discharge in Polymeric-insulated Cables

For extruded polymeric-insulated cables, electrical ageing is normally the main ageing mechanism. Electrical ageing processes include PD, electrical treeing, water treeing and charge injection. Compared with thermal ageing, where the effects are imposed on a whole cable, electrical ageing typically occurs at various defects and therefore tends to be localized [20]. For example, Figure 2.7 illustrates, on an XLPE cable's cross section, typical PD producing defects, electrical trees and water trees. Defects like voids, protrusions or contaminants may be introduced unintentionally during material processing, cable manufacture, transportation or installation. PD can initiate once applied electric field across the insulation is higher than a threshold level at which the corresponding voltage on the conductors is the PD inception voltage. At these defects, should there be enough electrical stress enhancement, PD is likely to initiate at operating voltages [20].

Electrical treeing may start from the PD defects mentioned above and water trees within polymeric insulation. PD from electrical treeing, as reviewed above, becomes externally measurable only seconds or minutes before breakdown. Water trees are microscopic structures formed under the conditions that a polymeric-

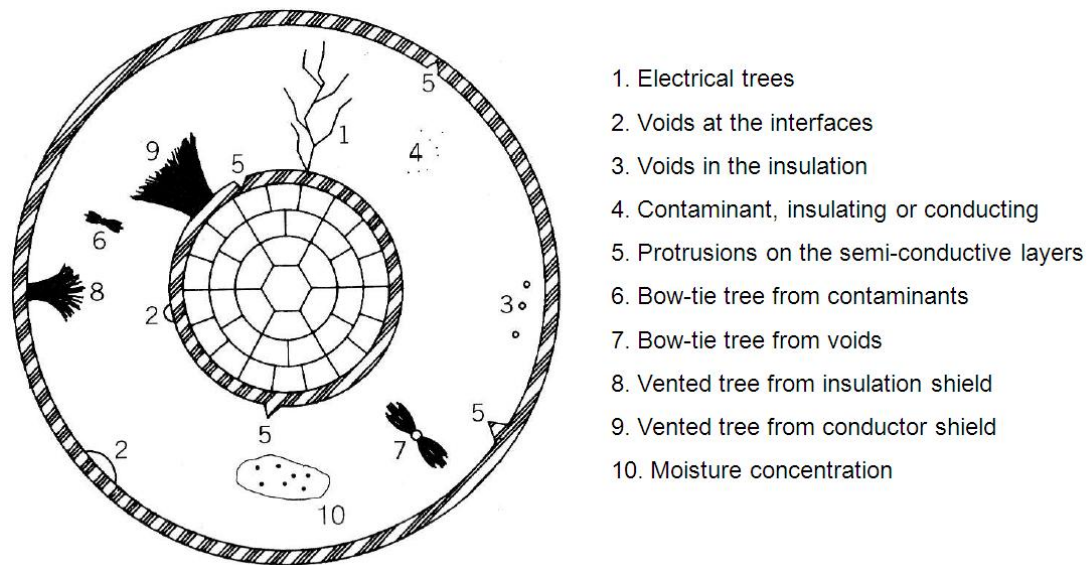


Figure 2.7: Defects in an XLPE cable [3].

insulated cable is in service and the insulation is exposed to moisture. Bow-tie trees may grow from defects like contaminants and voids within the insulation while vented trees may grow from one of the cable conductors, normally from either of the semi-conductive layers. How water trees lead to failure has not been clearly understood, but it was reported that electrical treeing tended to initiate at defects which were in the vicinity of water trees [22]. While detectable PD may not sustain within the water trees, PD does take place in the electrical treeing areas within them [22].

Although the defects in Figure 2.7 relate to an XLPE cable, they are generally faced by the other extruded polymeric insulation, i.e., PE and EPR. Water trees can grow in PE and EPR insulation although it has been observed that water trees grow slowly and are hard to detect in EPR insulation [3]. EPR insulation is also much more resistant to PD. Since different insulation materials can have different resistances to PD, when carrying out PD analysis, in addition to knowing PD sources (e.g., void, protrusion, electrical treeing, etc.) and PD characteristics (e.g., magnitude, number and phase position), taking into account the type of insulation material is necessary [20; 21].

Compared with cables that are made under well-defined factory conditions, cable accessories are assembled on site and, therefore, are subject to more uncertain fabrication quality. For example, bad workmanship can result in incorrectly

assembled joints and poorly installed terminations, and conditions in the field have an increased possibility to introduce defects like voids, protrusions and contaminants. Such defects will cause local electrical stress enhancement in the cable joints and terminations and make them susceptible to PD. Figure 2.8 shows some typical PD defects found in a cable joint. Knife cuts can be caused during removing a bonded semi-conductive layer. Cavities are created from poor bonding in interfaces. Another typical defect, surface tracking, can result from surface discharges occurring at the interface between the cable insulation and the joint insulation. Surface discharges can gradually produce carbonized tracks on the insulation surface. The same types of defect may also exist in cable terminations [21]. Due to the increased possibility of introducing defects, the cable joints and terminations are more vulnerable to ageing [20].

In order to prevent defective cables from being placed into service, PD testing has been one of the routine tests (in the factory after manufacturing) for extruded polymeric-insulated cables. For XLPE cables in particular, PD testing is thought to be the most revealing test for the electrical integrity of this cable type [3]. Since electrical ageing is the main ageing mechanism of extruded polymeric-insulated cables and each of the electrical ageing processes is likely to be associated with PD activities, PD tests have also been used as a diagnostic tool in field tests (acceptance testing or maintenance testing) for the cables as well as relevant cable accessories [8; 20].

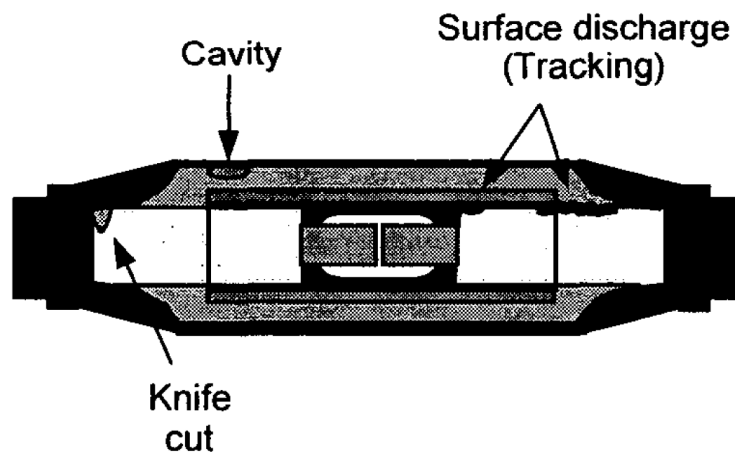


Figure 2.8: PD producing defects in a joint [21].

## 2.4 Partial Discharge Measurement for HV Cables

### 2.4.1 PD Pulse Representation and Propagation

A PD pulse consists of an electronic component and an ionic component, which result from a flow of electrons and ions respectively. Since the velocity of electrons in a gas is much higher than that of ions, the pulse shape can be described by a relatively large magnitude, short duration pulse (electronic portion) followed by a much longer duration, lower magnitude pulse of the same polarity (ionic portion) [15]. An example of the theoretical PD pulse is shown in Figure 2.9. Theoretical

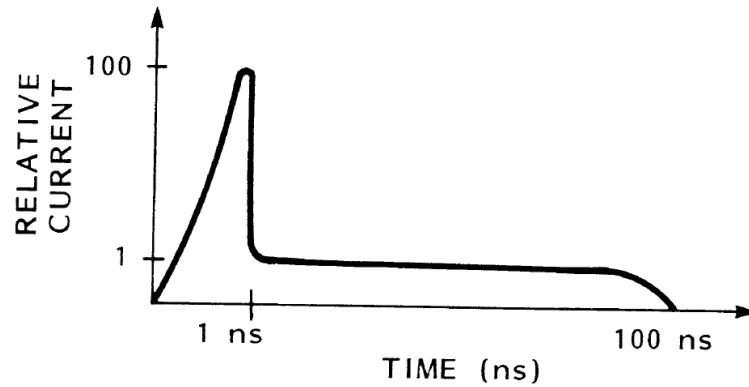


Figure 2.9: Theoretical PD pulse shape in a small void. The duration and magnitude of the pulse depends on void characteristics such as size, gas type and pressure, electric field [15].

analysis has shown that the electronic portion of the PD pulse lasts less than 1 ns while the ionic portion has a duration of about 100 ns [15]. Measured PD pulses from electrical treeing in epoxy showed that the electronic portion had the risetime of 0.3 – 0.8 ns and a full width at half maximum (FWHM) of about 1.5 ns [15]. Once the void was significantly aged, the PD pulse risetime can increase up to 10s of ns and its width can broaden to hundreds of ns [23].

The electronic portion of a PD pulse can be represented by a Gaussian pulse [24; 25]. Assuming a PD current pulse of  $I(t)$ , the expression is

$$I(t) = I_0 \exp(-t^2/2\sigma^2) \quad (2.1)$$

where  $I_0$  is the peak current and the full width at half maximum (FWHM) is



calculated as  $2.36\sigma$ . The corresponding PD voltage pulse can be obtained by  $V(t) = RI(t)$  where  $R$  is the resistance of a current shunt. The frequency response of the PD voltage pulse is

$$F(\omega) = V_0\sigma\sqrt{2\pi}\exp(-\omega^2\sigma^2/2) \quad (2.2)$$

where  $V_0$  is the peak voltage of  $RI(t)$ , which is also Gaussian.

When a PD takes place in an HV cable, the PD pulse will propagate away from the PD source in both directions along the cable. Due to high frequency attenuation and dispersion of the cable, the PD pulse will spread and its spectrum will be changed. If the frequency-dependent attenuation  $\alpha(\omega)$  of the cable is known, the attenuation effect on the spectrum can be calculated by

$$F(\omega) = V_0\sigma\sqrt{2\pi}\exp(-\omega^2\sigma^2/2 - \alpha(\omega)l) \quad (2.3)$$

where  $l$  is the distance propagated along the cable. The spectrum can be transformed into the time domain to give the attenuated PD pulse shape. Analytical solutions were presented in [26] but dispersion effects cannot be included in (2.3) if an analytical solution is to be pursued. Nevertheless, in terms of PD detection, high frequency attenuation was found to have a much greater effect than dispersion [27]. It was argued in [27] that the effects of attenuation and dispersion of the HV cable are coupled, i.e., greater dispersion is accompanied by higher attenuation. The dispersion effect resulting from PD pulse propagation should be small and perhaps insignificant because the frequency components of the pulse will be attenuated significantly before they can disperse to an appreciable degree [27].

While the Gaussian pulse expression is suitable for describing PD pulses with symmetric shapes, it is not appropriate for those asymmetric PD pulses. As an example, both kinds of original PD pulse were reported in [28], where compared with the symmetric pulse of few ns duration, the asymmetric one having a much longer tail had a duration of 50 ns. To account for these asymmetric PD pulses, a method was proposed as representing an asymmetric pulse by a sum of many Gaussian pulses [25; 26]. The attenuation influence during propagation along the cable can be evaluated on the asymmetric PD pulse through considering the attenuation to the Gaussian pulses in the pulse respectively and summing the resulting pulses. More specifically, it is carried out by applying the cable attention

constant to the spectrum of each Gaussian pulse according to (2.3), transforming each resulting spectrum into the time domain, and finally summing the obtained time domain pulses to determine the asymmetric PD pulse as modified by the attenuation effects.

### 2.4.2 High Frequency Losses in HV Cables

High frequency attenuation of PD pulses as they propagate in HV cables is a result of high frequency losses in the cables. Causes of the high frequency losses can be different in different types of cable. For PILC cables, their constructions do not include semi-conductive layers. The high frequency losses mostly come from the skin effect in the cable inner and outer conductors and the insulation loss (i.e., the dissipation factor  $\tan \delta$  of the insulation dielectric). While the loss from the skin effect is roughly proportional to square root of frequency, the insulation loss is roughly proportional to frequency. As a result, the losses in PILC cables at low frequencies ( $< 1$  MHz) are dominated by the skin effect and those at high frequencies are dominated by the insulation loss [29].

For polymeric-insulated cables, apart from the losses from the skin effect and  $\tan \delta$  of the insulation, losses caused by the insulation displacement current (i.e., the cable charging current) flowing through the inner and outer semi-conductive layers were found to be significant and probably dominant among different losses [30]. Since the insulation displacement current increases linearly with both the insulation dielectric constant and frequency, the semi-conductive (semicon) layer losses will also be increasing with them [30; 31]. Furthermore, there are other losses caused by interaction of the cable outer conductor with the rest of the cable structures. For the outer conductor made of concentric neutral wires, the losses were found to be a function of the number of wires, as the displacement current may have to flow circumferentially in the outer semicon layer before reaching a neutral wire and therefore result in increased dissipation in the outer semicon layer [29; 32]. For the outer conductor made of copper tapes, ageing (oxidation and corrosion of the copper tapes) will worsen the contact between the tape turns and cause more current spiral down the tapes instead of flowing across them. This ageing effect directly results in increased attenuation and decreased propagation velocity. Moreover, the spiralling current will generate axial magnetic fields which can further induce eddy current losses in the inner conductor and the semicon layers [29; 33]. For an unjacketed cable, its concentric wire outer conductor is

not held against the outer semicon layer by a cable jacket. This makes the outer conductor contact with the outer semicon intermittent. Losses in this kind of cable will depend on the separation (capacitance) between the concentric wires and the outer semicon as well as the distance between points where the concentric wires and the outer semicon are actually in contact [34].

To have an idea of what sorts of part different loss mechanisms play in high frequency attenuation of a polymeric-insulated cable, taking a relatively new copper tape shielded cable as an example, Figure 2.10 shows its high frequency attenuation broken down to show contributions from various loss causes. The “LF Meas.” result was obtained by treating the cable as a lumped capacitor and included losses in the insulation and semicon layers (i.e., “Diele. Loss” in Figure 2.10). The “HF Meas.” result was measured by treating the cable as a transmission line and therefore should include losses from the skin effect,  $\tan \delta$  of the insulation and other possible loss causes. Figure 2.10 shows separately an extra loss type called “Proximity Effect + Spiraling Effect” which is a result of the current spiraling down the copper tape outer conductor and the generated

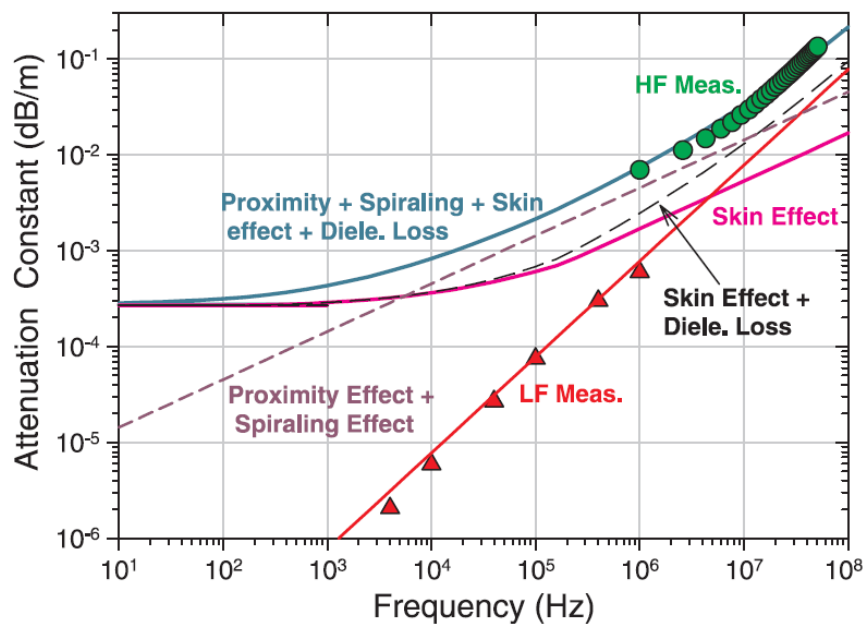


Figure 2.10: A 15 kV EPR cable’s high frequency attenuation broken down to contributions from various causes. “LF Meas.” and “HF Meas.” are the cable attenuation measured by an impedance analyzer and a transmission line impedance analyzer respectively [29].

axial magnetic fields induced eddy current losses in the cable inner conductor and semicon layers. The reason for presenting the extra loss was that summing the losses from the skin effect and  $\tan \delta$  of the insulation did not agree with the “HF Meas.” result [29].

Although there are various causes of high frequency losses in HV cables, it was summarised that the main cause is the losses in the semicon layers for XLPE cables and  $\tan \delta$  of the insulation for PILC cables [35]. For EPR cables, since EPR compound properties can vary from manufacture to manufacture, high frequency losses in EPR cables are either like the case of XLPE cables or closer to the case of PILC cables. High frequency losses in both the semicon layers and the insulation are frequency dependent and therefore result in frequency dependent attenuation. The frequency dependent attenuation causes a PD pulse to decrease in magnitude and broaden in pulse width as a function of distance propagated, which limits the optimum PD detection bandwidth. For example, for an initial PD pulse of 1.5 ns FWHM, the optimum detection bandwidth was found to be 350 MHz [15]. The pulse can be attenuated significantly and the pulse width (FWHM) can be lengthened to several tens of ns after a few hundred meters propagation. As a result, the optimum detection bandwidth will decrease correspondingly to a range of 10 – 20 MHz [31]. By considering typical cable loss characteristics and typical test lengths, the optimum detection bandwidth of 10 MHz was suggested for cables with loss characteristics like XLPE cables while as little as 300 kHz was suggested for those like PILC cables [35]. Apart from implications for PD detection, high frequency losses in HV cables can be optimised towards attenuating surge voltages substantially. The objective is to protect inductive devices like motors and transformers directly connected to switchgear and power electronic whose operation will generate very fast transients that can cause overvoltages across the first turns of the inductive devices [36; 37].

### 2.4.3 PD Detection in HV Cables

PD detection in HV cables can be generally divided into off-line and on-line detection. Off-line detection is carried out with a cable being disconnected from a circuit/system and a separate voltage source is used to energise the cable. On-line detection is carried out while the cable is in service, i.e., no service outage or separate voltage source is needed. Some advantages of on-line detection are such that tests under different load conditions can be performed and trend analysis is

enabled by continuous monitoring. Some advantages of off-line detection are that PD inception and extinction voltages can be found and PD that only occurs at elevated voltages can be measured [8; 9].

In terms of the separate voltage source required by the off-line detection, transportation of the voltage source becomes an issue of concern when carrying out field tests. Power frequency ac voltage sources tend to be large and heavy due to the high capacitive power demand of the cables and therefore make the tests very expensive. Commonly used alternative voltage sources are very low frequency (VLF) voltage sources and damped ac voltage sources. VLF (usually 0.1 Hz) sources are considered to provide more complete information of a cable system and at the same time minimise harmful space charges caused by using the dc high-potential test method (the dc hi-pot test) [38]. Damped ac voltage sources, such as the oscillating wave test system (OWTS) [39], use a dc voltage source to charge the cable capacitance and then discharge the cable through a wave-shaping circuit. The wave-shaping circuit can be adjusted to give out various oscillating frequencies, usually from some tens of Hz to a few kHz. Damped oscillation cycles mean that the cable is subject to the peak voltage level only in the first cycle and therefore the possibility of damaging the cable due to the elevated test voltage is reduced. Both kinds of alternative source are lower in weight and have less power demand than power frequency sources do. However, one common disadvantage of the alternative sources is that measured PD characteristics may differ from those obtained with power frequency sources.

A typical test setup of the off-line PD detection is shown in Figure 2.11. Both ends of the cable are disconnected from the circuit/system. Proper terminations

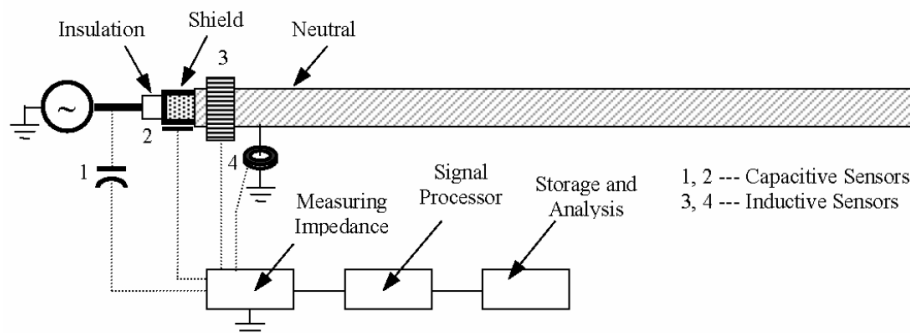


Figure 2.11: Typical test setup of the off-line PD detection for a cable [9].

have to be applied to both the cable ends so that they are PD-free at the desired test voltages. A voltage source is connected to one end of the cable (near end) and the other end (far end) is left open. In a single terminal test, only the near end is fitted with PD sensors while in a multi-terminal test, both the near end and the far end are fitted with PD sensors. PD sensors can be capacitive or inductive. Coupled PD signals produce voltage drops over corresponding measuring impedances. The voltage drops can be recorded, stored and analyzed by suitable signal processing devices. In case of the on-line PD detection, tests are carried out while the cable is in service. Both the cable ends are connected to the circuit/system. Sensor types 2, 3 and 4 in Figure 2.11 are generally employed [9].

Sensor type 1 is widely used in the off-line detection. Capacitive coupling is accomplished by connecting a high voltage capacitor to the cable's inner conductor at one end of the cable. The capacitor has to be PD-free at applied test voltages. The capacitor filters out the power frequency voltage but provides a low impedance path for short PD pulses. Measurement of the PD pulses is fulfilled by a detection impedance connected between the capacitor and the ground. Different impedances can be employed depending on specific applications. For example, for measuring apparent discharge, an impedance according to IEC 60270 [12] should be used. However, for PD location, commercially available systems usually have bandwidths in the 5 – 20 MHz range [9] and proper impedances have to satisfy the system bandwidths. Furthermore, for ultra wideband (UWB) measurement, a detection impedance needs to have a bandwidth of 100 kHz – 1 GHz [15].

Sensor of type 2, capacitive couplers, have mostly been seen in applications to cable accessories, especially the accessories of extra high voltage (EHV) cables [40; 41; 42]. A diagram of the capacitive coupler is shown in Figure 2.12. The sensor is formed by attaching a metallic foil on top of the outer semicon layer so that the foil forms a voltage divider between the inner and outer conductors. In other words, the cable capacitor is used as a coupling capacitor to filter the power frequency voltage and PD voltage pulses can be measured between the foil and the outer conductor. The sensors are applied to individual joints so that they have high sensitivities to PD in the joints. In practice, they are installed in the joints or on the cables close to them. A dual model, i.e., two capacitive sensors placed longitudinally or circumferentially in a joint or the adjacent cables, is often adopted to discriminate between PD in the joint and external noise. The bandwidth of this type of sensor can range from within several tens of MHz to

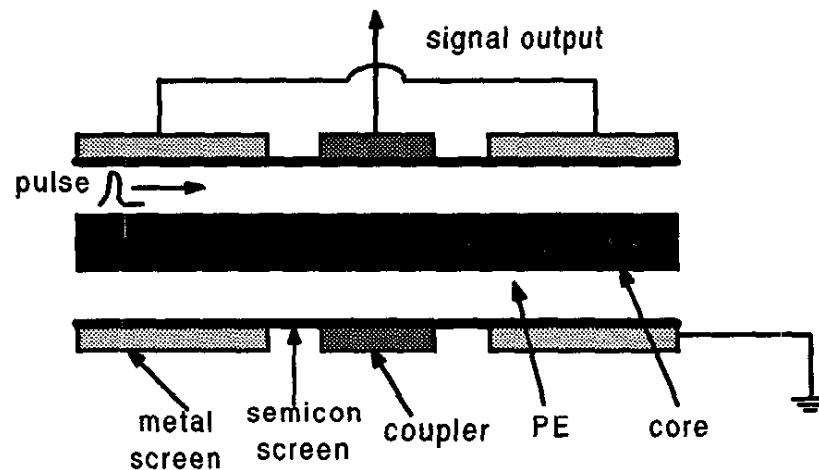


Figure 2.12: Schematic diagram of a capacitive coupler [43].

few hundred MHz [43; 44].

Sensor type 3 uses coils or high frequency current transformers to couple with PD induced magnetic fields around the cable. The magnetic fields are a result of non-ideal shielding effects of the cable outer conductor and/or non-uniform distributions of PD currents in the outer conductor. For cables with concentric neutral wire outer conductors, PD current pulses are forced to follow the helical wires and therefore result in a small magnetic field outside the cable [45]. Figure 2.13 shows the current direction on the cable's outer conductor and a coil sensor used to couple with the induced magnetic field. The coil sensor was reported to have a bandwidth up to 300 MHz [45]. For cables with solid or tape outer conductors, PD pulses are said to need to travel certain distances before the PD currents become uniformly distributed in the outer conductor and the initial non-uniform current distribution will result in a magnetic field outside the cable [46]. In this case, high frequency current transformers can be used to couple the magnetic field. The high frequency current transformers, i.e., sensor type 4, will be discussed in more detail in the following section.

Both sensor types 2 and 3 can be used in off-line detection as well as on-line detection. Both have a high sensitivity to a PD taking place in close proximity. Sensor type 2 has been widely used to detect PD in cable joints [47]. Electrodes of the sensor are either prefabricated in a joint or installed in the adjacent cables, for which modifications to the cable outer conductors are required. The coil version of sensor type 3 has the advantage that it can be directly clamped around the

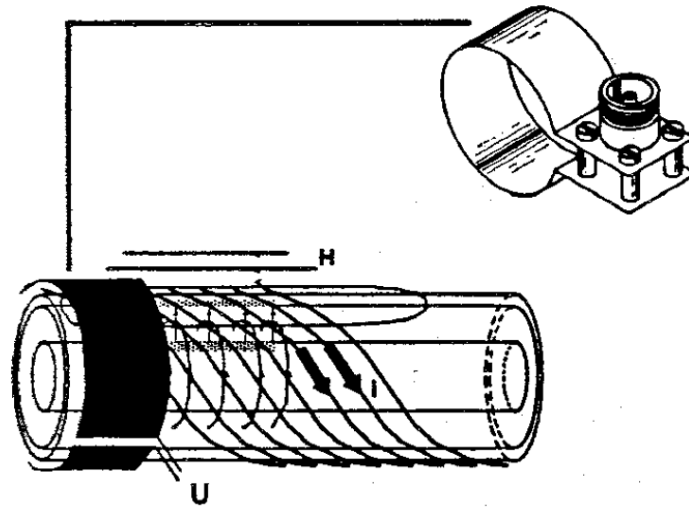


Figure 2.13: Coil around the plastic outer sheath of a cable having an outer conductor made of helical wires for PD detection [45].

plastic outer sheath of a cable and thus no modification of the cable is required. However, while both sensor types performed equally well under laboratory conditions, sensor type 3 had an appreciable increase in detection threshold when subject to high ambient noise levels under on-site conditions [48]. Sensor type 2's performance was not compromised under on-site conditions since the sensor was put underneath of the cable outer conductor and therefore was shielded from ambient noise.

All the sensors shown in Figure 2.11 are based on electromagnetic detection. On the other hand, acoustic detection has also been evaluated in terms of its effectiveness in PD detection and location for cables [49; 50]. While absorption of PD induced acoustic signal by the cable insulation is very high, and consequently the detection sensitivity has large reduction with distance away from the PD source, detection of the acoustic signal with a reasonable sensitivity is possible in the vicinity of the PD source. As a result, acoustic detection is sometimes being used for exact final location of PD sources in cable accessories [9]. Another advantage of acoustic detection is that it is inherently immune to electromagnetic interference and thus can be used in situations where electromagnetic detection is not effective because of electromagnetic interferences [8].



### 2.4.4 PD Detection using a Current Transformer

The sensor type 4 in Figure 2.11 is a current transformer (CT) of which a basic diagram is shown in Figure 2.14. The current transformer (CT) generates a

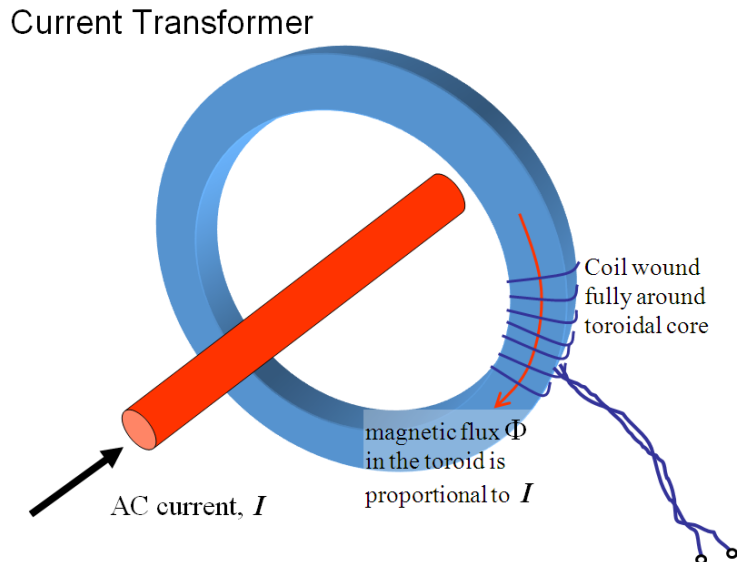


Figure 2.14: Diagram of a current transformer.

voltage in response to a current flowing through its aperture. The current induced magnetic field is inductively coupled to a coil in the CT to produce the voltage. Ideally, the voltage output is proportional to the current input. The theory of the CT will be presented in Section 6.1.

A typical design of the CT is a ferrite core wound with some coils and the coils are terminated with a load usually  $50\ \Omega$  for PD measurement. This kind of CT is called a high frequency current transformer (HFCT). Sometimes a split core is used and two parts of the core are hinged together, which will allow the HFCT being clamped onto a conductor without interrupting the circuit. The voltage output of the HFCT is proportional to the current flowing through it at a given fixed frequency. The ratio between the output voltage and the input current is defined as the transfer impedance (in volt/ampere or ohm) of the HFCT. Common HFCTs have bandwidths within tens of MHz but specialist HFCTs having bandwidths higher than 1 GHz are commercially available. Within the bandwidth limits, the HFCT usually has a flat frequency response, i.e., the transfer impedance remains constant with frequency. The HFCT can be used to measure very small currents, at the order of microamperes [51]. In addition, since there is

no direct connection to the circuit under test, the HFCT has the minimal impact on the circuit operation. These characteristics make the HFCT very attractive in practices of PD detection for cables. Both PD detection and location can be achieved. By installing around earth connections or cable conductors at terminations, the HFCT has been widely used to carry out on-line PD detection for cables [52; 53; 54; 55]. Figure 2.15 shows an on-site installation case of the HFCTs. PD location is mostly carried out off-line while a cable is disconnected from a circuit/system. This is both because of a reduced noise level and requirements of PD location methods. In order to effectively localize PD sites, specific location methods can be used to account for different situations [56; 57].

A Rogowski coil is another kind of CT commonly used as a PD sensor. Figure 2.16 shows an example of the Rogowski coil. It differs from the HFCT in that it normally uses a non-magnetic core. By using a non-magnetic core, the Rogowski coil cannot be saturated by large ac currents and its performance is not affected even by very large dc currents [59]. However, the non-magnetic core design makes the Rogowski coil less sensitive at low currents and low frequencies, which can be insufficient for detecting PD. To overcome this, some magnetic cores can be used to replace the air core [59]. The output voltage of the Rogowski coil is proportional to the rate of change of the current (i.e.,  $dI/dt$ ) on a conductor

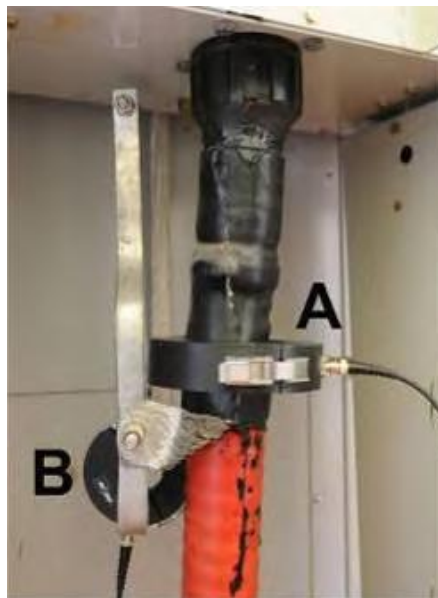


Figure 2.15: HFCTs installed on a 3 core 11kV cable, (A) around the cable conductor, (B) around the cable earth connection [55].



Figure 2.16: Rogowski coil placed in a metal enclosure [58].

through the coil. The Rogowski coil has been used to detect PD for both cable accessories and cables by installing around cable sections at joints or terminations, or around cable earth connections [58; 60; 61; 62].

The CT type of sensor, in particular the HFCT, has proved effective in both off-line and on-line PD detection for cables. Actually, while the coupling capacitor (sensor type 1 in Figure 2.11) or the HFCT are often used for off-line testing, on-line testing almost always uses an HFCT as the sensor [5].

## 2.5 Conclusions

Electrical ageing is the main ageing mechanism for polymeric-insulated cables. Although there are different causes of electrical ageing, all of them are likely to result in PD activities. PD is indicative of local insulation conditions of the cables. After PD excitation, a PD pulse will travel away from the PD site and propagate along a cable. The PD pulse is subject to attenuation and dispersion in the propagation process. The effect of dispersion was found to be insignificant when compared to that of attenuation. Attenuation to the PD pulse is a function of the distance propagated. After a few hundred meters propagation, the optimum detection bandwidth of a PD pulse can decrease from hundreds of MHz to around 10 MHz.

PD measurement for HV cables can be carried out both off-line and on-line. Various PD sensors are available to couple the PD signal capacitively or inductively. Among the sensors, the CT type of sensor, especially the HFCT, is a particularly convenient one that has found widespread use in PD detection for the cables. HFCTs are quite often applied at cable terminations where the cable

---

conductors and earth connections are accessible. Detected PD signals are subject to changes caused by the processes of PD coupling (from source sites onto cable conductors), propagation and detection. This can make it difficult to interpret the PD measurement results. Investigating the relationship between the PD currents excited at PD source sites and the PD measurement results from HFCTs experimentally is both difficult and limited. Exploring this problem through modelling is potentially advantageous and a possible approach is introduced in the next chapter.

# Chapter 3

## FDTD Methodology and its Application in PD Modelling

### 3.1 Introduction

Finite-Difference Time-Domain (FDTD) methods are used in electrodynamics as a numerical modelling technique to solve EM waves problems. They are based on discretizing and solving Maxwell's equations, and since first application to electromagnetic waves by Yee in 1966 [63], they have found more and more applications in scientific and engineering problems dealing with interaction of electromagnetic fields with surrounding objects, for example, in antenna design, radar, wireless communication, electromagnetic medical devices, earth/ionosphere models in geophysics and so on. Being a time domain technique, FDTD solutions for transient responses can be converted to the frequency domain to cover a wide frequency range with one single simulation run, which is ideal for simulating partial discharge (PD) pulses, a kind of broadband pulse.

In this chapter, there is a brief review of FDTD applications in the power industry and in solving electromagnetic problems, the FDTD technique's development since its first introduction and a brief review of its basic algorithm. After that, an application to PD measurement for GIS (which resembles a cable in a larger scale but with a simpler structure) will be described. The final objective of this chapter is to examine various aspects of using the FDTD technique to investigate PD measurement for high voltage (HV) cables and draw some conclusions and suggestions on this topic.

## 3.2 Review of FDTD Applications in Power Industry

The FDTD technique was found to be a useful tool within the field of studies on high voltage (HV) insulation systems and PD monitoring techniques by Judd in 2000 [64]. The FDTD technique was illustrated by these concepts:

- Modelling of PD excitation, propagation & detection.
- PD simulated as a current pulse between nodes in the FDTD mesh.
- Resulting electric charge dipole in the insulation corresponds to space charge.
- Radiated electric fields on the coaxial cross section of a GIS could be evaluated.

For example, Figure 3.1 shows PD induced electric fields on a cross section of a 400 kV GIS. Generally, good agreement between simulations and either theoretical or experimental results was obtained and potential future applications of FDTD in this field were discussed [64]. Pommerenke and Sakaguchi [65] indicated that because of the large dimensions of structures like a GIS or a SF<sub>6</sub> insulated transmission line as well as complex structures like GIS elbows and HV cables incomplete shields and joints, electromagnetic (EM) wave propagation will have,

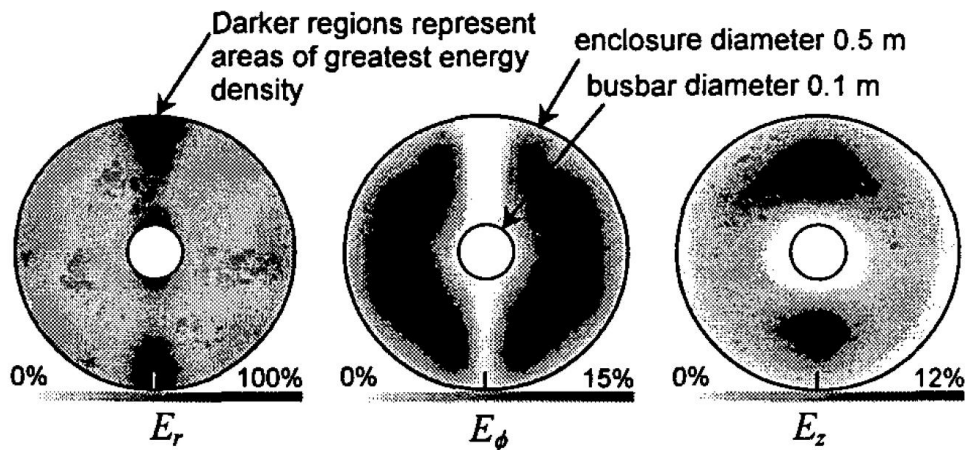


Figure 3.1: Electric field distribution on a cross section through a 400 kV GIS at 1.2 m from a PD source at the bottom of the GIS. The shading intensity of each plot is scaled relative to that of the radial component,  $E_r$  [64].

other than the TEM mode, higher modes (i.e., TE and TM modes) and will result in complicated phenomena that cannot be well predicted by theoretical analysis or circuit theory approximation based simulations that can only deal with TEM waves. It is, therefore, necessary to move on to use “Maxwell solvers” which can provide approximation solutions to Maxwell’s equations. The available “Maxwell solvers” were summarised and possible error sources involved in simulations were discussed. A list of questions were proposed to enable a proper selection of suitable methods for specific applications and moreover, for the FDTD technique, some rules were suggested to help achieve trustworthy results [65].

After being introduced to this field, the FDTD technique quickly spread and has been used in modelling of PD in GIS, PD in transformers and other power industry problems involving fast transients, which will be discussed in the next sections. However, it seems there have been relatively few contributions of using FDTD to model PD in high voltage (HV) cables particularly in recent years.

### 3.2.1 FDTD Modelling of PD in GIS

Modelling PD in GIS is believed to be one of the initial applications in this field, where the FDTD technique has been used to simulate PD-induced EM waves with special regards to those in the ultra high frequency (UHF) band (i.e., 300 MHz - 3000 MHz). Recent research has mainly been carried out by Japanese researchers. For example, Okabe et al. [66] investigated PD induced EM waves, regarding different modes excited (e.g., TEM, TE<sub>11</sub> and TE<sub>21</sub>) and PD excitation directions, their propagation characteristics in an L-shaped section of GIS by FDTD simulations. Experiment results shown for the TE<sub>11</sub> mode agreed with the simulated propagation and resonance characteristics. The L-shaped section was found to result in mode conversions after the EM waves propagated through the junction and make the propagation characteristics of the EM waves differ significantly with the PD excitation directions. Hikita et al. [67] compared the EM waves propagation in an L-shaped section of a GIS to that in a straight section by using FDTD modelling. It was summarised that while the attenuation to the EM waves in the L-shaped section was mainly resulting from higher modes reflection and conversion, the attenuation in the straight GIS where there was no reflection was attributed to the effect of the higher modes velocity dispersion. This work was followed by two contributions [68; 69] in which the problem was investigated by experiments with a 66 kV model GIS and a 154 kV model GIS

respectively. FDTD modelling was conducted in parallel and the combination of the experimental and simulation results showed that the TEM mode was not reflected at the L-shaped section while the high frequency components above the cut-off frequency of the TE<sub>11</sub> mode were reflected.

In another contribution [70], a method of locating adhering metallic particles in GIS (i.e., if a particle is on the centre conductor or on the tank) was proposed based on solely judging the time duration of the measured EM waves emitted by the particle-generated PD. The method was evaluated by FDTD modelling on a 66 kV GIS and a 500 kV GIS respectively and was found to be more effective for larger tank dimensions and smaller particle sizes. Yoshimura et al. [71] moved on to investigate the EM waves propagation and associated mode conversions (between TEM, TE<sub>11</sub> and TE<sub>21</sub>) in a T-branch section of a GIS. FDTD simulations were carried out to predict the mode conversions due to the EM waves propagation through the T-branch and the findings were confirmed by experiments. A comparison between the FDTD models of a T-branch section and an L-shaped section showed that the mode conversion characteristic of the TE<sub>11</sub> mode was similar in the two sections.

Instead of only modelling the GIS centre conductor and tank, Hoshino et al. [72] created a complete FDTD model for UHF PD detection in a GIS in which insulators and disc UHF couplers in the GIS were also included, and by precise modelling of the components, the model was believed to be capable of calibrating sensitivity of UHF couplers by only using modelling, i.e., in the absence of measurement. Fast fourier transform (FFT) and transmissivity of the obtained EM waves were compared to show that the simulations generally agreed with the experiments. In addition, leakage of the EM waves through an insulator spacer was also investigated by using the FDTD model suggesting that it was difficult for TEM modes to leak from the spacer. Apart from spaces and insulators, there are disconnecting parts within a GIS, e.g. a circuit breaker and a disconnecter. Hikita et al. [73] investigated the disconnecting part's influence on PD-induced EM waves propagation by using a 66 kV model GIS and inserting different lengths of gap into its centre conductor and measuring the EM waves at positions before and after the gap. The experiments showed no TEM wave could travel through the gap and there was a tendency that with the increase of the gap length the cutoff frequency of the EM waves that propagated through the gap also increased. This tendency was further recognized in the FDTD simulations in which the gap



length was varying step by step to show dependence of the cutoff frequency on gap length.

FDTD modelling has already been used to study various issues involved in PD phenomena in GIS, while in some cases experiments were conducted and simulations were carried out for comparison [68; 69]. Other typical application of FDTD modelling is to optimise UHF couplers installation positions on the GIS tanks so as to achieve better detection and location of PD. Hu et al. [74] used FDTD modelling to investigate PD location accuracy problems in a GIS T-branch and a GIS circuit breaker. Electric fields generated by a PD source were measured at different positions around the circumference of the GIS tanks and were used in locating the PD source. Finally, an improved coupler installation scheme was proposed for achieving better PD location accuracy in the investigated GIS.

### 3.2.2 FDTD Modelling of PD in Transformers

Judd et al. [75] reviewed PD monitoring for power transformers using the UHF method, in which topics from excitation of UHF signals by PD in transformers and the UHF signal propagation in the transformers to PD detection by externally installed UHF couplers and analysis of the UHF signals to determine the arrival times for PD location were discussed. A very simple transformer FDTD model including a metal tank, a bushing, an HV conductor with a PD source at one end and a UHF coupler was used to allow visualization of the excitation and detection of the PD-induced UHF signals (see Figure 3.2).

A power transformer is made up of various components like iron cores, windings and bushings which can make the propagation of the PD-induced EM waves inside the transformer very complicated. It is, therefore, convenient to make use of FDTD modelling to predict the EM waves propagation in the transformer and the resulting attenuation and distortion subject to the presence of the transformer components. Yang et al. [76] created a simplified transformer model consisting of a tank, oil insulation, a gasket and a hatch plate and carried out FDTD simulations to find out the best position for installing UHF couplers. Furthermore, the presence of the bolts fastening the hatch plate, the gasket and the tank was found to decrease the UHF signals in their adjacent area. Tang et al. [77] used a current filament to represent a PD source in the FDTD simulations and analyzed the relation between the pulse width and total charge of the PD current pulse and the magnitude of the excited EM waves. A conductor cylinder and spiral coils

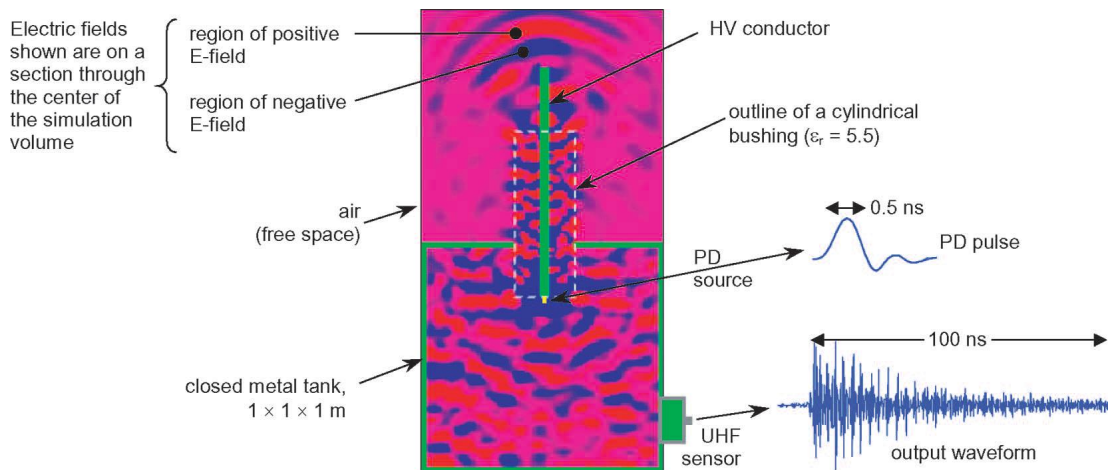


Figure 3.2: Visualization of the basic principles of UHF PD detection in a transformer. The PD-induced electric field is detected by a UHF sensor mounted on the tank [75].

were respectively created in a transformer tank to investigate the obstruction's effect on the propagation of the EM waves.

More recently, Ishak et al. [78] created a cylinder and a cuboid metal obstacles in the centre of a transformer tank and a PD source and a detection point were respectively put at each side of the obstacle. With PD excited along different directions, it was observed that the obtained arrival time differences varied to different extents from theoretical values. Wang et al. [79] created a simplified converter transformer model which consisted of a tank, oil, cores and windings, tap switches and bushings. Another model including only the tank, oil and the bushings was used to allow comparison research into the EM waves propagation with and without the transformer's internal components. Sensors were arranged at different positions aiming to find out the optimal UHF sensor installation position where the highest magnitude and energy of the EM waves can be retained. In order to account for transformer winding's complicated structure, Zhao et al. [80] used an FDTD model with only a small part of the winding (10 turns and 4 segments) with each turn bound by oil paper. A PD source was put within oil paper between turns, in oil between two segments and in oil outside of the winding respectively and the EM waves were recorded at the positions with different distance to the winding to show the winding's effects on the UHF signals excited by PD at different positions.

A review of the state of art of radiometric PD detection was given by Judd in [81]. Applications of radio frequency (RF) PD detection in power industry

were summarised and some research challenges and opportunities in this field were presented. A spiral antenna model was used to show that the step response obtained by the FDTD simulation agreed well with the measured signal in magnitude. There was an expectation that modelling techniques would be more and more used in assisting with the design process of UHF sensors to help improve their response characteristics.

Reid et al. [82] tested three designs of UHF PD sensor by obtaining their responses to a step electric field from both measurement and FDTD simulations. Results showed reasonable agreement in the response peak-to-peak voltages and the differences between the responses were attributed to simplification in the models and inaccurate geometry modelling caused by discretizing the three-dimensional models with cubic cells. It was summarised that FDTD modelling can be employed in the design stage of a sensor to predict the sensor's response and this should benefit the design process of new sensors with reducing the development time. The feasibility of using FDTD modelling to predict UHF PD sensor's response was further evaluated by Ishak et al. [83], in which two types of existing sensor together with a UHF sensor calibration rig were modelled and the results showed good agreement between the simulation and measurement in both the output voltages from the sensors and their frequency responses. Permittivity of the sensor material and the sensor dimensions were varied in the simulations to show it would be easier to test different designs in software than to physically get them made and tested. These examples illustrate the FDTD method as an effective tool in designing UHF PD sensors.

### 3.2.3 FDTD Modelling of PD in HV Cables

Field PD sensors are usually installed directly on or in HV cables or cable accessories to couple EM fields radiated by a PD. Sensitivities in detecting PD can depend on a lot of factors like sensor geometries, materials and installation positions, as well as propagation characteristics of the cables. Experimentally optimising the sensors sensitivities is both laborious and time consuming, of which the situation is similar to those in optimising design and installation of UHF PD sensors for a GIS or a transformer.

Solving the problem through FDTD modelling has already been much sought after by some researchers. Heinrich et al. [84; 85] investigated the optimisation of radial symmetric sensors which would be attached on the outer semi-conductive

layer of an XLPE cable. A two-dimensional FDTD model was created for the sensors. The sensitivities of the sensors with varied length and thickness were evaluated by both simulations and experiments. The results showed good agreement considering the fact that the semi-conductive layer's dispersive properties and some of the cable details were not yet taken into account. Furthermore, magnetic field distribution in the cable and the sensor was visualized for different time steps, which should assist with understanding the coupling process of the sensor. Pommerenke et al. [86; 87] created a three-dimensional FDTD model for a silicone rubber 110 kV cable joint to evaluate different sensor configurations performance of PD detection for the cable joint. The joint model was found to be in agreement with measurements in attenuation factors up to 400 MHz although dispersion was not taken into account for the semi-conductive objects in the model, which was achieved by adjusting effective values for the semi-conductive materials properties in the modelling process until the best match between simulations and measurements was achieved. Five sensor configurations were investigated with the cable joint model and their sensitivities in PD detection for the cable joint were compared, which showed that FDTD modelling was effective in finding out the optimal coupling sensor configuration for PD detection even if a complex object like a cable joint was involved. PD location, noise discrimination and charge estimation, all of which can be fulfilled by FDTD simulations, were suggested as further information to assist in the optimisation/comparison of the coupling sensors.

Semi-conductive (semicon) layers in HV cables relieve the electric field concentration between conductor and insulation. Semicon materials have frequency-dependent dielectric properties, which if handled with the normal FDTD method will involve running separate simulations for each frequency of interest and furthermore the materials can have very high permittivity of 1000s at low frequencies which means far more cells will be required in FDTD models and result in an excessive increase in calculation load. Unfortunately, properly accounting for the semicon layers is essential if high frequency properties of the cables are of concern. Jobava et al. [88] proposed a simple alternative to the FDTD method. Assuming the multiple dielectric layers of a cable were replaced by a single homogenous layer of either semicon or insulation, corresponding characteristic impedances were calculated and averaged by weight to obtain the characteristic impedance of the cable. After that, the propagation constant was calculated and by using

transmission line theory, signals propagating in the cable were evaluated. Both experiments and FDTD simulations were carried out to verify the calculation results by the proposed method.

Similarly dealing with the effects of cable semicon layers and stating that an existing transient analysis program like Electro-Magnetic Transients Program was not sufficient in this case, Baba et al. [89] used FDTD modelling to investigate, with the semicon layers set to different conductivities, transient responses of a cable. Not only the transient responses but also the propagation velocity in the cable were found to depend on the semicon conductivities. A chart was presented to suggest in what conductivity range shall the cable's equivalent series impedance and shunt admittance be calculated with or without considering the effects of the semicon layers. The results were expected to be useful in developing distributed circuit models for HV cables, and it was indicated that the shunt admittance of the semicon layers should be represented by both conductance and capacitance, which is in agreement with the lumped circuit model proposed for HV cables by Stone and Boggs [30].

However, both the simple method or distributed circuit models are based on transmission line theory and therefore will be limited to TEM wave analysis. In order to enable full wave analysis by FDTD modelling, Jobava et al. [90] used a hybrid method in computing a two-dimensional FDTD cable model consisting of inner and outer conductors, inner and outer semicon layers and an XLPE insulation layer, where the semicon was especially treated with a dispersive algorithm while the rest of the model was using the normal non-dispersive FDTD algorithm. The frequency-dependent dielectric properties of the semicon were measured and fitted by a 1 pole Debye medium's expression. Comparisons between an FDTD simulation with the proposed hybrid scheme, the normal FDTD method with separate runs to account for each frequency and actual measurement showed good agreement in producing the cable attenuation factor with frequency. The proposed hybrid method was expected to be able to improve efficiency in FDTD modelling of HV cables when including dispersion effects resulting from the semicon layers.

Power cables can be directly buried (e.g., in soil) and therefore the cables will be subject to changes of temperature and humidity in the surrounding area. The surrounding changes can have effects on the cable insulation, for example, water trees grown in XLPE cables are results of specific humidity levels under which

the trees will not develop, as well as high frequency properties of the cables. Papazyan et al. [91] found in their experiments that above 70 MHz the propagation characteristics of a cable were apparently influenced by the surrounding medium. They moved on to create three-dimensional FDTD cable models with helical wire screens and straight wire screens and compare the propagation characteristics from the models. When they were put in different surrounding media, it was observed that the helical wire screen model was affected by the surrounding media while the straight wire screen model was not. The problem was further discussed in [92] where modal analysis of wave propagation was included to confirm findings from the experiments and the FDTD simulations. Differences resulting from pitch angles of the helical wire screens, permittivities and conductivities of the surrounding media were considered by further FDTD simulations. A comparison between FEM and FDTD methods for calculating the cable attenuation constant showed FEM agreed ideally with the analytical result while FDTD tended to have a larger error. However, for carrying out relative studies like in this case comparing effects of different screen designs on the propagation characteristics of the cable, the objective was not compromised by the less accuracy achieved by the FDTD method. Moreover, the robustness, affordable computation load and simpler graphical user interface (GUI) for modelling complex structures like cable helical wire screens were emphasized as additional advantages of the FDTD method. Figure 3.3 shows the cross sections of a two-dimensional (2D) FEM model and a three-dimensional (3D) FDTD model for a 12 kV XLPE cable respectively. While the 2D FEM model could only model the separation between

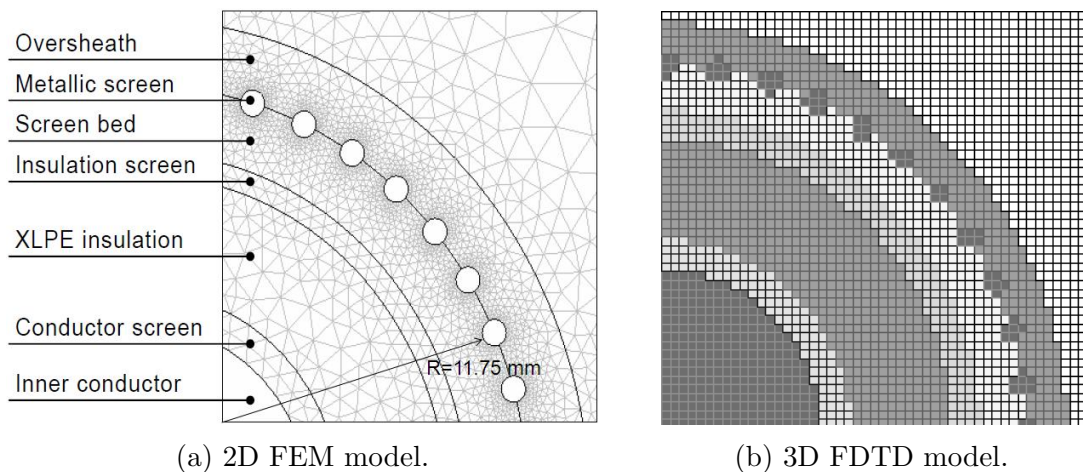


Figure 3.3: FEM and FDTD gridding on the cross section of a 12 kV XLPE cable [92].

the metallic screen wires, by the 3D FDTD model spiralling of the screen wires in the longitudinal direction was considered.

While topics like sensitivity optimisation of field PD sensors and high frequency properties of HV cables have been much visited, little attention has been paid to PD excitation in cables, propagation along the cables and detection of PD-induced currents using the PD sensor like high frequency current transformers (HFCTs). It is the objective of this research to study these problems and try to provide HV cable insulation diagnostics based on PD detection with some knowledge to improve interpretation of PD measurement results obtained in the field.

### 3.2.4 Other Applications in Power Industry

FDTD modelling has seen applications in power industry across the areas where electromagnetic field distribution issues are of concern. Three typical application examples are mentioned here.

Electromagnetic compatibility of equipment is going to be tested under specified electromagnetic conditions to guarantee that the equipment can cope with actual electromagnetic environments in the real world. For example, resistance to electrostatic discharges is usually tested by using an electrostatic discharge (ESD) simulator. Wang et al. [93] developed an FDTD model for ESD simulators by which the current and field resulting from the ESD simulators can be predicted. Apart from creating basic structure of an ESD simulator, the model physically included lumped resistors and capacitors (for example, a capacitor was modelled by a dielectric sandwiched by two metal conductors, see Figure 3.4). The simulated ESD output currents and radiated fields agreed well with measurement results. The model was considered suitable for parametric studies and investigating ESD radiated fields interaction with other structures.

Predicting and evaluating electromagnetic field distribution in a high voltage substation is essential for both planning and operation of the substation. In particular, switching operations of circuit breakers and disconnecting switches can result in transient currents and the currents will excite transient electromagnetic fields that will present a challenge for the normal functionality of electronic equipment. It is, therefore, advisable to account for the issue at the design stage of the equipment so as to prevent them from malfunctioning in the substations. Musa et al. [94] used FDTD modelling to determine, following transient currents on one

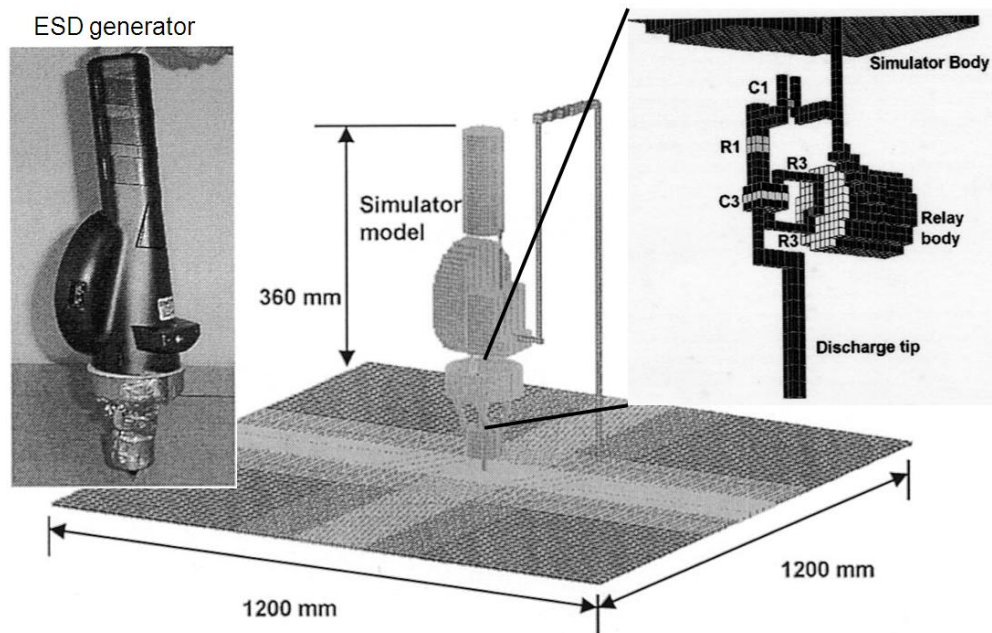


Figure 3.4: ESD generator and its FDTD model. The zoomed in view on the right shows some details of the generator head in the model. “C” and “R” represent the physically modelled capacitance and resistance respectively [93].

bus bar, the resulting electric and magnetic field strength at different positions under the bus bar, where three bus bars were modelled to represent a typical situation in a high voltage air-insulated substation. Transient electromagnetic fields were found to be dependent on factors like distance to the bus bars, spectra of the transient currents and ground conditions. Potential applications like modelling a complete high voltage air-insulated substation model with circuit breakers and disconnecting switches connected to the bus bars to conduct electromagnetic compatibility studies were envisaged.

Wind turbine generators are usually installed at solitary locations like on a hill or offshore on the sea so as to make most out of the wind power without being influenced by obstacles like mountains and buildings. This also makes the turbines likely be struck by lightning, which will result in ground potential increase that may cause damage to electronic equipment inside and surrounding the turbines. Therefore, protection against lightning is very important for wind turbine generator systems. Yamamoto et al. [95] carried out impulse tests on an actual wind turbine generator and in accordance with the test setup created a wind turbine FDTD model to investigate the ground potential increase around the



wind turbine foundation following a transient current injection. Good agreement between the tests and the simulations was observed for the voltage magnitudes measured around the turbine foundation. Furthermore, simulations were carried out to consider individually (only the ground system modelled) the ground system's transient response. A transfer function was obtained from the simulations, which would enable working out the ground potential increase caused by any type of lightning waveform.

### 3.3 Electromagnetic FDTD Technique

#### 3.3.1 Development of the FDTD Technique

Accurate determination of electromagnetic fields within a region and interactions of the fields with material bodies can be achieved by using Maxwell's equations. However, exact analytical solutions only exist for simple regions and bodies like a cube, a sphere and a cylinder. For arbitrary shape problems, numerical methods normally have to be used.

In 1966, Yee [63] made the first contribution to apply the finite-difference time-domain (FDTD) technique to solving Maxwell's equations, after which FDTD has grown in popularity for solving time domain electromagnetic field problems. It is implemented by introducing a space mesh in the volume of interest and replacing Maxwell's equations with a set of finite difference equations. Figure 3.5 shows the Yee cell, which remains at the core of many FDTD codes. Yee managed to apply this method to isotropic, non-dispersive media with perfect conductor boundary conditions. He devised a two-dimensional model in which incident TM waves would be diffracted by a conducting square and obtained results comparable to those given by closed form solutions to a similar question. However, Yee did not get the algorithm's stability condition right. Based on Yee's algorithm, Taflove [96] derived the correct stability condition. Errors of the FDTD technique were evaluated by solving a two-dimensional problem and comparing with exact analytical solutions, which showed maximum errors of 10%. It is in Taflove's work in 1981 [97] that the "FD-TD" acronym was first used.

Figure 3.6 shows an example of using FDTD to investigate an F-111 aircraft's responses to severe electromagnetic incidents like lightning or an electromagnetic pulse caused by a nuclear burst. The FDTD model of the aircraft (without internal components, i.e., only the aircraft fuselage) used three-dimensional rect-

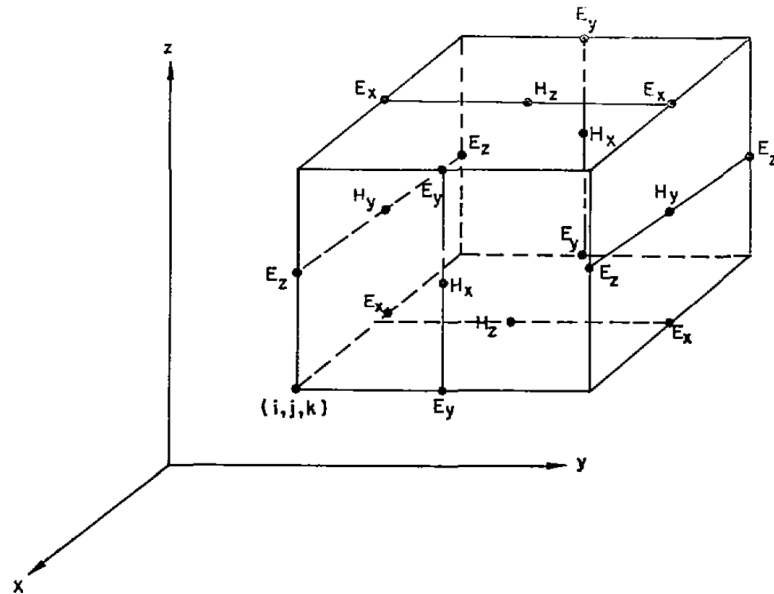


Figure 3.5: Original Yee cell illustrated in [63]. Both electric fields  $E$  and magnetic fields  $H$  are divided into  $x$ ,  $y$  and  $z$  components in according to the Cartesian coordinate.  $(i, j, k)$  is a simplification of  $(i \times \Delta x, j \times \Delta y, k \times \Delta z)$  where  $\Delta x$ ,  $\Delta y$  and  $\Delta z$  are the space step on the  $X$ ,  $Y$  and  $Z$  axes respectively.

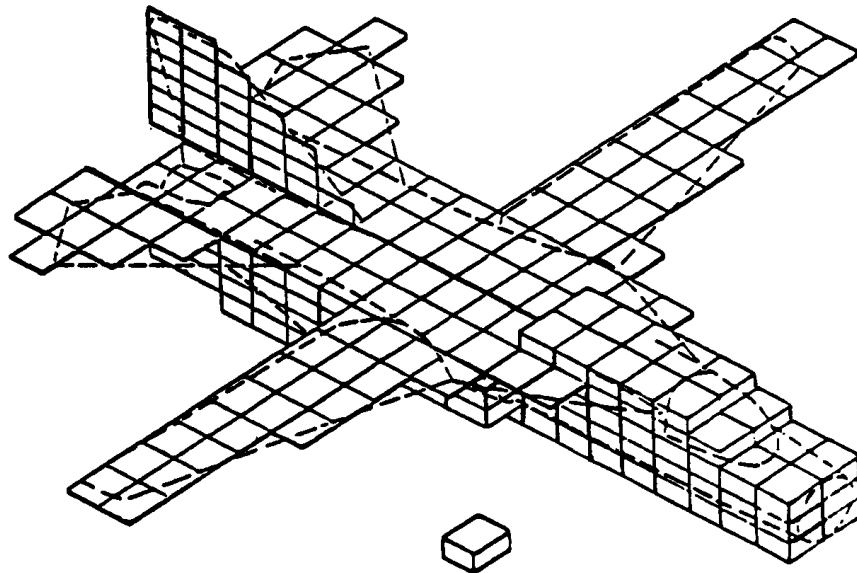


Figure 3.6: F-111 aircraft FDTD model [98].

angular cells having dimensions of  $\Delta x = 1$  m,  $\Delta y = 0.5$  m and  $\Delta z = 1$  m and had  $28 \times 28 \times 28$  cells in total. Non-square cells were used so as to have improved modelling of details in the  $y$  direction. The aircraft model was placed at the centre of the problem space and there was a certain number of cells between any of the model's extremities and the outer edges of the space where the radiation boundary condition was applied [98].

One main difficulty of using the FDTD technique to solve field problems is that the domain in which the fields have to be computed is often unbounded. In practice, the computed domain must be limited since no computer has an infinite data storage capacity. Therefore, a method has to be used to not only limit the computed domain but also make the domain boundary look as if it is unbounded to the fields propagating towards it. This kind of method is called absorbing boundary conditions. Yee [63] used "hard" truncation in boundary conditions, which would reflect outgoing waves in a way that the surface of a conductor does. Taflov [96] then proposed a "soft" truncation boundary condition, which could reduce boundary reflections significantly. However, in extension to three-dimensional problems, the "soft" boundary condition in conjunction with the three-dimensional FDTD formulations would tend to be unstable. Mur [99] proposed a highly absorbing boundary condition (ABC) that can be used for both two- and three- dimensional electromagnetic field problems. The first and the second order approximations of the proposed boundary conditions were derived and the relevant FDTD formulations were produced. The results of a two-dimensional problem showed for the second order boundary condition that waves propagating towards the boundary were well absorbed once the excitation source was 5 nodes or more from the boundary of the mesh. Moreover, a method for resolving incident fields was proposed by considering the question region as a total field domain that computes total fields, surrounded by a scattered field domain that computes scattered fields and applies absorbing boundary conditions [99].

There is an alternative ABC, which is created by adding lossy material layers outside the domain boundaries and by properly configuring the layers properties so that they will be perfectly matched to the FDTD domain, i.e., being reflectionless for any outgoing waves. This technique is called perfectly matched layer (PML) and was first proposed by Berenger [100]. Berenger's PML theory was described as splitting each electric and magnetic field component into two orthogonal subcomponents, which leads to modified Maxwell's equations and means the

PMLs are made of materials that cannot be physically realized. Berenger's PML requires to modify the FDTD formulations in the PMLs and makes it difficult to have a physical insight into the PML's mechanism. Therefore, replacing the PML material with a uniaxial anisotropic material which is according to Maxwell's equations was suggested by Sacks [101] and Gedney [102]. By properly choosing the anisotropic constituent material properties, the plane between the FDTD domain and the PMLs can be perfectly reflectionless. This approach was found to be physically and mathematically equivalent to Berenger's PML but is more straightforward in application and more computationally efficient. Furthermore, the uniaxial PML can be readily extended to nonorthogonal FDTD methods and other computational electrodynamic methods such as finite-element methods. Besides the PML boundary, another commonly used ABC is the LIAO boundary [103]. It is based upon space-time extrapolation of the fields adjacent to the computed domain boundary and is therefore an estimation method. LIAO boundary absorption is not as ideal as the PML boundary but it does not need extra layers outside the computed domain, which results in far less memory requirement and calculation load.

Being a time domain method, the FDTD technique is able to cover a wide frequency range and therefore is particularly suitable for modelling broadband signals like pulses. If a pulse is used as an excitation source in an FDTD model, wide band frequency results can be easily obtained from a single simulation run followed by the fast Fourier transform (FFT). However, the FDTD formulations require that the constituent material parameters of permeability  $\mu$ , permittivity  $\varepsilon$  and conductivity  $\sigma$  are all constants. This actually undermines the FDTD's capability of covering wide band frequencies because many materials of interest have properties that vary significantly with frequency.

One way of addressing this issue is by making separate computer runs with each run covering a narrow frequency range and using relevant constituent parameters. This method is flawed and makes it difficult to accurately model highly dispersive materials, since one would have to use sinusoidal excitation at each frequency and run for much longer to reach steady-state conditions. Therefore, a frequency-dependent FDTD formulation ((FD)<sup>2</sup>TD) for dispersive materials was proposed by Luebbers [104]. This is achieved by a modification of the Yee FDTD formulations to account for materials with frequency-dependent complex permittivities. The corresponding frequency information is Fourier transformed

to a time-domain function so that it can be computed in the modified FDTD formulations. Results of using the modified formulations to compute reflection coefficients on an air-water interface for which permittivity and conductivity vary significantly with frequency were in excellent agreement with the exact analytical results, while the results by the traditional FDTD formulations using constant permittivity and conductivity showed significant deviation. Although only frequency-dependent permittivity was considered, extension to frequency-dependent permeability in a lossy magnetic medium is straightforward. The ((FD)<sup>2</sup>TD) improvement makes it possible to consider almost any materials in an FDTD model.

### 3.3.2 Basic Algorithm of the FDTD Technique

Maxwell's equations relating electric fields  $E$ , magnetic fields  $H$ , electric flux density  $D$  and magnetic flux density  $B$  in an isotropic medium are shown as follows:

$$\frac{\partial \mathbf{B}}{\partial t} + \nabla \times \mathbf{E} = 0 \quad (3.1)$$

$$\frac{\partial \mathbf{D}}{\partial t} - \nabla \times \mathbf{H} = \mathbf{J} \quad (3.2)$$

$$\nabla \cdot \mathbf{D} = \rho \quad (3.3)$$

$$\nabla \cdot \mathbf{B} = 0 \quad (3.4)$$

where  $\mathbf{J}$  is the total current density and  $\rho$  is the total charge density. The constitutive relations are:

$$\mathbf{D} = \varepsilon \mathbf{E} \quad (3.5)$$

$$\mathbf{B} = \mu \mathbf{H} \quad (3.6)$$

where  $\varepsilon$  and  $\mu$  are the permittivity and the permeability of the medium respectively. By substituting the constitutive conditions into (3.1) and (3.2), and considering a free space problem where  $\mathbf{J} = 0$  and  $\rho = 0$ , we obtain:

$$\frac{\partial \mathbf{H}}{\partial t} = -\frac{1}{\mu_0} \nabla \times \mathbf{E} \quad (3.7)$$

$$\frac{\partial \mathbf{E}}{\partial t} = \frac{1}{\varepsilon_0} \nabla \times \mathbf{H} \quad (3.8)$$

where  $\varepsilon_0$  and  $\mu_0$  are the permittivity and the permeability of free space respectively.  $\mathbf{E}$  and  $\mathbf{H}$  are three-dimensional vectors so in (3.7) and (3.8) each expression actually includes three equations, which, represented in Cartesian coordinate are:

$$\begin{aligned} \frac{\partial}{\partial t}(E_x\vec{x} + E_y\vec{y} + E_z\vec{z}) = \\ \frac{1}{\varepsilon_0} \left[ \left( \frac{\partial H_z}{\partial y} - \frac{\partial H_y}{\partial z} \right) \vec{x} + \left( \frac{\partial H_x}{\partial z} - \frac{\partial H_z}{\partial x} \right) \vec{y} + \left( \frac{\partial H_y}{\partial x} - \frac{\partial H_x}{\partial y} \right) \vec{z} \right] \end{aligned} \quad (3.9)$$

$$\begin{aligned} \frac{\partial}{\partial t}(H_x\vec{x} + H_y\vec{y} + H_z\vec{z}) = \\ -\frac{1}{\mu_0} \left[ \left( \frac{\partial E_z}{\partial y} - \frac{\partial E_y}{\partial z} \right) \vec{x} + \left( \frac{\partial E_x}{\partial z} - \frac{\partial E_z}{\partial x} \right) \vec{y} + \left( \frac{\partial E_y}{\partial x} - \frac{\partial E_x}{\partial y} \right) \vec{z} \right] \end{aligned} \quad (3.10)$$

where  $\vec{x}$ ,  $\vec{y}$  and  $\vec{z}$  are unit vectors for  $\mathbf{X}$ ,  $\mathbf{Y}$  and  $\mathbf{Z}$  axis respectively. Considering a one-dimensional (1D) problem of a plane wave travelling in the  $z$  direction having  $E_x$  and  $H_y$  and other  $E$  and  $H$  components as zero, (3.9) and (3.10) then become

$$\frac{\partial E_x}{\partial t} = -\frac{1}{\varepsilon_0} \frac{\partial H_y}{\partial z} \quad (3.11)$$

$$\frac{\partial H_y}{\partial t} = -\frac{1}{\mu_0} \frac{\partial E_x}{\partial z}. \quad (3.12)$$

Replacing both the time and space derivatives in (3.11) and (3.12) with corresponding finite difference approximation, we get

$$\frac{E_x^{n+1/2}(k) - E_x^{n-1/2}(k)}{\Delta t} = -\frac{1}{\varepsilon_0} \frac{H_y^n(k+1/2) - H_y^n(k-1/2)}{\Delta x} \quad (3.13)$$

$$\frac{H_y^{n+1}(k+1/2) - H_y^n(k+1/2)}{\Delta t} = -\frac{1}{\mu_0} \frac{E_x^{n+1/2}(k+1) - E_x^{n+1/2}(k)}{\Delta x} \quad (3.14)$$

where  $n$  and  $k$  represent indices for discretised time  $t = n \cdot \Delta t$  and space  $z = k \cdot \Delta x$ . (3.13) and (3.14) can be rearranged so that the unknown values and the known values fall on separate sides of the equations

$$E_x^{n+1/2}(k) = E_x^{n-1/2}(k) - \frac{\Delta t}{\varepsilon_0 \cdot \Delta x} [H_y^n(k+1/2) - H_y^n(k-1/2)] \quad (3.15)$$

$$H_y^{n+1}(k+1/2) = H_y^n(k+1/2) - \frac{\Delta t}{\mu_0 \cdot \Delta x} [E_x^{n+1/2}(k+1) - E_x^{n+1/2}(k)]. \quad (3.16)$$

It can be seen in (3.15) and (3.16) that the field components are updated in a way that takes the previous time-step's values and includes contributions from the surrounding components of the other field such that the calculation is interleaved both in time and space. This is the basic working mechanism of the FDTD method. The interleaving in time and space of the algorithm, which is also known as solving for  $E$  and  $H$  in a 'leapfrog' manner, is visualized in Figure 3.7 [105].

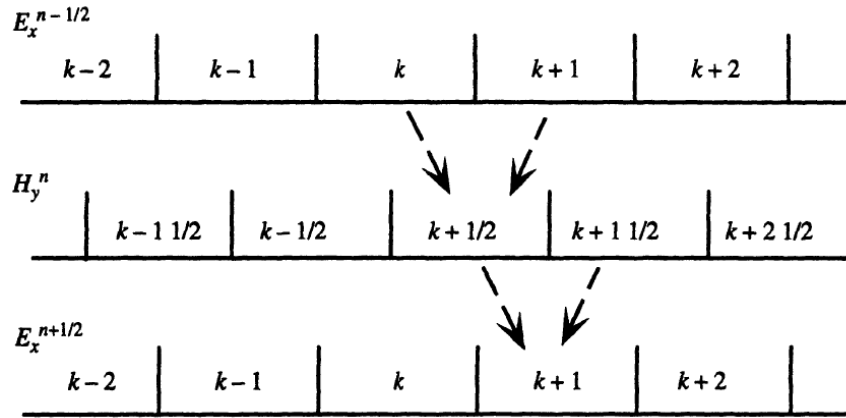


Figure 3.7: Updating and interleaving of the  $E$  and  $H$  fields of the FDTD formulations for the 1D plane wave problem. For example, to calculate  $E_x^{n+1/2}(k+1)$ , the value of  $E_x^{n-1/2}(k+1)$  and the neighboring values of  $H_y^n$  at  $k+1/2$  and  $k+1 1/2$  are required [105].

FDTD formulations for two-dimensional (2D) and three-dimensional (3D) problems can be worked out in a similar manner by replacing time and space derivatives in (3.9) and (3.10) with corresponding finite difference approximations. For example, Figures 3.8 and 3.9 [105] show the interleaving in time and space for 2D and 3D problems respectively.

In the FDTD formulations, selection of the time-step and cell size is not independent. The rule governing this is often called stability condition of the FDTD method. Essentially, electromagnetic (EM) waves travelling through a cell must not be capable of exceeding the speed of light  $c$ , which for the 1D FDTD formulations results in the condition  $\Delta t \leq \Delta x/c$ . For any known medium, achieving this condition means the distance that the EM waves travel in one single time-step will not be larger than the cell size. The 1D condition can be extended to be used in the 2D and the 3D FDTD formulations by considering potential diagonal travelling paths, which are  $\Delta t \leq \Delta x/(c\sqrt{2})$  and  $\Delta t \leq \Delta x/(c\sqrt{3})$  respectively.

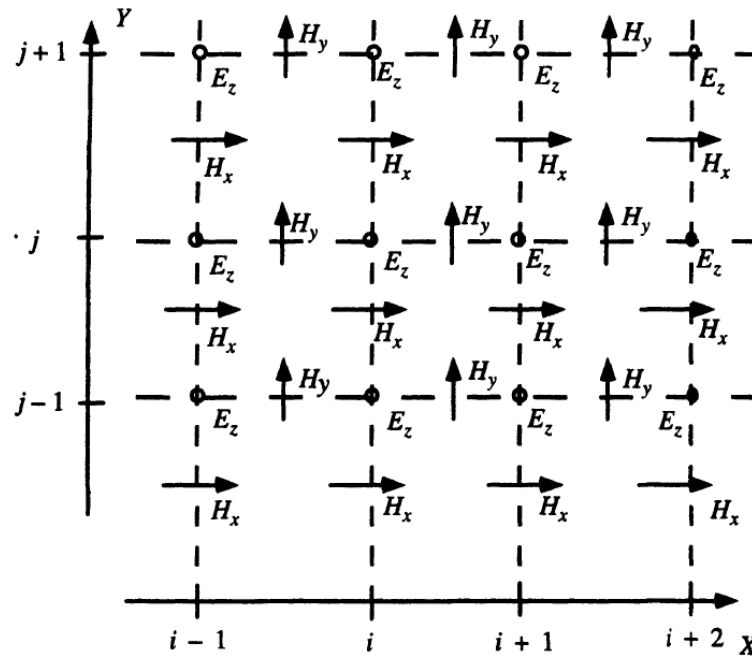


Figure 3.8: Interleaving of the  $E$  and  $H$  fields of the FDTD formulations for a 2D problem, a transverse magnetic wave consisting of  $E_z$ ,  $H_x$  and  $H_y$  [105].

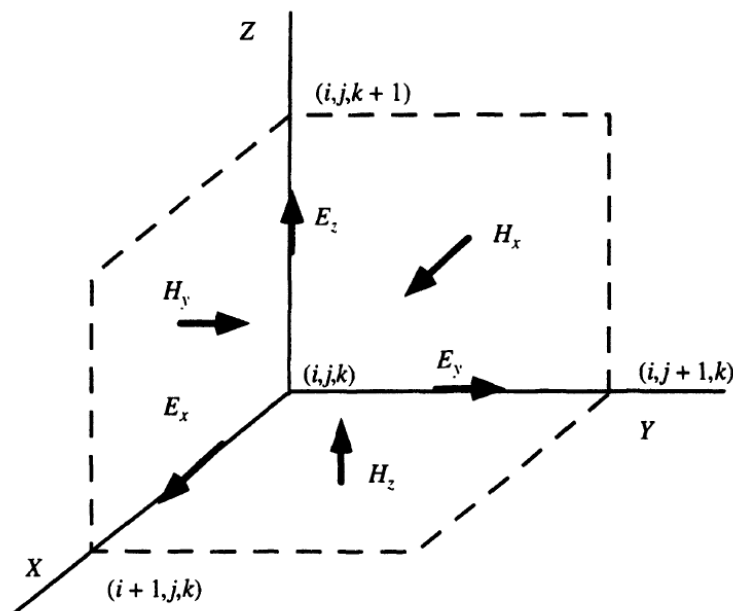


Figure 3.9: Interleaving of the  $E$  and  $H$  fields of the FDTD formulations for a 3D problem, which is also known as the Yee cell [105].



The condition can be further generalized for  $n$  dimensional formulations and is known as Courant condition [105]:

$$\Delta t \leq \frac{\Delta x}{\sqrt{n} \cdot c}. \quad (3.17)$$

Specifically, for a 3D problem with a cell size of  $(\Delta x, \Delta y, \Delta z)$ , the following condition was derived by Taflove in 1975 [96].

$$\Delta t \leq \frac{1}{c} \left( \frac{1}{\Delta x^2} + \frac{1}{\Delta y^2} + \frac{1}{\Delta z^2} \right)^{-1/2} \quad (3.18)$$

The above discussion is mostly about using the FDTD method to simulate 1D electrodynamic problems in free space. In practice, the problems will be complicated by presence of various media and complex geometries, limited computing resources, requirements for post-processing and so on. For discussion of the FDTD method so as to solve different kinds of problems there are many textbooks [98; 105; 106]. For carrying out practical FDTD simulations, both open source and commercial software package are available. Commercial software usually has a powerful graphical user interface and is both able to deal with complex problems and easy to use, for example “XFDTD” by Remcom [107] and “FDTD Solutions” by lumerical [108]. XFDTD (ver. 7.1) was employed for all the FDTD simulations in this research and its interface is shown in Figure 3.10.

The FDTD technique has been widely used to investigate PD phenomena in power equipment and FDTD modelling of PD in GIS seems to be drawing most of the attention. From this point of view, as well as a GIS having a coaxial structure similar to that of an HV cable’s, it is reasonable to start from GIS to have first some practical ideas of FDTD modelling of PD and then move on to the smaller and more complex case of modelling PD in HV cables.

### 3.4 FDTD Modelling of PD Location in GIS

A defect in GIS, such as a protrusion on the inner conductor or a free metallic particle, will result in concentration of electric fields around it and then the occurrence of PD. The UHF method has been widely employed to measure PD for GIS, by which not only PD detection but also PD location can be realized. The UHF method can be regarded as involving three steps, which are: excitation

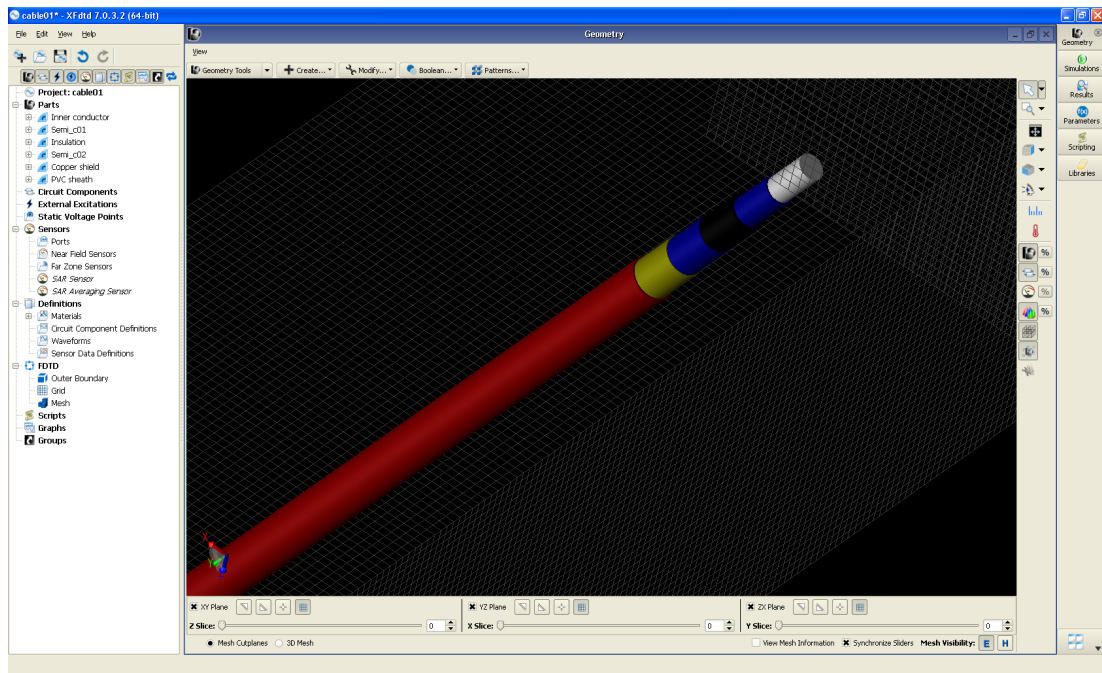


Figure 3.10: Interface of XFDTD. From object modelling to FDTD simulations, all work can be carried out effectively by following the tree menu on the left hand side of the software interface. The model shown in the interface is for an 11 kV EPR cable sample.

of the UHF signal by a PD, propagation of UHF signals within the GIS, and extraction of UHF signals from the GIS using a coupler [109]. Figure 3.11 shows an illustration of the three steps. PD location can then be carried out based on the arrival time difference between UHF signals extracted by two couplers, one on each side of the PD source. Time-of-flight calculation is usually used for PD location, in which GIS is approximated to a one dimensional structure. This approximation is reasonable for a straight part of GIS. However, GIS is sometimes built very compact so that it can have many right angle bends and tee sections. To investigate how corners or tee sections of GIS will influence PD location accuracy is therefore of interest and provides a good basis for demonstrating the application of FDTD methods to practical PD problems.

The three steps of UHF method can be well simulated using FDTD and there are great flexibilities, e.g., positions and directions of PD source, positions of sensor. FDTD has shown its power in investigating the propagation characteristics of PD induced EM waves within real GIS structures like a right bend or a tee section where it is difficult to apply theoretical analysis. However, little attention has been given to the influences of real GIS structures on PD location accuracy.

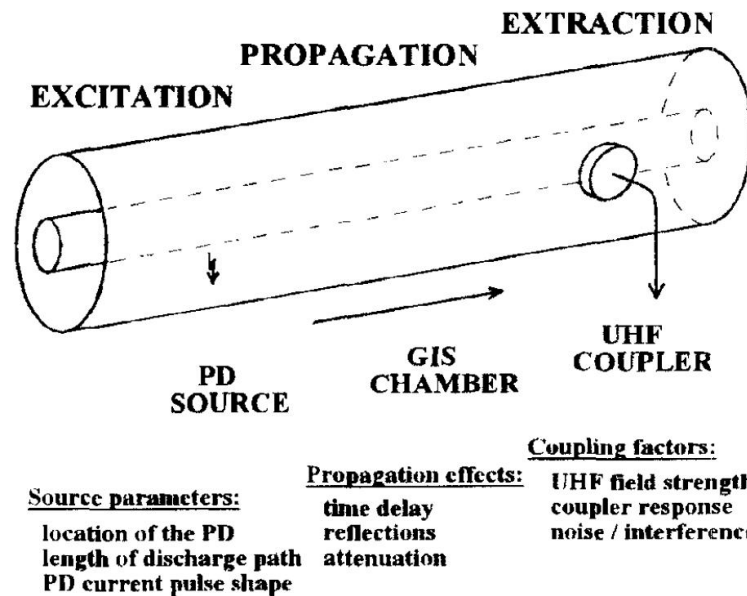


Figure 3.11: Three steps of the UHF detection of in GIS [109].

Here, FDTD modelling has been used to investigate PD location accuracy in a GIS tee section. A PD source on a fixed cross-section of GIS but at different positions was considered, which for a 1D model would be regarded as the same but this is not the case in the real 3D world. Location errors using different sensor combinations suggest the preferable positioning of UHF sensors in this case. The proposed positioning of sensors was then evaluated in a simple model built to represent a GIS circuit breaker.

### 3.4.1 Simulation of PD Within a GIS Tee Section

A GIS tee section model was created using XFDTD. Figure 3.12 shows the dimensions of the tee section and the positions of PD source and sensors in the model. This simple model is based on dimensions of a typical 400 kV GIS. The cross-section containing the PD source was in the vertical part of the GIS, 2 m below the junction centre. PD would be excited at positions p1, p2 and p3 respectively, which are equally spaced at 90° around the cross-section. The position opposite to p3 was omitted because it is symmetrical to p3 with respect to the sensors in the model. The PD source was a radial current filament 10 mm long separated from the tank by a 20 mm gap. The radial current filament can make current flow such that charges are moving as they should in a radial electric field. For

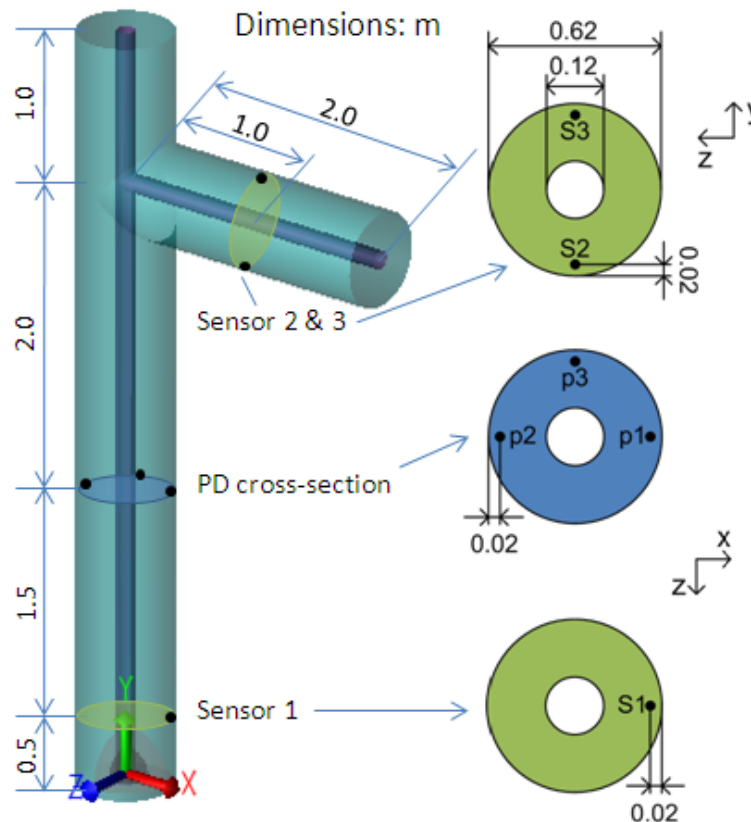


Figure 3.12: GIS tee section model used in FDTD simulations. On the right is the positioning of the PD source and sensors on certain cross-sections.

example, in Figure 3.12, charges at  $p3$  will be moving in the  $z$  direction. The PD source was realized in the model by a voltage source in XFDTD. By using the source editor shown in Figure 3.13, the source impedance, magnitude and waveform can be specified. Here an input impedance of  $50 \Omega$  (default value) was used and the “waveform” option was selected as “real pulse”, which will be discussed in detail later.

Two sensor cross-sections were defined in the vertical and horizontal arms of the GIS. Three sensors were defined to record the electric fields at the positions of  $S1$ ,  $S2$  and  $S3$  respectively. As shown in Figure 3.12, sensor 1 ( $S1$ ) was on the vertical cross-section while sensor 2 ( $S2$ ) and sensor 3 ( $S3$ ) were on the horizontal cross-section. All sensors were represented in the model by electric field point sensors separated from the GIS tank by 20 mm. The sensors were measuring total field. The recorded total field generally had a dominant (radial) component due to the boundary condition near to the PEC surface of the GIS tank.

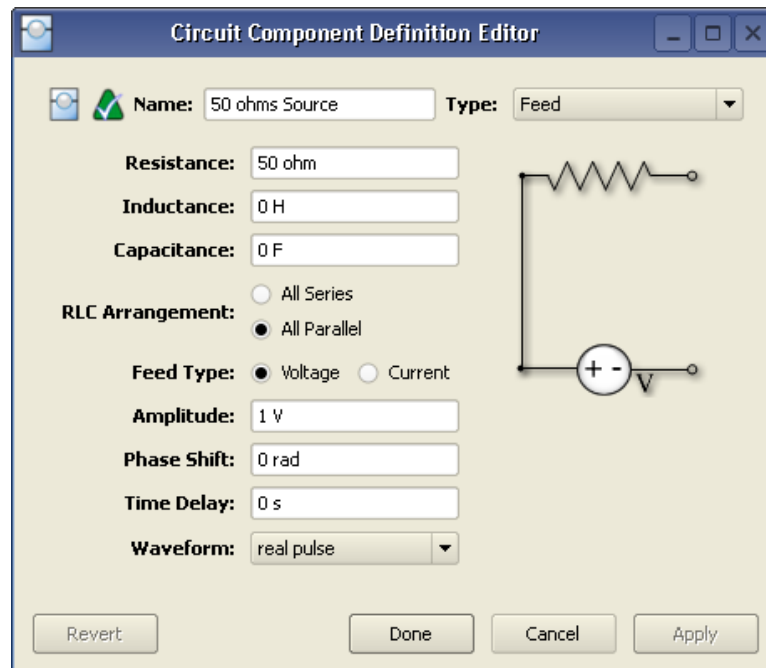


Figure 3.13: Setting up a voltage source in XFdtd.

The HV busbar and the tank were considered as perfect conductors in the model. The three open ends were on the same plane with the corresponding outer edges of the modelling space, i.e., no separation between the model and the space edges at these directions. For the other three directions there was a 10 cell separation from the tank to the space edges. The ends were closed with the perfect conductor (PEC) boundaries. The rest of the outer edges were by default using the absorbing boundary condition of perfect matched layer (PML). The simulations used an equal mesh size of  $\Delta x = \Delta y = \Delta z = 10$  mm to divide the model into cells, requiring a time step of 19.26 ps. The PD source waveform used in the simulations is shown in Figure 3.14. This pulse is an actual experimental pulse from a point-plane PD source configuration containing SF<sub>6</sub> gas, which was previously acquired using a digital sampling oscilloscope with a bandwidth of 13 GHz [25]. One simulation requiring 2000 time steps (38 ns) of results takes about 9 minutes on a Dell workstation with a Xeon CPU of 2.67 GHz and 12 GB RAM. Electric fields radiated by the PD were recorded by the three sensors and would be used to assess the PD location.

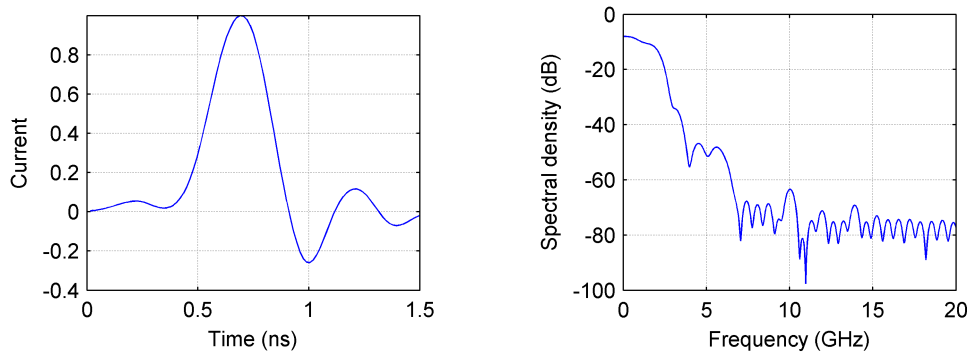


Figure 3.14: Input PD pulse (normalized). (a) Pulse waveform. (b) Frequency spectrum. The PD pulse was recorded in SF<sub>6</sub> gas [25].

### 3.4.2 PD Location for the Tee Section

PD location for the GIS tee section is realized based on the sketch in Figure 3.15. The idea of time-of-flight calculation is that, supposing  $d$  denotes the distance between the cross-section including S1 and the cross-section involving PD,  $d$  can

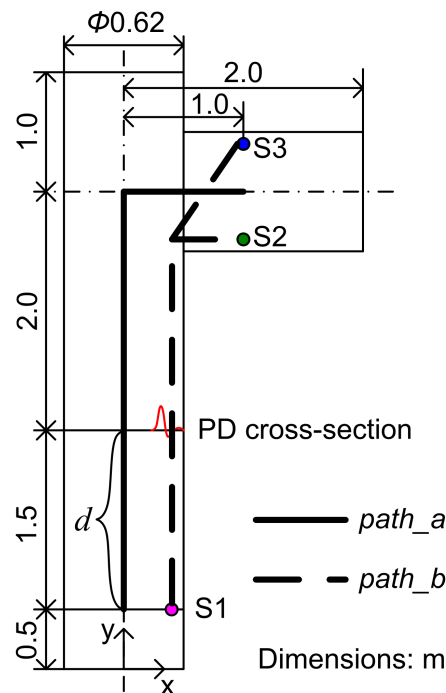


Figure 3.15: Approximation of the PD location problem within the tee section,  $path_a$  was used as the distance  $D$  between sensors for time-of-flight calculation.

be calculated by the equation

$$d = \frac{D - c\Delta t}{2} \quad (3.19)$$

where  $D$  is the total distance along the HV busbar between the two cross-sections that include sensors on either side of the PD source and  $\Delta t$  is the arrival time difference of the signals recorded by two sensors (S1-S2 or S1-S3 in this example).  $c$  is the speed of EM waves travelling in SF<sub>6</sub> gas, which equals the velocity of light in vacuum. It can be seen from Figure 3.15 that the true value of  $d$  should be 1.5 m, which will be used to calculate location errors later. The value of  $D$  is normally obtained by assuming EM waves are travelling axially along the centre of GIS, which is shown in Figure 3.15 as *path\_a*. However, the true 3D character of GIS will have an influence on the propagation of EM waves, e.g., for the PD source at p1, Figure 3.15 shows a more direct travelling path is *path\_b* rather than *path\_a*, which may lead to potential location inaccuracy when *path\_a* is being used in calculation. Since without advance knowledge of the 3D location of the PD source, it is impossible to know the real travelling path of PD induced EM waves for time-of-flight calculation, one possible solution is to investigate the influence of the tee section on PD location accuracy through sensors at different positions and then suggest a preferable sensor positioning to minimise the influence.

Following the simulations, output signals from the sensors were three components of electric fields ( $E_x$ ,  $E_y$  and  $E_z$ ) at S1, S2 and S3. Figure 3.16 shows examples of  $E_y$  signals recorded at S1 and S3 in a simulation where the PD source was at p1. The arrival time of each individual signal was obtained by first squaring the signal and then taking the time of the data point whose magnitude first exceeded a certain threshold relative to the peak value of the squared data. Threshold values of 0.5%, 1% and 2% were employed in this research. Time difference  $\Delta t$  was calculated by subtracting the arrival time of the electric field signals recorded by (S1, S2) or (S1, S3). Table 3.1 shows the time differences using the different threshold values when the PD source was at p1. The PD location was then conducted with  $\Delta t$  using (S1, S2) and (S1, S3) sensor combinations. Table 3.2 shows the location results. The variation of the results was due to both the different positions of the PD source on the cross-section (p1, p2 or p3 shown in Figure 3.12) and the different threshold values used in determining the arrival time.

Simulations were then repeated for the PD source situated close to the inner

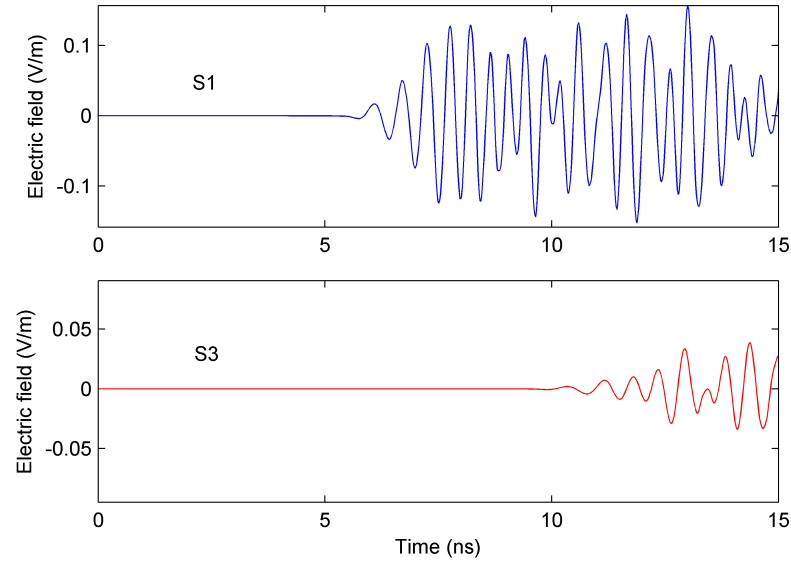


Figure 3.16:  $E_y$  signals recorded at S1 and S3. An arrival time difference is seen between the two signals, which will be measured and used in PD location.

Table 3.1: Arrival time differences for the PD source at p1.

Threshold value (%)	Arrival time difference $\Delta t$ (ns)	
	S1-S2	S1-S3
0.5	4.43	5.14
1	4.62	5.72
2	4.62	5.97

Table 3.2: PD location results on the  $y$ -axis using S1-S3 and S1-S2 when the PD source was close to the GIS tank wall. Solid lines represent the location results and dotted lines represent the true position of PD at  $y = 1.50$  m.

Sensor pair	Threshold value (%)					
	0.5		1.0		2.0	
S1-S3	1.56(p2)	1.54(p3)	1.55(p2)	1.50(p3)	1.50(p2)	1.49(p3)
	1.48(p1)		1.39(p1)		1.35(p1)	
S1-S2	1.67(p2)	1.67(p3)	1.58(p3)	1.56(p2)	1.56(p1)	1.56(p2)
	1.58(p1)		1.56(p1)		1.34(p3)	



conductor, as shown in Figure 3.17. More accurate location results might be expected for this arrangement since the approximation of time-of-flight calculation may better match the real travelling path of EM waves. Table 3.3 summarises the location results, and it is evident that the range of variation of the location results is less than those shown in Table 3.2.

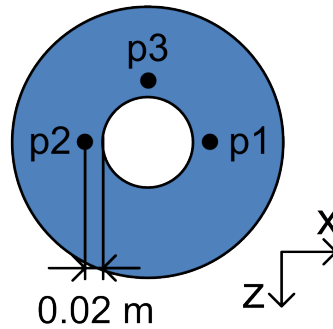


Figure 3.17: PD source on the same cross-section but separated by 20 mm from the HV conductor.

Table 3.3: PD location results on the  $y$ -axis using S1-S3 and S1-S2 when the PD source was close to the HV conductor.

Sensor pair	Threshold value (%)								
	0.5			1.0			2.0		
S1-S3	1.54(p3)	=====	1.49(p1)	1.49(p1)	=====	1.48(p3)	1.48(p1)	=====	1.44(p3)
	1.43(p2)	=====		1.43(p2)	=====		1.40(p2)	=====	
S1-S2	1.67(p1)	=====	1.67(p3)	1.67(p3)	=====		1.63(p3)	=====	1.58(p2)
	1.62(p2)	-----		1.62(p1)	-----	1.62(p2)	1.57(p1)	-----	

### 3.4.3 Discussion

According to the principle of time-of-flight calculation, the PD location accuracy will depend on how well the assumption that EM waves are travelling along the centre of GIS matches the actual condition. Equation (3.19) indicates that if a smaller  $d$  than the true value is obtained, the distance  $D$  has been underestimated and vice versa. It can be seen from Tables 3.2 and 3.3 that locating using S1-S3 tends to yield lower values of  $d$  than using S1-S2. In particular, when the

PD source is close to the HV conductor, Table 3.3 shows that all the location results using S1-S2 are above  $y = 1.5$  m, which means the measurement of  $D$  used in time-of-flight calculations may overestimate the total distance that the PD induced EM waves were travelling between S1 and S2. By similar reasoning, it also suggests that the distance between S1 and S3 was underestimated.

The simulation results indicate that a tee section does introduce some inaccuracy for PD location in GIS. However, the inaccuracy can vary depending on where UHF sensors are installed as well as the method used for determining arrival times. Figure 3.18 summarises the average location errors using S1-S3 and S1-S2 versus the threshold values used in determining the arrival time for the PD location. It can be seen that the location errors using S1-S3 are smaller than

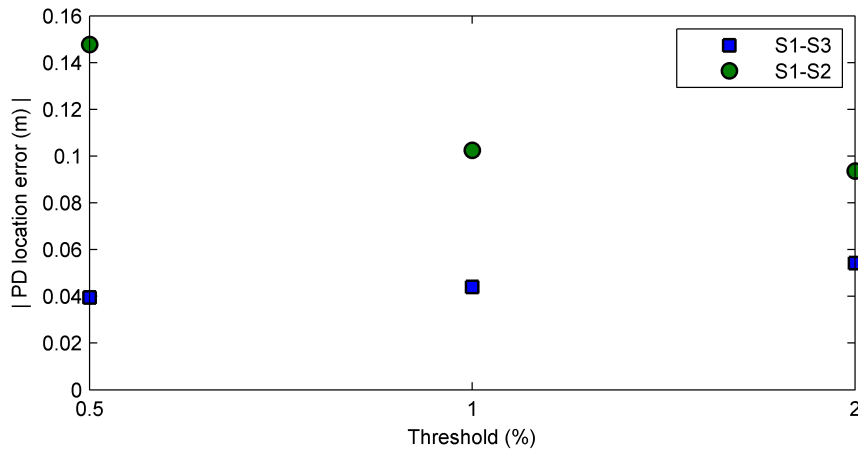


Figure 3.18: PD location errors using S1-S3 and S1-S2 with different thresholds.

those using S1-S2 for all three thresholds. It is likely that S3 being located further than S2 from the PD source makes the real travelling path of the PD induced EM waves closer to the assumed value of  $D$  in the time-of-flight calculation. So for the GIS model of Figure 3.12, installing a UHF sensor at the position of S3 rather than S2 may be a better choice.

In order to further demonstrate the use of FDTD in GIS PD location, a simple model was built for a GIS circuit breaker. The model includes two tee sections between which is a larger diameter chamber representing the breaker (contacts assumed to be closed). Figure 3.19 shows a sketch of the model. A PD cross-section was selected in the middle of the vertical part of the model making the true value of  $d = 2.2$  m. Both the PD positioning arrangements of Figures

3.12 and 3.17 were again tested. Simulations were carried out with comparable configurations to those used for the previous model and the PD location was performed using S1-S3, S1-S2, S4-S3 and S4-S2 respectively. Table 3.4 shows the location results when a threshold of 1% was used. It can be observed that the

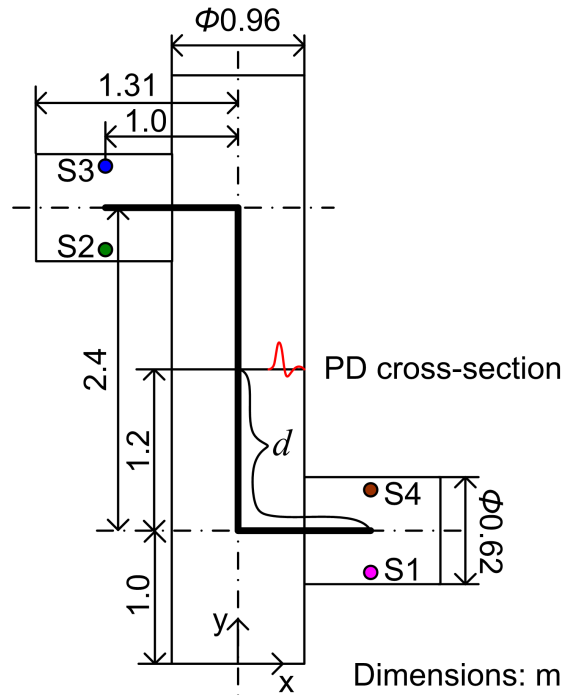


Figure 3.19: The model built for a circuit breaker in GIS.

Table 3.4: PD Location results on the  $y$ -axis using S1-S3, S1-S2, S4-S3 and S4-S2 with the threshold of 1%.

(a) PD source close to the tank.

S1-S3	S1-S2	S4-S3	S4-S2
2.38(p2) ———— 2.02(p1) ———— 2.20(p3)	2.59(p2) ———— 2.00(p1) ———— 2.36(p3)	2.40(p2) ———— 1.85(p1) ———— 2.05(p3)	2.61(p2) ———— 1.83(p1) ———— 2.20(p3)

(b) PD source close to the HV conductor.

S1-S3	S1-S2	S4-S3	S4-S2
2.31(p2) ———— 2.06(p1) ———— 2.20(p3)	2.51(p2) ———— 2.06(p1) ———— 2.39(p3)	2.32(p2) ———— 1.87(p1) ———— 2.00(p3)	2.51(p2) ———— 1.87(p1) ———— 2.20(p3)

results using S1-S3 have the smallest deviation from the true PD cross-section when compared to those using others. Figure 3.20 shows the average location errors versus the threshold values. It can be seen that the errors using S1-S3 were

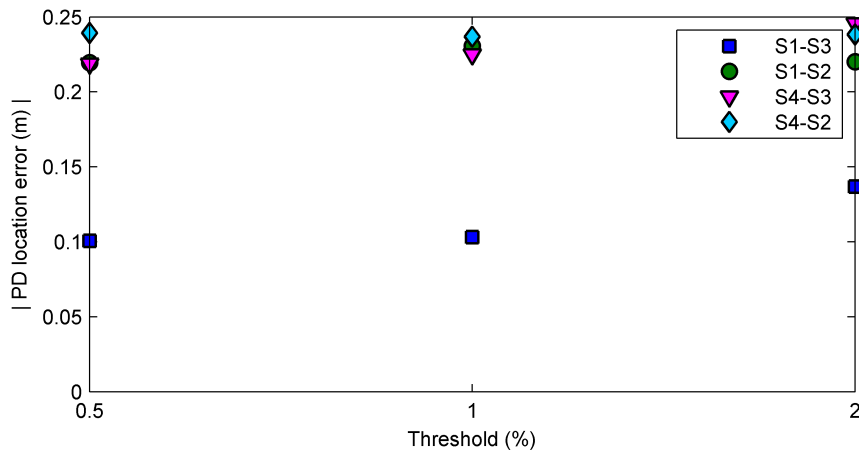


Figure 3.20: PD location errors for the GIS circuit breaker model.

always the smallest among all the sensor combinations. Therefore, S1 and S3 may be the best positions to install UHF sensors for this circuit breaker arrangement. This result is in agreement with that from the previous model shown in Figure 3.12.

FDTD simulation results presented in this section show that PD location accuracy in GIS will be influenced if PD induced EM waves pass through a tee section. PD occurring on a fixed cross-section of GIS, depending on its position (close to the tank or the core conductor), will have different influence on the location accuracy. The PD positions close to the tank tend to result in more inaccuracy. Moreover, the influence can be different according to the positioning of UHF sensors. The location errors predicted by using the different sensor combinations suggest that a PD source would be located with better accuracy when the UHF sensor located in the branch part of a GIS tee section is installed on the far side of the tank from the direction in which UHF signals from the PD arrive. Of course, this cannot be assured without prior knowledge of where the PD source will be, but consideration of the results presented here for different coupler positions may assist with the more accurate interpretation of arrival time differences. Furthermore, at the design stage, there may be some cases in which the effects that have been reported can help with the selection of preferred coupler

mounting positions.

Considering that PD location error in GIS can be  $\pm 0.25$  m in determining the plane of the PD source, which is due to geometry alone without considering the inaccuracy of the timing measurements, the PD location results from the simulations using the proposed sensor positioning fall into this error range. Nevertheless, more GIS models of different dimensions need to be taken into account in simulations before general conclusions can be drawn. The findings presented here would benefit from future experimental study in practical applications.

## 3.5 Implementing FDTD Modelling of PD in HV Cables

An HV cable's structure is like a mini version of GIS with inner and outer conductors of the cable corresponding to the HV conductor and the tank of a GIS. Using FDTD modelling to investigate PD phenomena in an HV cable is, however, more complex because the cable's semi-conductive layers of which properties vary significantly with frequency play an important role in PD pulse propagation along the cable. Moreover, the widely used PD detection devices like HFCTs are a kind of inductive coupling sensor which is usually made by winding many turns of thin wire onto a toroidal coil. This means there will be too much physical detail if a physical representation of an HFCT is to be developed in an FDTD model.

For this reason, implementing FDTD simulations of PD measurement for HV cables is challenging. This work proposes a specific modelling framework to overcome the difficulties, which will be introduced later. This section discusses various aspects involved in FDTD modelling of HV cables, summarising some rules of thumb for practices. These principles should be applicable to FDTD modelling of the HV cables carried out with other FDTD software packages although XFDTD has exclusively been used in this research.

### 3.5.1 Creating FDTD Models of HV Cables

Creating FDTD models of cables generally includes two steps: 1) three-dimensional (3D) modelling of the cable structure based on the cable geometry and dimensions; 2) assigning a corresponding material, i.e., defining material properties, for each individual component within the cable structure. Some practical experience

has been gained in efforts to create appropriate FDTD models for the cables investigated in this study and those which are thought to be useful across different applications and platforms are summarised as follows:

1) 3D modelling of the cable structure. A polymeric-insulated HV cable generally consists of several coaxial layers. For example, the cross-sectional structure of an 11 kV ethylene-propylene rubber (EPR) insulated cable is shown in Figure 3.21. From inside to outer layer, there are: inner conductor (ca-

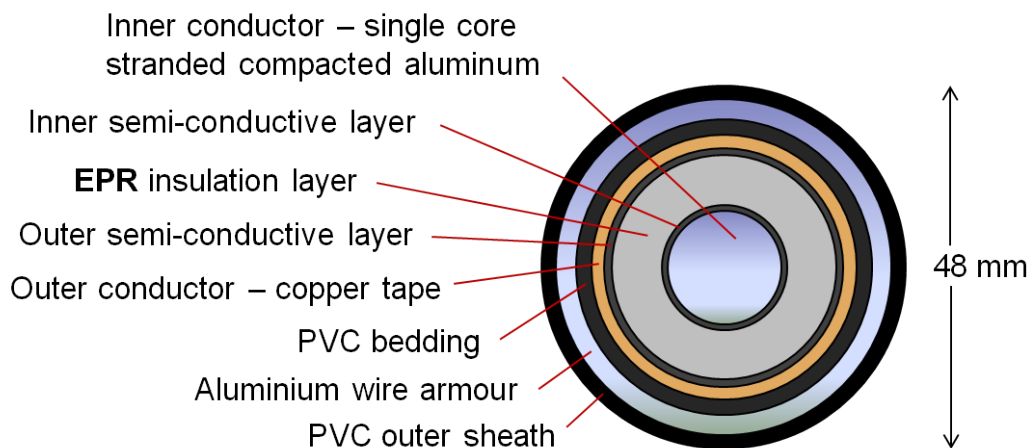


Figure 3.21: Cross-sectional structure of an 11 kV EPR cable.

ble/centre/HV conductor), inner semi-conductive layer (inner semicon/conductor semicon/conductor shield/conductor screen), insulation layer, outer semi-conductive layer (outer semicon/shield semicon/insulation shield/ground shield/insulation screen), outer conductor (shield/screen/ground conductor), bedding layer, armor layer and outer sheath (over sheath).

In creating an FDTD model of the cable, the layers outside of the outer conductor (i.e., the bedding layer, the armor layer and the outer shield) do not have to be included since they should have no effect on the cable's internal electromagnetic characteristics. The layers inside of and including the outer conductor are essential for the model. Ideally, they should be created exactly according to their actual geometries and dimensions. However, some of the required layers may have very fine detailed geometries. For example, inner conductors made of stranded wires and outer conductors of spiraling tapes or concentric wires, including these details into the FDTD model can prove to be modelling intensive as well as computing intensive. There has been research taking into account detailed

geometries of the outer conductors to investigate their effects on high frequency properties of the cables [32; 33; 92], but in many other examples, these details are not considered.

In this study, both the inner and outer conductors were created as solid conductors regardless of the detailed geometries. The created outer conductor did not necessarily use its actual thickness. This is because either in terms of the cable characteristic impedance or skin effects, the dimension that is relevant is only the inner radius of the outer conductor. In other words, the thickness of the outer conductor is not important for the problem discussed here. In practice, the outer conductor was made thicker than the actual thickness so that it would not become a limit for setting the spatial resolution of the FDTD mesh (in this case, the outer conductor which is made of spiralling copper tapes happened to be the thinnest layer). Not having to use a smaller FDTD mesh brings significant reductions in computation loads, as will be shown later.

2) Assigning materials to the components. The created FDTD cable model included the cable's inner and outer conductors, inner and outer semi-conductive (semicon) layers and insulation. The conductors are usually made of metals such as copper and aluminium. The semicon layers are made of semicon materials. The semicon materials are a kind of dispersive material of which electrical properties will change with frequency (also called frequency-dependent material). The insulation is made of polymers, e.g., ethylene-propylene rubber (EPR) and cross-linked polyethylene (XLPE).

To assign corresponding materials to the cable components is to define each individual material's electric and magnetic properties in the FDTD model. First, the materials of the cable components are all non-magnetic materials. Therefore, their magnetic properties are the same as that of vacuum's, i.e., permeability in vacuum  $\mu_0 = 4\pi \times 10^{-7}$  H/m. In terms of electric properties, apart from permittivity in vacuum  $\epsilon_0 = 8.854 \times 10^{-12}$  F/m, there are relative permittivity  $\epsilon_r$  and conductivity  $\sigma$  (or more generally, complex relative permittivity  $\epsilon^*$  whose real and imaginary parts can be related to  $\epsilon_r$  and  $\sigma$  respectively). In order to make the FDTD model as accurate as possible, it is crucial that  $\epsilon_r$  and  $\sigma$  should be set, to the best of one's knowledge, according to each material's actual properties.

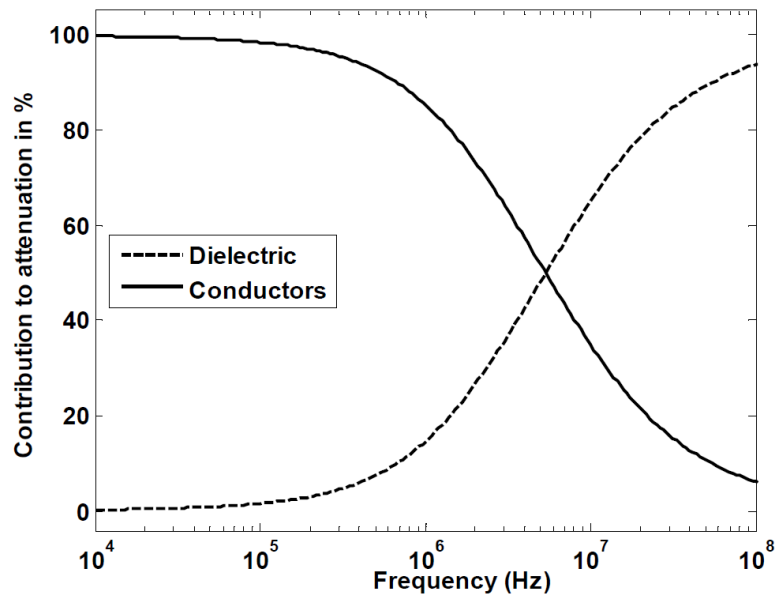
In practice, this setting procedure will be subject to available data of the material properties as well as the capability of a software package to define different kinds of material. It is not always practical to have every material accurately

defined in the FDTD cable model. However, some simplifications in defining the materials can be acceptable provided that the FDTD model produced results will not be affected significantly, which is like what has been done in creating the outer conductor of the FDTD cable model. The FDTD cable model was created to simulate PD phenomena in the cable. A PD current pulse propagating in the cable is subject to changes rooted in high frequency loss of the cable. The FDTD cable model cannot be accurate for simulating PD if it is not able to represent the actual cable high frequency loss. Thus, before proper definitions of the materials in the FDTD model can be done to get the high frequency loss characterised, a review of the causes of high frequency loss in the cable is necessary.

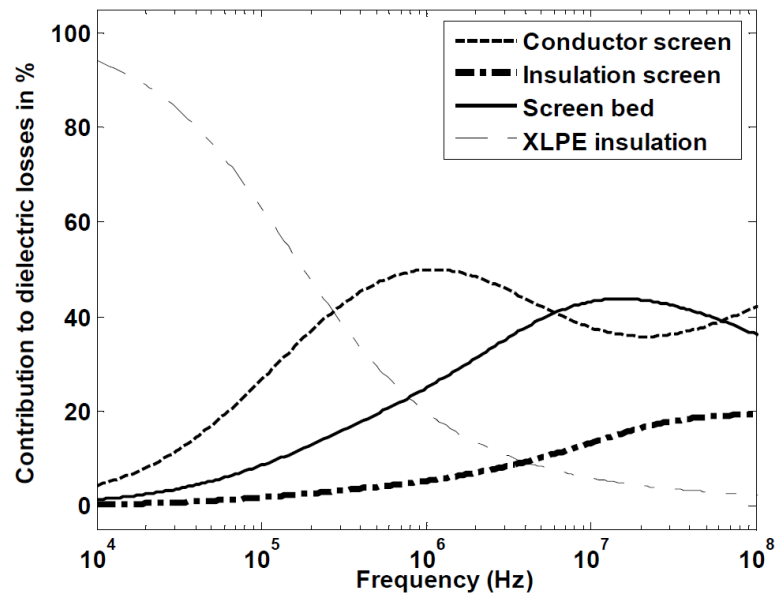
As suggested by Stone and Boggs in 1982 [30], high frequency loss in a polymeric-insulated HV cable is a result of combined contributions from the skin effect losses in the inner and outer conductors, the insulation loss and losses in the inner and outer semicon layers. Since then, many studies have been conducted on high frequency loss/attenuation and wave propagation characteristics of the cables [29; 31; 110; 111; 112]. Most of them have considered medium voltage (MV) distribution class cables although there were different cable details as well as different methods. Generally, it has been agreed that the skin effect loss is dominant at relatively low frequencies while those in the insulation and semicon layers dominate at relatively high frequencies.

In terms of dividing between the relative low and high frequencies, the maximum frequency of the low frequencies is usually between 1–10 MHz. For instance, it was summarised by Xu et al. [29] that the skin effect losses in the inner and outer conductors tend to be important at relatively low frequencies ( $< 1$  MHz). At high frequencies (in the MHz range), the losses in the insulation and semicon layers will dominate. Moreover, depending on whether the cable insulation has a relatively large dissipation factor,  $\tan \delta$ , either the insulation loss or the semicon losses will be playing a more important role [29]. For example, an EPR cable with an insulation  $\tan \delta$  of 0.02 in the MHz range was found to have the insulation loss dominating the high frequency loss to at least 20 MHz [33]. In contrast, for XLPE cables with very small insulation  $\tan \delta$  at  $10^{-4}$  level, the high frequency loss will be dominated by the semicon losses. For example, relative contributions from different layers of XLPE cables to the high frequency loss were investigated by Mugala et al. [112]. Figure 3.22 shows the result of a 12 kV XLPE cable. The losses in the insulation and semicon layers (“Dielectric” trace in Figure 3.22a) be-





(a) Between dielectric and conductors.



(b) Between semicon and insulation.

Figure 3.22: Relative contributions to the high frequency loss of a 12 kV XLPE cable. The “Conductors” trace represents the skin effect losses in the inner and outer conductors. The “Dielectric” trace includes losses in the insulation and semicon layers. The screen bed is an extra semicon layer on top of the insulation screen in the investigated cable [112].

come higher than those caused by the skin effect in the conductors from 5 MHz and account for more than 90% of the cable attenuation at 100 MHz. Moreover, Figure 3.22b shows that, from 1 MHz, the losses in the semicon layers start to dominate in the total dielectric losses.

Based on the above discussion, in order to accurately construct the cable high frequency loss in a corresponding FDTD model, material definitions for the components in the model should have (a) the skin effect in the conductors, (b) the insulation loss and (c) the semicon losses being sufficiently pronounced in later FDTD simulations. Regarding the FDTD cable model created according to step 1), ways to consider the effects causing the losses are discussed as follows. The discussion is based on the use of XFDTD (ver. 7.1).

(a) The skin effect is used to describe the phenomenon that at very high frequencies, currents flowing through a good conductor will be concentrated in a thin outer layer of the conductor. Typically, in a coaxial cable, the currents flowing through the inner conductor will be concentrated on its outer surface while those through the outer conductor will be concentrated on its inner surface [113]. The thickness of the thin layer in which most of the currents concentrate is called the skin depth  $\delta_s$  and can be calculated as

$$\delta_s = \frac{1}{\sqrt{\pi f \mu \sigma}} \quad (m) \quad (3.20)$$

where  $f$  is the current frequency,  $\mu$  is the permeability of the conductor and  $\sigma$  is the conductor's conductivity. In order to simulate the skin effect in a good conductor using FDTD modelling, it is necessary to satisfy a general rule of thumb of the FDTD method, which is 10 FDTD cells per wavelength [105]. This means that extremely small cells have to be used for the conductor because in a good conductor, the wave phase velocity and the wavelength will be extremely small. For example, inside copper ( $\sigma = 5.8 \times 10^7$  S/m,  $\mu = \mu_0 = 4\pi \times 10^{-7}$  H/m), at frequencies such as 1 GHz, there will be  $\delta_s = 2 \mu\text{m}$  and  $\lambda' = 2\pi\delta_s = 13 \mu\text{m}$ . An FDTD cell of  $1.3 \mu\text{m}$  would be required to satisfy the 10 cells per wavelength rule, which is impractical for usual FDTD applications. Therefore considering the skin effect in the conductors of the FDTD cable model is not practical and consequently no skin effect caused losses will be evaluated.

In XFDTD, a conductor can be defined by the “perfect conductor [107]”. The “perfect conductor” has infinite conductivity and all electric fields within it are zero. No loss will be introduced by use of the “perfect conductor” in an FDTD

model. Another way of defining a conductor in XFDTD is to use the “nondispersive material [107]” by which the conductivity can be entered as a constant value. Either by the “perfect conductor” or the “nondispersive material”, XFDTD will not consider the skin effect in the FDTD calculation because of that, as explained before, too small FDTD cells are required. However, the “nondispersive material”, it does provide a “surface conductivity correction” option which is supposed to be used for conductors which require to include the skin effect [107]. Nevertheless, the option works for one “evaluation frequency” only, i.e., for sinusoidal wave excitations. This option is not sufficient for use with a PD which is a broadband pulse. Thus, for a PD excitation, the losses caused by the skin effect in the cable conductors cannot be evaluated. As a result, either defining the cable conductors by the “perfect conductor” or the “nondispersive material” would not make any significant difference. In this study, for approximating the reality as closely as possible, both the inner and outer conductors of the FDTD cable model were defined by the “nondispersive material” with conductivities specified according to the conductor materials. However, based on the previous discussion, using the “perfect conductor” should produce effectively the same result and be simpler/quicker in terms of the execution of FDTD simulations.

(b) The insulation loss arises from the fact that practical dielectric media will have conductivity and will cause energy dissipation within them. In particular, the insulation loss is used to describe the ac conductivity that results in energy dissipation. The energy dissipated per period is proportional to the imaginary part of the dielectric media’s complex permittivity [114]. The complex (relative) permittivity  $\epsilon^*$  can be related to the ac conductivity  $\sigma_{ac}$  by

$$\epsilon^* = \epsilon' - j\epsilon'' \tag{3.21}$$

$$\sigma_{ac} = \omega\epsilon_0\epsilon'' \tag{3.22}$$

where  $\epsilon'$  and  $\epsilon''$  are real and imaginary parts of  $\epsilon^*$ . The ac conductivity  $\sigma_{ac}$  is proportional to frequency. To include  $\sigma_{ac}$  caused loss for dielectric media within an FDTD model will require the media’s frequency domain information being moved to time domain and included into FDTD formulations. To that end, there are different methods. One of them involves adding extra formulations to the basic FDTD expressions. The extra formulations are used to include information regarding the media, e.g., the frequency-dependent  $\sigma_{ac}$ . Formulations of some frequency-dependent media are demonstrated in [105].

In XFDTD, dielectric media are categorized into non-dispersive and dispersive materials. For typical cable insulation such as EPR and particularly XLPE, the quantities in (3.21) are regarded as approximately constant up to at least 100 MHz [15]. Therefore, at frequencies of interest, both EPR and XLPE need not be considered as dispersive materials in which electromagnetic waves of different frequencies are travelling at different speed. In terms of non-dispersive materials, XFDTD always uses the same set of “Maxwell’s equations for linear, isotropic, non-dispersive materials [107]” for the FDTD formulations. No extra formulation or any other solution is included to account for frequency-dependent properties. Therefore, the ac conductivity  $\sigma_{ac}$  caused insulation loss cannot be considered by XFDTD. The insulation of the created FDTD cable model had to be defined as an ideal dielectric medium by specifying  $\epsilon_r$  and zero conductivity.

(c) The semicon losses result from radial displacement currents flowing through the semicon layers and thus energy dissipation within the semicon layers due to their significant conductivities. For example, 0.1 – 1 S/m is common for a distribution cable’s outer semicon layer [32]. Semicon materials are dispersive materials, which means both real and imaginary parts of the complex permittivity  $\epsilon^*$  (3.21) are a function of frequency. For example, Figure 3.23 shows properties of a semicon layer from a 15 kV cable [27]. To consider the frequency-dependent

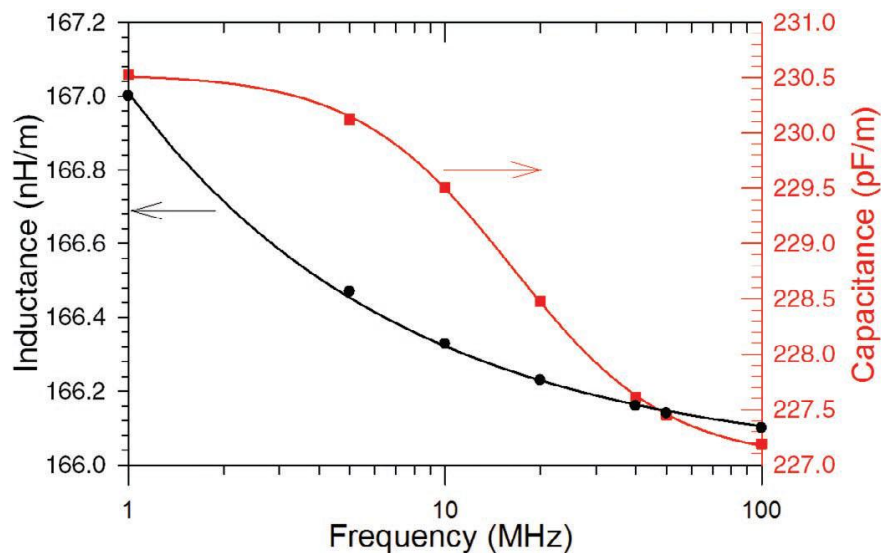


Figure 3.23: Measured relative dielectric constants (real part of  $\epsilon^*$ ) and conductivities (a function of imaginary part of  $\epsilon^*$  according to (3.21)) of the semicon material in an 15 kV cable over a frequency range of 1 – 100 MHz [27].

properties of the semicon layers in the FDTD model, one way is to use effective values for the semicon properties [87], which uses constant effective values instead of frequency-dependent values and therefore does not require different FDTD formulations. Another way would be to implement FDTD formulations for frequency-dependent media. There are variable methods available, such as numeric convolution, auxiliary differentiation equation (ADE) and  $z$ -transform [105]. These methods are able to transform frequency domain information into the time domain so that the information can be included into FDTD formulations.

XFDTD provides two frequency-dependent media types. They are the Debye/Drude medium and the Lorentz medium. The Debye/Drude medium is suitable for representing the semicon properties. There are 1 pole and 3 pole Debye/Drude media available in XFDTD. Parameters required to specify the media are according to the definition of the Debye relaxation model where number of poles can vary from 1, 2, ...,  $n$  [115]. The parameters can be determined by fitting the definition's expression to the semicon properties. In this study, a 3 pole Debye/Drude model was used to fit the semicon properties. Parameters obtained from the fits were entered into XFDTD to specify relevant Debye/Drude media. Finally, the specified Debye/Drude media were assigned to define the semicon layers in the FDTD models of cables.

Above all, although there are three main causes which are (a) the skin effect in the conductors, (b) the insulation loss and (c) the semicon losses contributing to the cable high frequency loss, in this study, only the effect from (c), the semicon losses, was considered by the FDTD cable models created using XFDTD. Fortunately, in many cases (particularly for XLPE cables), the semicon losses are the dominant cause of the high frequency loss. It will be shown later that while only accounting for the semicon losses in the FDTD models, for both an EPR cable and an XLPE cable, to what extent agreements can be obtained between the simulated and measured high frequency losses. A better agreement was achieved for the XLPE cable. Nevertheless, the agreements only held within certain frequency ranges, e.g.,  $< 50$  MHz and  $< 200$  MHz for the EPR cable and the XLPE cable respectively. Above these frequencies, differences between the simulated and measured high frequency losses became larger and larger. This was following using the Debye model's expression to fit the semicon properties. While at frequencies  $< 100$  MHz, the fit results were acceptable. From 100 MHz up, the results started to diverge more and more from the semicon properties.

It is unreasonable to expect that an FDTD cable model will produce exactly the same high frequency loss as that of an actual cable. However, within a few hundred MHz, a good agreement between the simulated and measured high frequency losses can be achieved through accurate measurement of the semicon properties, proper fit to the measured semicon properties using the Debye model's expression, and using fit obtained parameters to define the semicon layers of the FDTD cable model. In practical applications, considering the facts that a typical PD at its origin has a bandwidth of several hundred MHz [15] and cable lengths being modelled are usually short (typically a few meters), an FDTD cable model whose predictions agree with the actual cable high frequency loss within hundreds of MHz is sufficiently accurate.

### 3.5.2 Choosing Appropriate FDTD Cell Sizes

The basic rule of thumb is "10 cells per wavelength" which means the cell size should be no larger than  $\lambda/10$ , one tenth of the wavelength [98]. The wavelength is derived from the highest frequency (shortest wavelength) of interest. In addition, from the consideration of meshing geometry features within a model, the cell size should be no larger than the smallest geometry feature within the model. Even when these two requirements are satisfied, using a smaller cell size can produce results with better accuracy. However, smaller cell sizes will result in larger total cell numbers which proportionally increase the calculation time for each FDTD iteration.

A proper cell size would be a good balance between the accuracy and computational efficiency of the FDTD model. To confirm that the chosen cell size is valid, a convergence study should be carried out, with special attention paid to thin layers of the model [65]. For example, starting from a largest possible cell size and keeping the rest of settings in the model the same and running the simulation, and then halving the cell size and running again, if there are significant variations between results obtained before and after halving the cell size, the cell size is not convergent yet. Continue halving the cell size consecutively until a cell size is found such that further reductions do not cause significant changes to the results.

For the model efficiency, apart from avoiding use of too much fine cell sizes, another common practice is to make use of the geometry features within the model. A cable model can have the axial dimension (e.g., a few meters) much

larger than the cross-sectional dimension (typically tens of mm). While applying a uniform cell size of  $(\Delta x, \Delta y, \Delta z)$ ,  $\Delta x = \Delta y = \Delta z$  to the model, the cell size will be subject to the dimension of the thinnest layer of the cable. This is usually one of the inner or outer semicon layers. For example, both semicon layers were less than 1 mm thick for the cables investigated in this study. When the cell size is determined by the semicon layer thickness and applied across the whole model, it will result in far more divisions in the axial direction than in the other two directions on the cable cross section. A very large total cell number in the model can be expected following the cell definition. Considering the fact that the cable model in the axial direction is extending without material or geometrical discontinuities, it is unnecessary to use a cell size as fine as that being used for the cable cross section. This suggests that the cell size in the axial direction of the model can potentially be increased so that the total cell number in the model can be reduced to accelerate the FDTD calculation without compromising the accuracy of the model. It has been found in the FDTD models created for this study that the simulated cable high frequency losses are not sensitive to the cell sizes in the axial direction. Actually, it will be shown later that increasing the axial cell size to 100 times of that for the cable cross section did not make much difference to the obtained high frequency losses of the cables. It has also been found that, for the cable cross section, a cell size set to half the thickness of the thinnest layer in the cable is sufficient to make the simulated high frequency losses convergent. This means that setting the cell size smaller will have little benefit for the obtained high frequency losses, which was true for both the cable models investigated.

To evaluate the effect of the cell size on the FDTD calculation time as well as the simulation output, an FDTD cable model was created according to the experience summarised in Section 3.5.1. Components within the model were associated with relevant material definitions. A cross section of the cable in the FDTD model is shown in Figure 3.24. While the axial cell size was fixed at  $\Delta y = 10$  mm, various cell sizes on the cable cross section, i.e.,  $\Delta x$  and  $\Delta z$ , were used.

Table 3.5 summarises, for each cell size, the total number of cells, the required computer resource and simulation running time. The time-step values were smaller than values calculated using (3.18). This was resulting from use of the Debye/Drude medium to represent the cable's semicon layers. Reducing the time-

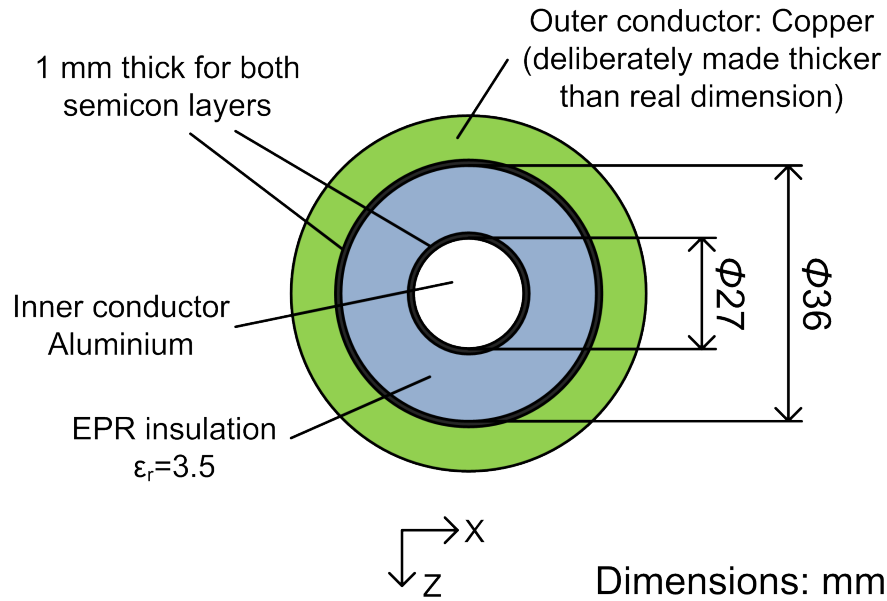


Figure 3.24: Cross section of an 11 kV EPR cable model. Inner conductor was set to aluminium conductivity of  $3.538 \times 10^7$  S/m. Outer conductor was set to copper conductivity of  $5.8 \times 10^7$  S/m. Properties of both semicon layers were using published data of a 12 kV cable's inner semicon [116] and represented by a 3 pole Debye/Drude medium in XFDTD.

Table 3.5: Cell sizes and FDTD simulation details.

Model details	Cable length: 2.2 m, Simulated time: 12 ns Source waveform: Gaussian pulse, 0.5 ns duration Boundary condition: $7 \times$ PMLs Free space padding: $20 \times$ cells			
PC hardware	Dell work station: 2.67 GHz Xeon CPU, 12 GB RAM			
Cell size (mm)	Time-step (ps)	Number of cells	Memory	Running time
(0.1, 10, 0.1)	0.165	$520 \times 222 \times 520$	2.6 GB	33 hrs, 16 m
(0.2, 10, 0.2)	0.330	$280 \times 222 \times 280$	909 MB	4 hrs, 35 m
(0.5, 10, 0.5)	0.825	$136 \times 222 \times 136$	325 MB	25 m
(1.0, 10, 1.0)	1.65	$88 \times 222 \times 88$	202 MB	5 m



step values was performed by XFDTD so as to account for the transient behavior of the Debye/Drude medium. In the “Number of cells” column, divisions in  $x$  and  $z$  directions do not seem to double while the cell size is halved in both directions. This is because of the 20 cells free space padding that were added to the top and bottom of each direction. If subtracting 40 from the divisions in either  $x$  or  $z$  direction, the remainder will be doubled. For example, from  $\Delta x = \Delta z = 1.0$  mm to  $\Delta x = \Delta z = 0.5$  mm, there are  $88 - 40 = 48$  and  $136 - 40 = 96$ . The total amount of memory does not seem to increase in proportion to the increase of the number of cells either. This is attributed to that the values also include the memory required by applying the PML boundary conditions. The running time is increasing faster than both the number of cells and the amount of memory do, which is a result of a “doubled effect” from halving the cell size. A smaller cell size means a larger amount of memory and a smaller time-step. The larger memory usage will make each FDTD iteration take a longer time and the smaller time-step will require more time-steps (iterations) to produce a same length of the simulation output (12 ns in this case).

For the four cell sizes used, results of the FDTD model were evaluated through electric fields recorded at different positions within the cable insulation and propagation speed of the electric fields. For example, Figure 3.25 shows, for the cell size of (0.5, 10, 0.5) mm, the electric fields recorded at the different positions. Summarising the results from the model applied with the four cell sizes, Figure

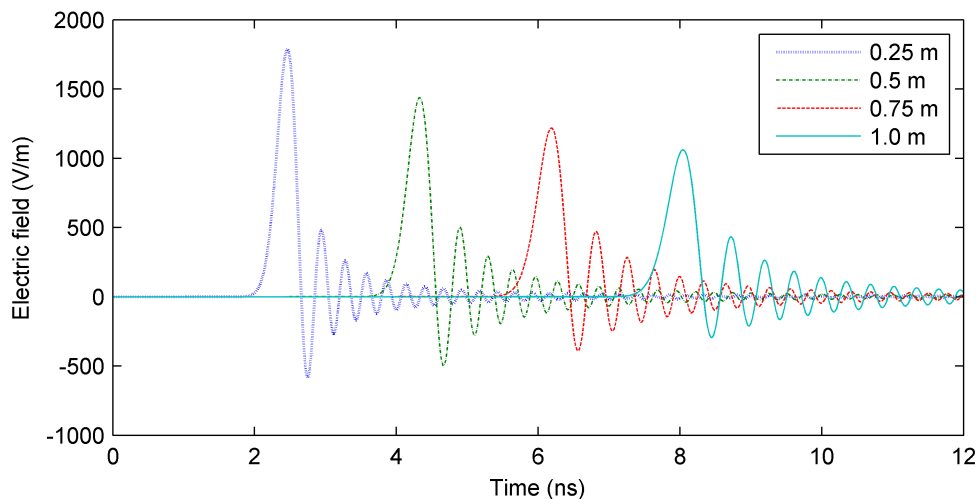


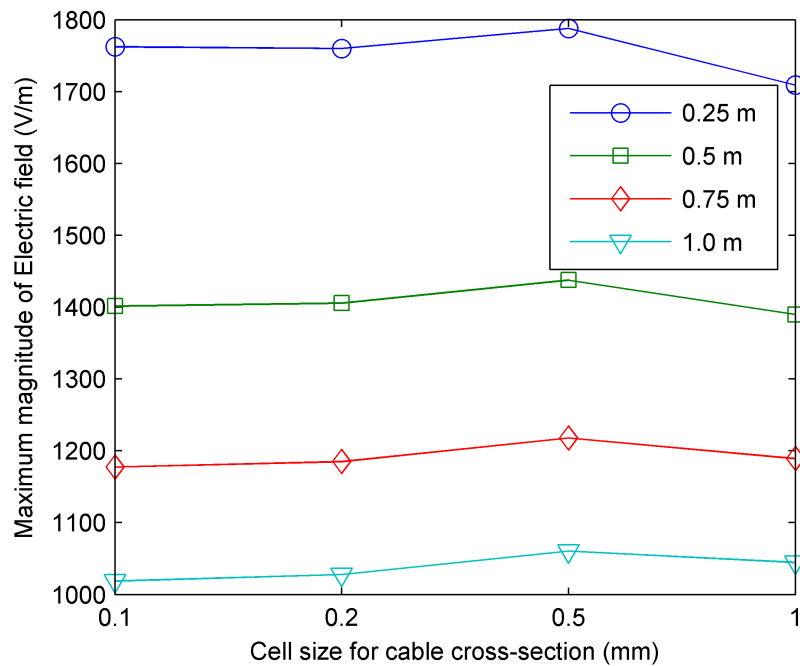
Figure 3.25: Recorded radial electric fields within the cable insulation at the positions of 0.25 m, 0.5 m, 0.75 m and 1.0 m from the source end.

3.26a shows that the electric field maxima were decreasing with increasing distance from the source. For the same position, differences between the maximum magnitudes from the different cell sizes were  $< 5\%$ . Figure 3.26b shows the speed of the electric fields was slower than the theoretical value for the EPR insulation with  $\epsilon_r = 3.5$ . This is because the semicon layers, having high permittivity and conductivity, will slow down the speed of electromagnetic waves travelling in the cable.

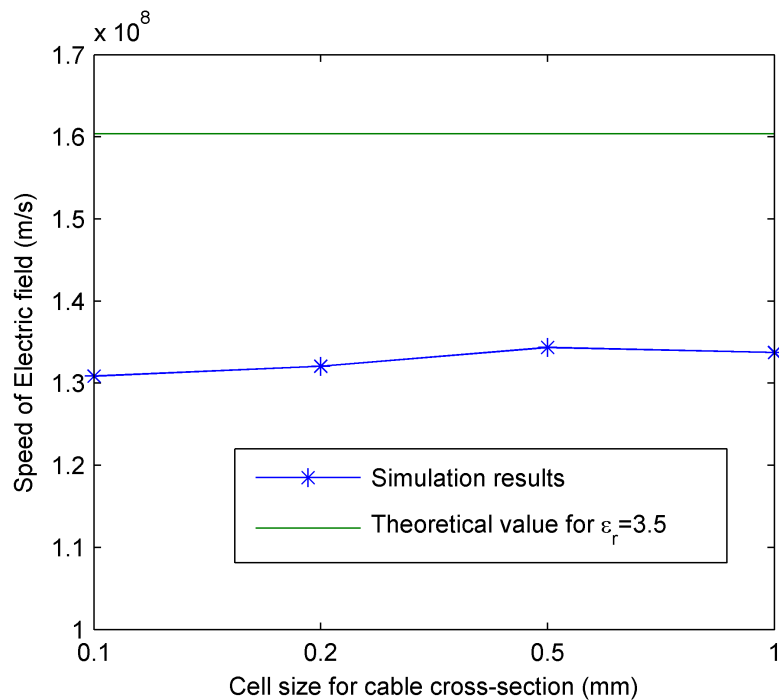
### 3.5.3 Setting Boundary Conditions

Since the FDTD algorithm is calculating the fields at the location of a cell based on the neighboring fields but the size of the FDTD model must be confined because of limited computer resources, boundary conditions have to be used on edges of the FDTD model so that the fields at the edges update correctly. Usually, this involves creating absorbing boundaries which absorb electromagnetic fields propagating outward from the edges of the model so that the fields are not reflected back to the FDTD cells in the model. In other words, the absorbing boundaries attempt to make the model look as if it is extending infinitely. In contrast to the absorbing boundaries, there are reflecting boundaries which simply reflect back the fields travelling outward.

XFDTD provides two absorbing boundaries which are (i) the perfect matched layer (PML) boundary and (ii) the second-order, stabilized Liao radiation boundary, and two reflecting/perfectly conducting boundaries which are (i) the perfect electric conductor (PEC) and (ii) the perfect magnetic conductor (PMC) [107]. The PML boundary is actually a kind of artificial absorbing material that absorbs electromagnetic fields propagating through it. Using the PML boundary will add extra cells, i.e., PML cells to each edge of the model, which increases the total cell number and thus the memory usage. Moreover, the PML cells require more calculation operations than normal FDTD cells do. Both factors combine to make PML computationally intensive. The advantage of PML is that it provides a better absorbing effect than the Liao boundary does. The Liao boundary is an estimate method. It estimates electromagnetic fields just outside the edges of the model by looking into the FDTD cells inside the edges and looking back in time. The Liao boundary requires at least 10 FDTD cells just next to the edges to be homogeneous, otherwise instability may occur. This condition is usually satisfied as there is a common practice of padding a certain number of free space



(a) Maxima of electric fields.



(b) Speed of electric fields.

Figure 3.26: Results from the cable model with the different cell sizes applied: (a) maxima of the radial electric fields recorded within the cable insulation and at the positions of 0.25 m, 0.5 m, 0.75 m and 1.0 m from the source end; (b) propagation speed of the electric fields. The speed was calculated based on the time difference between peaks of the electric fields recorded at different positions.

cells to the model edges. The advantage of the Liao boundary is that no extra cells are added and therefore it is less computationally intensive. While absorbing boundaries are frequently used in FDTD models, the reflecting boundaries can be advantageous in some situations to reduce memory usage and thus save calculation time. For example, if one edge of the model is totally defined by the perfect conductor material, then removing free space padding for this edge and applying directly on this edge a reflecting boundary is an efficient option.

In terms of applications to the FDTD cable models in this study, where both PML and Liao absorbing boundaries were applicable, they were found to produce very similar results. Liao would use less memory and calculation time. For example, the amount of memory used by the cell size of (0.5, 10, 0.5) mm in Table 3.5 was 324.7 MB where the PML boundary was used. Switching to the Liao boundary reduced the memory usage to 179.1 MB. Furthermore, for the cable models, it was difficult to create a matched load for the cable ends. A cable end terminated with a matched load will not have electromagnetic fields being reflected back into the cable. Interestingly, by applying the PML boundary directly to a cable end, it behaved like a matched load with no reflection from the cable end being seen in simulation results, where as the Liao boundary was not able to produce the same “matched” effect. However, without being able to explain this effect reasonably, it is not yet clear that if this is only a characteristic of XFDTD software specifically or whether it applies to the PML boundary in general. The reflecting boundaries like the PEC boundary are useful to simulate a short-circuit termination for the cables as well as saving computing resources by applying to any cable end terminated totally by the perfect conductor (PEC) material.

### 3.5.4 Creating PD Source and Modelling of TDR measurement

#### 3.5.4.1 Evaluation of Excitation Sources in XFDTD

A PD event will excite pulse current to flow through a short distance at the PD source location. A current filament has been found to represent a PD source in an FDTD model properly [77]. In XFDTD, a current filament can be created using either a current source or a voltage source. Equivalent circuits of the current and voltage sources in XFDTD are shown in Figure 3.27. Waveform, amplitude and

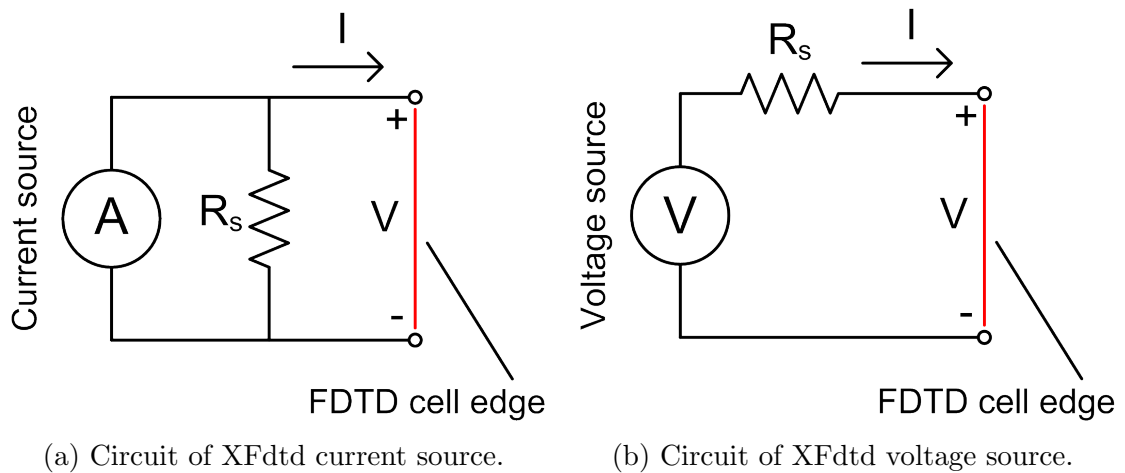


Figure 3.27: Current and voltage sources in XFdtd.

impedance of the sources can be specified. Inclusion of the source impedance aims to simulate in reality that how a device such as a circuit and an antenna is driven by a source [107]. Typically, the source impedance should be selected to match the characteristic impedance of the device. Alternatively, since a  $50\ \Omega$  coaxial cable is quite frequently used to connect an exciting source to a device, setting the source impedance to  $50\ \Omega$  can be practiced to approximate the effect of the coaxial cable.

To evaluate XFdtd's current and voltage sources and their setups in terms of suitability for representing a PD source, a free space cube was defined with a current filament at its centre to investigate electromagnetic waves radiated by the current filament. Figure 3.28 shows a diagram of the cube. Current and voltage sources were tested sequentially to represent the current filament in the model. The source waveform was a  $0.1\ \text{ns}$  duration Gaussian pulse for both kinds of source. Furthermore, the source impedance was set to  $50\ \Omega$  and  $0\ \Omega$  in each case. Results from the simulations are shown in Figure 3.29. Apart from the  $0\ \Omega$  current source, the other three source configurations all had a bipolar current waveform, which is inappropriate for a PD pulse as this will result in the amount of net charge in the PD (area under the pulse) being nearly  $0\ \text{pC}$ . This was further evidenced by the voltage waveform at the source position. Figures 3.29c and 3.29d show that while the other sources had a pulse voltage, the  $0\ \Omega$  current source had a step voltage. The amount of charge in the PD or the PD level can be calculated by  $\Delta Q = C\Delta U$  where  $\Delta U$  is the voltage change at the PD source position. Thus, apart from the  $0\ \Omega$  current source, the other

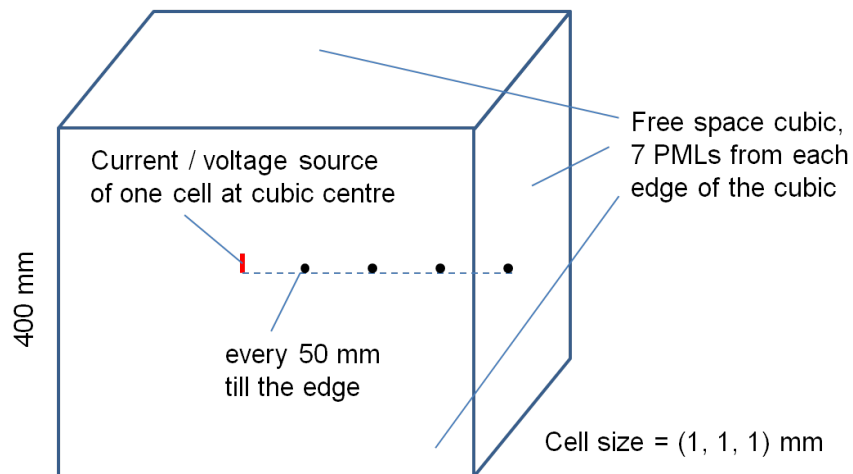


Figure 3.28: A 400 mm free space cubic used to evaluate excitation sources in XFDTD. An uniform cell size of 1 mm was used and to each edge of the cubic, 7 layers of the PML boundary were added. A 1 mm source was put at the cubic centre. Four point sensors were evenly spaced between the source and one edge of the cubic to record electromagnetic fields radiated by the source.

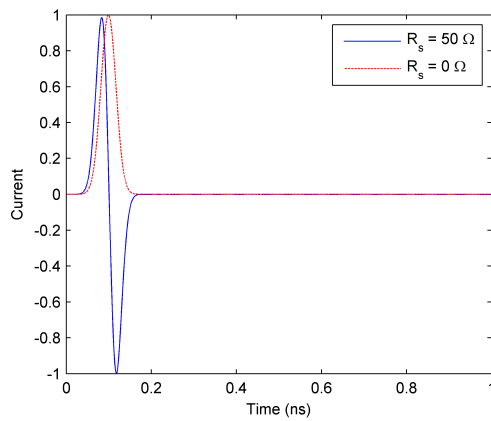
sources will nearly have a 0 pC PD level. To evaluate electromagnetic radiation characteristics of the sources, electric fields recorded by the point sensor right on the cubic edge were considered approximately to be the far-field waveform. The result of the  $0 \Omega$  current source (Figure 3.29e) has shown that the far-field waveform is approximately proportional to the time derivative of the current waveform ( $di/dt$ ) [113].

In summary, among the XFDTD source specifications being tested, the  $0 \Omega$  current source was found appropriate for representing a PD source in the FDTD model.

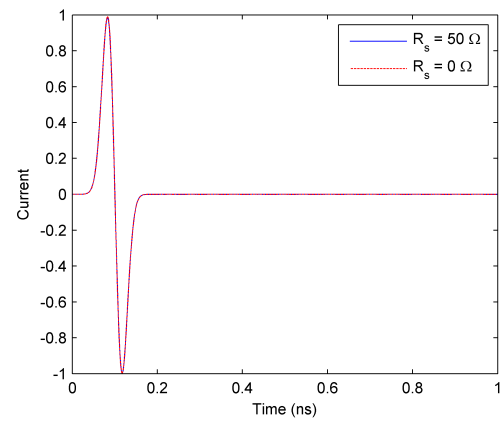
#### 3.5.4.2 FDTD Modelling of TDR Measurement on Cables

This is not main part of the research, but is included because of the practical implications for launching pulses into an HV cable in the FDTD model.

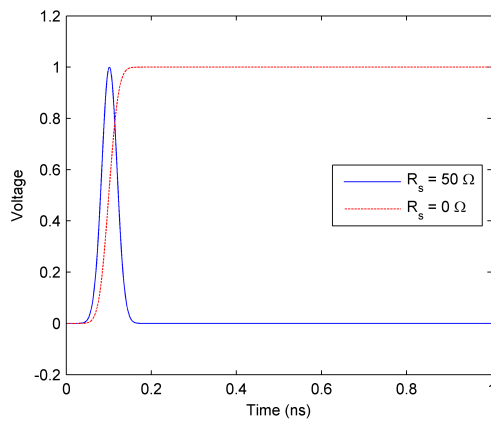
Time domain reflectometry (TDR) is a long-established method for fault location on cables. It is also the most popular method for locating PD defects in HV cables [117]. A diagram of the TDR measurement principle on an HV cable is shown in Figure 3.30. A fast pulse is injected from one end of the cable. The pulse will be reflected when reaching a point where the characteristic impedance changes. Different reflections can be expected depending on the nature of the



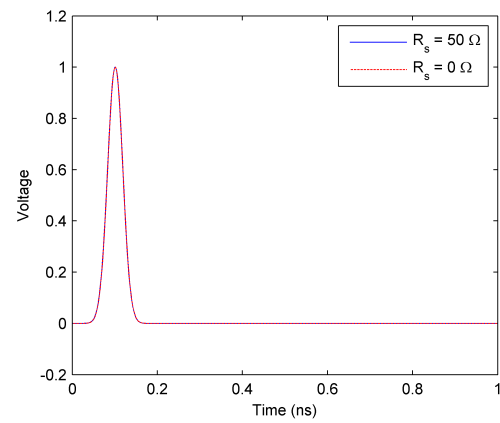
(a) Current waveform of current source.



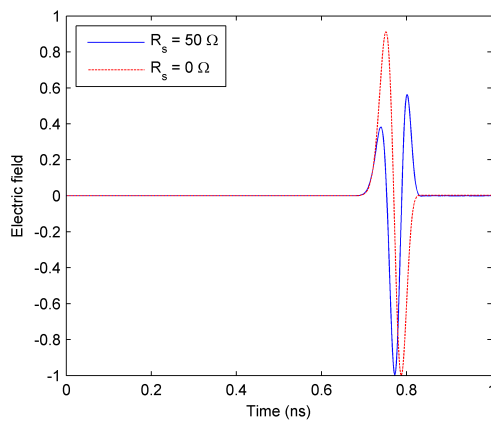
(b) Current waveform of voltage source.



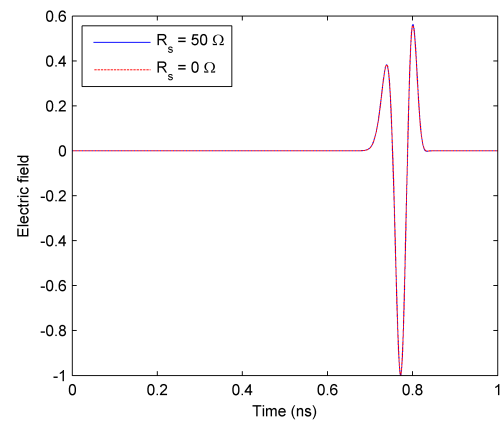
(c) Voltage waveform of current source.



(d) Voltage waveform of voltage source.



(e) Far-field waveform of current source.



(f) Far-field waveform of voltage source.

Figure 3.29: Evaluation of current and voltage sources in XFtd. Source impedances of  $50 \Omega$  and  $0 \Omega$  (replacing  $R_s$  by an open-circuit and a short-circuit for the current and voltage sources respectively) were tested in simulations. Output from the simulations has been normalized.

defect. Defect location is realized by measuring the time difference between the incident pulse and the reflected pulse, together with a knowledge of the signal propagation velocity.

FDTD modelling of the TDR measurement is interesting in terms of predicting the types of cable defect that could cause a measurable reflection of an injected pulse. For example, considering a practical TDR test could probably at best resolve a voltage “reflection/incident coefficient” of “1/1000”, if the modelling result shows that the maximum amplitude of the reflection is 1000 times smaller than the incident amplitude, the defect is less likely to be measurable in practice.

According to Figure 3.30, a basic diagram for FDTD modelling of the TDR measurement is shown in Figure 3.31. Following the diagram to create an FDTD model, it was found that simply connecting a current or a voltage source between

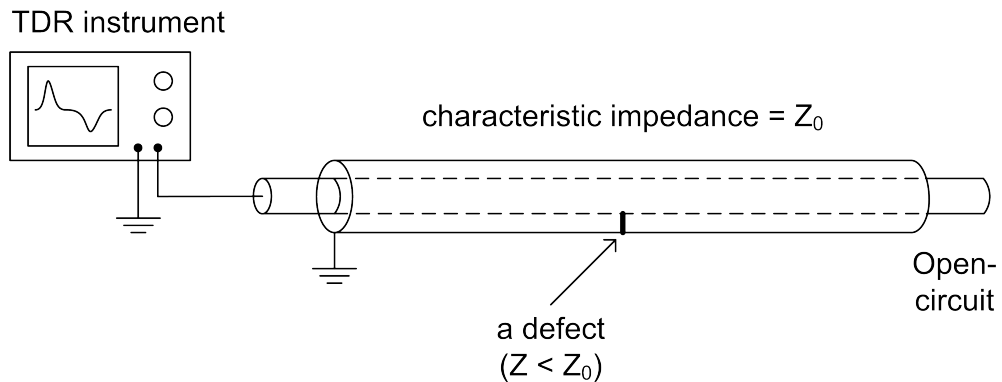


Figure 3.30: Diagram of TDR measurement on an HV cable. An incident pulse is injected from one end of the cable. The other end of the cable is open circuit. There is a conducting defect within the cable insulation, from which an inverse polarity reflection is expected.

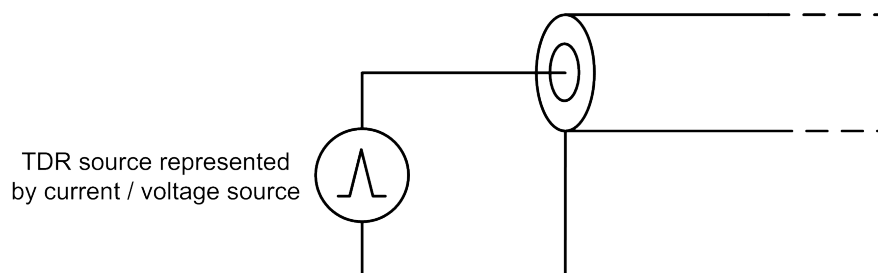


Figure 3.31: Diagram of FDTD modelling of TDR measurement. An excitation source (either current or voltage source) is connected between the inner and outer conductor at one end of the FDTD cable model. The other end of the cable model is open circuit.



the inner and outer conductors did not produce a satisfactory TDR result. There would be significant “ringing” between the incident pulse and the pulse reflected from the other end of the cable (open circuit) so that the reflection from a defect located somewhere in the cable cannot be identified. The “ringing” was resulting from the inappropriate method of coupling the incident pulse into the cable. In order to reduce the “ringing” in the results, two kinds of TDR input module were proposed to replace the basic connection scheme. Figure 3.32 shows the modules. One is to make 4 or 8 evenly spaced resistor connections between the

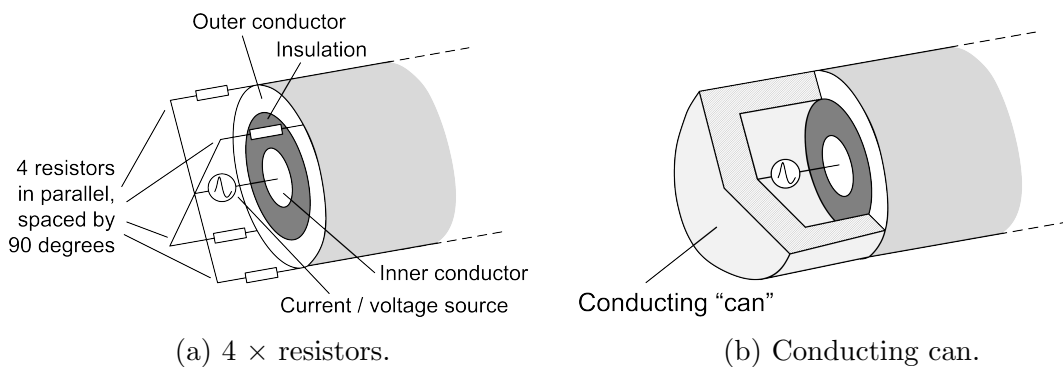
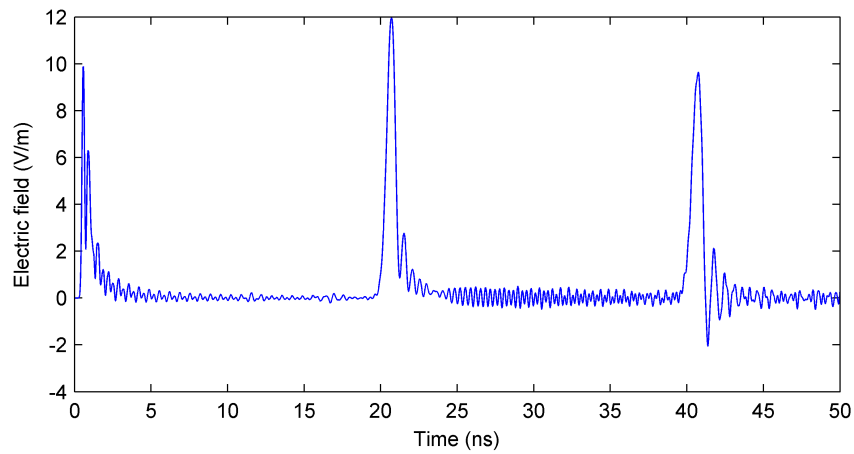


Figure 3.32: Two kinds of TDR input module for FDTD modelling of TDR measurement.

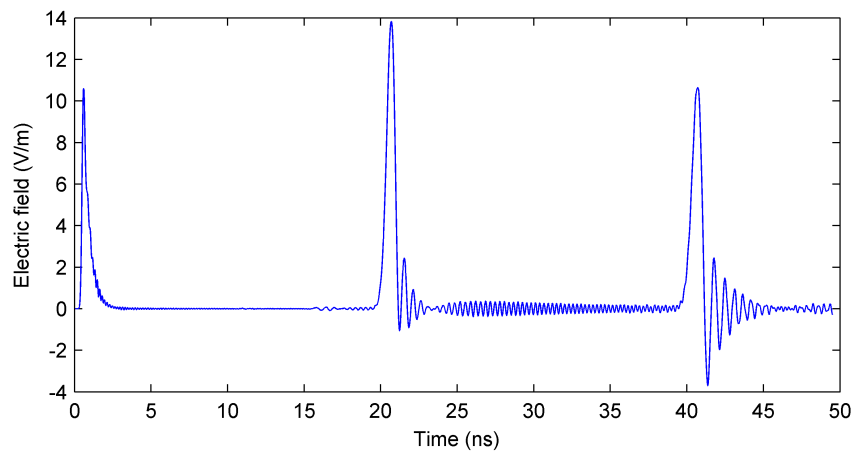
inner and outer conductors. The other one is using a “conducting can” to fulfill the connection. Comparing to the simple arrangement in Figure 3.31, both the proposed modules can improve coupling from the source to the cable because the input current is balanced by the symmetrical arrangements. FDTD models using both the modules have produced results with lower “ringing” (see Figure 3.33). The “conducting can” would be preferred as it has a simpler structure and the excitation source is completely screened by this setup.

## 3.6 Conclusions

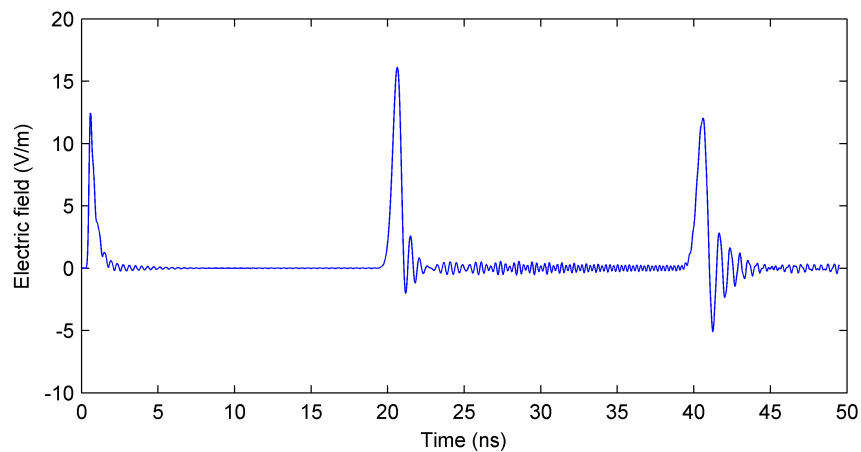
The FDTD technique has been widely used in power industry to model PD or PD-like transients in high voltage and power devices. For modelling of PD in cables, some research has been seen looking into the detection sensitivity of capacitive couplers and high frequency properties of cables. To the best of the author’s knowledge, using FDTD modelling to investigate the processes involved in HFCT-based PD detection has never been carried out. This should include



(a) Using the simple arrangement in Figure 3.31.



(b) Using the 4×resistor input module in Figure 3.32a.



(c) Using the conducting can input module in Figure 3.32b.

Figure 3.33: TDR modelling results by using the different TDR input modules. The cable model was same as that in Figure 3.24 but without the semicon layers (i.e., semicon properties replaced by the neighboring conductor properties). The first pulse in the results was the incident pulse and the second and third pulses were the reflection from the other end of the cable.

excitation of PD in cables, PD propagation along the cables and PD detection by HFCTs. The basic FDTD technique requires that material properties remain constant at frequencies of interest. For materials with frequency-dependent properties, one option is to carry out separate runs with each run to cover a narrow frequency range. This situation can be improved through a modification of the basic FDTD expression and presently the capability of dealing with frequency-dependent materials (or dispersive media) is already built in many commercial modelling packages (including XFDTD, which is employed in this work).

By using FDTD modelling to investigate the PD location accuracy in both a GIS tee section and a GIS circuit breaker, factors that would influence the location accuracy were evaluated. The optimal positions for PD sensor installation where a better location accuracy can be expected were suggested. A cable is like a mini version of GIS. FDTD modelling of PD in cables is, however, more complex due to the fact that the semi-conductive (semicon) layers in the cables have properties that vary significantly with frequency. The semicon layers cannot be ignored since they can play a dominant role in high frequency responses of the cables. Appropriate FDTD models of the cables should reproduce high frequency properties of the cables as accurately as possible. To this end, experience gained in this work when attempting to create FDTD models and improve their accuracy was summarised to facilitate future work. The experience includes creating FDTD cable models, assigning material definitions to components within the models, choosing appropriate FDTD simulation parameters and discussion on some specific issues like setting up an excitation source which can well represent a PD source and alternative input arrangements for modelling of TDR measurement to suppress unwanted resonances of the pulse in the results.

# Chapter 4

## Characterisation of Cable Semicon Properties

### 4.1 Introduction

There are usually two semi-conductive (semicon) layers in modern polymeric-insulated HV cables. One is between the inner conductor and the insulation and the other is between the insulation and the outer conductor. The two semicon layers are called the inner semicon layer (or the conductor screen, etc.) and the outer semicon layer (or the insulation screen, etc.) respectively. Their purpose is to provide an intermediate conductive interface between the conductors and the insulation, so as to relieve electric field concentration between them and around surface imperfections and protrusions. The semicon layers are often made of a mixture of insulating polymer and carbon black [118] and blending of the mixture can vary from manufacturer to manufacturer. Dielectric properties of the semicon layers will depend on not only the mixture itself, but also many environment variables like frequency, temperature, pressure, etc. The semicon layers have been found to dominate high frequency properties of polymeric-insulated HV cables [30]. Therefore, to investigate high frequency properties of the cables, using either analytical or numerical methods, obtaining dielectric properties of the cable semicon layers is essential in terms of getting calculated high frequency properties to agree with those from experimental measurements.

This chapter starts from reviewing the definition of dielectric properties and the lumped equivalent circuits of dielectric materials. After that, state of art dielectric measurement techniques as well as those specially developed for the

measurements of cable semicon properties are summarised. Finally, dielectric properties of the outer semicon layer of an 11 kV EPR cable were measured by a dielectric spectroscopy. Using different dielectric relaxation models, both the measured semicon data and some published semicon data were fitted. The obtained parameters of the dielectric relaxation models will be used later in both analytical calculation and creating FDTD models of the cables.

## 4.2 Definition of Dielectric Properties

Dielectric properties of the semicon layers are the complex relative permittivities of the semicon mixtures. Permittivity or dielectric constant of an insulating medium, as we usually know, is proportional to the energy stored in a capacitor filled with the medium. Air/vacuum is the most common dielectric medium that has a permittivity of  $\epsilon_0 = 8.854 \times 10^{-12}$  F/m. Permittivity of any other dielectric medium is often represented by the relative permittivity  $\epsilon_r$  (or relative dielectric constant) which is obtained as the ratio of the measured capacitance  $C$  of a capacitor filled with the dielectric medium to the geometrical capacitance  $C_0$  of the same capacitor but with the dielectric medium replaced by air. Generally  $\epsilon_r$  can be calculated as follows in an ideal, parallel-plate capacitor

$$C_0 = \epsilon_0 A/h \quad (4.1)$$

$$\epsilon_r = C/C_0 = \epsilon/\epsilon_0 \quad (4.2)$$

where  $A$  and  $h$  are the capacitor plate's area and the separation between the two plates (refer to Figure 4.1).

For a non-ideal dielectric medium, if the capacitance is measured at different frequencies (for example applying a voltage  $U(\omega)$  where  $\omega$  is the angular frequency of the alternating voltage  $U$ ) the measured capacitance  $C$  should also be a function of  $\omega$ . Furthermore, in practice the angle between the current  $I(\omega)$  going through the capacitor and  $U(\omega)$  will not be exactly  $90^\circ$  and normally will be smaller than  $90^\circ$ , which is because there is no perfect dielectric that has no conductivity and therefore no ideal capacitor which has no loss. This will result in the measured capacitance,  $C^*(\omega)$ , a complex quantity

$$C^*(\omega) = C'(\omega) - jC''(\omega) \quad (4.3)$$

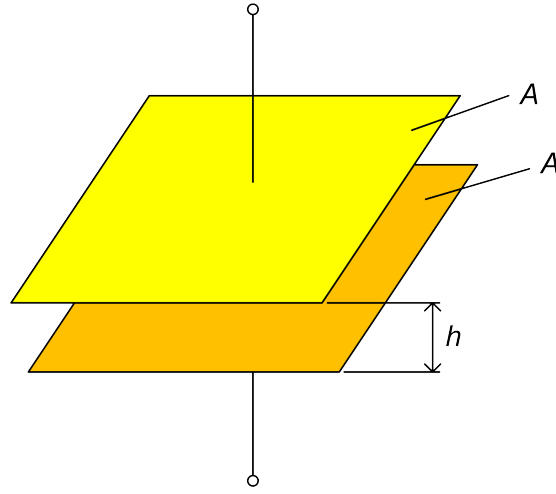


Figure 4.1: Parallel plate capacitor consisting of two plates (area  $A$ ) separated by a gap  $h$ .

where the real part  $C'$  represents the ordinary capacitance while the imaginary part  $C''$  represents the dielectric loss component. Accordingly, a complex dielectric function can be derived by the ratio of  $C^*$  to  $C_0$

$$\epsilon^*(\omega) = \epsilon'(\omega) - j\epsilon''(\omega) = C^*(\omega)/C_0. \quad (4.4)$$

$\epsilon^*$  is called the complex relative permittivity of the material filling the capacitor. Its real part  $\epsilon'$  is simply the relative permittivity  $\epsilon_r$  in (4.2) while its imaginary part  $\epsilon''$  is proportional to loss dissipated per period in the capacitor.

The loss dissipated is caused by leakage current which flows through the capacitor under a voltage supply. The leakage current is associated with the filling material's leakage resistivity/conductivity. At low frequency the loss is attributed to dc conductivity  $\sigma_{dc}$  which is due to ions transportation. At high frequency, dipole movements come into play and become the source of most of the loss dissipated. In contrast to  $\sigma_{dc}$ , this property at high frequency is sometimes called ac conductivity  $\sigma_{ac}$  or bulk-AC conductivity and will increase linearly with frequency [119]. In addition, there is another definition widely used in engineering applications to represent the loss dissipated in the dielectric, which is the tangent of the loss angle,  $\tan \delta$ . It is defined by the ratio of the active current to the reactive current and can be given by the complex permittivity as

$$\tan \delta = \epsilon''/\epsilon' \quad (4.5)$$

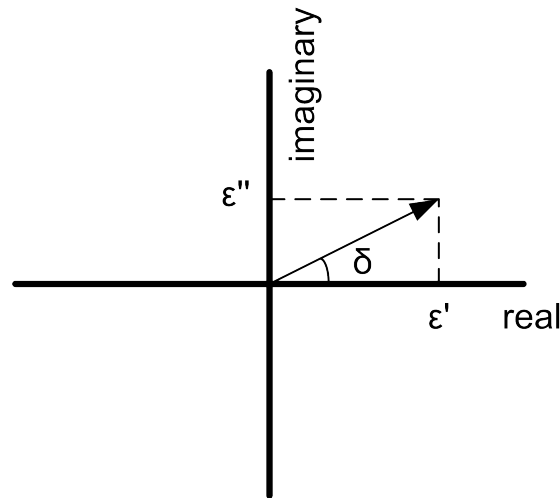


Figure 4.2: Relation between the loss angle  $\delta$  and the complex permittivity in (4.4) mapped in the complex plane.  $\delta$  is the angle between the complex permittivity vector and the real axis [119].

where  $\delta$  is the loss angle and in the complex plane it is the angle between the complex permittivity and the real axis as shown in Figure 4.2. The ac conductivity  $\sigma_{ac}$  can be related to  $\tan \delta$  by

$$\sigma_{ac} = \omega \epsilon_0 \epsilon_r \tan \delta = \omega \epsilon_0 \epsilon'' \quad (4.6)$$

where  $\omega$  is the angular frequency and  $\epsilon_r$  is the relative dielectric constant, i.e.,  $\epsilon'$  the real part of the complex permittivity.

### 4.3 Lumped Element Equivalent Circuits

To measure complex permittivity, the most straightforward method is to start by preparing a plate capacitor with a sample sandwiched between the two conductors and then apply to the capacitor a voltage and measure the resulting current so that the sample's complex admittance/impedance can be calculated. However, this method only gives accurate results in relatively low frequency ranges. Once the sample's complex admittance/impedance is obtained, then by choosing an equivalent circuit for the sample together with the dimensions of the sample under test, the complex permittivity can be worked out. There are two basic equivalent circuits which are normally used for representing the response of a dielectric to alternating driving fields and are the fundamentals of most of the

measuring techniques for the dielectric properties. They are the  $G - C$  parallel circuit model and the  $R - C$  series circuit model respectively. Figure 4.3 shows the diagrams of the two circuits and their voltage and current vector representations.

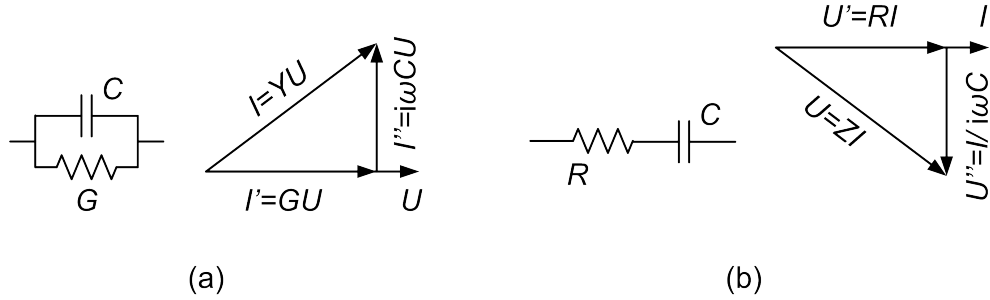


Figure 4.3: Parallel and series equivalent circuits for dielectric materials. (a) The parallel equivalent circuit,  $I'$  flowing through  $G$  and  $I''$  flowing through  $C$  are in phase and in quadrature with the reference voltage  $U$  respectively. (b) The series equivalent circuit,  $U'$  across  $R$  and  $U''$  across  $C$  are in phase and in quadrature with the reference current  $I$  respectively [115].

For the parallel circuit the total admittance  $Y$  consisting of the conductance  $G$  and the capacitance  $C$  is used,

$$Y(\omega) = G(\omega) + j\omega C(\omega) \quad (4.7)$$

$$I(\omega) = Y(\omega)U(\omega) = [G(\omega) + j\omega C(\omega)]U(\omega) \quad (4.8)$$

where  $U$  is the driving reference voltage and  $I$  is the resulting current. For the series circuit the total impedance  $Z$  consisting of the resistance  $R$  and the capacitance  $C$  is used,

$$Z(\omega) = R(\omega) + 1/j\omega C(\omega) \quad (4.9)$$

$$U(\omega) = Z(\omega)I(\omega) = [R(\omega) + 1/j\omega C(\omega)]I(\omega) \quad (4.10)$$

where  $I$  is the driving reference current and  $U$  the resulting voltage.

Since either the admittance  $Y$  from the parallel circuit or the impedance  $Z$  from the series circuit can be used to represent a same sample, it is automatically true that  $Z$  is the reciprocal of  $Y$  and moreover there are conversion equations by which given the components of either one of the circuits the components of the other circuit can be worked out. For example, if the impedance  $Z$  of the series



circuit is provided, the conductance  $G$  and the capacitance  $C$  of the parallel circuit can be obtained by

$$G = \frac{\omega^2 C_0^2 R_0}{1 + (\omega C_0 R_0)^2} \quad (4.11)$$

$$C = \frac{C_0}{1 + (\omega C_0 R_0)^2} \quad (4.12)$$

where  $C_0$  and  $R_0$  are the components of the series circuit.

Although the two equivalent circuits can be converted between each other they are actually looking at different aspects of a material's dielectric properties. The  $G - C$  parallel circuit is a natural way of describing physical phenomena in which the current in phase with  $U$  (through the conductance  $G$ ) and the current in quadrature with  $U$  (through the capacitance  $C$ ) exist in parallel while the  $R - C$  series circuit is suitable for cases where two physically different regions are in series with one another [115].

In measuring the complex permittivity, usually the complex impedance  $Z$  is obtained and its real and imaginary parts are corresponding to the resistance  $R_0$  and conductance  $C_0$  of the series circuit. The corresponding conductance  $G$  and capacitance  $C$  of the parallel circuit can be found out by using (4.11) and then the complex permittivity can be calculated by

$$\epsilon' = C \times \frac{h}{\epsilon_0 A} \quad (4.13)$$

$$\epsilon'' = G \times \frac{h}{\omega \epsilon_0 A} \quad (4.14)$$

where  $A$  and  $h$  are the area of the capacitor plate and the separation between the two plates. In addition, there is an alternative way of finding out the complex permittivity from measured admittance/impedance data. Based on the complex capacitance defined in (4.3), the relation between the current  $I$  and the voltage  $U$  can be written as

$$I(\omega) = j\omega C^*(\omega)U(\omega) \quad (4.15)$$

which if compared to (4.8) gives out

$$C^*(\omega) = Y(\omega)/j\omega = \epsilon_0[\epsilon'(\omega) - j\epsilon''(\omega)](A/h). \quad (4.16)$$

Therefore, if the area  $A$  of the capacitor plate and the separation between the two plates  $h$  are known, the complex permittivity can be worked out.

## 4.4 Review of Dielectric Measurement Techniques

### 4.4.1 Frequency Domain and Time Domain Methods

The complex permittivity can be measured across a frequency range of  $10^{-6} - 10^{12}$  Hz with different measurement techniques covering different frequency bands. The lumped circuit methods which are based on measuring  $U(\omega)$  and  $I(\omega)$  in Figure 4.3 to work out  $Y(\omega)/Z(\omega)$  are able to provide reasonable accuracy in a range of  $10^{-6} - 10^7$  Hz. Above this range, the method will be increasingly suffering from sample dimension effects, parasitic impedances resulting from cables and connectors, etc. From  $10^7 - 10^{11}$  Hz, distributed circuit methods which are based on reflection/transmission measurements can be employed. For frequencies ranging from  $10^{10} - 10^{12}$  Hz, there are “quasi-optical” methods of which one scheme is making use of an interferometer to obtain complex transmission coefficients. Above  $10^{12}$  Hz, Fourier transform spectrometers can be used to obtain the complex permittivity [114].

The techniques mentioned above are all frequency domain methods. As a counterpart, there are time domain methods. Basically, a dielectric response function  $f(t)$  is defined to describe the response of a dielectric medium to applied electric fields. The function can be derived by measuring either polarization or depolarization currents flowing through a sample if a step-function charging field is applied [115]. A conversion from the measured response function to the complex permittivity can be done by using Laplace or Fourier transform [120]. Comparing with the frequency domain methods, the time domain methods are easier to use as no highly sophisticated devices are required, and moreover, since one measurement is able to cover various frequencies, it is also less time consuming. However, the expense paid for such simplification is reduced accuracy, and furthermore the usual time domain setup can only be used at low frequencies, such as  $\leq 10$  kHz. For higher frequencies, a different test arrangement and faster digital oscilloscopes are required [114].

### 4.4.2 Implementation of Frequency Domain Method

A basic implementation scheme of frequency domain measurements using the lumped circuit methods is shown in Figure 4.4. The complex impedance  $Z_s^*$  of

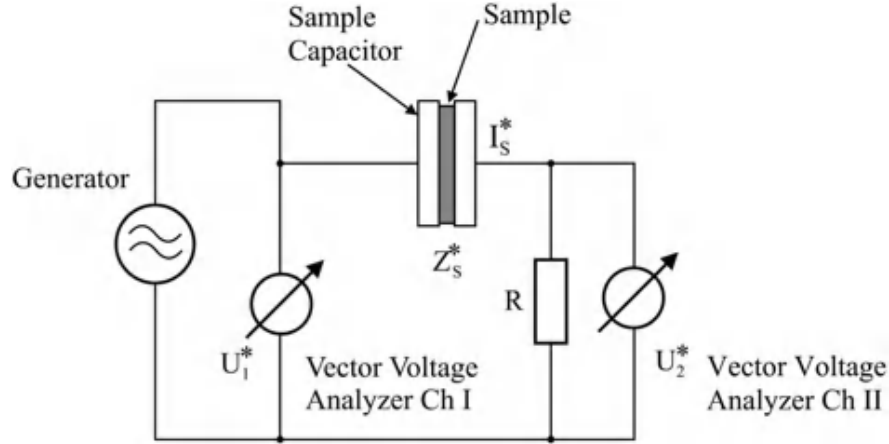


Figure 4.4: Basic implementation scheme of the lumped circuit methods [114].

the sample is calculated from the measured data by

$$Z_s^*(\omega) = \frac{U_s^*(\omega)}{I_s^*(\omega)} = R \left[ \frac{U_1^*(\omega)}{U_2^*(\omega)} - 1 \right]. \quad (4.17)$$

In a real measurement device, the scheme in Figure 4.4 is seldom followed since using the resistor  $R$  will present several limitations to the measurements. Practical devices usually have modified schemes so as to improve measurement accuracy and accommodate different frequency ranges. The lumped circuit methods are efficient for the measurements at frequencies  $\leq 10$  MHz, higher than which treating the sample as a lumped element circuit becomes progressively less accurate.

Measurements at frequencies from 10 MHz to 100 GHz can be covered by the distributed circuit methods. Certain kinds of test cell are used to accommodate samples as well as carry measurement signals. Network analyzers are often employed to carry out required reflection/transmission measurements. One typical scheme of the distributed circuit methods is shown in Figure 4.5 where a sample is mounted in a test cell and the test cell is connected via bidirectional couplers to a vector voltmeter. In practice, many test cells and schemes have been proposed according to specific requirements of samples and applications. For example, an open coaxial line resonator whose resonant system was formed by introducing a

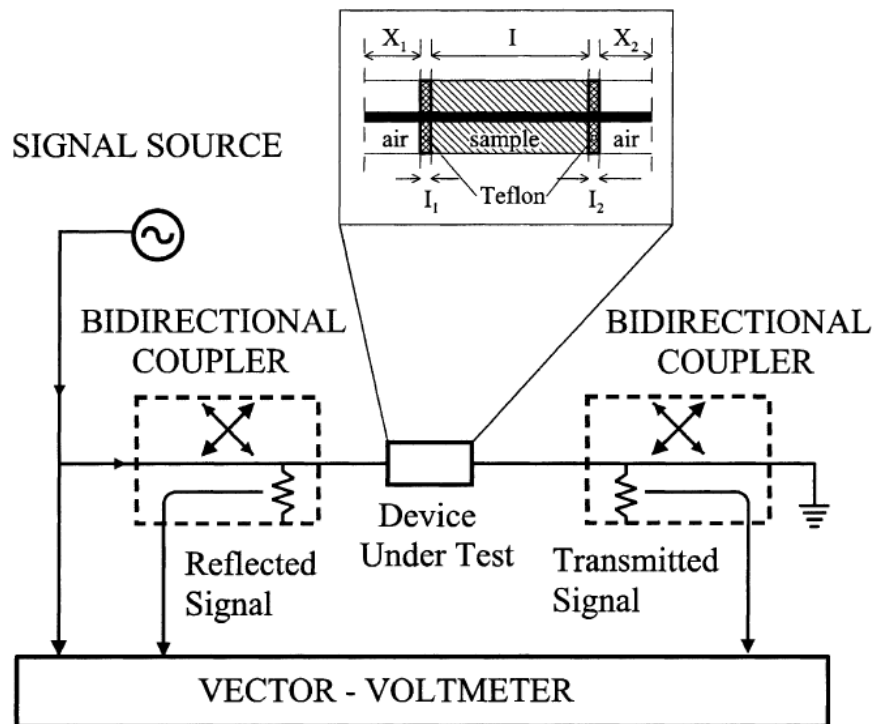


Figure 4.5: Distributed circuit methods using a vectorial network analyzer with a transmission line test cell [114].

capacitive gap in a coaxial line's centre conductor and terminating the coaxial line with a dielectric sample was presented to carry out non-destructive measurements of the complex permittivity of the sample. Accurate results were obtained for some dielectric solids, liquids, and biological tissues up to 4 GHz [121]. An open-ended coaxial line was used as a sensor to determine the complex permittivity of biological tissues from 10 MHz to 1 GHz, where two network analyzers of different bandwidths were combined to achieve the frequency range, and it was suggested that a proper selection of dimensions of the coaxial line is essential for the measurement accuracy. Using the proposed coaxial line sensor, experiments conducted on some liquid and tissue samples found highly reproducible and accurate results [122; 123].

Directly measured variables from the distributed circuit methods are usually not the complex permittivity. Some formulating has to be performed before the complex permittivity can be calculated from the directly measured variables. For example, in order to obtain properties of high loss dielectric media, Bérubé et al. [124] compared four impedance models for an open-ended coaxial line test

cell. Formulating of the four models was discussed and the accuracy of each model was evaluated in the work of measuring the complex permittivity of saline solutions from 1 – 20 GHz. Pournaropoulos et al. [125] reviewed the admittance models proposed in the last decades for an open-ended coaxial line sensor and compared their accuracies by calculating the complex permittivity in dielectric measurements of liquid samples from 1–40 GHz. Ritz and Dressel [126] proposed, for semi-conductive samples, a rigorous formation as well as a simplified formation to extract the complex permittivity from measured impedance data. The rigorous and the simplified formulations were able to give out accurate results up to 5 GHz and 1 GHz respectively.

Apart from the coaxial line test cells, other test cells like waveguide, resonators and cavities have also been widely used. Reviews of available test cells and schemes, from different aspects, have been produced by researchers [127; 128; 129]. Kaatze and Feldman [127] summarised, for liquid samples, various dielectric spectroscopy techniques covering a frequency range from  $10^{-6}$  –  $10^{12}$  Hz. Both frequency domain and time domain methods were reviewed and their accuracies and limitations were discussed. Gregory and Clarke [128] summarised, for dielectric measurements on polarity liquids, available techniques as reflectometric methods, coaxial sensors, transmission methods, resonance methods, admittance cell methods and time domain methods. A comprehensive review of the test setup of each method, measurement procedures and calibration steps was conducted to facilitate choosing an optimal measurement scheme depending on specific requirements. Krupka [129] categorized available methods into resonant and non-resonant methods for complex permittivity measurements at microwave frequencies. For each kind of method, different test cells were evaluated in terms of their operating frequencies and accuracies. While the non-resonant methods are able to carry out broadband measurements, they have relatively low sensitivities in measuring dielectric losses, and therefore are suitable for materials with relatively high losses. The resonant methods are particularly good for very low loss materials and can give out more accurate measurements of relative dielectric constants (real part of the complex permittivity), whereas they are typically used at one fixed frequency.

Nowadays there are dielectric spectroscopy systems which are making use of different measurement methods to accommodate measurement requirements of various frequency bands. For example, a dielectric spectroscopy system from

Novocontrol can consist of a dielectric converter (10  $\mu$ Hz–10 MHz), an RF impedance analyzer (1 MHz–1 GHz)/a network analyzer (300 kHz–3 GHz), dedicated test cells, shielding unit, temperature control system and data acquisition unit so that the complex permittivity measurement can be carried out at frequencies from  $< 1$  Hz to a few GHz and at temperatures from  $-160^\circ\text{C}$  to  $400^\circ\text{C}$ .

## 4.5 Review of Dielectric Measurements on Cable Semicon

For measuring dielectric properties of the cable semicon layers, samples are cut from the semicon layers and prepared as small pieces of various sizes (e.g., a few mm in diameter or square), and in most cases the samples are less than 1 mm in thickness. Dielectric measurements on the samples are performed to obtain the semicon properties so as to have accurate analytical and numerical modelling of the cables. The final objective will be to investigate high frequency properties of the cables using these models. To this end, an ideal measurement should reproduce those conditions that the samples would be experiencing while the cables are in operation, since the semicon properties depend on frequency as well as environment conditions like temperature and pressure. In practice, the frequency-dependent properties of the semicon are most sought after. At high frequencies ( $\geq 1$  MHz), dielectric constants of the cable semicon are typically between 100 and 1000, and conductivities are between 0.01 and 1 S/m [31]. In terms of the temperature and pressure dependence, they are usually investigated at a few temperatures and pressures at which the complex permittivity is measured over frequency.

Depending on actual requirements as well as available devices, the measurements can be carried out either by using the lumped circuit methods or the distributed circuit methods. The former one should be easier to use but has a limited bandwidth of 10 MHz maximum. The later one is able to achieve a very high bandwidth, e.g., a few GHz. It is also more versatile since there have been many measurement setups being proposed, which would allow a choice to be made based on specific samples and frequency ranges. However, these techniques are usually not able to be used immediately, both because dedicated test cells have to be made separately and vectorial network analyzers are not widely available. Furthermore, some kinds of impedance model are required to relate the measure-

ment result to the complex permittivity. These impedance models are not readily available and need to be worked out based on geometries and dimensions of the actual test cells, which may not be an easy task.

Broadband measurements of the cable semicon properties have been conducted where high frequency properties of the cables are of interest. Stone and Boggs [30] measured, for semicon samples from a cable's inner and outer semicon layers, capacitance and conductance up to 120 MHz by using an RF impedance analyzer. Guo and Boggs [33] measured dielectric constants and conductivities of ground semicon (outer semicon layer) samples from a 15 kV cable in both radial and circumferential directions from 1 – 100 MHz. Properties of the conductor semicon (inner semicon layer) were, in their work to calculate the cable high frequency loss, assumed to be the same as those of the ground semicon. That was because the conductor semicon was cross-linked to the cable insulation and could not be removed. Xu and Boggs [130] argued that, at frequencies  $\geq 10$  MHz, dielectric measurements on a plate capacitor sample using an impedance analyzer can suffer from errors caused by losses in the conducting electrodes (e.g., silver paint coating) of the capacitor sample. Therefore, two equations were proposed, for square and circular samples respectively, to calculate maximum frequencies to which accurate measurements are likely to happen based on the low frequency dielectric constant and DC conductivity of a sample.

Apart from using RF impedance analyzers for the measurements, there were some measurements using network analyzers in combination with specially designed test cells, which can achieve frequency ranges well beyond 100 MHz. Heinrich et al. [131] presented a measurement setup for determining the complex permittivity of semicon samples from different HV cables. The setup consisted of a coaxial line, a sample holder and a temperature control unit which would allow temperature-dependent measurements from 10°C to 85°C. The test procedures involved reflection measurements using a HP network analyzer and extracting dielectric constants and conductivities from the measured impedance data. Semicon samples from both XLPE and EPR cables were measured from 100 kHz–500 MHz and temperature measurements were also carried out to find out the temperature dependence of the semicon properties. Mugala et al. [116; 132] developed “one-port” and “two-port” test cells which are shown in Figure 4.6, for measuring the cable semicon properties.

Based on the test cells, “one-port” and “two-port” measurement methods

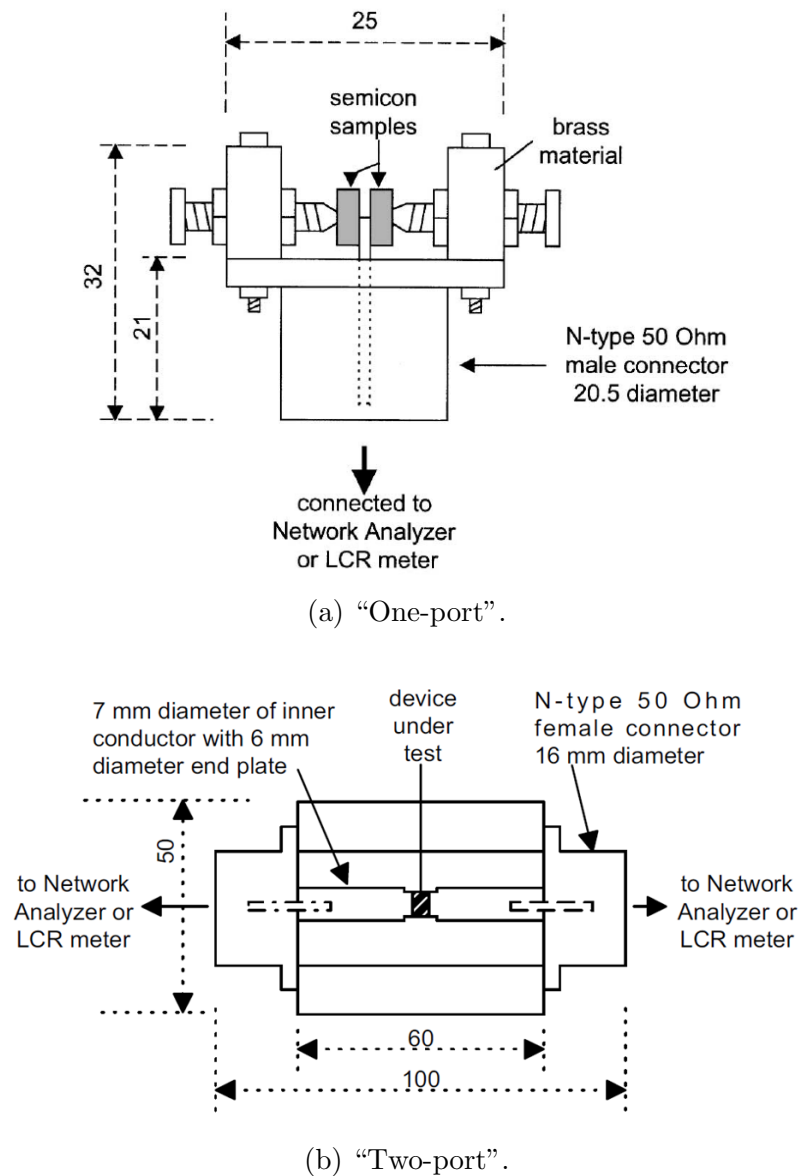


Figure 4.6: “One-port” and “two-port” test cells developed by Mugala et al [116; 132].

were respectively demonstrated. For the “one-port” method, measurements were carried out by using a HP LCR meter and a HP network analyzer in the frequency ranges of 20 Hz–1 MHz and 300 kHz–500 MHz respectively. Obtained complex permittivities were fitted using the Cole-Cole model’s expression whose parameters were then used to establish an analytical model for the corresponding cable [112]. While the “one-port” method was designed to measure the complex permittivity of the cable semicon, the “two-port” method was proposed to measure the complex permittivity for both the cable semicon and insulation. Besides



the “two-port” test cell, a different formulating to derive complex permittivities was proposed to account for the very low dielectric constant and loss of the cable insulation. The “two-port” measurements were carried out from 10 kHz–100 MHz on semicon samples from a medium voltage cable as well as XLPE and polycarbonate samples. Satisfactory results of the complex permittivity were obtained for both kinds of sample, while for the insulation samples, results of the “one-port” method had apparent scatter at frequencies  $\geq 1$  MHz [116].

In this study, towards creating three-dimensional FDTD models of the HV cables and simulating PD phenomena in the cables using the FDTD models, a good estimate of the cable semicon properties will improve the accuracy of the FDTD models in reproducing high frequency properties of the cables. Unfortunately, there is no RF impedance analyzer available nor the expertise in producing a sophisticated test cell for making use of a network analyzer. Therefore, another method was firstly attempted to obtain the semicon properties, aimed at performing measurements with as few changes as possible to conditions of the semicon layers in a real cable, based on the fact that the conditions like pressure and temperature, both have apparent effects on the semicon properties. In addition, this method did not require any semicon being removed from the cable, which is potentially advantageous since in many cases, the semicon layers will not be able to be removed from the cable insulation. However, results from the proposed method were disappointing even within a 2 MHz frequency range. More errors would be expected if moving on to measurements at higher frequencies, since the assumption that a sample can be treated as a lumped circuit in the measurements will be more and more inaccurate. Furthermore, in the measurements, electric fields were applied to the samples in a way that was perpendicular to the actual electric field direction when a cable is being energised, which may cause more uncertainties in the results. Hence, the proposed method was not further attempted, and instead, a Novocontrol dielectric spectroscopy system was used to measure the semicon properties.

## 4.6 Measurement Result and Fit Using Dielectric Models

Semicon samples were taken from the outer semicon layer of an 11 kV EPR cable. The outer semicon layer was made of semicon tapes. Small pieces measured  $28 \times 28$

mm squares were cut out of the tapes. Silver paint was applied to both sides of each piece (see Figure 4.7). The samples were sandwiched in a three-electrode test cell provided with the dielectric spectroscopy system. Figure 4.8 shows a picture of the system and the test cell. Measurements of the semicon properties were carried out over a frequency range of 1 kHz–10 MHz. Only the outer semicon layer of the cable was tested. The inner semicon layer was bonded to the cable insulation and harder to remove intact.

Dielectric spectroscopy is able to measure various electric quantities (from the measured impedance, quantities like permittivity, conductivity, inductance

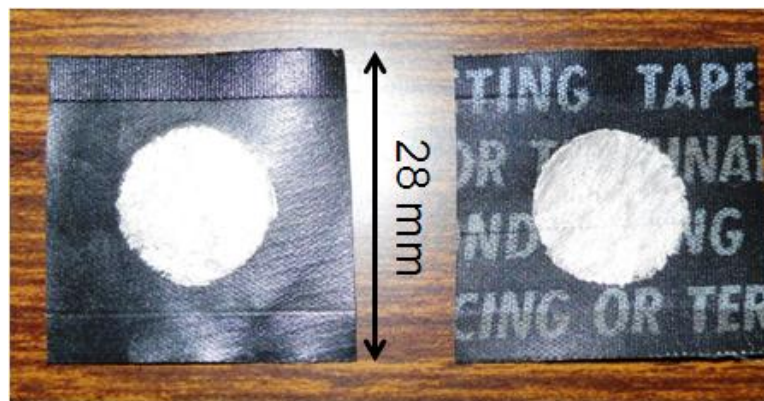


Figure 4.7: Silver painted semicon samples.

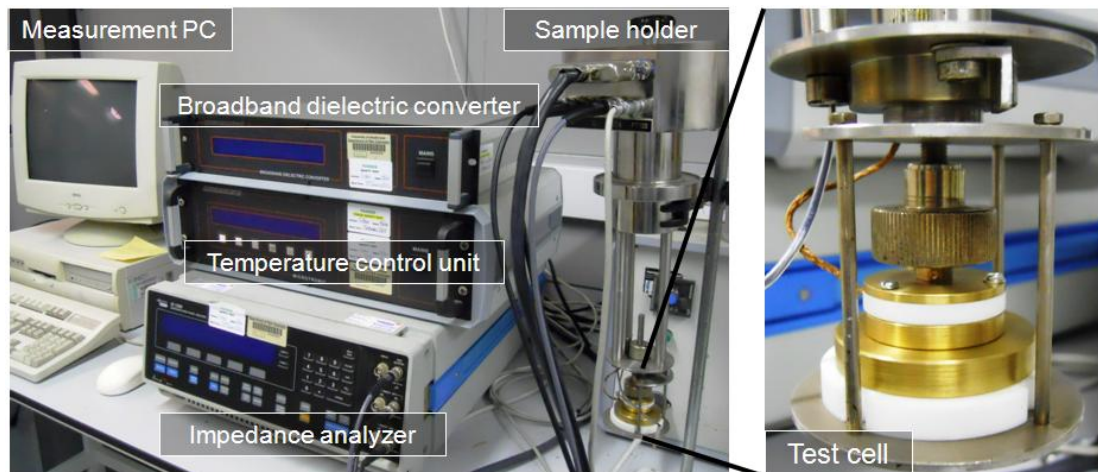


Figure 4.8: Novocontrol dielectric spectroscopy system. Measurement is carried out through the measurement PC. After specifying in the software interface sample dimensions, the measurement frequency range and requested electric quantities, the system can complete the measurement over the frequency range.

and so on are calculated by the system's software) at frequencies up to 10 MHz, which is not as good as those in the above reviewed works where hundreds MHz was achieved. Alternatively, the measured data (complex permittivity  $\epsilon^*$  of the semicon sample) in the 10 MHz range were fitted using some dielectric models, and then with the established dielectric models, semicon properties at frequencies  $> 10$  MHz were predicted.

Two dielectric relaxation models which are the Debye model and the Cole-Cole model were used to fit the measured data. Basic expression of the Debye model for the complex permittivity (4.4) is

$$\epsilon^*(\omega) = \epsilon_\infty + \frac{\epsilon_s - \epsilon_\infty}{1 + i\omega\tau} + \frac{\sigma_{dc}}{i\omega\epsilon_0} \quad (4.18)$$

where  $\epsilon_s$  is the static permittivity,  $\epsilon_\infty$  the permittivity at infinite frequencies,  $\tau$  the relaxation time of the Debye response and  $\sigma_{dc}$  is the dc conductivity [115]. The dc conductivity's contribution to the dielectric loss makes the last term in (4.18). For the second term in (4.18), if there is more than one Debye response (or Debye pole) present simultaneously in a material, this term can be added accordingly. For example, a Debye material consisting of  $n$  poles is represented as

$$\epsilon^*(\omega) = \epsilon_\infty + \sum_{i=1}^n \frac{\epsilon_{si} - \epsilon_\infty}{1 + i\omega\tau_i} + \frac{\sigma_{dc}}{i\omega\epsilon_0} \quad (4.19)$$

where  $\epsilon_{si}$  is the static permittivity from the  $i$ th Debye response and its relaxation time is  $\tau_i$ . However, behaviors of most dielectric materials vary to different extents from the Debye model, and therefore changes have to be made to (4.18) to accommodate the variations. A modified expression is proposed by Cole and Cole as

$$\epsilon^*(\omega) = \epsilon_\infty + \frac{\epsilon_s - \epsilon_\infty}{1 + (i\omega\tau)^{1-\alpha}} + \frac{\sigma_{dc}}{i\omega\epsilon_0} \quad (4.20)$$

where  $\alpha$  denotes the mathematical operation of tilting the  $\epsilon'' - \epsilon'$  graph (i.e., the Cole-Cole plot) by  $\alpha\pi/2$ . The Cole-Cole expression is able to correctly map small variations from the ideal Debye model, but since  $\alpha$  is a purely empirical factor introduced to describe experimental results, it does not have explicit physical meanings [115]. Furthermore, similar to the Debye model, the Cole-Cole expression (4.20) can also be augmented to reflect multiple responses existing

simultaneously. For example a 2 pole Cole-Cole expression is

$$\epsilon^*(\omega) = \epsilon_\infty + \frac{\epsilon_{s1} - \epsilon_\infty}{1 + (i\omega\tau_1)^{1-\alpha_1}} + \frac{\epsilon_{s2} - \epsilon_\infty}{1 + (i\omega\tau_2)^{1-\alpha_2}} + \frac{\sigma_{dc}}{i\omega\epsilon_0} \quad (4.21)$$

where  $\alpha_1$  and  $\alpha_2$  are the empirical factors for the two poles respectively.

Figure 4.9 shows, for the outer semicon layer of the 11 kV EPR cable, the measurement result (1 kHz–10 MHz) and corresponding fit results obtained using the Cole-Cole model and the Debye model respectively. The relative dielectric constant is simply  $\epsilon'$ , the real part of the complex permittivity  $\epsilon^*$ . The conductivity was calculated from the imaginary part  $\epsilon''$  of  $\epsilon^*$  by (4.6). The fit results show that the Cole-Cole model produced a good fit to the measured data. Actually, it was based on the Cole-Cole model's prediction of the semicon properties in the 1 kHz–100 MHz range that fit using the Debye model was carried out. The result of the Debye model was basically “wave-shaped” suggesting presence of more than one Debye response, and the Debye model produced conductivities that tended to deviate from the result of the Cole-Cole model at low frequencies

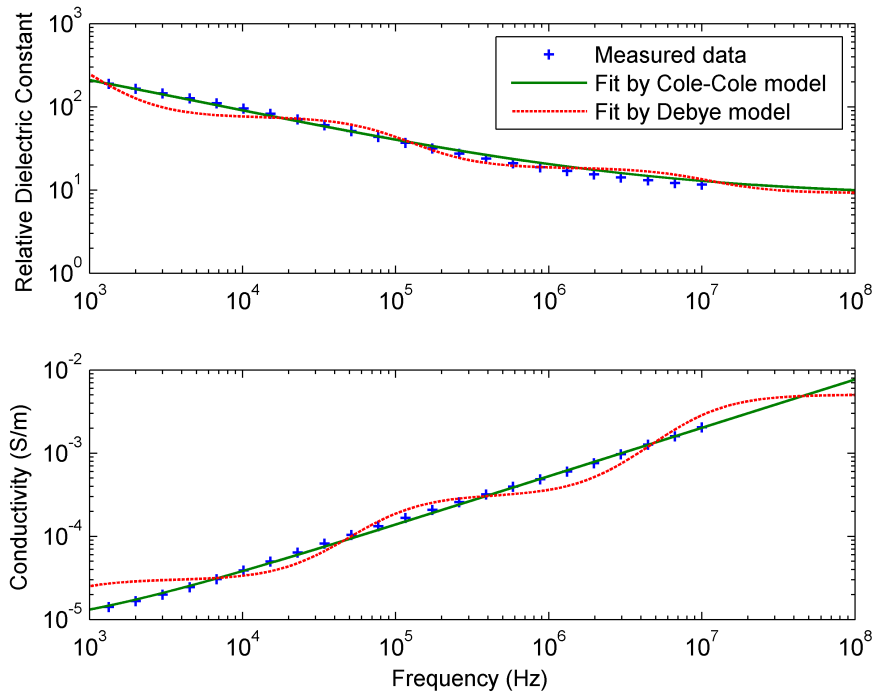


Figure 4.9: Dielectric properties of the outer semicon layer of an 11 kV EPR cable. Fits were using the Cole-Cole model (4.20) and a 3 pole Debye model respectively.

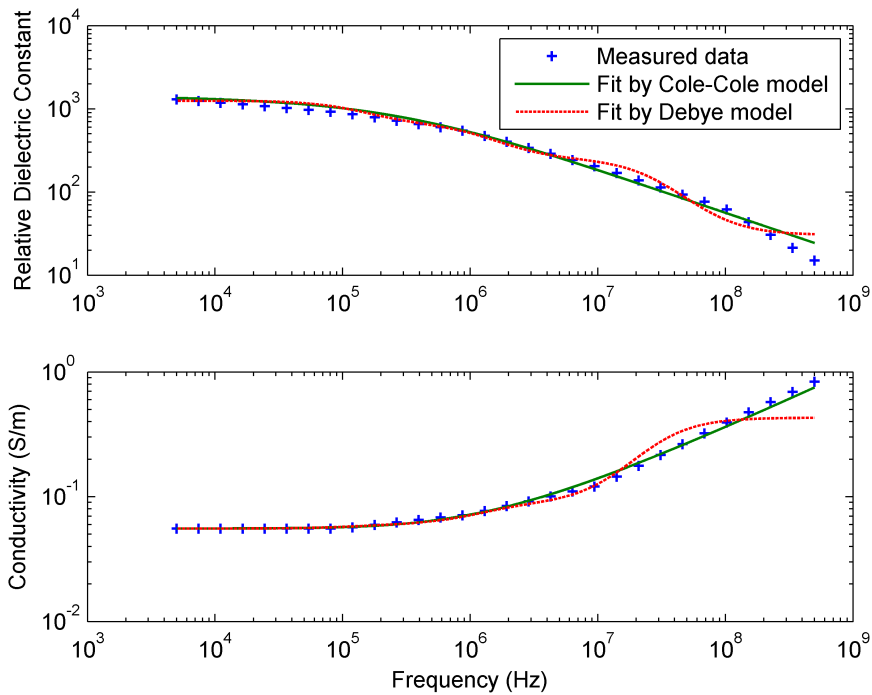
$< 7$  kHz and high frequencies  $> 50$  MHz.

Fit using the dielectric models was also carried out for published data of the inner and outer semicon of a 12 kV XLPE cable. Fit results are shown in Figure 4.10. Table 4.1 summarises, for the semicon layers of both the EPR and XLPE cables, the fit obtained parameters of the 3 pole Debye model. The 12 kV XLPE cable was one of the two medium voltage XLPE cables whose inner and outer semicon layers were measured from 5 kHz–500 MHz by using the “one-port” test cell [132]. The measurement results were recorded from the paper and fitted using both the Debye and the Cole-Cole models. Again, for the conductivity, Figure 4.10 shows that results of the Debye model start to deviate from the measured data and those of the Cole-Cole model at high frequencies ( $> 100$  MHz). The conductivity seems to approach the convergence at the high frequencies. According to (4.6), this can be explained in that the effect of increasing frequency was compensated by decreasing of the imaginary part  $\epsilon''$  of  $\epsilon^*$ . If comparing with the results of the Cole-Cole model, the conductivity deviation can be attributed to the semicon properties which cannot be well described by the Debye model.

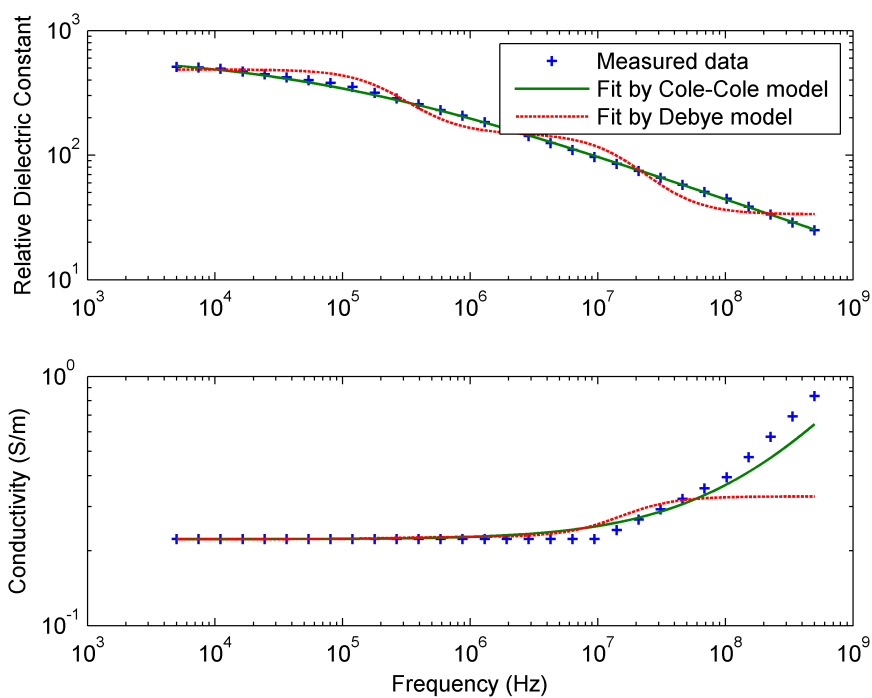
The Cole-Cole model was able to fit the measured data efficiently, both in Figures 4.9 and 4.10. Presumably, in creating FDTD models for the cables, using the results of the Cole-Cole model to define the semicon properties would be preferable. However, there is no available definition of a Cole-Cole medium in the used software package, while the 1 pole and 3 pole Debye media are available. As a result, the fit results of the Debye model will be used to define the cable semicon layers in all the created FDTD cable models. At the same time, the

Table 4.1: Parameters obtained by using a 3 pole Debye model to fit the cable semicon properties.

Parameter	11 kV EPR cable		12 kV XLPE cable	
	Outer semicon	Inner semicon	Outer semicon	Inner semicon
$\sigma_{dc}$ (S/m)	$6.77 \times 10^{-6}$	/	0.22	0.056
$\epsilon_{\infty}$	9.21	/	33.54	30.4
$\tau_1$ ( $\mu$ s)	0.017	/	0.0098	0.0056
$\epsilon_{s1}$	9.17	/	114.48	217.58
$\tau_2$ ( $\mu$ s)	1.79	/	0.67	0.12
$\epsilon_{s2}$	56.75	/	338.76	403.13
$\tau_3$ ( $\mu$ s)	304.3	/	114717	1.23
$\epsilon_{s3}$	801.8	/	338.74	600.42



(a) Dielectric constant and conductivity of a conductor screen sample.



(b) Dielectric constant and conductivity of an insulation screen sample.

Figure 4.10: Dielectric properties of the inner and outer semicon layers of a 12kV XLPE cable [132]. The published properties from 5 kHz–500 MHz were fitted using the 2 pole Cole-Cole model (4.21) and a 3 pole Debye model respectively.

results of the Cole-Cole model will be used in another practice which is using the analytical method to calculate the propagation constant of the cables. Details can be found in Chapters 5 and 8.

## 4.7 Conclusions

Dielectric properties of the cable semi-conductive (semicon) layers are characterised by their complex (relative) permittivities. Measurement of the complex permittivity in a range of  $10^{-6} - 10^{12}$  Hz is possible with different techniques. The lumped circuit methods are quite efficient but work only at frequencies  $\leq 10$  MHz. The distributed circuit methods can cover frequencies up to 100 GHz but require sophisticated equipment like vector network analyzers as well as specially designed test cells. There has been a lot of interest in measuring the complex permittivity over broadband frequency ranges, in particular in biology related fields where tens of GHz is not uncommon. In terms of measuring the cable semi-con properties to enable modelling high frequency properties of the cables, some work was reported to carry out the measurement in hundreds of MHz frequency ranges. The used methods were usually a combination of both the lumped circuit method and the distributed circuit method. Special test cells were developed to accommodate the cable semicon samples and provide proper ports from which connections to network analyzers can be made.

In this work, the complex permittivity of a cable's outer semicon layer was measured using a dielectric spectroscopy system up to 10 MHz. The measurement result was fitted with the Cole-Cole model, and then using the obtained Cole-Cole model, the complex permittivity values at frequencies  $> 10$  MHz were predicted. Furthermore, by fitting to the prediction of the Cole-Cole model, the Debye model of this outer semicon layer was also obtained. The parameters of the Cole-Cole and the Debye models will be used in calculating the analytical model and creating the FDTD model of the cable respectively in Chapters 5 and 8. Some cable semicon properties were also taken from published work and fitted with both the dielectric models by following the same procedures. The corresponding results will be used in modelling a cable of the same type as that reported in the published work, which is because both semicon layers of the cable are bonded to the insulation and cannot be removed for measurement.

# Chapter 5

## Measurement of Cable Responses

### 5.1 Introduction

High voltage (HV) cables are a kind of coaxial cable and can be treated as transmission lines for electromagnetic (EM) analysis. A transmission line is fundamentally a two-port network of which transfer function can be obtained as a function of input frequency. Combining the transfer function and the spectrum of input, output of the two-port network can be predicted. Assuming a PD is excited within the cable insulation, the pulse will travel in both axial directions of the cables and can be detected at cable terminations where the cable outer conductors are accessible and PD current sensors can be applied. This process can be divided into three stages, which are (i) PD coupling onto the cable inner and outer conductors, (ii) PD propagation in the cables, and (iii) PD detection by the PD sensors. By considering the cable length propagated by the PD as a two-port network, the propagation caused effects on the PD pulse magnitude and shape can be represented by the transfer function of the two-port network.

Attenuation of the PD signal is caused by the high frequency loss in the cables, which can be made up of different individual loss components depending on different HV cables [29]. For example, in polymeric-insulated HV cables there are the skin effect losses in inner and outer conductors, insulation loss and losses in semicon layers. High frequency properties of the cables can be investigated through transmission/reflection measurement, time domain reflectometry (TDR) measurement or developing analytical models [133; 134]. In this chapter, transmission measurements using a network analyzer were carried out on both an EPR and an XLPE cable samples to obtain transmission responses of the cables. The



high frequency loss or attenuation constant of the cables were obtained using both TDR measurement and the analytical method. The attenuation constant will be compared with those obtained in FDTD simulations to help improve the accuracy of the FDTD cable models. In addition, the cable insulation permittivities were evaluated as a function of frequency by impedance measurements.

## 5.2 Cable Sample Details

Two lengths of cable were available for practical experiments. One is a 43.1 m 11 kV EPR cable manufactured 1983 according to BS 6622. The EPR cable was taken out of service following a breakdown in 2009 and was sent to the laboratory for further investigation into the fault. Two faults located respectively at 2.11 m and 9.66 m from one end of the cable were revealed by using the time-difference-of-arrival (TDOA) location method [135]. After the faulty sections had been removed, a 1.03 m section (cable sample 1) was cut for the following measurement of cable frequency responses. The other length of cable is a 20 m 11 kV XLPE cable manufactured according to BS 7870-4.10 in 2010. The XLPE cable is brand new and was donated by a sponsor of this research. A 0.98 m section (cable sample 2) was cut for the cable frequency response measurement. The cross-section views and descriptions of the two cables are shown in Figures 5.1 and 5.2 and the dimensions are listed in Table 5.1, where  $r_1$  and  $r_5$  are corresponding to inner radii of each cable's structure 1 and 5.

Table 5.1: Details of the cable samples.

Parameter	Cable sample 1	Cable sample 2
Conductor radius $r_1$	10.8 mm	7.5 mm
Radius $r_5$	15.6 mm	12 mm
Inner semicon thickness	0.7 mm	0.4 mm
Insulation / thickness	EPR / 3.8 mm	XLPE / 3.4 mm
Outer semicon thickness	0.3 mm	0.7 mm
Cable type	BS 6622, 11 kV	BS 7870-4.10, 11 kV
Manufacture year	1983	2010

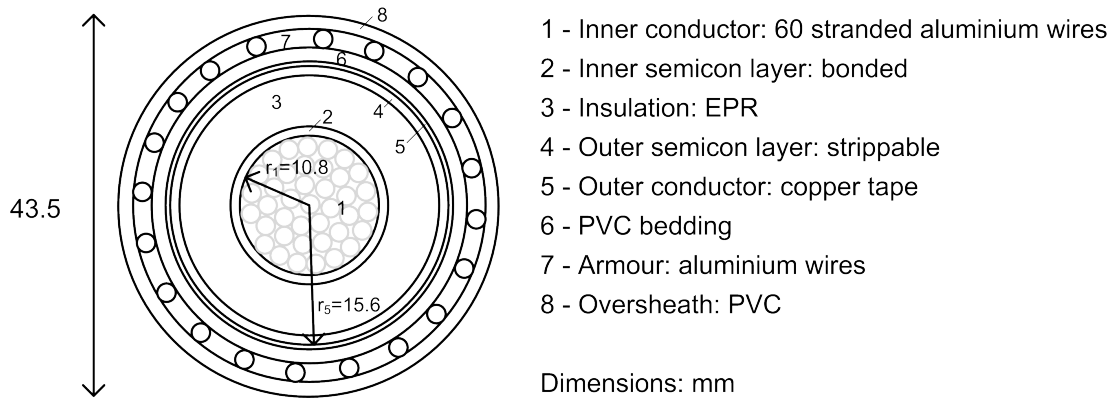


Figure 5.1: Structure of the 11 kV EPR cable sample. The inner conductor has a total area of  $500 \text{ mm}^2$ .  $r_1$  is the radius of the inner conductor and  $r_5$  is the inner radius of the outer conductor. The inner semicon layer is bonded to the inner conductor. The outer semicon layer is basically semicon tape and is strippable.

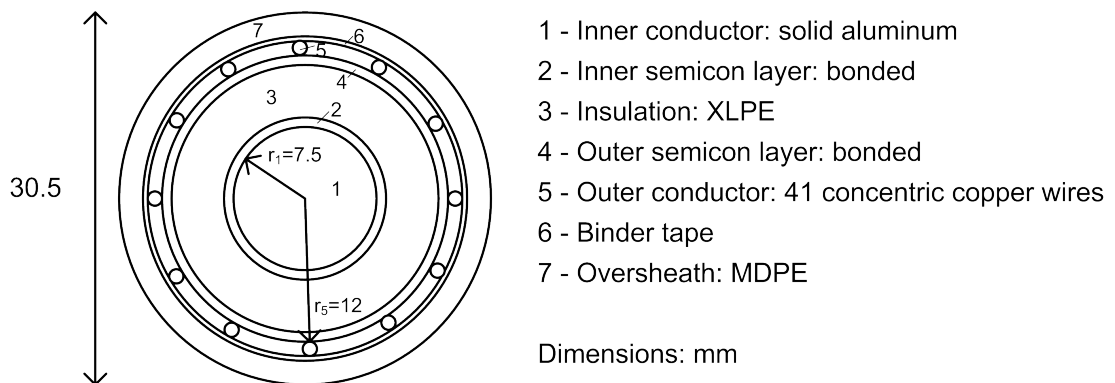


Figure 5.2: Structure of the 11 kV XLPE cable sample. The inner conductor has a total area of  $185 \text{ mm}^2$ .  $r_1$  is the radius of the inner conductor and  $r_5$  is the inner radius of the outer conductor. Both the inner and outer semicon layers are bonded and non-strippable. MDPE is acronym of medium-density polyethylene.

### 5.3 Cable Transmission Line Model

According to transmission line theory, transmission line effects can be ignored provided the signal propagating on a transmission line has a wavelength  $\lambda$  which is far larger than the length  $l$  of the transmission line, e.g.,  $l/\lambda \leq 0.01$  [113]. This condition, if applied to a 1 m long polymeric-insulated HV cable with an insulation relative permittivity  $\epsilon_r = 2$ , can be met for signals with frequency  $\leq 2.12$  MHz. Considering the fact that a PD pulse in solid dielectric typically has an initial bandwidth of a few hundred MHz [15; 30] and in-situ PD tests can be dealing with cables a few kilometers long, transmission line effects generally do have to be taken into account when investigating the PD pulse propagation in the cables.

A transmission line is usually represented by an equivalent circuit model. Basically, the transmission line is divided into small segments each of length  $\Delta l$ . The equivalent circuit for each segment is shown in Figure 5.3. Analyzing this the model leads to the “telegrapher’s equations” [113], in which a complex parameter has been introduced as the propagation constant

$$\gamma = \alpha + j\beta \quad (5.1)$$

where  $\alpha$  is the attenuation constant expressed in dB/m or Nepers/m and  $\beta$  is the phase constant expressed in rad/m and generally both are a function of frequency. The propagation constant can be used to characterise the transmission line effects on the signals propagating on it. Its real part  $\alpha$  is related to signal

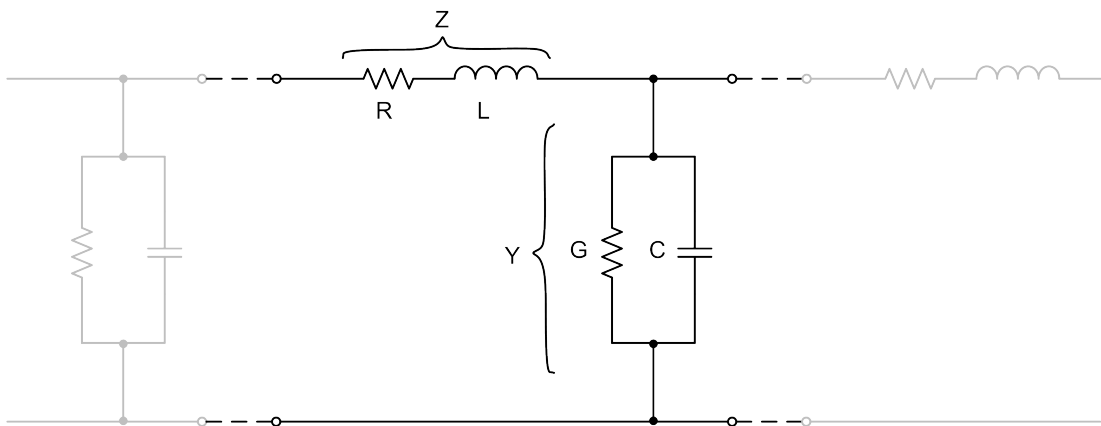


Figure 5.3: One element of the transmission line equivalent circuit.

attenuation, and for a short pulse like a PD pulse, it will result in magnitude decrease and width increase. Its imaginary part  $\beta$  is related to signal traveling velocity, and for a PD pulse consisting of broadband frequency components, different frequency components will have different velocities which will result in pulse shape distortion.

In order to account for different dielectric layers effects in a polymeric-insulated cable, an improved transmission line equivalent circuit was proposed by Stone and Boggs in 1982 [30]. The equivalent circuit has been widely adopted and applied to investigating cable high frequency properties. Figure 5.4 shows the equivalent HV cable circuit element in which the series impedance  $Z$  represents the resistance and the skin effect of the cable inner and outer conductors and the parallel admittance  $Y$  consists of three components resulting from the inner and outer semicon layers and the insulation layer respectively. Each semicon layer is represented by a parallel combination of a resistance and a capacitance while the insulation layer is purely capacitive. The resistance is neglected for the insulation layer since solid dielectric is generally very low in loss, i.e., very small  $\tan \delta$  [31].

In terms of practically calculating the transmission line effects on an input signal, the transmission line can be seen as a two-port network where each port consists of two terminals. By combining the transfer function of the two-port network with the spectrum of the signal appearing at the input port, the transmission line effects on the signal can be evaluated, or in other words, the signal at

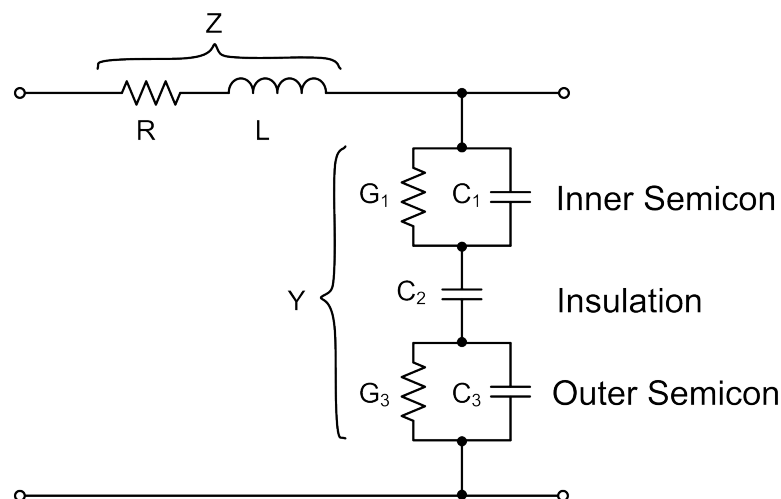


Figure 5.4: One element of the equivalent circuit proposed by Stone and Boggs for polymeric-insulated cables.

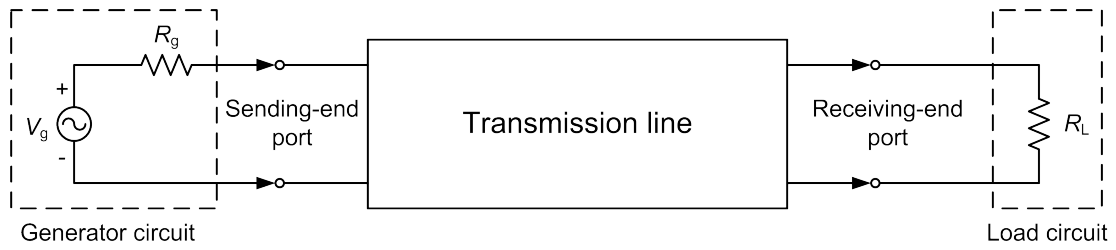


Figure 5.5: A transmission line represented by a two-port network [113] whose sending-end port is connected to a generator with source voltage  $V_g$  and resistance  $R_g$  and receiving-end port is connected to a load  $R_L$ .

the output port can be obtained. Figure 5.5 shows that the two-port network's sending-end port (input) and the receiving-end port (output) are connected with a generator circuit and a load circuit respectively, which, if replacing the source voltage  $V_g$  and resistance  $R_g$  with a current source and a capacitance respectively, will look quite similar to PD generation, propagation and detection in a cable. The propagation effects, i.e., transmission line effects of the cable on the PD are represented by the two-port network in Figure 5.5 and its transfer function  $TF_{two-port}$  can be derived from the cable propagation constant  $\gamma_c$  as

$$TF_{two-port} = e^{-\gamma_c D} \quad (5.2)$$

where  $D$  is the length of the cable. Apart from the transmission line effects, other effects involved in practices of cable PD detection like coupling of the PD pulse onto the cable conductors (analogue to the generator circuit in Figure 5.5) and effects of PD sensors on the PD pulse (analogue to the load circuit in Figure 5.5) can also be represented by corresponding two-port network transfer functions.

The transfer function representations of the effects involved in cable PD detection will make sense. A PD pulse is usually subject to many effects before it is finally detected and displayed on screen. By representing each effect as a corresponding transfer function, practices of cable PD detection can be seen as a “black box” which has included all the relevant transfer functions. Thus, given an input pulse, the output pulse which in reality is detected by using equipment like a PD monitoring system can in theory be alternatively worked out through a series of numerical calculation. It is based on this assumption that a framework for modelling of PD detection in cables was developed, details of which will be discussed in Chapter 7.

## 5.4 Cable Frequency Response

### 5.4.1 Transmission Measurement

A network analyzer can perform various measurements among which a transmission measurement will give out transmission response of a device connected between the “RF out” and “RF in” ports of the network analyzer. Figure 5.6 shows the HP 8714C RF network analyzer used in this work. In a typical trans-

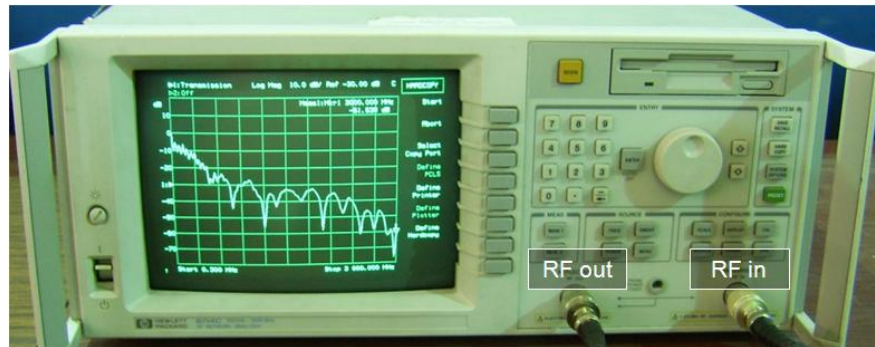


Figure 5.6: HP 8714C RF network analyzer, work frequency 0.3-3000 MHz.

mission measurement, the network analyzer provides at the “RF out” port a fixed magnitude incident signal of different frequencies in a specified frequency range (i.e., sweep frequency). The incident signal is sent to a device under test and a portion of it can be transmitted through the device. The transmitted signal will be measured at the “RF in” port and compared to the incident signal to produce the transmission response of the device.

For the HP 8714C RF network analyzer, the transmission response is calculated as

$$Transmission (dB) = 10 \log \left( \frac{P_{trans}}{P_{inc}} \right) \quad (5.3)$$

where  $P_{trans}$  is the power transmitted through the device and  $P_{inc}$  the incident power [136]. In terms of a transmission response measurement on a cable sample, the measurement result can be normalized to the transmission response of a unit length of the cable by

$$Transmission (dB/m) = \frac{1}{l} \times 10 \log \left( \frac{P_{trans}}{P_{inc}} \right) \quad (5.4)$$

where  $l$  is the cable sample length under test.

Transmission measurements were conducted on the two cable samples described in the previous section. The measurement configuration is shown in Figure 5.7. A cable sample was connected between the “RF out” and the “RF in”

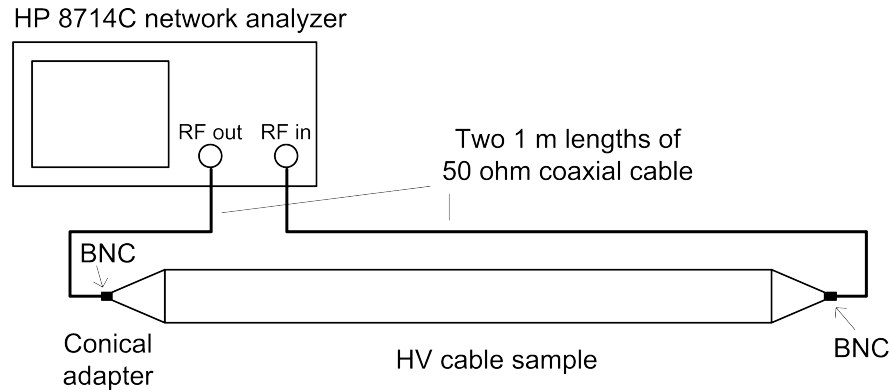


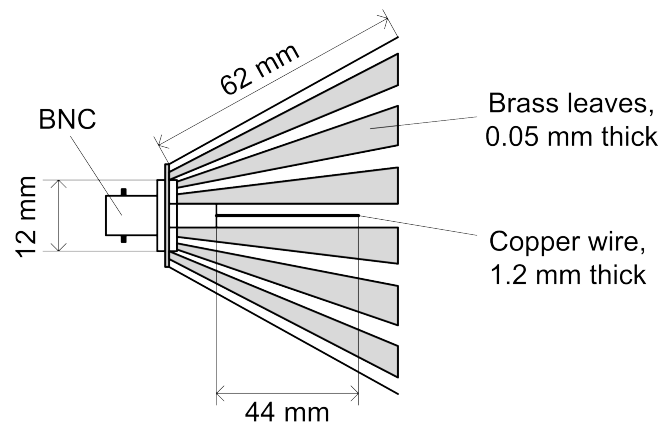
Figure 5.7: Diagram of transmission measurement using the HP 8714C network analyzer. Conical transitional connections were constructed between the measurement system and the cable under test.

ports of the network analyzer. Conical adapters were used to make transitional connections from 50  $\Omega$  coaxial cables to both ends of the cable sample so as to minimise geometrical discontinuity effects. A diagram of the conical adapter and one of the connections are shown in Figure 5.8. The measured transmission responses normalized to dB/m are shown in Figure 5.9.

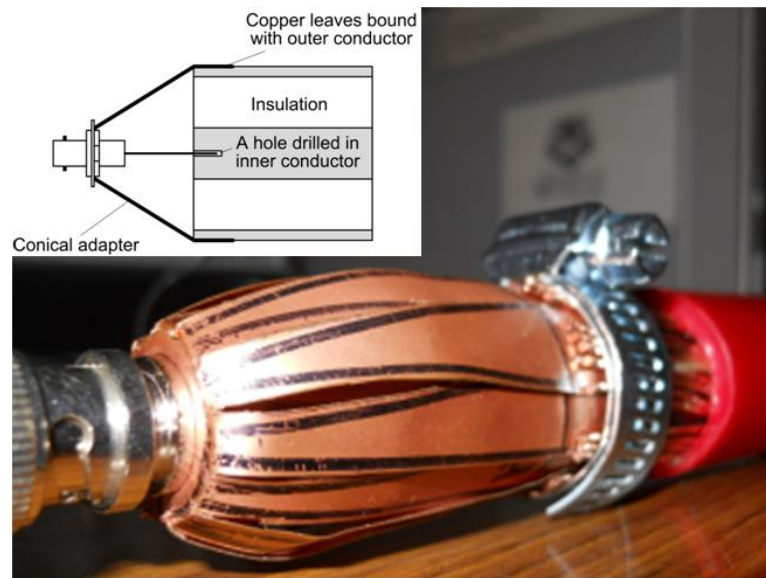
The measurement system has an input/output impedance of 50  $\Omega$  while HV cables typically have characteristic impedances less than 50  $\Omega$ . The characteristic impedances of the two cable samples described in Table 5.1 can be estimated by using the impedance formula for a lossless coaxial cable [113]

$$Z_0 = \frac{60}{\sqrt{\epsilon_r}} \times \ln\left(\frac{b}{a}\right) \quad (5.5)$$

where  $\epsilon_r$  is the relative permittivity of the the cable insulation and  $a$  and  $b$  are radii of the cable’s inner and outer conductors. The characteristic impedance of cable sample 1 (EPR, using  $\epsilon_r = 3$ ) is estimated as 12.7  $\Omega$  and 9.9  $\Omega$  by assuming the semicon layers as the insulation and the conductor respectively and for cable sample 2 (XLPE, using  $\epsilon_r = 2.3$ ) 18.6  $\Omega$  and 14.2  $\Omega$ . Therefore, impedance mismatch is inevitable between the cables and the measurement system, which means the measured responses actually included both the cable attenuation and



(a) Diagram of the conical adapter.

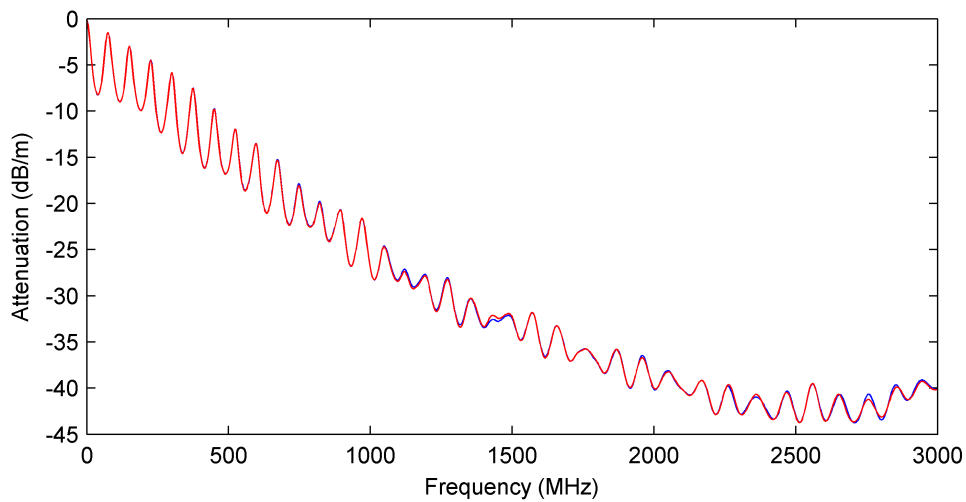


(b) Actual connection.

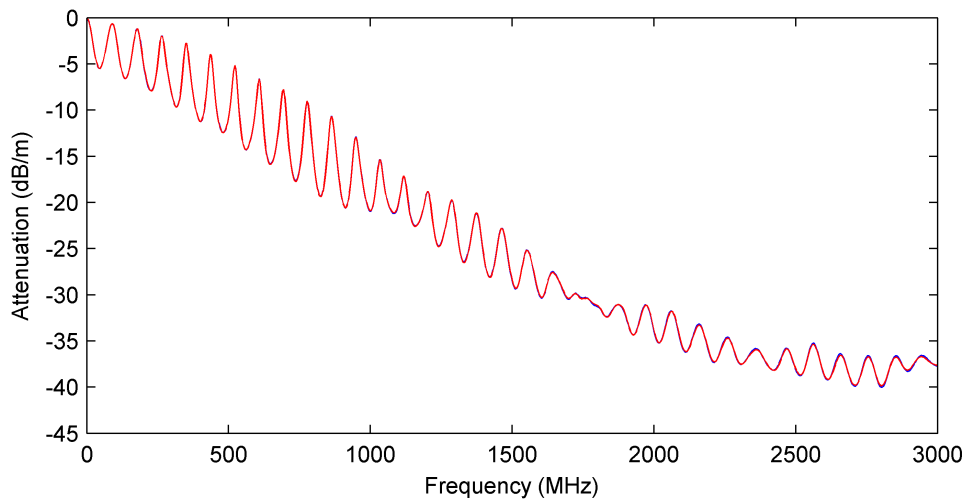
Figure 5.8: Diagram and photo of the conical adapter. The adapter was used as an interface between the measurement system and the cable samples. (b) shows one of the end connections of cable sample 2 under test. A cross-sectional view shows the internal connection.

the impedance mismatch effects. However, this would be a good illustration of the processes that a PD pulse in an HV cable would go through. Impedance mismatches present during PD excitation and detection and attenuation due to propagation in the cable together contribute to a “filter” which transfers the excited PD pulse at a PD source to the finally detected PD signal from a PD sensor. Application of this “filter” concept will be shown later by introducing the proposed framework for modelling of PD detection in cables.





(a) Normalized transmission response of cable sample 1 (EPR).



(b) Normalized transmission response of cable sample 2 (XLPE).

Figure 5.9: Transmission measurement results of both cable samples. For each cable sample, the measurement was repeated by swapping the cable end connections to the measurement system. The results were found almost the same.

### 5.4.2 Reflection Measurement

With a reflection measurement, the impedance plot for a device under test can be obtained. This impedance represents the input impedance of the device or for a transmission line represented cable, the characteristic impedance. However, the measured impedance can also be the lumped impedance of the cable provided that the measurement is carried out in a low frequency range within which the transmission line effects can be neglected so that the cable can be approximated

by a lumped circuit. The low frequency range (or a maximum frequency) can be estimated for both cable samples (about 1 m long) based on transmission line theory: firstly, say satisfying a condition of  $l/\lambda \leq 0.01$  where  $l$  is the cable length and  $\lambda$  the source signal wavelength as being able to neglect the transmission line effects [113]; secondly, since EPR insulation usually has a relative permittivity in the range of  $\epsilon_{EPR} = 3.1 - 3.3$  and XLPE insulation,  $\epsilon_{XLPE} = 2.2 - 2.3$  [4], the travelling speed of electromagnetic (EM) waves within each cable will be decreased by  $c/\sqrt{\epsilon_r}$  where  $c$  is the EM wave speed in vacuum; as a result, the maximum frequencies will decrease and 1.7 MHz and 2.0 MHz were obtained for cable samples 1 and 2 respectively. For measurements below either maximum frequency the corresponding cable sample will behave like a lumped circuit and the measured impedances can be seen as the lumped circuit impedances.

Using the arrangement shown in Figure 5.10, measurements were carried out for both cable samples in two steps: 1) measuring the 0.23 m 50  $\Omega$  coaxial cable impedance without a cable sample connected; 2) connecting a cable sample and repeating the impedance measurement. The impedance measured in the second step was actually a parallel combination of the 50  $\Omega$  coaxial cable impedance and the cable sample impedance. Therefore, the 50  $\Omega$  coaxial cable impedance was used to compensate the impedance data from the second step. This is done by simply subtracting the capacitances calculated using the impedance data from the second step by those from the first step. For comparing with the network

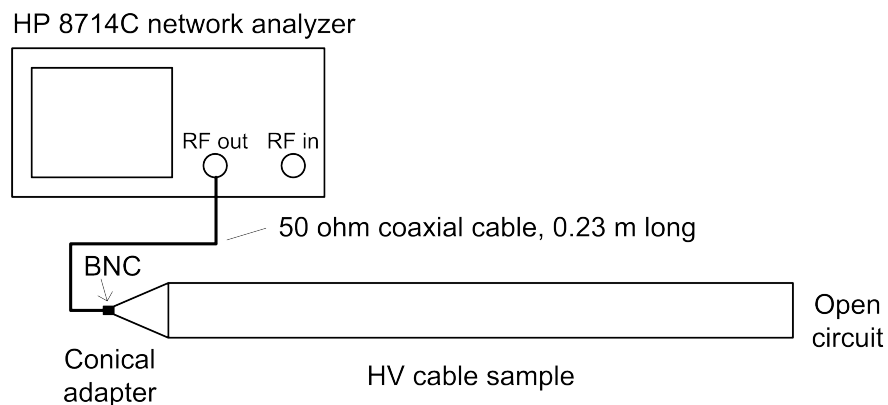


Figure 5.10: Diagram of the reflection measurement using the HP 8714C network analyzer. One cable end was connected to the network analyzer “RF out” port and the other end was open circuit. The 50  $\Omega$  coaxial cable was 0.23 m long, capacitance of which would contribute to the measured impedance and, therefore, had to be removed by prior normalization of the measurement.

analyzer measurements, the cable sample impedance was also measured by using a “voltage measurement” method. The measurement setup is shown in Figure 5.11 where a lumped resistor is connected in series with the cable sample. The cable impedance was worked out based on the recorded voltage ratio between the voltage over the cable sample and the signal generator output.

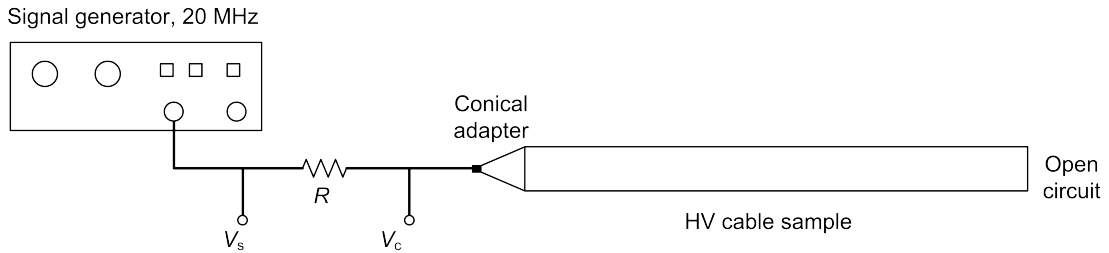


Figure 5.11: Diagram of the “voltage measurement” method.  $V_s$  is the signal generator output and  $V_c$  is the voltage over the cable sample. Both voltages were measured through a 10x probe with an oscilloscope. The measurement results tended to converge with increase of  $R$  values and 10 k $\Omega$  was finally used in the measurements for both cable samples.

Given the lumped impedance data obtained in the measurements and the cable sample dimensions in Table 5.1 insulation permittivities of the cable samples were calculated. The calculation was based on the Stone and Boggs proposed equivalent circuit in Figure 5.4 while some simplifications had to be done. Firstly, by considering each cable sample as a cylinder capacitor filled with the cable dielectrics, losses from the cable conductors were neglected so the impedance  $Z$  was removed from the equivalent circuit. Secondly, for the admittance  $Y$ , the impedances resulting from both the inner and outer semicon layers were thought to be far smaller than that of the insulation layer for the following reasons: (a) the semicon layers are much thinner than the insulation layer; (b) the semicon materials have much higher permittivity and conductivity than the insulation material does [31; 137]. Therefore, the semicon layer impedances  $G_1//C_1$  and  $G_3//C_3$  in the equivalent circuit in Figure 5.4 were removed (i.e., the semicon layers are regarded as extension of the conductors) and the admittance  $Y$  was simplified to include only the cable insulation layer, a pure capacitance  $C_2$ . Following the simplifications, it turns out that the measured cable sample impedance

$Z_{cable}$  (with the real part neglected) is approximated as

$$Z_{cable} \approx Z_2 = \frac{1}{j\omega C_2} \quad (5.6)$$

where  $Z_2$ ,  $C_2$  are the impedance and the capacitance of the cable insulation layer respectively. The relative permittivity of the insulation material  $\epsilon_r$  can be derived by using the formula for a cylindrical capacitor [113]

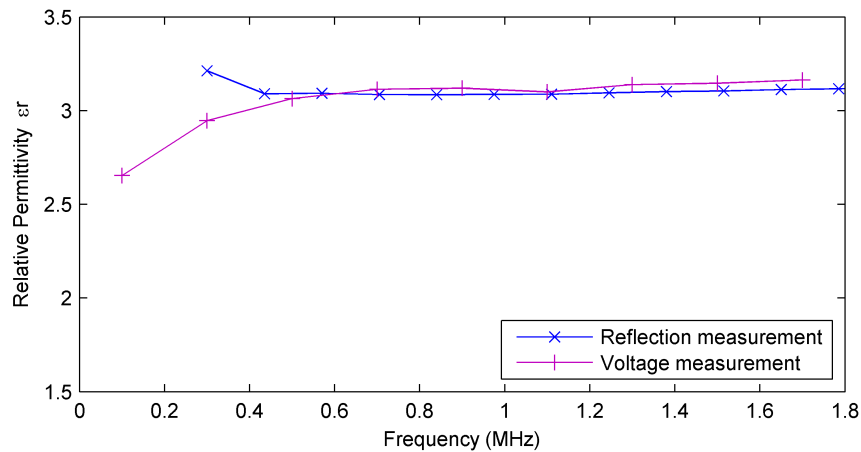
$$C = \frac{2\pi\epsilon_0\epsilon_r}{\ln(b/a)} \times l \quad (5.7)$$

where for this case  $a$  and  $b$  are the insulation layer inner and outer radii respectively and  $l$  is the length of the cable sample.

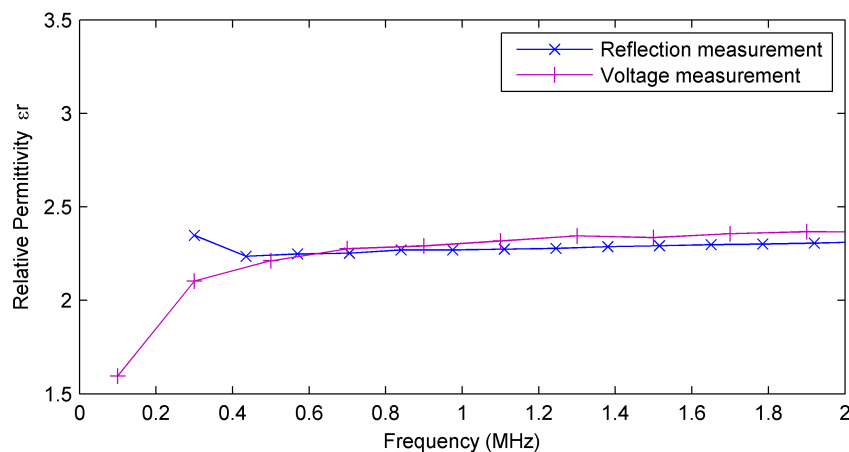
Relative permittivities were calculated by using the impedance data from both the reflection measurement and the “voltage measurement”. Table 5.2 shows some of the directly measured data as well as the calculation process. Figure 5.12 shows the results of cable samples 1 and 2 up to the maximum frequencies where the lumped impedance assumption was valid. It can be observed that below 0.5 MHz, both the results from the reflection measurement and the “voltage measurement” started to diverge from those at frequencies above 0.5 MHz. This was because the impedances of the cable samples increased with the decrease of measurement frequencies. For the reflection measurement method this resulted in the cable samples looking more and more like open circuit and for the “voltage measure-

Table 5.2: Measured data from different methods and calculation towards the insulation permittivity of cable sample 1 (EPR).

Impedance measurement using the network analyzer			
Frequency (MHz)	Impedance ( $\Omega$ )	Capacitance (pF)	Relative permittivity
0.3	11.3-j832.7	645	3.22
0.435	20.5-j575.2	619	3.08
0.57	13.3-j434.8	621	3.09
...			
“Voltage measurement”			
Frequency (MHz)	Vs (V) / Vc (V)	Capacitance (pF)	Relative permittivity
0.3	7.02 / 0.58	532	2.95
0.5	6.99 / 0.34	591	3.06
0.7	6.98 / 0.24	615	3.11
...			



(a) Insulation permittivity of cable sample 1 - EPR insulated.



(b) Insulation permittivity of cable sample 2 - XLPE insulated.

Figure 5.12: Cable insulation permittivities obtained from both the reflection measurement and the “voltage measurement”.

ment” this made the cable sample impedances comparable to the series resistance used in the measurement, both of which would result in decrease of measurement accuracies. Other error sources like the lumped impedance assumption, approximations made to the equivalent circuit and the accuracy in measuring the cable sample dimensions all contributed to the measurement uncertainties. However, both measurement methods agreed reasonably in the permittivity values from 0.5 MHz to each upper frequency with maximum differences of 1.64% and 2.94% for cable samples 1 and 2 respectively. Values of  $\epsilon_{EPR} = 3.1$  and  $\epsilon_{XLPE} = 2.3$  were taken from these results and will be used in creating the FDTD cable models.

While the cable insulation layer is represented by a pure capacitance  $C_2$  in

Figure 5.4, a more general equivalent circuit was shown in Figure 4.3 using either a parallel or a series combination of a resistance and a capacitance. If using the parallel one, the insulation impedance  $Z_2$  and dissipation factor  $\tan \delta$  of the cable sample can be represented as

$$Z_2 = \frac{1}{G_2 + j\omega C_2} \approx \frac{G_2}{\omega^2 C_2^2} - j \frac{1}{\omega C_2} \quad (5.8)$$

$$\tan \delta = \frac{G_2}{\omega C_2} \quad (5.9)$$

where  $G_2$  and  $C_2$  are the parallel equivalent conductance and capacitance of the cable insulator layer. On the right of the (5.8) formula, real and imaginary parts correspond to the real and imaginary parts of the measured complex impedances respectively. Since the imaginary parts have already been used to calculate the cable insulation permittivity, it seems reasonable to use the real parts to estimate the dissipation factor  $\tan \delta$ . By substituting the measured impedances into (5.8) and (5.9),  $\tan \delta$  of each cable sample was obtained and compared with reference values suggested for cables rated lower than 36 kV in [4]. For cable sample 1 as  $\tan \delta = 0.03$  compared with a reference value of 0.02 and for cable sample 2 as  $\tan \delta = 0.01$  which more than twice as large as referenced 0.004. The estimation of  $\tan \delta$  was subjected to more errors than that of the permittivity. This was both because of the measured real parts were very small (a few  $\Omega$ ) compared to the network analyzer output impedance of 50  $\Omega$ , and the real parts were not able to be compensated by normalizing the instrument as was done for the imaginary parts.

However, at least for cable sample 1 (EPR), a third party report [138] has shown measured  $\tan \delta$  of 0.0015 and 0.0038 on two lengths of the same kind of cables of which the former one was stored and the latter one had been in operation for 22 years. The increase in  $\tan \delta$  was attributed to insulation degradation while in service. The tests were carried out in a step-up style until the cable rated voltage. It is, therefore, concluded that the reflection measurement was able to give out the cable insulation permittivity with a reasonable accuracy whereas failed in the efforts to work out the insulation  $\tan \delta$ .

## 5.5 Characterisation of Cable Propagation Properties

### 5.5.1 Using TDR Measurement

In order to obtain the propagation constant (5.1) of the cable samples, time domain reflectometry (TDR) measurements were carried out on longer sections of the two cables. The 11 kV EPR cable length was 28.3 m and the 11 kV XLPE cable length was 16.0 m. The cables details are described in Section 5.2. The TDR measurement setup is shown in Figure 5.13. An avalanche pulse generator was used to provide an input pulse with a sub-nanosecond rise time and 10 V magnitude. The output of the pulse generator was connected with a tee adapter. One port of the tee adapter was connected to coaxial cable 1 (50  $\Omega$ , 1.0 m long) onto a LeCroy scope with a bandwidth of 1 GHz. The other port of the tee adapter was connected to coaxial cable 2 (50  $\Omega$ , 22.3 m long) onto a cable sample. The conical adapter shown in Figure 5.8 was used to provide transitional connection from the coaxial cable 2 to the cable sample. The other end of the cable sample was open circuit. The coaxial cable 2 had to be 22.3 m to create a long enough time delay between the first two pulses in the TDR response so that they didn't overlap.

The measurements and data processing were conducted by following the pro-

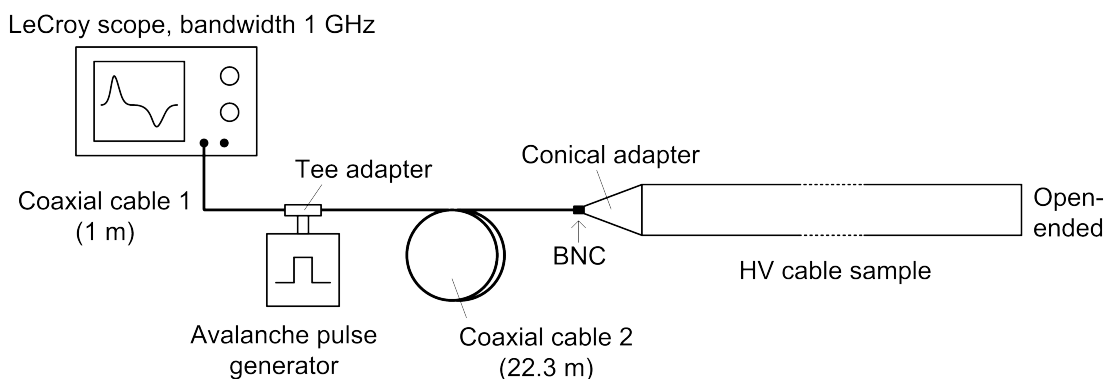


Figure 5.13: Diagram of the TDR measurement setup. This is actually what the connection looked like in one of the measurements. In the other measurement the HV cable sample was disconnected and this end of the coaxial cable 2 was short-circuited. In practical measurements a 10 dB attenuator had to be used before the scope so as to limit the input magnitude within the scope measurement range.

cedures suggested by Papazyan et al. [139] where a calibration method for TDR measurement was proposed to obtain accurate propagation constants up to a maximum frequency of 300 MHz. The method involved deriving a formula and doing corresponding measurements so as to remove systematic errors from the connecting cables and correct for the impedance mismatch between the measurement system and the cable. The formula required two measurements: 1) without connecting the cable sample, conducting the first TDR measurement with one end of the coaxial cable 2 short-circuited; 2) connecting the cable sample as that shown in Figure 5.13 and doing the second TDR measurement. Figure 5.14 shows the TDR response from the first TDR measurement where the first reflected pulse  $V_{short}$  was extracted by using time domain windowing. Figure 5.15 shows the overall TDR response with the 28.3 m long 11 kV EPR cable attached in the second TDR measurement.  $V_{adapter}$  and  $V_{cable}$ , which are the first and second reflected pulses respectively, were extracted from the response by using time domain windowing. The propagation constant  $\gamma_c$  of the cable under test can be worked out by

$$e^{-\gamma_c 2l} = \frac{\text{FFT}[V_{cable}] \times \text{FFT}[V_{short}]}{(\text{FFT}[V_{adapter}])^2 - (\text{FFT}[V_{short}])^2} \quad (5.10)$$

where FFT is the fast Fourier transform. Detailed procedures of deriving (5.10)

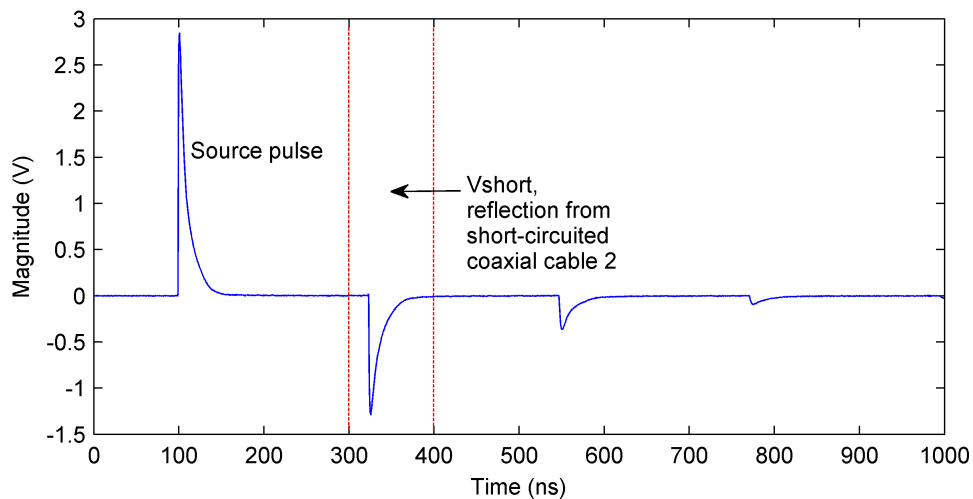


Figure 5.14: TDR measurement 1 - response of the short-circuited 50  $\Omega$  coaxial cable 2. The source pulse has a rise time of less than 1.0 ns and a full width at half maximum (FWHM) of 7.2 ns.



can be found in Appendix A.

The extracted pulses were then substituted into the formula to work out the cable propagation constants. The real parts of the propagation constants  $\alpha$  are shown in Figures 5.16 and 5.17 for the EPR and the XLPE cables respectively.

While it was possible to characterise the attenuation in a frequency range less

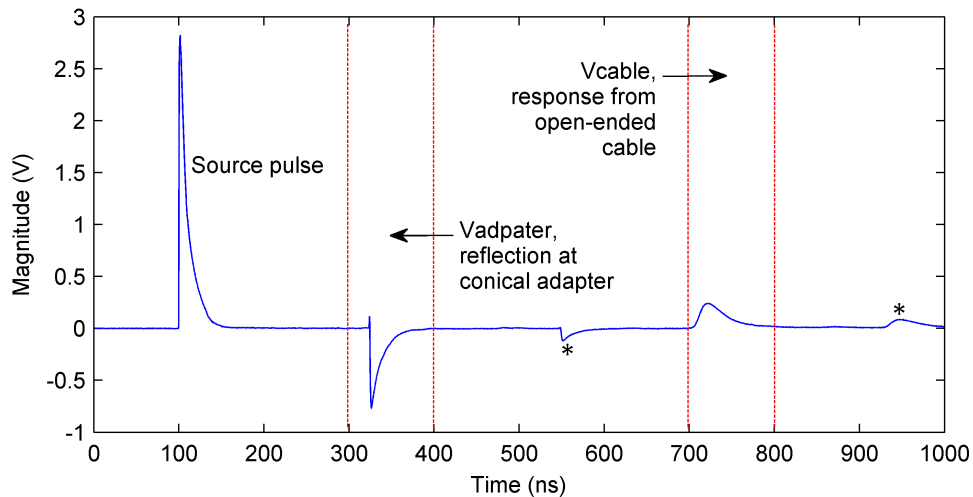


Figure 5.15: TDR measurement 2 - response of the open-ended 28.3 m long 11 kV EPR cable. \* The smaller pulses following the two reflected pulses were caused by the impedance mismatch at the tee adapter.

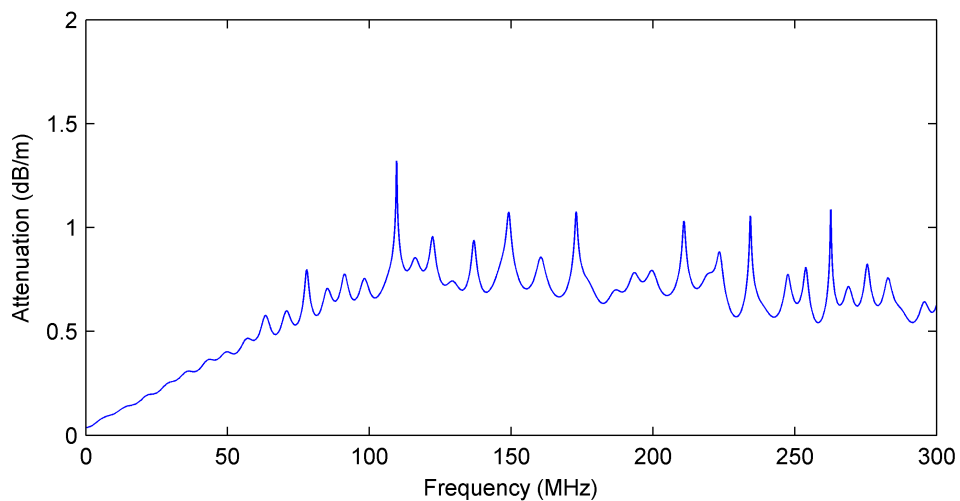


Figure 5.16: Measured attenuation for the 11 kV EPR cable. The periodic peaks are an artifact resulting from the FFT algorithm and the smaller signal magnitude at higher frequencies [139].

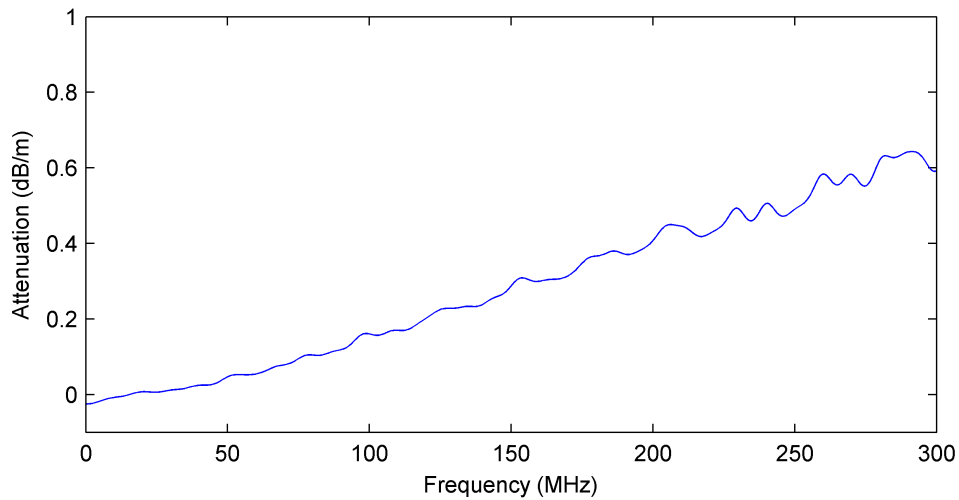


Figure 5.17: Measured attenuation for the 11 kV XLPE cable.

than 100 MHz for the EPR cable, those for the XLPE cable were obtained appropriately up to 300 MHz. This is both because that an EPR cable usually has higher attenuation than an XLPE cable does and the EPR cable under test had been in operation for 22 years. It should be noted that there was small offset in both the attenuation results at zero frequency. This is probably due to non-ideal connections in the measurement system causing impedance mismatch, as the calibration method in [139] assumed a perfect match at the tee adapter but in reality apparent reflections were observed from the adapter.

### 5.5.2 Using Analytical Method

The cable propagation constants were also calculated using an analytical method. According to the lumped equivalent circuit shown in Figure 5.4 for per unit length of polymeric-insulated cables, the series impedance  $Z$  of a cable with a tape outer conductor was calculated according to [30] using Equation (5.11) (refer to Table 5.3 for symbols used in all equations in this section)

$$Z = \frac{1}{2\pi r_1} \sqrt{\frac{j\omega\mu_0}{\sigma_1}} + \frac{j\omega\mu_0}{2\pi} \ln\left(\frac{r_5}{r_1}\right) + \frac{1}{2\pi r_5} \sqrt{\frac{j\omega\mu_0}{\sigma_5}} \quad (5.11)$$

Table 5.3: Symbol representations

$Z$	-	series impedance ( $\Omega/m$ )
$Y$	-	parallel admittance (S/m)
$r_1$	-	radius of inner conductor (m)
$r_5$	-	inner radius of outer conductor (m)
$\sigma_1$	-	conductivity of inner conductor (S/m)
$\sigma_5$	-	conductivity of outer conductor (S/m)
$\omega$	-	$2\pi f$ , angular frequency (rad/s)
$\mu_0$	-	$400\pi \times 10^{-9}$ (H/m)
$\epsilon_0$	-	$10^{-9}/36\pi$ (F/m)
$a_i, b_i$	-	inner and outer radii of layer $i$ (m)
$\epsilon'_i, \epsilon''_i$	-	real and imaginary parts of layer $i$ complex permittivity
$\alpha$	-	attenuation constant (Nepers/m), 1 Neper = 8.68 dB
$\beta$	-	phase constant (rad/m)

while that of a cable with a concentric wire outer conductor was calculated according to [132] using

$$Z = \frac{1}{2\pi r_1} \sqrt{\frac{j\omega\mu_0}{\sigma_1}} + \frac{j\omega\mu_0}{2\pi} \ln\left(\frac{r_5 + \rho}{r_1}\right) + \frac{1}{2\pi\rho n} \sqrt{\frac{j\omega\mu_0}{\sigma_5}} \quad (5.12)$$

where  $\rho$  is radius of each concentric wire. The parallel admittance  $Y$  is a series combination of the admittance  $Y_1$ ,  $Y_2$  and  $Y_3$  respectively from the inner semicon layer 1, the insulation layer 2 and the outer semicon layer 3. The admittance formula is the same for both types of cable

$$Y = \frac{1}{\sum_{i=1}^3 \frac{1}{Y_i}} \quad (5.13)$$

$$Y_i = j\omega C_i^*, \quad C_i^* = \frac{2\pi\epsilon_0(\epsilon'_i - j\epsilon''_i)}{\ln(b_i/a_i)} \quad (5.14)$$

where  $C_i^*$  is the complex capacitance of layer  $i$ . Finally, the cable propagation constant  $\gamma_c$  is calculated by

$$\gamma_c = \sqrt{ZY} = \alpha + j\beta \quad (5.15)$$

$$v_p = \frac{\omega}{\beta} \quad (5.16)$$

where  $v_p$  is the phase velocity (m/s) of the cable.

For substituting parameter values into Equations (5.11) to (5.15), the dimen-

sional parameter values of the two cables are available from Table 5.1. Conductivities of copper and aluminium are  $5.8 \times 10^7$  S/m and  $3.54 \times 10^7$  S/m [113] respectively. The EPR insulation has a complex permittivity real part  $\epsilon'_2 = 3.1$  and  $\tan \delta = 0.004$ , which was concluded in the reflection measurement section. The XLPE insulation has  $\epsilon'_2 = 2.3$  and  $\tan \delta = 0.0005$  [4]. The complex permittivity imaginary part can be calculated using (4.5). Complex permittivities of the semicon layers were taken from the Cole-Cole model results obtained in Chapter 4. For the 11 kV EPR cable, the measured outer semicon permittivities are as shown in Figure 4.9. Properties of the inner semicon could not be measured because of its bonding to the insulation and therefore were set to same as the outer semicon permittivities. For the 11 kV XLPE cable, both the inner and outer semicon layers are bonded to the insulation and thus their properties could not be measured. Alternatively, the published inner (conductor screen) and outer (insulation screen) semicon properties shown in Figure 4.10 were taken as estimations of the corresponding semicon properties.

Based on these approximations to the unknown properties, evaluation of Equations (5.11) to (5.15) produced Figures 5.18 and 5.19. The calculated attenuation constant  $\alpha$  (real part of the propagation constant  $\gamma_c$ ), in particular for the 11 kV EPR cable, had apparent deviation from the measurement result. In order to get a better fit to the measurement observations and finally determine what parameters to use in the FDTD cable models, the parameters of the unknown properties

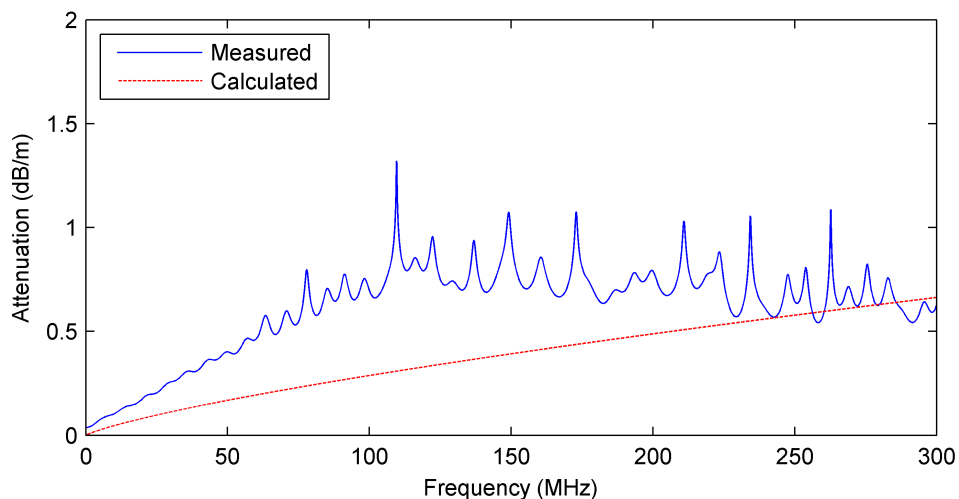


Figure 5.18: Measured and calculated attenuation for the 11 kV EPR cable. Unknown inner semicon properties were set to the same as those of the outer semicon.

were modified in a “trial and error” manner. For example, as to the EPR cable’s inner semicon, its dc conductivity was increased by 3500 times (seems the EPR cable got completely different inner and outer semicon as inner semicon is bonded to the insulation and outer semicon is lapped semicon tapes), while for the XLPE cable, its inner and outer semicon permittivities were multiplied by 2 and 0.65 respectively. After the changes, reasonable agreement between the calculated and measured attenuation was achieved for both cables, which can be recognized from Figures 5.20 and 5.21.

The measured and calculated results were compared at specific frequencies to evaluate errors of the analytical method. For example, at 50 MHz the measured and calculated attenuation and phase velocity are as listed in Table 5.4. The

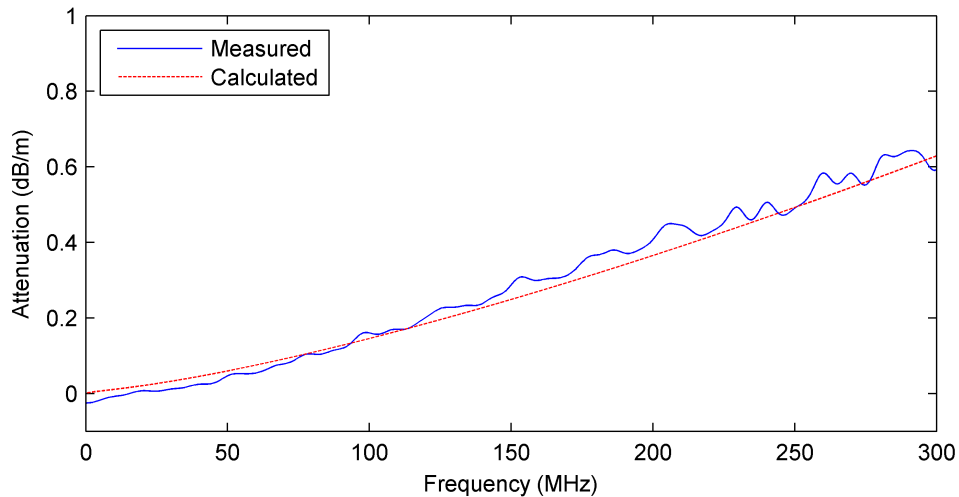


Figure 5.19: Measured and calculated attenuation for the 11 kV XLPE cable. Both inner and outer semicon properties were using published data as estimations.

Table 5.4: Comparison between the measured and calculated (using modified semicon properties) attenuation and phase velocity at 50 MHz.

	Attenuation		
	Measured (dB/m)	Calculated (dB/m)	Difference (%)
EPR	0.4015	0.3544	13.3
XLPE	0.0469	0.06372	26.4
	Phase velocity		
	Measured (m/ns)	Calculated (m/ns)	Difference (%)
EPR	0.1509	0.1539	2.0
XLPE	0.1708	0.1657	3.1

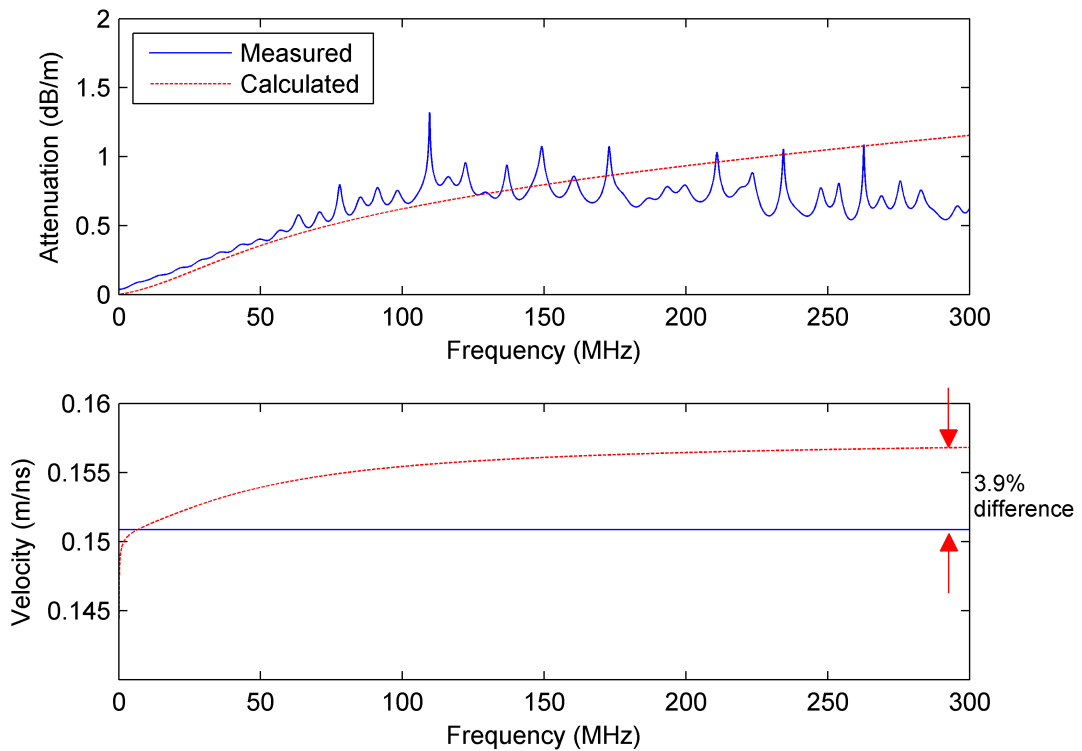


Figure 5.20: Measured and calculated attenuation and phase velocity for the 11 kV EPR cable after changes being made to the inner semicon properties. The calculated and measured attenuation shows an acceptable agreement up to about 100 MHz.

errors in calculating the cable attenuation constants were mainly due to being unable to obtain good estimates of the semicon properties [30]. Furthermore, dc offset also played a part as by simply subtracting the dc offset from the measured attenuation the errors between the measured and the calculated attenuation at 50 MHz would drop to 2.7% and 12.8% respectively for the EPR cable and the XLPE cable. The measured phase velocity was obtained from the TDR response by using the arrival time difference between the first reflection and the cable open-ended reflection, that is, two pulses framed by the dotted lines in Figure 5.15. The cable attenuation constants calculated using the analytical method will be used to improve the accuracy of the FDTD cable models in the following work.

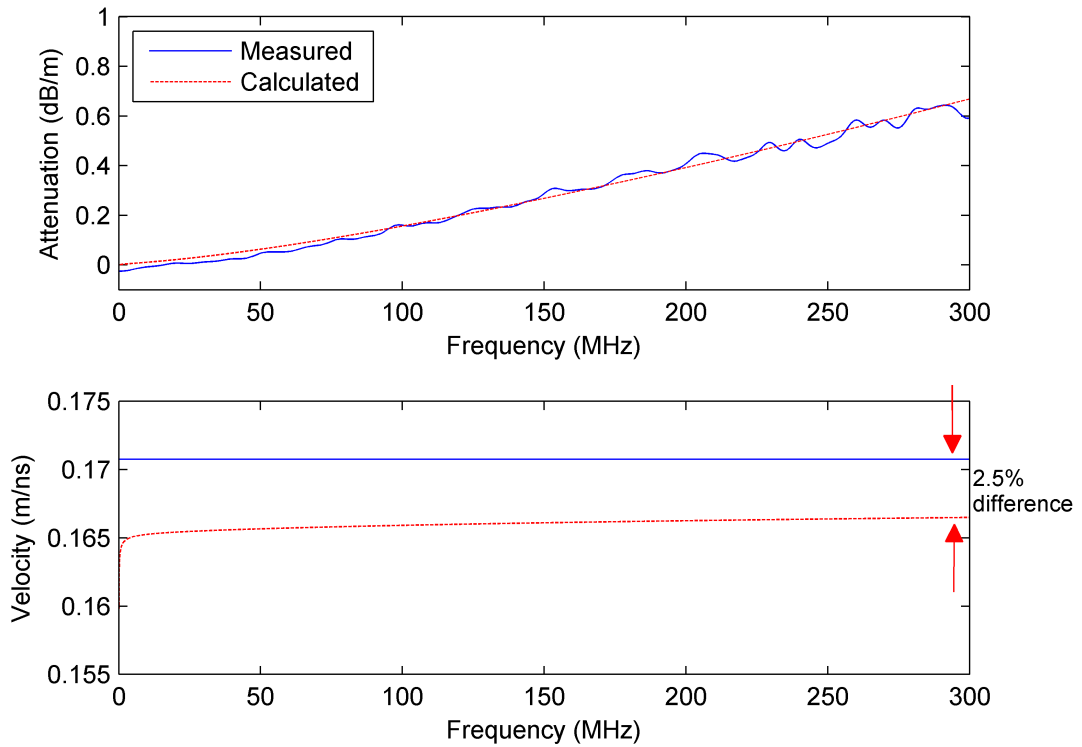


Figure 5.21: Measured and calculated attenuation and phase velocity for the 11 kV XLPE cable following modifications of both inner and outer semicon properties. The calculated and measured attenuation finds a better agreement up to at least 300 MHz.

## 5.6 Conclusions

Details of the two 11 kV cables used in this work, with EPR and XLPE insulation respectively, were presented. By treating a cable as a transmission line, its effect on voltages and currents on it can be represented using the equivalent circuit model of the transmission line. By representing each of the cable's semi-conductive (semicon) layers as a parallel combination of a resistance and a capacitance, an improved equivalent circuit model was proposed by Stone and Boggs in 1982. The model has been widely used to investigate high frequency losses in polymeric-insulated cables.

Using a RF network analyzer, transmission and reflection measurements were carried out on cable samples of about 1 m long cut from both the cables. The transmission responses show that, for either cable, the incident signal input is subject to attenuation as a function of frequency. The reflection measurement

produced impedance data that were used to derive dielectric constants of the cable insulation. Dielectric constants of 3.1 and 2.3 were summarised for the EPR and XLPE insulation respectively after comparing the results from both the reflection measurement and the “voltage measurement”.

In order to obtain propagation constants for both cables, TDR measurements were performed to characterise the EPR and XLPE cables attenuation up to 100 MHz and 300 MHz respectively. Another way of finding out the cable propagation constant is using the analytical model. By adjusting the cable semicon properties obtained in Chapter 3, in a “trial and error” manner, results from the analytical model were able to achieve acceptable agreements with those from the TDR measurements. The effort in improving the accuracy of the analytical model is beneficial both in terms of calculating the propagation constant in extended frequency ranges and the benefits for improving the accuracy of the FDTD cable models to be created.



# Chapter 6

## Measurement of HFCT Transfer Functions

### 6.1 Introduction

A high frequency current transformer (HFCT) is a current transformer which is used to convert broadband currents into corresponding voltages for easier measurements. An HFCT typically has a bandwidth of three to six decades of frequency (e.g., 100s Hz to 100s MHz) and current levels that can be measured are usually lower at milliamperes to hundreds of amperes [59]. HFCTs have found many applications for example RF transmitters, induction heaters, electronic power circuits, pulse power systems and condition monitoring or fault diagnostics [59].

An HFCT is basically made up of a magnetic core (usually with high permeability, e.g., ferrite cores), windings on the core and a load connected between the winding terminals. Figure 6.1 shows a typical diagram of an HFCT which has one-turn primary and multi-turn secondary and a resistive load is connected to the secondary terminals for converting the secondary current to a corresponding voltage. The turns ratio arrangement (one-turn primary and multi-turn secondary) combined with the use of a resistive load at the secondary can increase the secondary voltage while at the same time alleviating the parasitic inductance problem that becomes more apparent at higher frequencies.

A simplified equivalent circuit of the HFCT is shown in Figure 6.2. Effects that are neglected include losses in the primary winding and the magnetic core and capacitive coupling between the primary and secondary windings. However, the

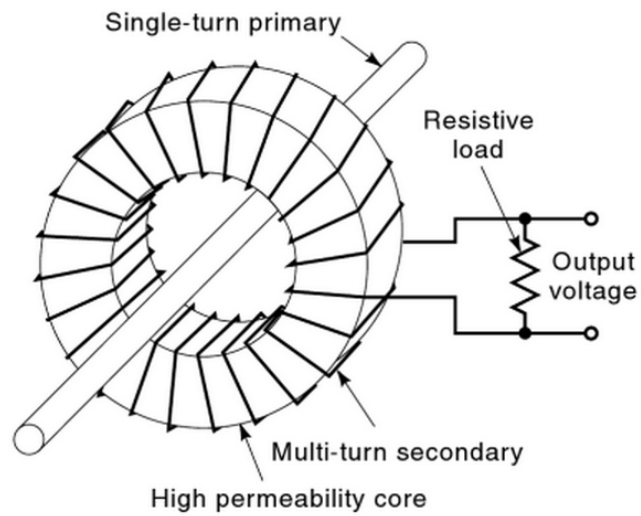


Figure 6.1: A typical diagram of an HFCT [59] with a one-turn primary and a multi-turn secondary feeding a resistive load.

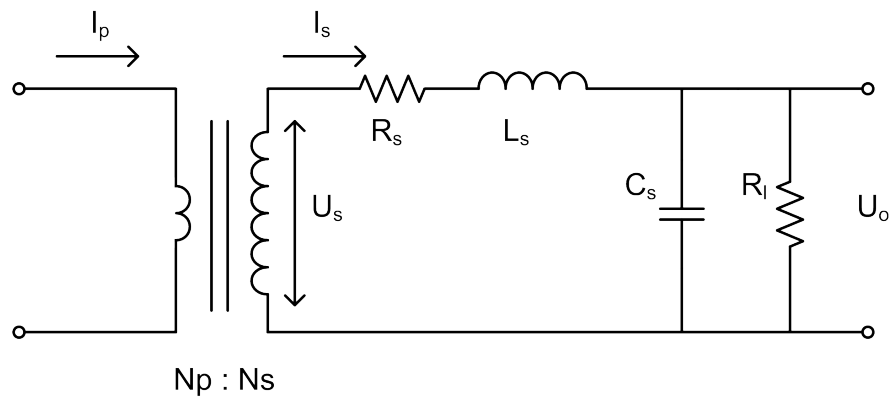


Figure 6.2: A simplified equivalent circuit of the HFCT.  $I_p$ , primary current;  $I_s$ ,  $U_s$ , secondary current and voltage;  $N_p$ ,  $N_s$ , primary turns and secondary turns;  $R_s$ , secondary winding resistance;  $L_s$ , secondary leakage inductance;  $C_s$ , parasitic secondary loading capacitance;  $R_l$ , output load resistance;  $U_o$ , HFCT output voltage.

simplification is acceptable within the purpose here using the equivalent circuit to analytically derive the HFCT transfer function.

Based on the equivalent circuit and transformer theory [140], it is possible to derive a transfer function between the primary current  $I_p$  (input) and the HFCT output voltage  $U_o$ . Firstly, the secondary voltage  $U_s$  can be calculated by

$$U_s = -N_s \frac{d\phi}{dt} \quad (6.1)$$

where  $\phi$  is the magnetic flux in webers passing through the magnetic core.  $\phi$  is produced in a magnetic core by the “magnetomotive force” (MMF) in a way that is similar to how currents are generated in a circuit by a voltage. Assuming that the HFCT is not loaded by  $R_l$  on its output (open-circuit secondary), the primary current  $I_p$  excites an MMF (in ampere-turns) that can be calculated by

$$MMF = N_p I_p \quad (6.2)$$

and the resulting  $\phi$  is

$$\phi = \frac{MMF}{R_m}, \quad R_m = \frac{l_m}{\mu_0 \mu_r A_c} \quad (6.3)$$

where  $R_m$  is the magnetic core reluctance (similar to resistance in an electrical circuit).  $l_m$  the magnetic path length in meters,  $A_c$  the cross-sectional area of the magnetic core in square meters.  $\mu_0 = 4\pi \times 10^{-7}$  H/m is the permeability of vacuum and  $\mu_r$  is the relative permeability of the core material.

By substituting (6.2) and (6.3) into (6.1), the secondary voltage  $U_s$  is then represented as

$$U_s = -\frac{N_p N_s \mu_0 \mu_r A_c}{l_m} \times \frac{dI_p}{dt}. \quad (6.4)$$

where  $N_p = 1$  for the HFCT. Secondly, in the equivalent circuit,  $U_o$  can be expressed in terms of  $U_s$  using Laplace transform notation as

$$U_o(s) = \frac{R_l}{s^2 R_l L_s C_s + s(L_s + R_l R_s C_s) + R_l + R_s} \times U_s(s). \quad (6.5)$$

By applying the Laplace transform to both sides of (6.4) and substituting into

(6.5), the transfer function between  $U_o$  and  $I_p$  is finally obtained as



$$U_o(s) = \frac{-sMR_l}{s^2R_lL_sC_s + s(L_s + R_lR_sC_s) + R_l + R_s} \times I_p(s) \quad (6.6)$$

where  $M = N_pN_s\mu_0\mu_rA_c/l_m$ . Using (6.6) and assuming that the HFCT components values are given, magnitude and phase responses of the HFCT transfer function can be plotted. In practice, a reverse process is often adopted, whereby plotting the HFCT transfer function through measurement first and then fitting to (6.6) is used to find out the unknown parameter values.

## 6.2 HFCT Specifications and Transfer Function Measurement Methods

There are two models of an HFCT which are of interest for the cable PD studies in this research. The HFCT specifications are shown in Table 6.1. HFCT 1 has already been used in UK industries to carry out on-line and off-line PD measurements for HV cables. Its 20 MHz bandwidth is appropriate for in-situ use, since for long cables, a PD pulse propagating along the cables for a few hundred meters is likely to have its higher frequency components attenuated significantly.

Table 6.1: Specifications of the HFCTs.

Parameter	HFCT 1	HFCT 2
Photo		
Manufacturer	IPEC	Bergoz
Part number	HFCT 100/50	FCT-016-05:1-WB
Transfer impedance	5.0 V/A	5.0 V/A
-3 dB bandwidth	90 kHz–20 MHz	10 kHz–1.2 GHz
Internal diameter	50 mm	16 mm
External diameter	110 mm	42 mm
Load resistance	50 $\Omega$	50 $\Omega$
Output connector	BNC	SMA

This will increase the pulse width and decrease the pulse magnitude and thus the optimum detection bandwidth will change with distance propagated by the pulse. By considering typical cable attenuation properties and typical test lengths, an optimum detection bandwidth of 10 – 20 MHz has been suggested by Boggs and Kreuger in their works [23; 31]. HFCT 2 has a bandwidth of higher than 1 GHz, which is preferred for fundamental laboratory studies on PD phenomena. The laboratory studies can be carried out on short cable samples so that PD pulses will be subject to less attenuation resulting from propagation. A PD pulse at its origin can have a duration down to one or two ns [141] or even hundreds of ps according to recent results [25; 142]. Theoretical analysis carried out by Boggs and Stone [15] have shown that for a Gaussian pulse with a 1.5 ns full width at half maximum, 350 MHz would be the optimum detection bandwidth. The 1 GHz bandwidth of HFCT 2 makes it a good choice for accurate measurement of these ns duration pulses.

The HFCT transfer impedances and bandwidths provided in the specifications are sufficient for choosing appropriate HFCTs for specific applications. However, they are not sufficient for investigating effects of the HFCTs on a PD pulse. To that end, HFCT transfer functions (i.e., transfer impedances at different frequencies) have to be obtained.

HFCT transfer functions can be obtained by either frequency domain or time domain measurement methods. Generally, the same measurement setup can be employed for both methods. The main difference between them is that they are using different signal sources as input to an HFCT under test. The frequency domain method uses a sinusoidal excitation source. By varying the source frequency and recording the source and the HFCT output magnitudes (and phases if required) at each frequency, the transfer function can be worked out and plotted against the measurement frequencies. The time domain method ideally should use either an impulse function or a step function as the excitation source. The impulse function is zero at every point apart from where the impulse is located while the step function is zero wherever before the step occurs and 1 thereafter. The response of a system following an impulse or a step function input is the system's impulse response and step response respectively. The impulse response can be calculated directly from the step response and vice versa. Either the impulse response or the step response is able to describe completely transfer characteristics of the system [143]. For a linear time-invariant (LTI) system, its transfer

function in the frequency/Laplace domain can be calculated from the impulse response of the LTI system through the Fourier/Laplace transform. By selecting a proper source as the input to the HFCT under test, the time domain method involves recording both the source  $U_{in}$  and the HFCT output  $U_{out}$  waveforms, and then the frequency dependent transfer function  $TF_{ct}$  can be calculated by

$$TF_{ct} = \frac{\text{FFT}[U_{out}]}{\text{FFT}[U_{in}/R_{load}]} \quad (6.7)$$

where FFT is the fast Fourier transform and  $R_{load}$  is the load resistance connected to the source. With one measurement, the time domain method gives the complex transfer function (both magnitude and phase) at all frequencies that are generated by applying FFT to the waveforms. This makes it particularly attractive for measuring HFCT transfer functions over broadband frequencies. The problem of using the time domain method is that it is not possible to create an ideal impulse function or an ideal step function in the real world. An actual pulse or step source cannot change instantaneously at the point where the pulse or the step occurs. They will have a rise time which is not zero. Since these sources are not really the impulse or the step function, the resulting responses are not the system's impulse or step responses. In other words, transfer characteristics of the system are not completely described by these responses. To what extent the characteristics are described, it is directly related to the sources available. It is the useful bandwidth of an actual source that specifies the frequency band of the transfer function obtained by using the time domain method.

## 6.3 Time Domain Measurement

### 6.3.1 Measurement Setup

For characterising the HFCT transfer functions using the time domain method, the test setup shown in Figure 6.3 was used. A step/pulse generator was connected to an oscilloscope by two lengths of coaxial cable. Between the two lengths of coaxial cable, there was a metal box to separate the centre and the screen of the coaxial cable to allow access of an HFCT to the inner conductor of the coaxial cable. The first length of coaxial cable connecting the step/pulse generator and the metal box was 22.3 m. The length had to be used so as to separate the source signal (in particular the pulse source) from the reflection caused by impedance

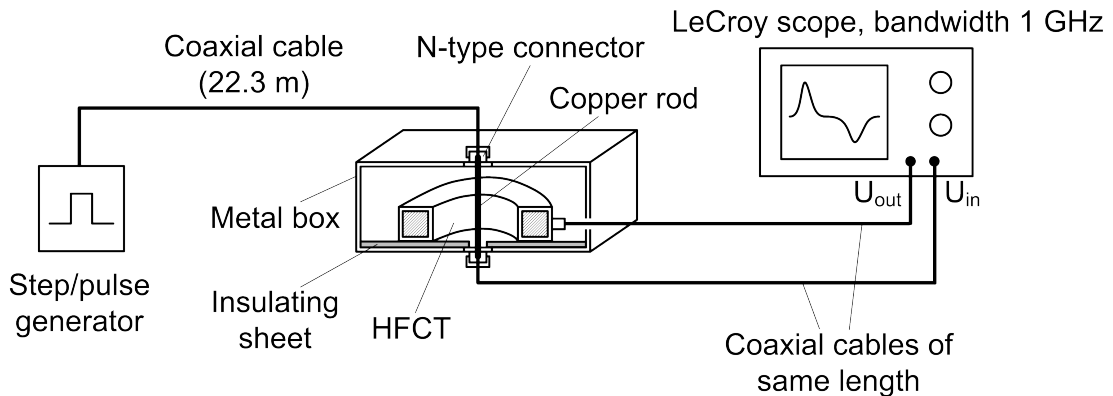


Figure 6.3: Diagram of the setup for measuring HFCT transfer functions. The HFCT is put in the box on an insulating sheet, which is to make sure that no electrical contact exists between the HFCT and the box. For some HFCTs, this is necessary to avoid disturbance sinusoidal waves being induced in both input and output waveforms.

mismatch at the connection to the metal box. The other length of coaxial cable connecting the metal box to the scope was 16.5 m. This length was of less concern since the  $50\ \Omega$  coaxial cable was matched by using the  $50\ \Omega$  input impedance of the oscilloscope. However, it would be better, if the length had been as short as possible to minimise HF attenuation. What did matter was that a same length of coaxial cable should be used to connect the HFCT output to the scope. By the same lengths of coaxial cable, it would minimise the time delay between the recorded traces of the HFCT output and the source input.

For access of the HFCT to the centre of the coaxial cable, previous arrangements had been attempted before the metal box was adopted. Compared with the other arrangements, using the metal box was found to improve the measurements in the following ways: 1) for a proper placement of the conductor going through the HFCT aperture, since the resulting transfer function may vary with whereabouts of the conductor around the HFCT aperture, this is essential in terms of making repeatable measurements; 2) for improvement of the measured transfer functions, especially in the high frequency range, the transfer functions have been obtained with less ripple in the band 100 – 500 MHz. This would be important for an HFCT with a frequency range up to GHz. The idea of using a metal box to accommodate an HFCT under test was from an HFCT manufacturer who suggested that a box would feed magnetic fields in a way as evenly as possible into the HFCT. The metal housing consists of a lid and a box body which are joined by screws. The screws also provide electric connections from the lid to

the box body. Two N-type connectors were mounted at the top and the bottom respectively. The centres of the N-type connectors are connected by a copper rod which will go through an HFCT when it is put in the box. A cross-sectional view of the metal box while an HFCT is being tested is shown in Figure 6.3 and a picture of it in use is shown in Figure 6.4.

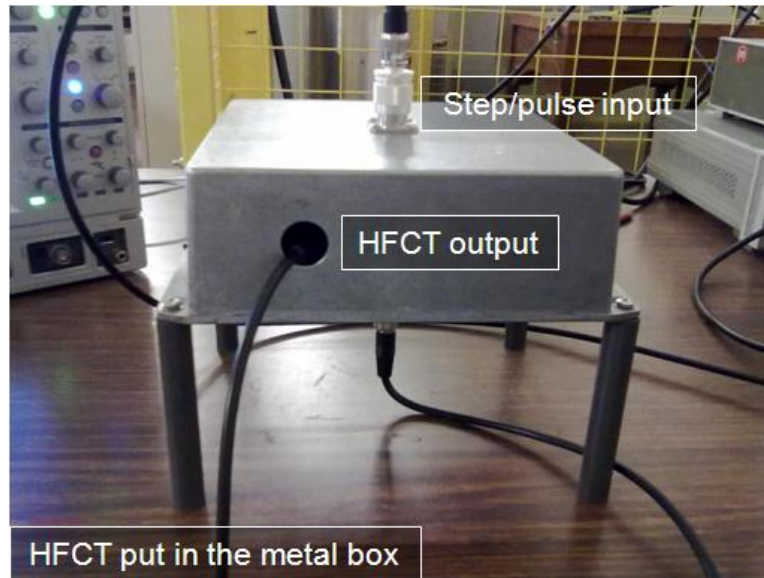


Figure 6.4: Measurement on-going with an HFCT under test inside the metal box. The housing is a die cast aluminium box. Dimensions of the box are  $(200 \times 200 \times 50)$  mm.

### 6.3.2 Pulse and Step Sources

For the exciting source input into the HFCT, there is an avalanche pulse generator which can provide a pulse with a sub-nanosecond ( $< 1$  ns) rise time and a signal generator that can produce a step function with a rise time of about 13 ns. The avalanche pulse was first investigated. A trace of the pulse was acquired for  $T = 0.1 \mu\text{s}$  and is shown in Figure 6.5a. The actual rise time was found as 1.1 ns. The avalanche pulse source typically has a rise time less than 1 ns. It is believed that the pulse was subject to high frequency attenuation when passing through the HFCT test setup, particularly the metal box. Figure 6.5b shows the FFT spectrum of the pulse from 10 MHz which was considered as the lowest resolvable frequency  $f_{low}$  of the spectrum. After a few hundred MHz, the spectrum magnitude was less than one tenth of the value at 10 MHz. 1 GHz was



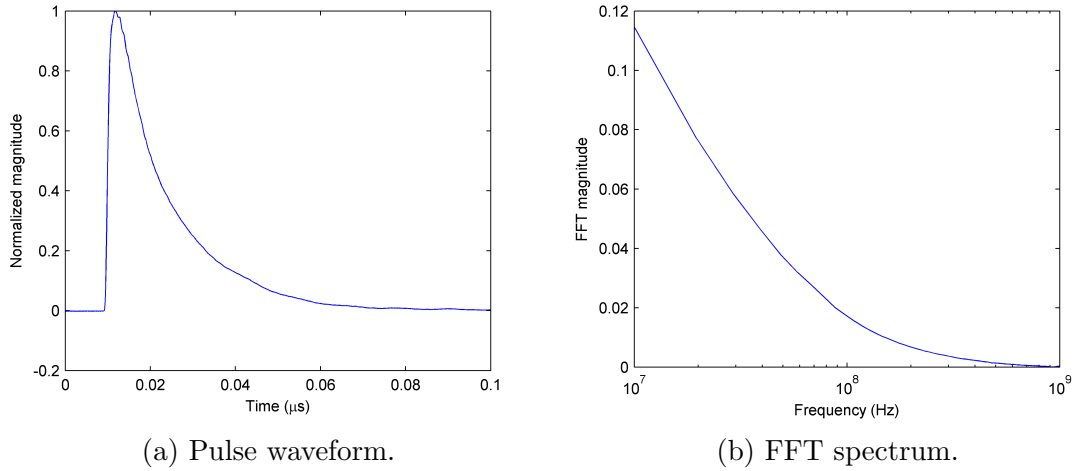


Figure 6.5: Waveform and the fast Fourier transform (FFT) of the avalanche pulse. The recorded pulse after passing through the HFCT has a rise time of 1.1 ns and a full width at half maximum (FWHM) of 10.2 ns.

considered as the highest usable frequency of the pulse. Actually, 1 GHz was also the bandwidth of the oscilloscope used to record the pulse. The lowest resolvable frequency  $f_{low}$  of the spectrum is inversely proportional to the acquisition time  $T$  [144] and can be calculated by

$$f_{low} = \frac{1}{T}. \quad (6.8)$$

An extended acquisition time will have  $f_{low}$  decreased and at the same time bring in more background noise which undermines the whole spectrum. Therefore, there has to be a compromise between  $f_{low}$  and the spectrum quality. As a result, using the avalanche pulse as the source can only obtain the transfer function in a relatively high frequency band, e.g., 10 MHz–1 GHz.

Figure 6.6 shows the waveform and spectrum of the step source. More specifically, it is a combination of two step functions, i.e.,  $u(t - t_1) - u(t - t_2)$  where  $u$  is the step function and  $t_1$  and  $t_2$  are the time delay. Comparing with the spectrum of the avalanche pulse, the step source spectrum is mainly located at low frequencies, e.g., 20 kHz–1 MHz. At 1 MHz, the spectrum magnitude was less than one tenth of the value at 20 kHz.  $f_{low}$  of the spectrum decreased to 20 kHz because of the 50  $\mu$ s acquisition time. The same rule applies to the step source that a longer acquisition time will decrease  $f_{low}$  so that characterising HFCT transfer functions at those frequencies is possible but more background noise will also be

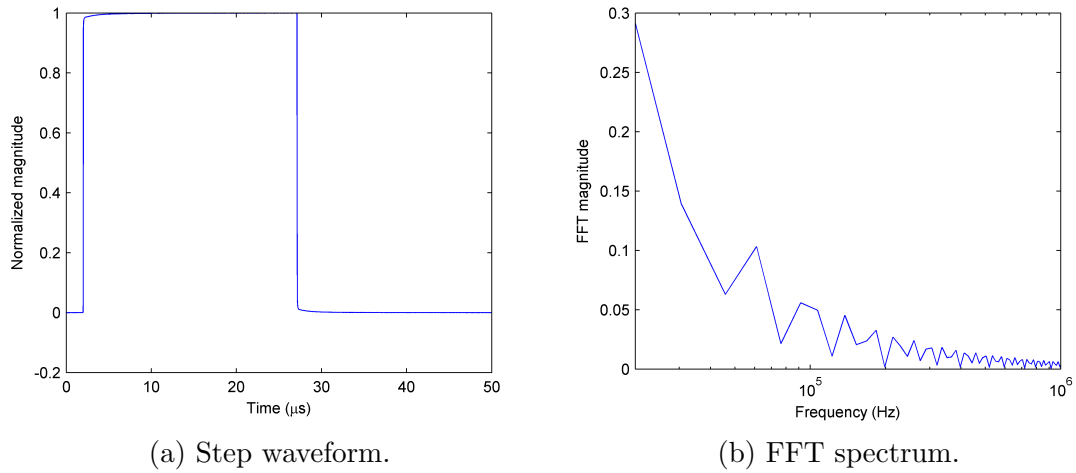


Figure 6.6: Waveform and the fast Fourier transform (FFT) of the step source. The rising edge has a rise time of 13 ns and the falling edge has a fall time of 15 ns. The spectrum ripple is an artifact of the FFT algorithm.

introduced into the spectrum and finally be included in the calculated transfer functions.

### 6.3.3 Measurement Procedures

Referring to the HFCT specifications in Table 6.1, it looks like that for either HFCT 1 or HFCT 2, only using the avalanche pulse or the step source as the input will not be sufficient for measuring the HFCT transfer functions. Therefore a combined scheme has been adopted for both. By using the avalanche pulse as the input, the HFCT's pulse response will be obtained. The pulse response can be substituted into (6.7) to calculate the high frequency part of the HFCT transfer function in the range of 10 MHz–1 GHz. Similarly, by using the step source, the HFCT's step response will be obtained to calculate the low frequency part of the HFCT transfer function in the range of 20 kHz–1 MHz. At frequencies between 1 – 10 MHz, the HFCT transfer function is yet to be resolved before its high frequency and low frequency parts can be joined together to cover both the high frequency and the low frequency ranges.

For joining the two parts of the HFCT transfer function, one possible solution is to have the minimum frequency of the high frequency part decreased from 10 MHz to 1 MHz and the maximum frequency of the low frequency part increased from 1 MHz to 10 MHz. This would make it possible to find a frequency between 1 MHz and 10 MHz where the two parts come very close and thus can be directly

joined. In terms of frequency limits, the transfer function calculated using (6.7) will have its maximum and minimum frequencies defined by FFT. The maximum frequency of FFT is

$$f_{max} = \frac{f_s}{2} \quad (6.9)$$

where  $f_s$  is the sampling frequency used by the oscilloscope to record the step/pulse response. The minimum frequency of FFT is

$$f_{min} = \frac{f_s}{N_{FFT}}. \quad (6.10)$$

where  $N_{FFT}$  is the number of points actually being used in FFT calculation. Therefore, in order to decrease the minimum frequency of the calculated transfer function, the number of points  $N_{FFT}$  used in calculating FFT in (6.7) needs to be increased. For a given step/pulse response trace, this can be done by padding zeros to the end of the trace, which is a method usually practiced for FFT to have the FFT spectrum a smaller frequency resolution. In this way, it is simply interpolating the FFT spectrum with more frequency points [145].

In practice, enough zeros were added to the end of the pulse response trace so that the minimum frequency of the calculated transfer function's high frequency part could be lowered to at least 1 MHz. For the low frequency part, the step response was sampled with  $f_s = 500$  MS/s which according to (6.9) should make the FFT maximum frequency 250 MHz. The calculated low frequency part of the transfer function, especially for HFCT 2, has shown noise arising with frequency. However, for frequencies  $\leq 10$  MHz, the noise can be well smoothed out by calculating running medians of the transfer function.

#### 6.3.4 Measurement Results and Discussion

The step and the pulse responses were measured respectively for both HFCT 1 and HFCT 2. Figures 6.7 shows the step and the pulse responses for HFCT 1. Substituting the responses into (6.7) and based on the above discussion about the frequency limits, the low frequency part (20 kHz–10 MHz) and the high frequency part (1 – 500 MHz) of HFCT 1 transfer function were calculated and shown in Figure 6.8. 5 MHz where the two parts of the transfer function had a difference of 1.1 % was selected as a joining frequency. By simply joining together

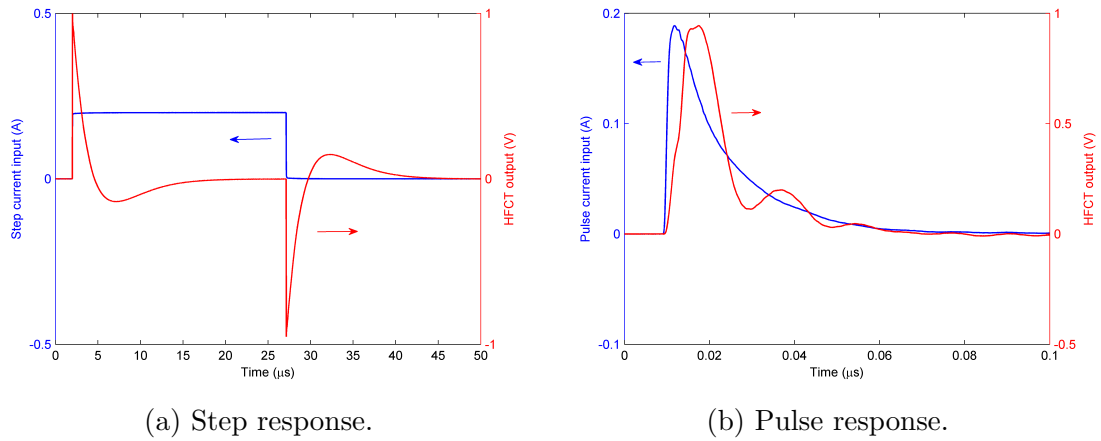


Figure 6.7: Step response and pulse response of HFCT 1. The step response was obtained by using the step source shown in Figure 6.6 as the input and was sampled with  $f_s = 500$  MS/s. The pulse response was obtained by using the avalanche pulse shown in Figure 6.5 as the input and was sampled with  $f_s = 10$  GS/s.

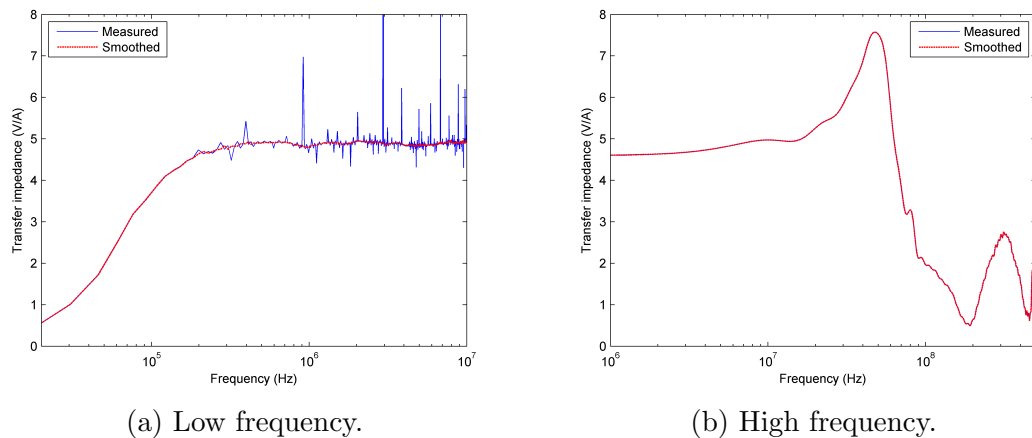


Figure 6.8: Low frequency (20 kHz–10 MHz) and high frequency (1 – 500 MHz) parts of HFCT 1 transfer function. From around 1 MHz upward, the low frequency part started to suffer from more significant noise, which can be smoothed out effectively by calculating running median of the transfer function.

the two parts at 5 MHz, the HFCT 1 transfer function covering frequencies from 20 kHz–500 MHz was obtained and shown in Figure 6.9.

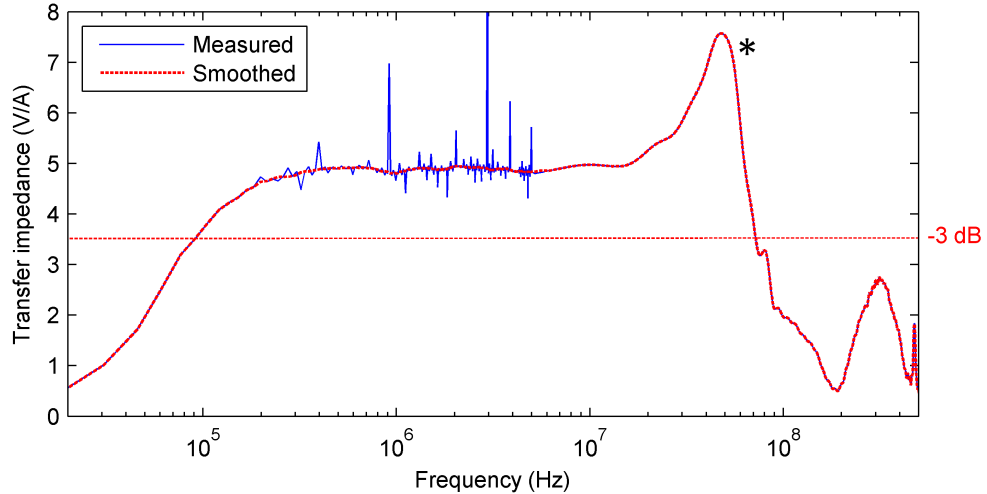


Figure 6.9: HFCT 1 transfer function from 20 kHz–500 MHz. \* The peak located around 50 MHz was resulting from that in measuring the transfer function, the conductor going through the HFCT aperture was at a position near the aperture edge which is shown in Figure 6.10a.

Referring to Table 6.1, HFCT 1 is described as having a -3 dB bandwidth of 90 kHz–20 MHz, while according to Figure 6.9, this bandwidth was about 90 kHz–70 MHz. Moreover, the transfer function was found to vary with the position of the conductor within the HFCT aperture. Figure 6.10 shows two positions which were near the edge and at the centre of the HFCT aperture. The transfer function shown in Figure 6.9 was obtained while the conductor was placed near the aperture edge. A peak in the transfer function was evident around 50 MHz. Figure 6.11 shows the result for the conductor position at the aperture centre, which does not show a peak at 50 MHz. This may be attributed to the coupling capacitance between the primary and the secondary of the HFCT was changed. The position near the aperture edge would have the capacitance maximised whereas at the centre the capacitance would be minimised [59]. The coupling capacitance will contribute to the secondary loading capacitance  $C_s$  in the HFCT equivalent circuit shown in Figure 6.2 and thus affect the HFCT output. Higher capacitance is more likely to cause a resonant frequency to move into the measurement band. In practical measurement, keeping the conductor at the aperture centre will be preferred so as to minimise the primary to the

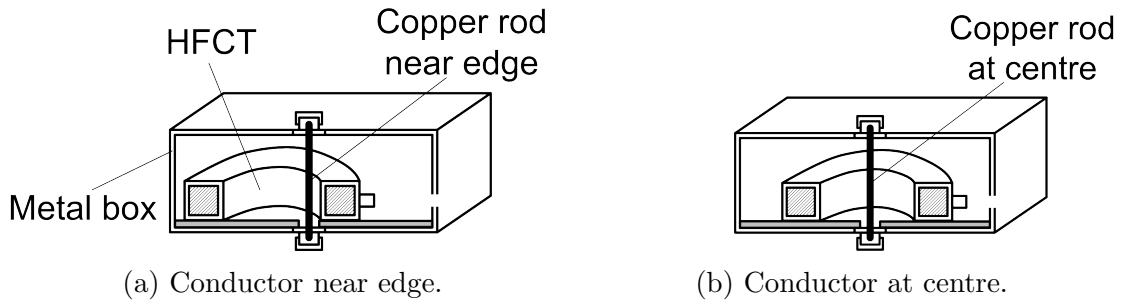


Figure 6.10: Position of the conductor in the HFCT aperture: near the edge and at the centre. In the pulse response measurement for HFCT 1, the HFCT output was found to vary with the conductor position in the HFCT aperture. The near the edge position was selected because this is the position suggested by the manufacturer for in-situ installation.

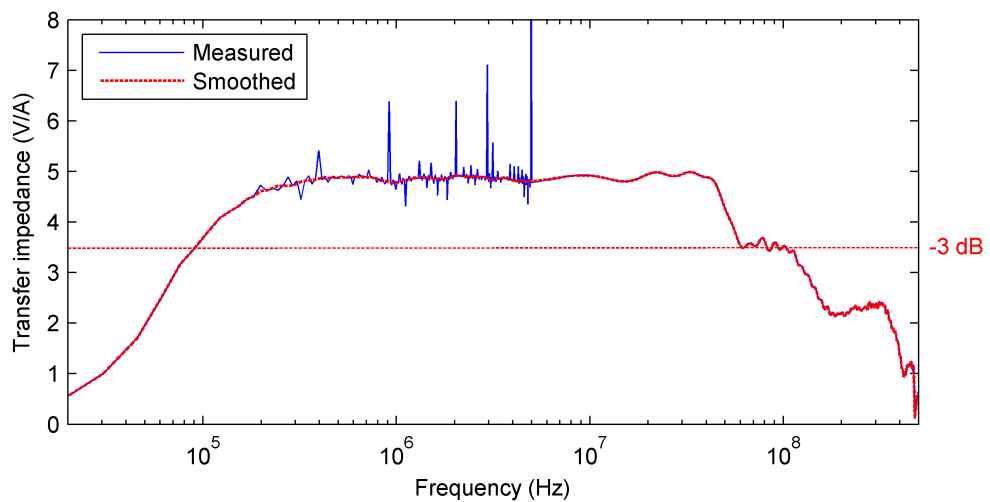


Figure 6.11: HFCT 1 transfer function from 20 kHz–500 MHz. In the transfer function measurement, the conductor going through the HFCT aperture was at the aperture centre.

secondary capacitance. However, for HFCT 1, the position near the aperture edge is suggested for in-situ installation by the manufacturer, which is probably due to that a higher sensitivity is attained when the conductor is close to this position, and this could avoid the need for additional mechanical support.

The same procedures for calculating the low frequency and the high frequency parts of the HFCT transfer function from the step and the pulse responses were applied to HFCT 2. The two parts were joined at 5 MHz to produce the transfer function from 8 kHz–1 GHz, which is shown in Figure 6.12.

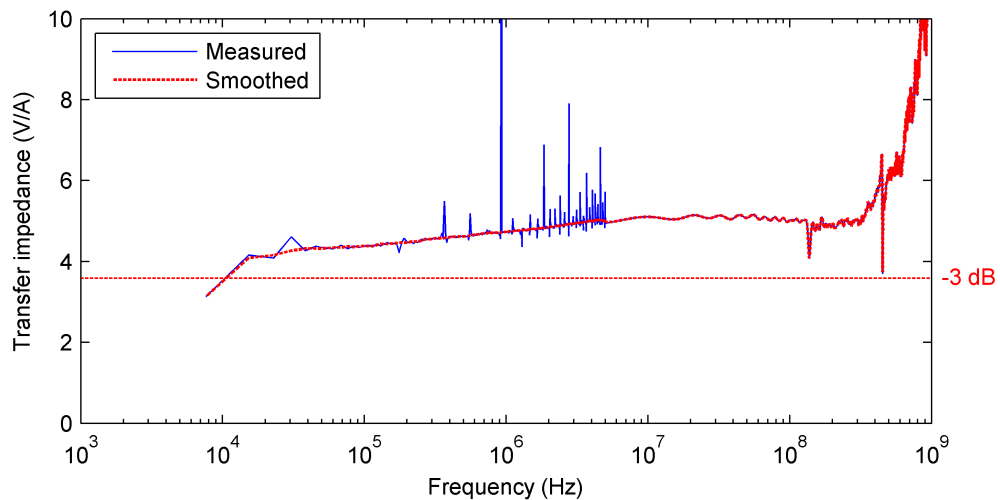


Figure 6.12: HFCT 2 transfer function from 8 kHz–1 GHz.

The lowest frequency of the obtained transfer function was determined as 8 kHz based on that the step response was acquired for 125  $\mu\text{s}$ . According to (6.8), frequencies lower than 8 kHz can be achieved by recording a longer step response. However, not without penalty, as more background noise will be introduced. Another possible solution is by “padding” the response trace with artificial samples of 0 V, or some dc offset while doing FFT. In this way, the spectrum band  $[0, f_s/2]$  of the response will be broken into more frequency points and, therefore, a higher frequency resolution is obtained. The “padding” way is actually doing spectral interpolation. In other words, by “padding” zeros to the trace, no extra information is gained, and it is calculating essentially the same approximation to the Fourier transform [145]. Tests using the 125  $\mu\text{s}$  long step response showed that a lowest frequency lower than 8 kHz could be obtained by “padding” zeros to the response trace, but with more zeros being

added, the calculated transfer function was gradually becoming convergent to a constant value instead of decreasing towards zero with frequency. Therefore, it was concluded that the effect of “padding” zeros is limited. In order to push down the lowest frequency of the obtained transfer function, recording a longer response trace could be unavoidable. Experience gained in this work suggested that a combination of recording longer step response traces and “padding” zeros was preferable and allowed characterising the HFCT transfer functions at lower frequencies.

Figure 6.13 shows that a 1000  $\mu\text{s}$  step response trace gave out the transfer function with a lowest frequency of 1 kHz while the noise in the transfer function increased somewhat. Comparing with the -3 dB bandwidth of 10 kHz–1.2 GHz suggested in Table 6.1, Figures 6.12 and 6.13 show that the obtained transfer functions had lower -3 dB cutoff frequencies of 10 kHz and 20 kHz respectively (The -3 dB cutoff frequency was evaluated by assuming a 5 V/A flat response although there was not a flat response for HFCT 2). The upper -3 dB cutoff frequency has exceeded the bandwidth of both the avalanche pulse and the oscilloscope and, therefore, cannot be confirmed.

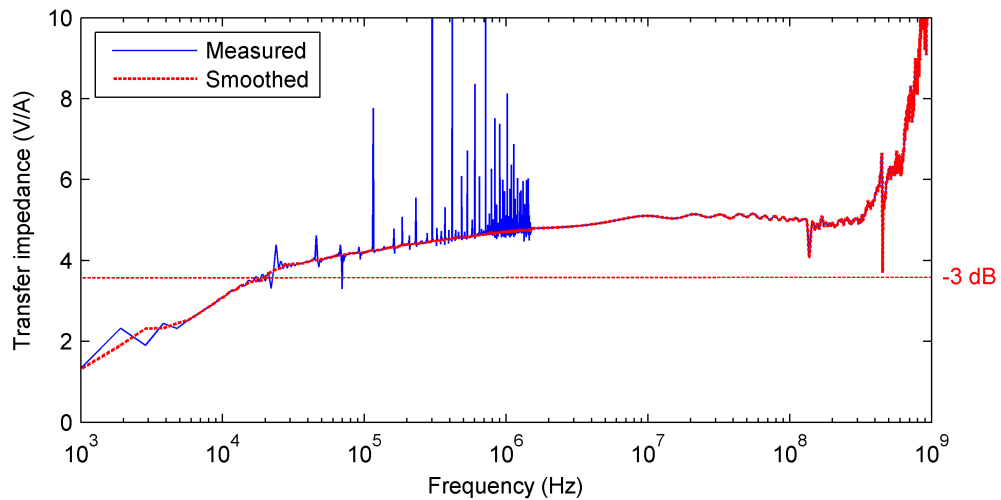


Figure 6.13: HFCT 2 transfer function from 1 kHz–1 GHz.



## 6.4 Frequency Domain Measurement

Frequency domain measurements were carried out to allow comparisons with the HFCT transfer functions obtained from the time domain measurements. The measurement setup shown in Figure 6.3 was used while the step/pulse generator was replaced by a signal generator that can provide sinusoidal sources of frequencies ranging from DC to 50 MHz. For both HFCT 1 and HFCT 2, the measurements were carried out from a frequency where the HFCT output was close to the vertical resolution of the oscilloscope until 50 MHz.

The obtained HFCT transfer functions and those from the time domain measurements are plotted on the same scale in Figures 6.14 and 6.15 for HFCT 1 and HFCT 2 respectively. They show that the transfer functions from the frequency and time domain measurements are in reasonable agreement with each other. While for HFCT 2, the transfer functions obtained using the different methods have apparent differences, the agreement was generally acceptable over the whole frequency range. The results suggest that the time domain method is as effective as the frequency domain method in characterising the HFCT transfer functions. Furthermore, since it is the smoothed time domain measurement results that were plotted in Figures 6.14 and 6.15, it means that calculating running medians of

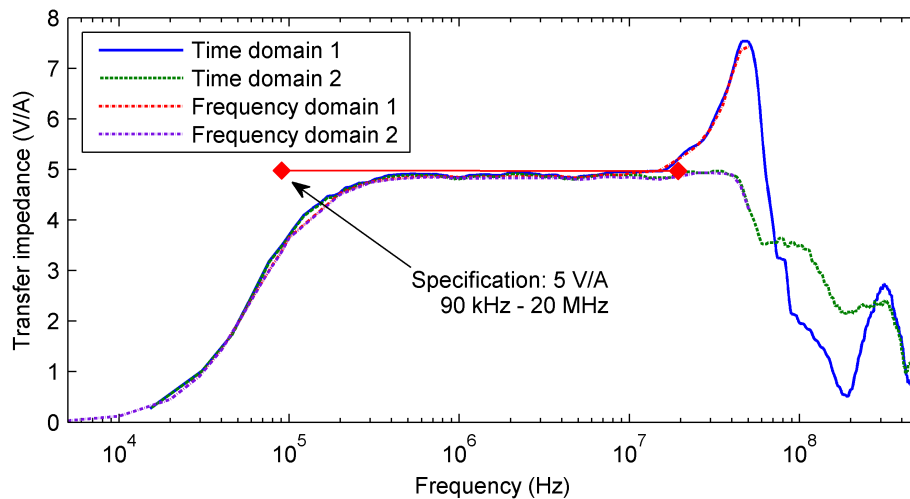


Figure 6.14: HFCT 1 transfer functions from both time domain and frequency domain measurements. Maximum differences between the transfer functions from the different methods were found as 3.8% and 3.3% for those numbered “1” (conductor near aperture edge) and “2” (conductor at aperture centre) respectively.

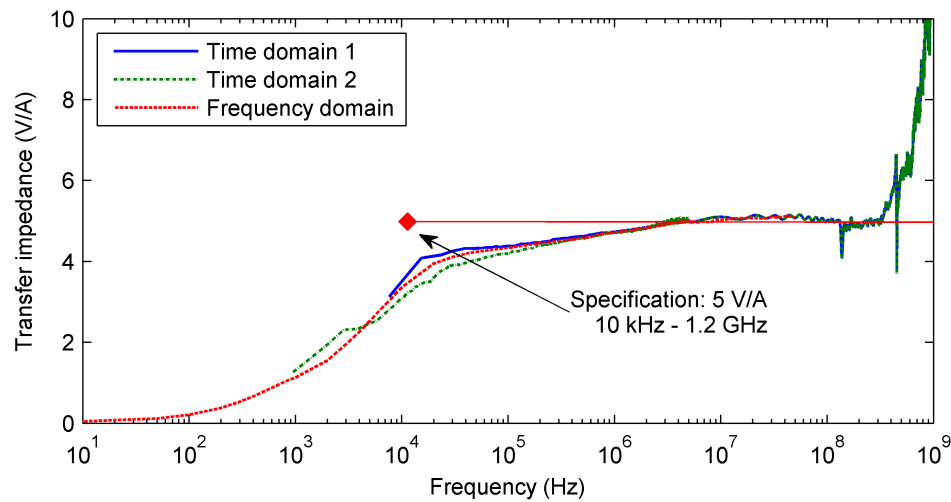


Figure 6.15: HFCT 2 transfer functions from both time domain and frequency domain measurements. Maximum differences of 9.4% and 18.3% were attained for the transfer functions between “Time domain 1” (125  $\mu$ s acquisition time) and “Frequency domain” and between “Time domain 2” (1000  $\mu$ s acquisition time) and “Frequency domain” respectively.

the transfer functions was effective in removing noise from the transfer functions, particularly those present in the low frequency parts calculated from the step responses of the HFCTs.

-3 dB bandwidths of the HFCTs from the manufacturer specifications in Table 6.1 are plotted as straight lines with square ends in Figures 6.14 and 6.15. For both HFCT 1 and HFCT 2, the lower -3 dB cutoff frequencies generally agreed with the measurement results. In terms of the upper cutoff frequencies, for HFCT 1, the time domain measurements of “1, near the edge” and “2, at the centre” got 60 MHz and 70 MHz respectively. Both are higher than the manufacturer data. The time domain results of HFCT 2 began to increase from 300 MHz, and after 900 MHz, quickly scaled up to a significant resonance peak at 1 GHz. This may be due to the fact that a combination of the measurement setup, the avalanche pulse and the oscilloscope started to reach its bandwidth capability of characterising the HFCT transfer function. The manufacturer data of HFCT 2 should be trustworthy as the -3 dB frequencies are shown in a calibration certificate provided with the HFCT. The certificate was obtained using a HP network analyzer with a sufficient bandwidth.

## 6.5 Conclusions

An analytical HFCT transfer function was determined based on a simplified equivalent circuit of the HFCT. Specifications of the two HFCTs used in this work were described. Both HFCT transfer functions were obtained using the time domain and the frequency domain measurement methods respectively. For each HFCT, the results from both measurement methods achieved an acceptable level of agreement. For HFCT 1, the measured -3 dB bandwidth differed from the manufacturer data and, moreover, the transfer function was found to depend on the position of the conductor within the HFCT aperture. The observed variation between the measurement result and the manufacturer data suggests that, to understand how an HFCT's voltage output is produced from input currents, proceeding to measure the HFCT transfer function and its dependency on the input position within the HFCT aperture is necessary.

While the frequency domain measurements are usually carried out at each individual frequency across a frequency range of interest, the time domain measurement only requires two tests to record a step response and a pulse response respectively. Furthermore, using the time domain measurement, the complex transfer function (both magnitude and phase) of the HFCT can be obtained conveniently through FFT calculation. The HFCT complex transfer function is required by a procedure within the proposed modelling framework to convert PD currents into the HFCT's voltage output.

# Chapter 7

## FDTD Modelling of HFCT-based PD Detection in Cables

### 7.1 Introduction

In PD measurement for a cable using HFCTs as PD sensors, the HFCTs are often installed at cable terminations where the cable outer conductor is accessible. In this case, the primary of each HFCT is the cable outer conductor and the input signal of the HFCT is the current through the outer conductor. A PD event in the cable will appear on the outer conductor as a current pulse. The current pulse will travel in both axial directions of the cable. When the pulse comes to a position (e.g., a termination) where an HFCT is installed, it will be detected by the HFCT and converted to the HFCT's voltage output. Therefore, to simulate the practice of using HFCTs to detect PD in cables, the expected outcome should be like that with a PD current pulse input, output from the simulation will be an HFCT's voltage output. In this way, it shall make it possible to have a comparison between measurement and modelling results, of which the final objective is to improve the interpretation of the results obtained in on-line PD measurement for cables.

Using FDTD modelling, details of the cables can be created as required, e.g., as those described in Chapter 5. A current source can be introduced within the cable insulation as a PD source and its time-domain waveform can be defined using either analytical functions like a Gaussian pulse or digitally sampled data from an actual PD current pulse measurement. However, the HFCT itself cannot be modelled directly using FDTD both because there is too much fine geometrical detail in an HFCT winding and the detail would require an extremely small FDTD

mesh, making the simulation computationally demanding. Therefore, a hybrid framework for applying FDTD modelling to HFCT-based PD measurement for cables is proposed in this chapter. First, a method of deriving currents through conductors in XFDTD is described. Using this method, currents through the outer conductors of FDTD cable models can be derived. Second, the derived current through the conductor onto which the HFCT is clamped is used together with the measured HFCT transfer function to give out the HFCT's response in post processing. This involves multiplying the FFT of the current by the transfer function and then using an inverse FFT to work out the output voltage over time. Based on the described method to account for the effect of the HFCT, a hybrid framework for FDTD modeling of HFCT-based PD measurement for cables is developed. The framework has included everything from a PD current source within the cable insulation to detection by an HFCT and is illustrated by using an experimentally measured PD pulse as input. The proposed framework will subsequently be used in a parametric study investigating coupling sensitivity between PD source currents and the corresponding PD currents on the cable outer conductor.

## 7.2 Measuring Currents in XFDTD

### 7.2.1 Method Evaluation with a Basic Circuit Model

Direct output results from XFDTD are parameters like electric and magnetic field vectors and magnetic flux and current densities at the gridding points throughout the simulated volume. No proper "current sensor" is provided in XFDTD to measure currents through a conductor in an FDTD model. In order to derive the currents, in particular for cable conductors, a method based on recording magnetic fields around the conductors and using Ampere's law to calculate the currents through the conductors was implemented. The method includes two steps. First, a sensor loop is created out of point sensors around a conductor of an FDTD model. The point sensor is used to record the magnetic field at a certain point of a model. Second, the recorded magnetic fields from these point sensors are used to derive currents through the conductor by using Ampere's law [146]. Since the magnetic fields are sampled at individual points, application of

Ampere's law shall be carried out via numerical integration, i.e.,

$$I = \sum \vec{H}_i \cdot \vec{\Delta}l \quad (7.1)$$

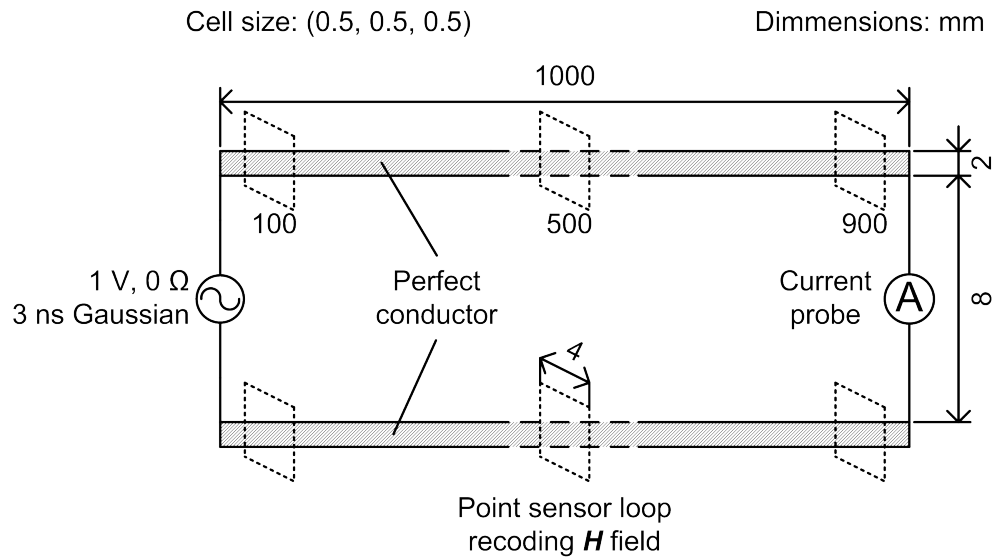
where  $\vec{H}_i$  is the appropriate magnetic field component at the point  $i$  of a sensor loop and  $\vec{\Delta}l$  is an interval on the integration path and is also a vector. It should be noticed that it has to be the correct vector component at each point so that the numerical integration does sum the contributions to  $H$  around a closed loop.

This method was tested by using a basic circuit model consisting of two 1 m long perfect conductors connecting a voltage source to a current probe as shown in Figure 7.1a. The voltage source waveform was defined as a Gaussian pulse having a 3 ns duration from beginning to end (This is the way that the width of a Gaussian pulse is executed in XFDTD although theoretically a Gaussian pulse has no start or end). The current probe was the circuit load as well as for recording currents at the load side. By perfect conductor, it is meant that electric fields within the conductors will be zero. At different positions along the axial direction of each conductor, three point sensor loops were created around the conductor. Figure 7.1a shows the circuit diagram and Figure 7.1b shows the created model in XFDTD.

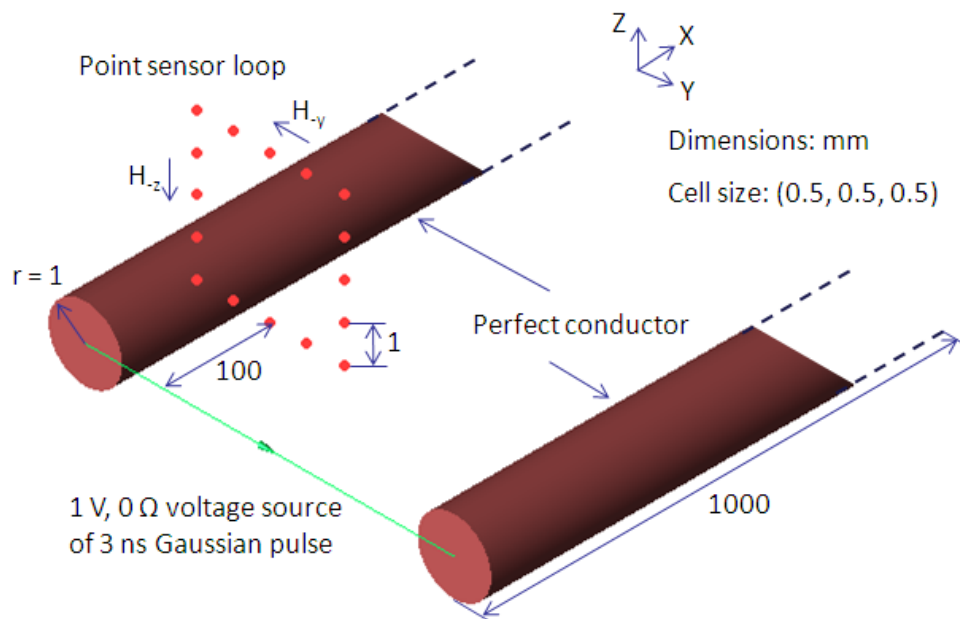
After running the FDTD simulation, computed magnetic fields at these points were recorded by the point sensors. For each sensor loop around either conductor, those magnetic field components which would contribute to  $H$  around the loop were extracted and by summing them according to (7.1), the current passing through the sensor loop (i.e., the current through the conductor) was calculated. Figure 7.2a shows the currents calculated from the different sensor loops on one of the conductors. The result has shown that the incident pulse of the source current looks very similar to those of the currents at 0.1 m and 0.5 m from the source. The current pulse recorded at 0.9 m from the source is both higher and wider, which was due to superposition of incident and reflected pulses. The reflection was a result of impedance mismatch between the pair of conductors and the load. The characteristic impedance of a pair of lossless wires (presumably infinitely long and far from any other objects) can be calculated by

$$Z_0 = (120/\sqrt{\epsilon_r}) \times \ln[(d/2a) + \sqrt{(d/2a)^2 - 1}] \quad (7.2)$$

where  $d$  is the distance between wire centres and  $a$  is wire radius [113]. A char-



(a) Model diagram. The source side of the circuit was a 1 V voltage source with a  $0\ \Omega$  internal impedance. The load side of the circuit was a current probe. The three sensor loops were located at 100, 500 and 900 mm from the source side on each conductor.



(b) Model created in XFDTD. Each point sensor loop was created as a 4 mm square. Distance between two point sensors of each point sensor loop was 1 mm while a uniform cell size of 0.5 mm was applied across the model.

Figure 7.1: A basic circuit model to evaluate the current deriving method.

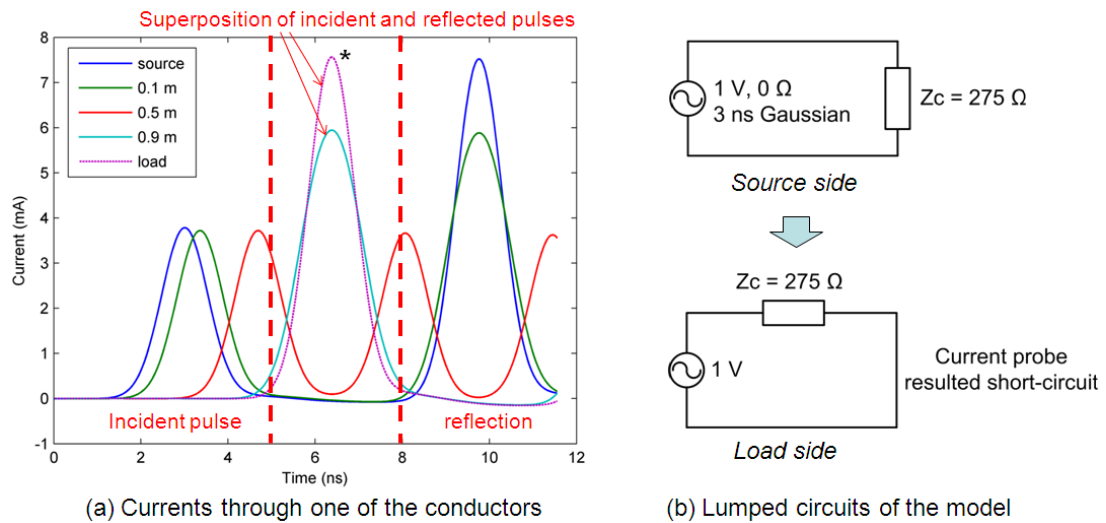


Figure 7.2: Currents derived using Ampere’s law and equivalent circuits of the model. The characteristic impedance of the pair of conductors is  $Z_0 = 275\Omega$ . Since the source impedance was  $0\Omega$  and the load side was short-circuited, the lumped circuits at the source and the load sides can be drawn, and the current at the load side can, therefore, be calculated as  $I_A = 1/275 = 3.6$  mA, which is about a half of the recorded load current (the purple dotted trace). \* The load current is in dotted line because the plotted polarity is just inverse to that from the simulation, for an easier comparison.

acteristic impedance,  $Z_0 = 275\Omega$  was obtained for the conductors of the basic circuit model while the load was the XFDTD current probe which is equivalent to a short-circuit. The derived currents on the other conductor were completely the same as those shown in Figure 7.2a but with opposite polarities.

In order to validate the currents derived by using the suggested method, lumped circuit and charge conservation analysis were conducted. By using lumped equivalent circuits to represent the source side and the load side of the circuit respectively, which is shown in Figure 7.2b, the maximum magnitude of the current at the load side was calculated as 3.6 mA. This was about half of the value actually recorded in the simulation. This phenomenon can be explained by the total reflection caused by the short-circuit load. For the current pulse, this results in a constructive adding of the incident and the reflected pulses, in other words the current magnitude should be doubled. Figure 7.2a also shows, for the current at 0.5 m, there are three individual pulses. The pulse width had to be made smaller before the pulses could be totally separated to enable evaluation of each pulse’s total charges (area under one pulse). Therefore, with source pulses set to widths of 1 ns, 300 ps and 100 ps respectively, the current-deriving procedures were re-



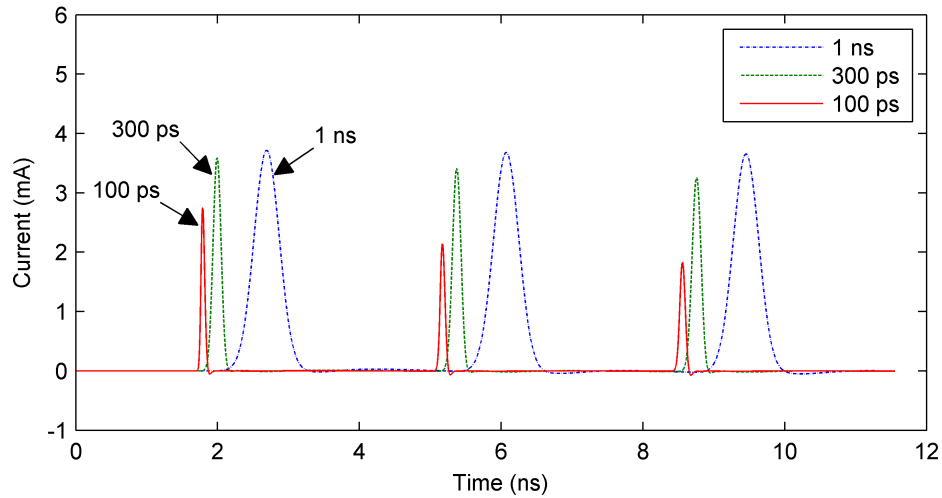


Figure 7.3: Current pulses at 0.5 m on the conductor.

Table 7.1: Integrated charges in each pulse.

Current pulse at 0.5 m	Pulse duration from beginning to end		
	1 ns	300 ps	100 ps
1st	1.65 pC	0.501 pC	0.167 pC
2nd	1.61 pC	0.483 pC	0.160 pC
3rd	1.58 pC	0.470 pC	0.156 pC

peated and charges of each pulse were calculated. Figure 7.3 shows the derived current pulses at 0.5 m. Table 7.1 shows the charge levels obtained for the 1st, 2nd and 3rd pulses of the derived current. The charge levels diminished slightly pulse by pulse. This is due to the fact that FDTD is a numerical algorithm and both the processes of deriving current using Ampere's law and calculating area under a pulse are numeric integrations which accumulate small errors over time. However, it is reasonable to conclude that the method is sufficiently effective for deriving current in XFDTD.

### 7.2.2 Application to a Basic Cable Model

The current deriving method for use with XFDTD was put to test on a basic model of a cable termination first. Based on the details of cable sample 1 described in Chapter 5, the basic cable model was created according to the diagram shown in Figure 7.4. It was a 2 m long cable section while the insulation was present only in the first half of the cable. For the second half, only the inner and outer conductors

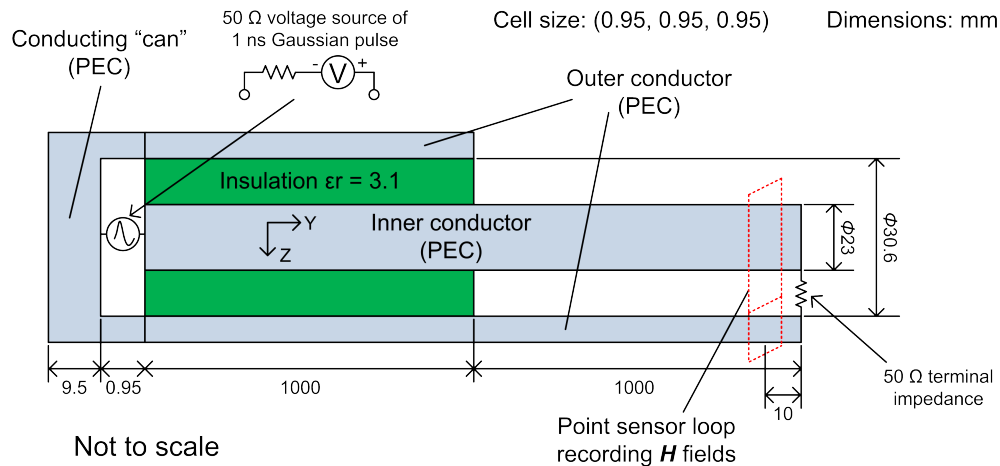


Figure 7.4: A basic cable model. The semicon layers were not considered in the model. Both inner and outer semicon layers were taken as conductors and merged into the cable conductors, i.e., the inner semicon layer merged into the inner conductor and the outer semicon layer merged into the outer conductor. Both cable conductors were using the perfect conductor (PEC) material within which electric fields are always zero.

were present, i.e., no insulation for this half. Furthermore, to simulate a situation where the cable is being under a PD test, the outer conductor in the second half was truncated. This was corresponding to a PD measurement practice where the cable outer conductor should be made accessible for installing an HFCT. For the cable model, truncating the outer conductor also made it possible to create sensor loops around both inner and outer conductors for deriving currents. The source side of the model was a voltage source accommodated in a conducting “can” (refer to Section 3.5.4.2). The use of the conducting “can” was for connecting the source to the outer conductor in a way that can make the source current flow as evenly as possible into the outer conductor. The load side was a 50  $\Omega$  terminal impedance connected between the inner and the outer conductors.

For applying the suggested method to derive currents through both inner and outer conductors, point sensor loops were created for the conductors respectively, at an axial position close to the load impedance. Figure 7.5 shows the created cable model in XFDTD. The half of the outer conductor subjected to truncation is referred to in the cable model as an “earth extension”. The created sensor loops were deliberately coincided at one edge so that on this edge, point sensors only need to be created once and can be used by both loops. Integration paths for the inner and the outer conductors were both in the anti-clockwise direction. This will make the derived currents have opposite polarities, since the currents

on the inner and the outer conductors are supposed to flow in opposite directions. Figure 7.6 shows the currents derived for both conductors. A good agreement was achieved between the inner conductor current and the outer conductor current. Some slight differences could be caused by geometrical differences and different

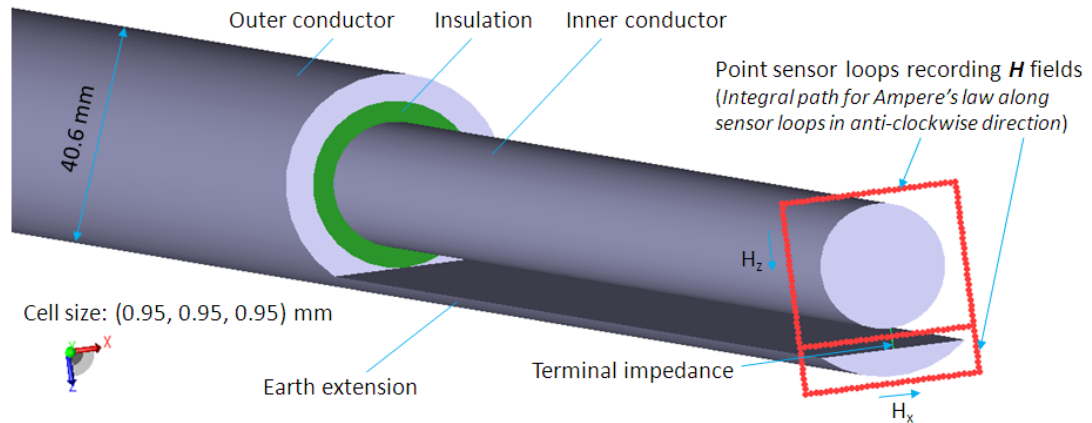


Figure 7.5: The basic cable model created in XFDTD. The outer conductor looks thicker than it should be even after incorporating the outer semicon layer. This was desired because this would not influence the simulation result and at the same time can prevent the outer conductor from being the smallest object in the model. The benefit will be not having to use smaller meshes and involve more computation load.

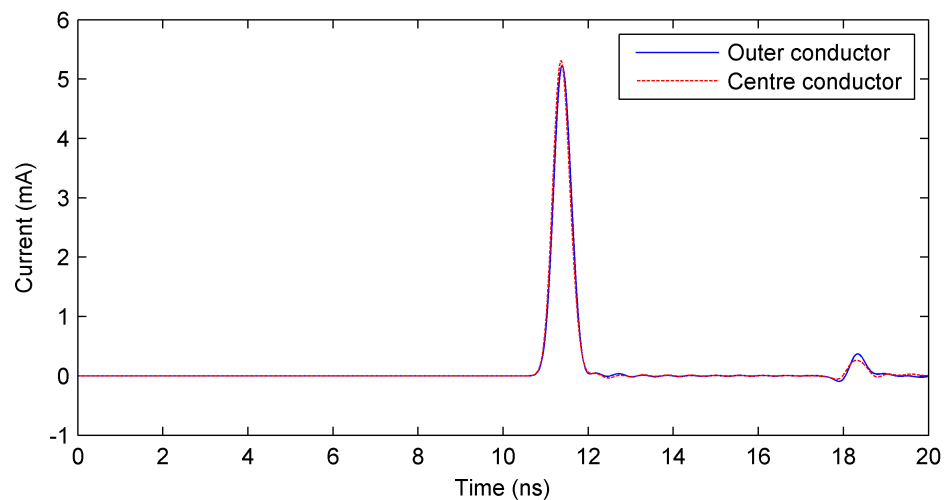


Figure 7.6: Currents through the cable inner and outer conductors. The currents were calculated by integrating the sensor loops recorded magnetic fields according to (7.1) along the integration paths drawn in Figure 7.5. When plotting the currents, polarity of the outer conductor current was reversed for a convenient comparison.

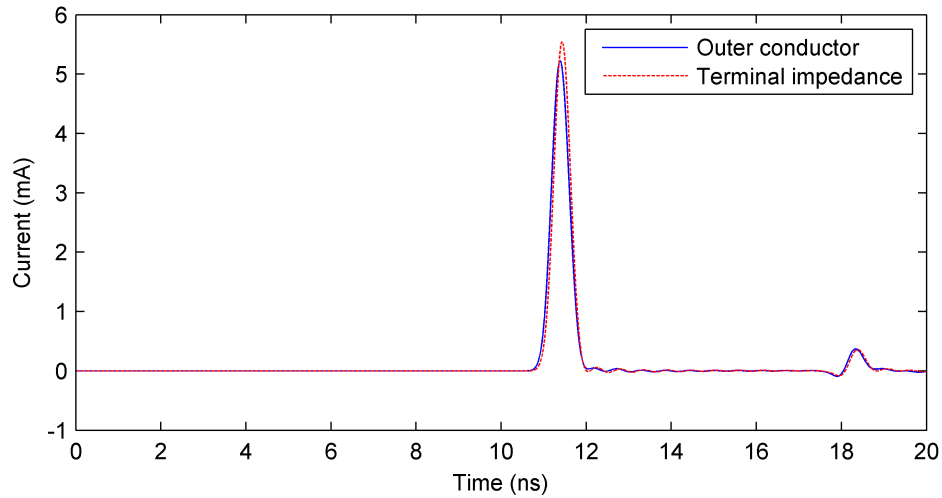


Figure 7.7: Currents through the cable outer conductor and the terminal impedance. The terminal impedance current was read directly from an output parameter coming with a resistor component in XFDTD.

numbers of the point sensors in the sensor loops. Figure 7.7 shows the load current and the outer conductor current. Given the fact that the sensor loops were 10 mm from the load, the agreement between the currents was still good. Therefore, it was concluded that the suggested method can meet the requirements of deriving currents through the conductors of an FDTD cable model.

## 7.3 Working out an HFCT's Voltage Output

### 7.3.1 Application of FFT and Transfer Function Methods

An HFCT cannot be easily realized by FDTD modelling because of the following reasons: (a) too much fine (e.g., many turns of thin wire) details make physically modelling the HFCT modelling difficult; (b) accounting for the fine details in FDTD requires sufficiently small meshes and can be computational intensive; (c) properties of the magnetic core are not easily measured and will be frequency-dependent. Therefore, while applying FDTD modelling to HFCT-based PD measurement for cables, feasibility of including the HFCT in the FDTD model has been ruled out. Instead, given the fact that it is PD-induced currents flowing on a cable outer conductor that actually pass through an HFCT aperture and determine its output voltage waveform, if the current through the cable outer

conductor of the FDTD model is derived and the HFCT transfer function with frequency is measured, a combination of the derived current and the measured HFCT transfer function can give out the HFCT's voltage output in post processing, i.e., after the FDTD simulation.

The combination was performed in two methods: 1) by doing FFT, multiplying FFT of the derived current by the measured HFCT complex transfer function and then using an inverse FFT to find the HFCT's voltage output; 2) by using transfer function models, establishing for the HFCT a proper transfer function model and applying the model to the current to obtain the HFCT's output. Method 1), by doing FFT, can be summarised as

$$\text{FFT}[V_{ct}] = \text{FFT}[I_{in}] \times TF_{ct} \quad (7.3)$$

$$V_{ct} = \text{IFFT}\{\text{FFT}[V_{ct}]\} \quad (7.4)$$

where  $I_{in}$  is the input current passing through the HFCT aperture,  $TF_{ct}$  is the measured HFCT transfer function and  $V_{ct}$  is the calculated HFCT's voltage output. This approach is straightforward in terms of simply multiplying FFT of the current by the HFCT transfer function and the only operation is by interpolation to make the frequencies of the measured transfer function agreed with the FFT frequencies. Since the measured transfer function data are directly applied, the FFT should be the most accurate. However, it was found to fail when the FFT of the input current had a highest frequency which was higher than that of the measured transfer function. While the time domain method is used to obtain the HFCT transfer function, this means that the sampling rate used in the transfer function measurement is not as high as that used to sample the input current, which is a very common situation for those currents derived from FDTD simulations. Moreover, referring to Chapter 6, the measured transfer functions actually have certain usable bandwidths which are subject to both the HFCT bandwidth and the measurement system bandwidth. For example, Figure 6.9 shows for HFCT 1 a usable bandwidth of 20 kHz–500 MHz. The usable bandwidths were usually lower than the highest frequencies of the obtained transfer functions. The highest frequencies can be calculated by (6.9), which was 5 GHz for the measured HFCT 1 transfer function. In other words, although HFCT 1 transfer function went up to the maximum frequency of 5 GHz, only the first 500 MHz was usable. Above 500 MHz, the transfer function was more and more undermined by uncertainties. Without taking this into account when using (7.3),

it will result in uncertain frequency components being included in the calculated HFCT's output.

Method 2) was proposed by Haghjoo et al. [147]. It is based on the transfer function model of a linear time-invariant (LTI) system and involves two stages: (a) fitting the measured transfer function data to the transfer function model; (b) applying the established transfer function model to the current input. For stage (a), the transfer function of a linear time-invariant (LTI) system in the Laplace ( $s$ ) domain [143], with input  $X(s)$  and output  $Y(s)$ , is written as

$$H(s) = \frac{Y(s)}{X(s)} = \frac{b_m s^m + b_{m-1} s^{m-1} + \dots + b_1 s + b_0}{a_n s^n + a_{n-1} s^{n-1} + \dots + a_1 s + a_0} \quad (7.5)$$

where  $b_i$ ,  $a_i$ ,  $m$  and  $n$  are parameters of the system. The transfer function can also be written in product-of-sums form as

$$H(s) = \frac{K(s - z_1)(s - z_2) \dots (s - z_m)}{(s - p_1)(s - p_2) \dots (s - p_n)} \quad (7.6)$$

where  $z_i$  and  $p_i$  are called zeros and poles of  $H(s)$  respectively, and  $K = b_m/a_n$  where  $b_m$  and  $a_n$  are the coefficients of the highest order of  $s$  in the numerator and denominator polynomials respectively. A system is said to be stable provided that with any bounded input, the system output is bounded [143]. This, in terms of the transfer function  $H(s)$ , the criterion is that all the poles must lie in the left half of the  $s$ -plane, i.e.,  $\text{Re}(p_i) < 0, i = 1, 2, \dots, n$ . While a LTI system is represented by the transfer function  $H(s)$ , the inverse of the LTI system is defined as

$$H(s)H_i(s) = 1 \implies H_i(s) = \frac{1}{H(s)} \quad (7.7)$$

$$H_i(s) = \frac{a_n s^n + a_{n-1} s^{n-1} + \dots + a_1 s + a_0}{b_m s^m + b_{m-1} s^{m-1} + \dots + b_1 s + b_0}. \quad (7.8)$$

For the inverse system to be stable the poles of  $H_i(s)$ , which are the zeros of  $H(s)$ , must lie in the left half of the  $s$ -plane. The LTI system is invertible when both  $H(s)$  and  $H_i(s)$  are stable, i.e., both the poles and zeros of  $H(s)$  should lie in the left half of the  $s$ -plane [143]. Being invertible will allow that, given any input signal, applying the system to obtain the system output and vice versa applying the inverse system to work out the input signal.

The transfer function in (7.5) and (7.6) is represented using the Laplace trans-

form and is suitable for describing the continuous-time LTI system. A continuous-time system cannot be directly processed on a computer before it is sampled at intervals, i.e., converted to a discrete-time system. The transfer function of a discrete-time LTI system is represented using the  $z$ -transform. A discrete-time LTI system whose input and output are  $X(z)$  and  $Y(z)$  respectively can have its transfer function  $H(z)$  and the inverse transfer function  $H_i(z)$  written as

$$\frac{Y(z)}{X(z)} = H(z) = \frac{b_0 + b_1z^{-1} + \cdots + b_{M-1}z^{-M+1} + b_Mz^{-M}}{a_0 + a_1z^{-1} + \cdots + a_{N-1}z^{-N+1} + a_Nz^{-N}} \quad (7.9)$$

$$H_i(z) = \frac{a_0 + a_1z^{-1} + \cdots + a_{N-1}z^{-N+1} + a_Nz^{-N}}{b_0 + b_1z^{-1} + \cdots + b_{M-1}z^{-M+1} + b_Mz^{-M}} \quad (7.10)$$

where  $a_i$ ,  $b_i$ ,  $M$  and  $N$  are parameters of the system. The discrete-time LTI system is invertible when both  $H(z)$  and  $H_i(z)$  are stable. This requires that  $M = N$  and both the poles and zeros of  $H(z)$  must lie inside the unit circle in the  $z$ -plane [143].

A continuous-time transfer function  $H(s)$  can be directly converted to the corresponding discrete-time transfer function  $H(z)$ . This is done by using a short sampling interval to make some discrete-time approximations of the continuous-time model [148]. There are different approximation methods available, e.g. zero-order hold, first-order hold, Tustin's approximation and so on. Tustin's approximation is performed by simply replacing the argument  $s$  in (7.5) by  $s'$  [148], i.e.,

$$H(z) = H(s'), \quad s' = \frac{2}{T_s} \cdot \frac{z-1}{z+1} \quad (7.11)$$

where  $T_s$  is the sampling interval of the discrete-time system. Implementing the system through the transfer function  $H(z)$  needs to use a "recurrence relation" which computes the next value of the system output based on the current and previous input values and the previous output values [145]. The "recurrence relation" can be derived from (7.9). By cross-multiplying (7.9) we obtain

$$(a_0 + a_1z^{-1} + \cdots + a_{N-1}z^{-N+1} + a_Nz^{-N})Y(z) = (b_0 + b_1z^{-1} + \cdots + b_{M-1}z^{-M+1} + b_Mz^{-M})X(z). \quad (7.12)$$

Having the inverse  $z$ -transform of (7.12) and applying the properties of  $z$ -transform,

there is

$$a_0 y_k + a_1 y_{k-1} + \cdots + a_{N-1} y_{k-N+1} + a_N y_{k-N} = b_0 x_k + b_1 x_{k-1} + \cdots + b_{M-1} x_{k-M+1} + b_M x_{k-M} \quad (7.13)$$

where  $y_i$  and  $x_i$  are the discrete-time LTI system's output and input respectively. Finally, rearranging (7.13) produces

$$y_k = [-(a_1 y_{k-1} + \cdots + a_N y_{k-N}) + b_0 x_k + \cdots + b_M x_{k-M}] / a_0. \quad (7.14)$$

where the current output  $y_k$  of the system is calculated based on the previous output values and the current and previous input values. By the “recurrence relation”, given an input, the system can be implemented through  $H(z)$  to find out the corresponding system output.

In this study, to establish transfer function models of HFCT 1 and HFCT 2 respectively, either 2nd or 3rd order of the continuous-time model  $H(s)$  in (7.5) was fitted to the measured HFCT complex transfer function data. Based on the smoothed HFCT transfer function measurement results of which magnitudes are shown in Figures 6.9, 6.11 and 6.13, the fit was carried out using the transfer function synthesizing method developed by Hassul and Shahian [149]. Procedures of the fitting involved evaluating (7.5) in the frequency domain (i.e., replacing  $s$  in (7.5) with  $j\omega$ ) and substituting into it the transfer function data at various measurement frequencies, which can generate a set of equations with  $b_i$  and  $a_i$  as unknown parameters. Solving the equations will find out the unknown parameters. A more detailed description of the fitting procedures can be found in Appendix B.

Some experience has been gained in efforts to formulate the transfer function. First, the fitting stage needs to take into account both agreement of the transfer function model with the measured HFCT transfer function and that the established transfer function model  $H(s)$  is invertible. In practice, the fit had to be carried out in different frequency ranges to optimise the agreement with the measured transfer functions. For the established  $H(s)$  to be invertible, satisfying the criteria that all of its zeros and poles lie in the left-half  $s$ -plane was always checked. Moving on to stage (b), applying the established  $H(s)$  to a current input so as to determine the HFCT's voltage output can be done by making use of the “recurrence relation” of  $H(z)$ . This will require conversions



from continuous to discrete-time transfer functions, i.e., from  $H(s)$  to  $H(z)$ . The  $H(z)$  obtained should be invertible as well, for which the requirement is that all of its zeros and poles lie inside the unit circle in the  $z$ -plane. Tustin's approximation has a capability of transforming stable continuous-time systems to stable discrete-time systems and vice versa [145]. This means that once  $H(s)$  is stable, after the conversion, the obtained  $H(z)$  will be stable. The actual conversions were performed in MATLAB (Version R2011b) where there is a built-in conversion function "c2d.m". It was found that  $H(z)$  obtained by using Tustin's approximation was always stable while those from other approximation methods like zero-order-hold (ZOH) could sometimes be unstable. Therefore, in doing the conversions, Tustin's approximation was used.

$H(s)$  was converted to  $H(z)$  for both the HFCTs. Frequency responses of the obtained  $H(z)$  are shown in Figures 7.8 and 7.9. Parameters of  $H(s)$  and  $H(z)$  are summarised in Table 7.2. It may look dubious to have some extremely small parameters for  $H(s)$ , like  $b_3 = 1.34 \times 10^{-23}$ ,  $a_3 = 3.08 \times 10^{-22}$ . However, bearing in mind that they belong to the  $s^3$  term of  $H(s)$  and when calculating the high frequency response of the transfer function, for example  $> 100$  MHz, the  $s^3$  term can have an order of  $10^{24}$  which will make  $b_3 s^3$  a reasonable value. Therefore, the extremely small parameter values of  $H(s)$  are not unusual for the investigated HFCT transfer functions.

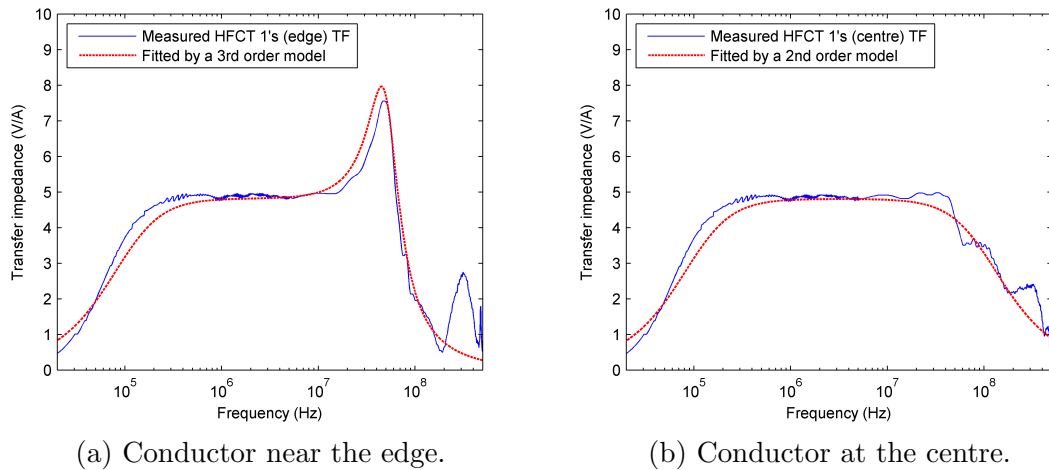


Figure 7.8: Frequency responses of HFCT 1 transfer functions with the conductor going through the HFCT aperture at different positions. Within 100 MHz, the maximum difference between the measured transfer function (TF) and the TF model is 14.4% and 15.2% in (a) and (b) respectively. Greater than 100 MHz, the TF models are approaching zero and do not agree with the measured transfer functions.

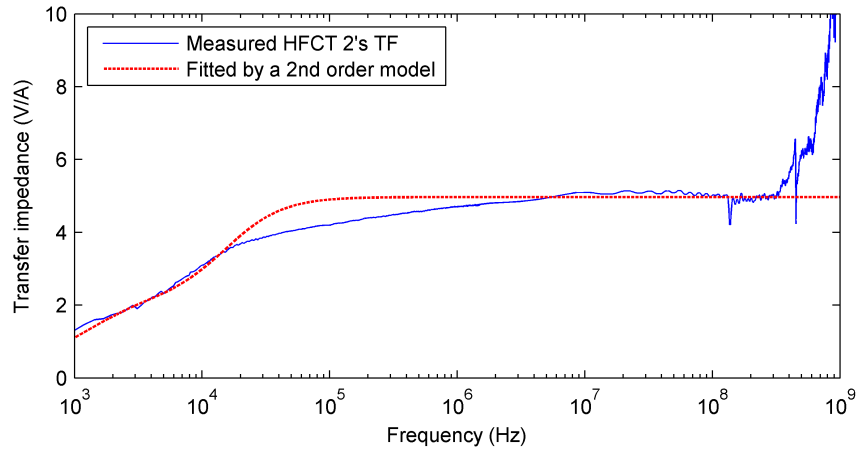


Figure 7.9: Frequency responses of HFCT 2 transfer function (TF). Within 300 MHz, an apparent disagreement between the measured TF and the 2nd order TF model is seen from 20 kHz–1 MHz, which has a maximum difference of 16.9%. Greater than 300 MHz, the disagreement is not uncommon as this part of the measurement result was not taken into account while fitting to establish the TF model.

Table 7.2: Parameters of the transfer functions  $H(s)$  and  $H(z)$  for the HFCTs.

Parameter	HFCT 1 (edge)	HFCT 1 (centre)	HFCT 2
$H(s)$	3rd order	2nd order	2nd order
$b_k$	$b_0 = 0.20$ $b_1 = 1.49 \times 10^{-4}$ $b_2 = 2.68 \times 10^{-13}$ $b_3 = 1.34 \times 10^{-23}$	$b_0 = 2.07$ $b_1 = 1.58 \times 10^{-4}$ $b_2 = 1.12 \times 10^{-15}$	$b_0 = 0.98$ $b_1 = 2.30 \times 10^{-3}$ $b_2 = 4.33 \times 10^{-8}$
$a_k$	$a_0 = 22.17$ $a_1 = 3.09 \times 10^{-5}$ $a_2 = 7.06 \times 10^{-14}$ $a_3 = 3.08 \times 10^{-22}$	$a_0 = 23.92$ $a_1 = 3.28 \times 10^{-5}$ $a_2 = 5.61 \times 10^{-14}$	$a_0 = 11.09$ $a_1 = 1.10 \times 10^{-3}$ $a_2 = 8.71 \times 10^{-9}$
$H(z)$	$H(s)$ converted to $H(z)$		
$b_k$	$b_0 = 0.087$ $b_1 = -0.17$ $b_2 = 0.085$ $b_3 = -0.0012$	$b_0 = 0.16$ $b_1 = -0.039$ $b_2 = -0.12$	$b_0 = 4.97$ $b_1 = -9.94$ $b_2 = 4.97$
$a_k$	$a_0 = 1.00$ $a_1 = -2.98$ $a_2 = 2.95$ $a_3 = -0.98$	$a_0 = 1.00$ $a_1 = -1.94$ $a_2 = 0.94$	$a_0 = 1.00$ $a_1 = -2.00$ $a_2 = 1.00$

For HFCT 1, a 3rd order model had to be used for the transfer function measured with the conductor near the edge of the HFCT aperture while a 2nd order model was used for that measured with the conductor at the aperture centre. Using the 3rd model, it was possible to characterise the 50 MHz peak present in the “near the edge” transfer function. Figures 7.8 shows that both the 3rd and 2nd order models are generally like band-pass filters because their frequency responses approach zero towards either low or high frequencies. In either Figures 7.8a or 7.8b, the difference between the measurement result and the transfer function model becomes more apparent at frequencies  $> 100$  MHz. For HFCT 2, Figure 7.9 shows that the transfer function model is like a high-pass filter. There are appreciable differences between the measured transfer function and the transfer function model in the frequency ranges of 20 kHz–1 MHz and  $> 300$  MHz. Figures 7.8 and 7.9 suggest that the transfer function models do not agree with the measurement results at some frequencies, but they can still be seen as effective in representing the HFCT transfer functions given the following reasons: (a) for both HFCTs, over the frequency ranges of interest, general agreements between the measured transfer functions and the established transfer function models were achieved; (b) for HFCT 2, despite the fact that the measurement was subject to more uncertainties in the high frequency range of  $> 300$  MHz, the transfer function model diverting away from the measurement result is, however, consistent with HFCT 2 specification in Table 6.1. Since the measured HFCT transfer functions can be represented properly by the transfer function models, it is expected that both method 1) (FFT) and method 2) (using transfer function models) will be effective in combining any current input with the HFCT transfer functions to give out the corresponding HFCT's voltage output.

### 7.3.2 Applying HFCT Transfer Functions to Gaussian Pulses

Effectiveness of the combination method using FFT and the one based on the transfer function model of an LTI system was evaluated using Gaussian pulses of different pulse widths. Figure 7.10 shows a Gaussian pulse with a full width at half magnitude (FWHM) of 10 ns and a -3 dB bandwidth of 31.2 MHz. The pulse was used as the current input into HFCT 1. The “near the edge” and “at the centre” transfer functions were respectively applied to convert the pulse to HFCT 1's voltage output. Figures 7.11 and 7.12 show the output waveform and FFT of the output. For either of HFCT 1 transfer functions used, FWHM of the first

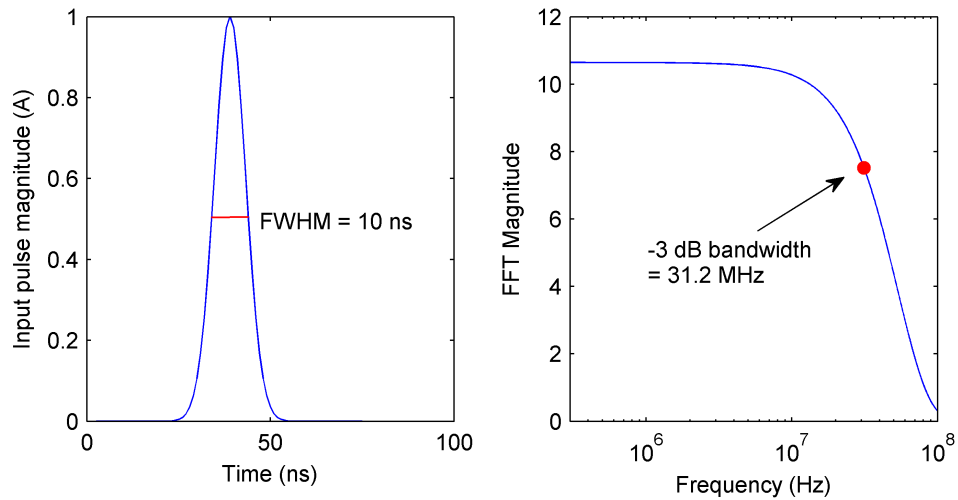
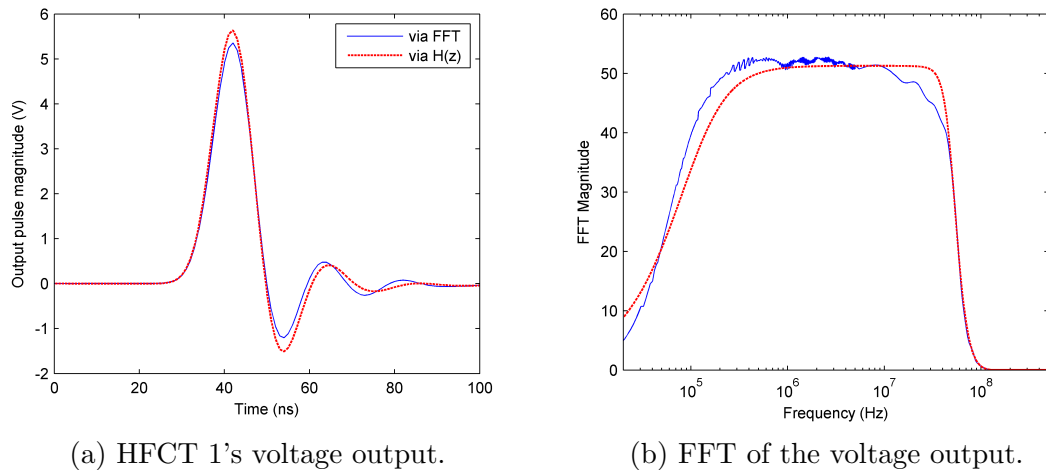


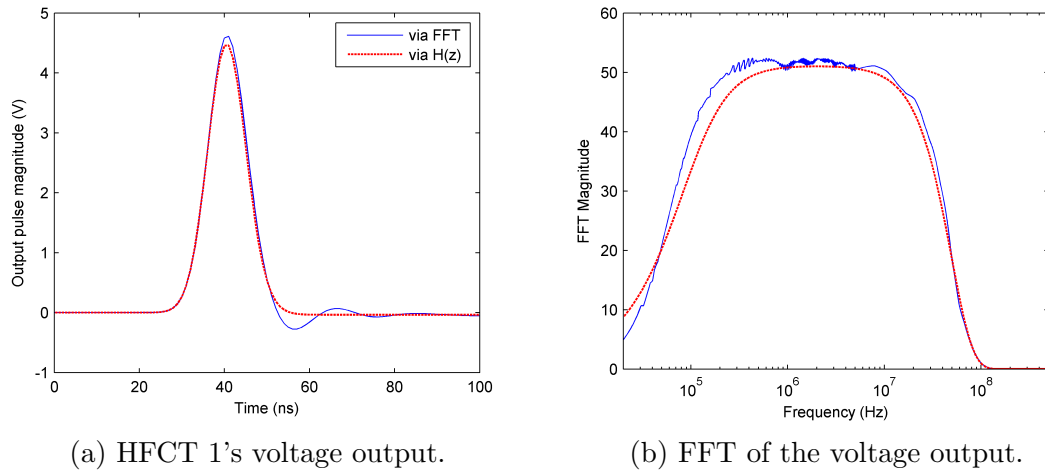
Figure 7.10: A Gaussian pulse with a 10 ns full width at half magnitude (FWHM). Sampling rate was 1 GS/s. The pulse was used as current input of HFCT 1 in the effectiveness evaluation of both the combination methods.



(a) HFCT 1's voltage output.

(b) FFT of the voltage output.

Figure 7.11: HFCT 1's voltage output obtained by combining the current input with the “near the edge” transfer function via both FFT and  $H(z)$ . FWHM of the first pulse is 10 ns same to the input pulse while overshoots are following thereafter. The peak values of the voltage output by the two methods are 5.4 V and 5.6 V respectively.



(a) HFCT 1's voltage output.

(b) FFT of the voltage output.

Figure 7.12: HFCT 1's voltage output obtained by combining the current input with the “at the centre” transfer function via both FFT and  $H(z)$ . FWHM of the first pulse is 10 ns. There are smaller overshoots comparing with those obtained using the “near the edge” transfer function. The peak values of the voltage output by the two methods are 4.6 V and 4.4 V respectively.

pulse in the obtained voltage output was 10 ns which is the same as that of the input pulse. Maximum magnitudes of the output were generally the maximum magnitude of the input pulse 1 A multiplied by the HFCT transfer impedance in specification, i.e., 5 V/A. The results would be expected as the -3 dB bandwidth 31.2 MHz of the input pulse was well below the upper cutoff frequency 70 MHz of HFCT 1. Overshoots were introduced after the first pulse. The overshoots were larger in Figure 7.11, which was caused by the 50 MHz peak in the “near the edge” transfer function. The 50 MHz peak also caused the output magnitudes in Figure 7.11 to be higher than those in Figure 7.12. In either Figure 7.11 or 7.12, there were some differences in the waveforms obtained by the different combination methods. This was attributed to the differences between the measured transfer functions and the  $H(z)$  represented transfer functions, as can be seen in Figure 7.8.

HFCT 2 transfer function was also applied to the pulse. Figure 7.13 shows the computed HFCT 2's voltage output. Compared with the output of HFCT 1, a better agreement between the results from the two combination methods was attained. The agreement may not be expected if looking at Figure 7.13b where the FFT results do not seem to agree with each other in the frequency range of 20 kHz–1 MHz. This can be explained by considering that the trace in 7.13a lasts for 100 ns and according to (6.8), 10 MHz would be the lowest revolvable

frequency of the trace. In other words, differences caused by the transfer function at frequencies  $< 10$  MHz will not be notified in the 100 ns trace.

The evaluation moved on to apply the HFCT transfer functions to a 1 ns Gaussian pulse. Figure 7.14 shows the 1 ns pulse and its FFT. With the pulse used as the current input into the HFCTs, Figure 7.15 shows the HFCTs' voltage output obtained by the FFT and the  $H(z)$  methods respectively. Apparent

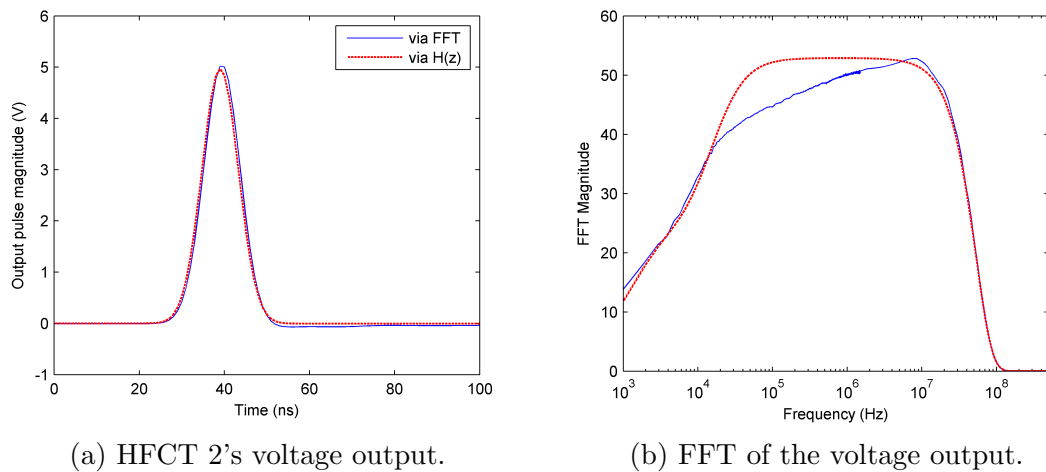


Figure 7.13: HFCT 2's voltage output. In FFT results of the voltage output, there exists an apparent disagreement in the frequency range of 20 kHz–1 MHz, which is subject to the differences between the measured and  $H(z)$  represented transfer functions, as shown in Figure 7.9.

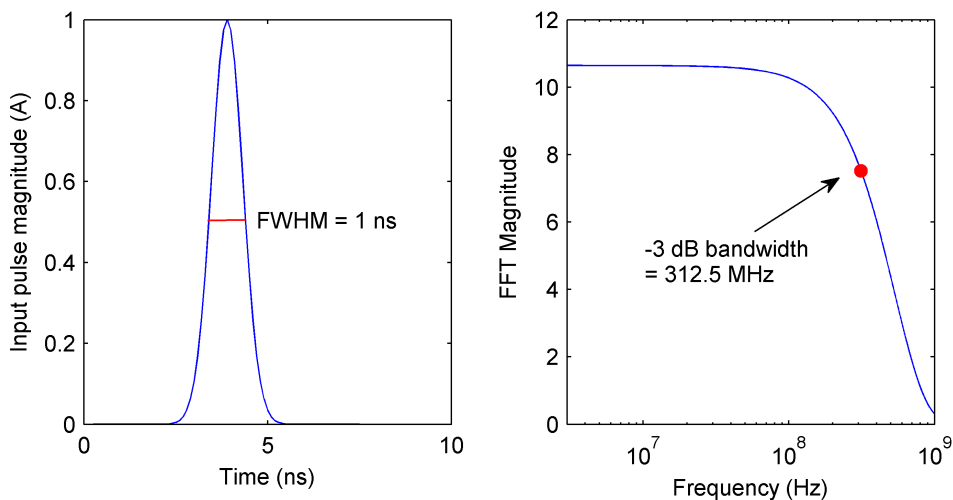


Figure 7.14: A Gaussian pulse with a 1 ns full width at half magnitude (FWHM). Sampling rate was 10 GS/s.

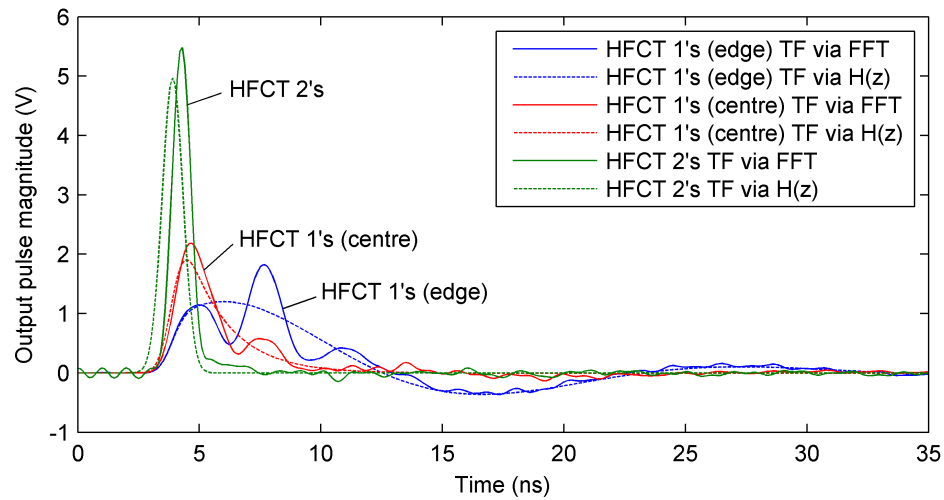


Figure 7.15: HFCTs' voltage output obtained by applying each HFCT transfer function (TF) via FFT and  $H(z)$  respectively. For those obtained via FFT, HFCT 2's output is 1 ns in FWHM and 5.5 V at maximum. Both HFCT 1 transfer functions have a 2 ns FWHM for the first pulse in the output. Magnitudes at maximum are 1.8 V and 2.2 V for the “near the edge” TF and the “at the centre” TF respectively. The output generated via  $H(z)$  is generally lower at maximums and does not include those multiple peaks in the FFT obtained output.

differences were observed between the voltage output from the different HFCT transfer functions. While HFCT 2 was able to maintain the output to input magnitude ratio of 5 V/A and the FWHM of 1 ns, HFCT 1's output has shown appreciable magnitude decrease and pulse width increase if compared with the output from the 10 ns pulse input. This can be explained by the fact that the 1 ns pulse had a -3 dB bandwidth of 312.5 MHz far beyond 70 MHz, i.e., the upper cutoff frequency of HFCT 1. There were also differences, for each HFCT transfer function, between the output obtained via FFT and  $H(z)$ . Generally, the  $H(z)$  produced output was lower in magnitude and “smoother” in waveform. In particular, for HFCT 2 transfer function, the output via  $H(z)$  came earlier than that via FFT. For the “near the edge” HFCT 1 transfer function, the output via  $H(z)$  didn't show the second peak that was even higher than the first peak in the output via FFT. These differences would be expected with reference to Figures 7.8 and 7.9 which show that at the high frequencies, e.g., > 200 MHz for HFCT 1 and > 300 MHz for HFCT 2, agreements between the measured and the  $H(z)$  represented transfer functions were largely poor. It can be envisaged that, if applied to narrower pulses, more differences will be expected between the

HFCT voltage output obtained via the different combination methods.

Applying the HFCT transfer functions using both the FFT and the  $H(z)$  methods to Gaussian pulses of various pulse widths is illustrated in Figure 7.16. These pulses were converted to the HFCTs' voltage output. The output from the different combination methods was compared in terms of the pulse width (FWHM) and the maximum magnitude. Differences in percentage between the pulse widths and between the maximum magnitudes are shown in Figures 7.17a and 7.17b respectively. Both seem to converge with the increase of the input pulse widths. When the input pulse width was  $\geq 5$  ns, the output width differences fell within 5% and the maximum magnitude differences within 10%. It appears that a pulse width of 1 ns is a limit below which the two methods are more unlikely to produce similar output. This is particularly true for the case of the “near the edge” HFCT 1 transfer function and results from the fact that it was not possible to make the transfer function model agree with the measured “near the edge” transfer function at the high frequencies  $> 200$  MHz.

The above discussion regarding working out an HFCT's voltage output can be summarised as follows, (a) either the combination method using FFT or the one using  $H(z)$  is able to give out the HFCT's voltage output according to their represented transfer functions; (b) the two methods shall give out similar output if applied to an input pulse with a pulse width (FWHM)  $\geq 2$  ns (or a -3 dB

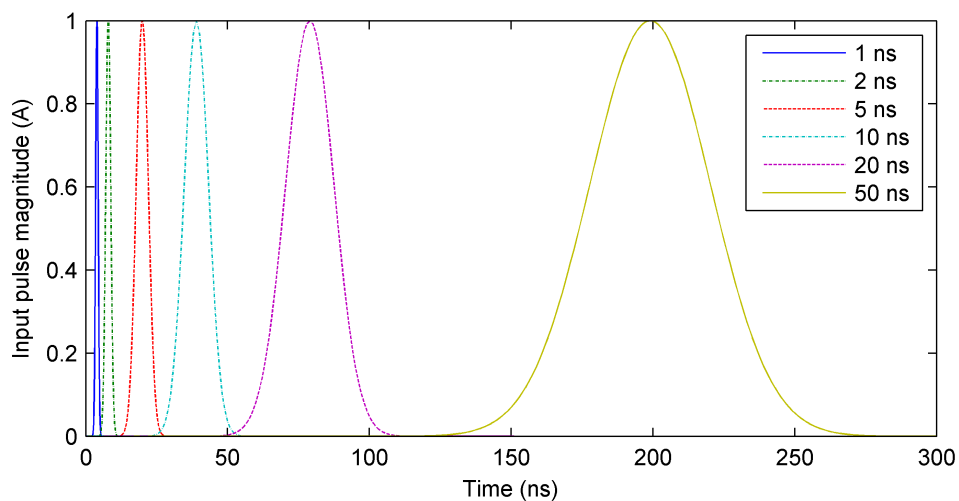


Figure 7.16: Gaussian pulses of various pulse widths. The pulse width (i.e., FWHM) and the -3 dB bandwidth of each pulse are: 1 ns, 312.5 MHz; 2 ns, 156.2 MHz; 5 ns, 62.9 MHz; 10 ns, 31.2 MHz; 20 ns, 15.6 MHz; 50 ns, 6.3 MHz.



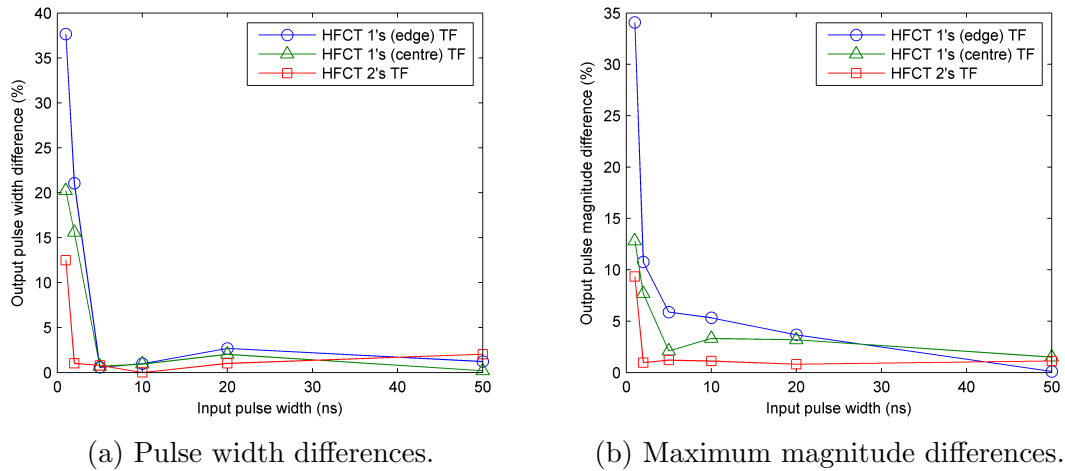


Figure 7.17: Differences between the output obtained via FFT and  $H(z)$ . The differences observed for the “near the edge” HFCT 1 transfer function (TF) are generally the biggest and subject to the most changes with the increase of the input pulse widths while those for HFCT 2 transfer function (TF) have the least changes.

bandwidth  $< 156.2$  MHz). Hence the question becomes one of which method should be used. The FFT method is able to be applied for any input that is sampled no higher than the sampling rate used to measure the HFCT transfer functions. The measurement sampling rate used was 10 GS/s in this work. For any input sampled with a sampling rate  $> 10$  GS/s, the FFT method will not work. Once applicable, the FFT method should be the most accurate in producing the HFCT's voltage output from any current input. The  $H(z)$  method will adapt to the current input sampled with any sampling rate. In many cases of XFDTD generated results, the sampling rate is far higher than 10 GS/s, where if applying an HFCT transfer function is required, the  $H(z)$  method can be used. One problem with the  $H(z)$  method is that, if the transfer function model  $H(s)$  is established as a band-pass filter like the ones for HFCT 1, the subsequent  $H(z)$  will be a band-pass filter no matter what the actual sampling rate is. For example, an input sampled with 10 MS/s will have its frequency spectrum a highest frequency of 5 MHz. If either of HFCT 1 transfer functions is to be used on the input, the transfer function should look like a high-pass filter instead of a band-pass one. In practice,  $H(z)$  created from  $H(s)$  using the 10 MS/s sampling rate will still be band-pass except that the upper cut-off frequency of the band-pass filter will be pushed very close to the highest frequency, i.e., 5 MHz. The problem, however, does not influence the output a lot in various tests carried out.

This can be explained in that the spectrum of the input usually has very small components close to the highest frequency so that the transfer function at these frequencies will not make a lot differences in the output.

## 7.4 Framework for Modelling of HFCT-based PD Detection in Cables

A hybrid approach to modelling of PD measurement for high voltage cables using HFCTs was developed. The approach is based on using FDTD modelling to investigate coupling of PD source currents onto the cable outer conductor and the methods described above to measure currents flowing on the outer conductor and work out an HFCT's voltage output while being input by those currents. Figure 7.18 illustrates this approach, which includes five steps:

1) "Original" PD current pulses were measured by the "direct PD measurement" method [25]. A needle was inserted through (but kept isolated from) the cable outer conductor to create a defect within a cable sample. The end of the needle was connected with a coaxial cable going to an oscilloscope using a  $50\ \Omega$  input impedance. The cable was energised and PD current pulses resulting from the needle (like a protrusion defect extended from the outer conductor) were recorded. Details of the measurement setup used and the recorded PD pulses will

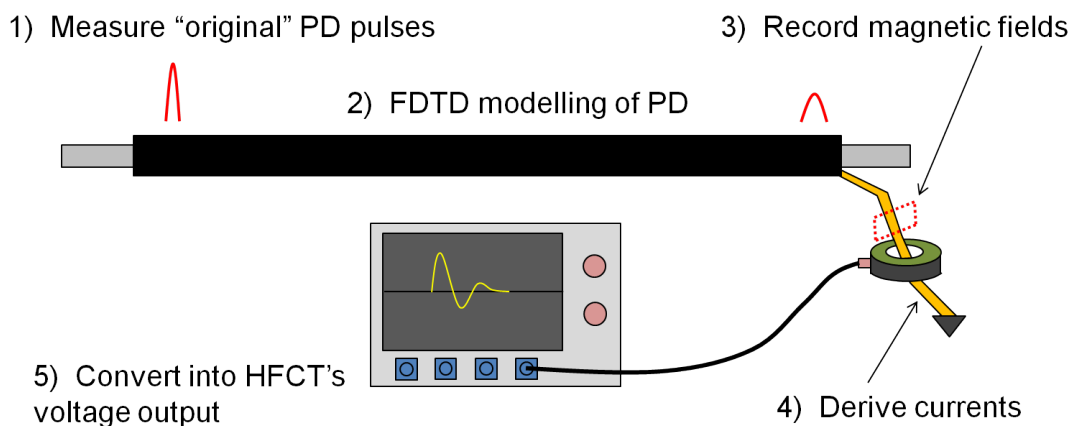


Figure 7.18: Framework for modelling of PD in a high voltage cable. Step 1) is by experiments. Step 2)–3) is FDTD modelling in XFDTD. Step 4)–5) involves measurement of the HFCT complex transfer function and post processing to work out its voltage output.

be shown later.

2) An FDTD cable model was created and one of the recorded PD waveforms from step 1) was used to define the excitation current as a data file within the model. Simulations were then carried out to characterise the effects of attenuation and distortion caused by coupling of PD currents from the PD source location to the cable outer conductor.

3) According to the described method of measuring currents in XFDTD, a sensor loop was created out of point sensors around the outer conductor of the FDTD cable model. The point sensor was used to record magnetic fields at a certain points of a model.

4) The recorded magnetic fields from these point sensors were used to derive currents flowing on the outer conductor by using Ampere's law. It should be noted that the correct vector component of  $\mathbf{H}$  is used at each point so that the numerical integration does sum the contributions to  $\mathbf{H}$  around a closed loop.

5) The HFCT complex transfer function was obtained by simultaneously measuring input and output of the HFCT and then dividing FFT of the output by FFT of the input. Step and pulse responses were measured respectively to construct the low frequency and high frequency parts of the transfer function. According to the above discussion of working out an HFCT's voltage output, the method of using the transfer function models was chosen for converting the current data derived at step 4) to determine the time-domain PD pulse output voltage of the HFCT.

For the step 1), measuring "original" PD pulses was courtesy of a colleague also working on this project [25]. A diagram of the measurement setup used is shown in Figure 7.19. The actual connection is shown in Figure 7.20. The experiment was conducted on a 1.5 m long 11 kV EPR cable sample which has a same structure as that of cable sample 1 (EPR) but is slightly larger in dimensions. Proper terminations were installed on both ends of the cable sample so as to avoid termination corona discharges. A potential protrusion defect was introduced into the cable insulation by using a hypodermic needle. The centre of a 50  $\Omega$  coaxial cable was connected with the needle and the other end of the coaxial cable was connected to the 50  $\Omega$  input of a LeCroy oscilloscope. Since it was a direct connection between the energised sample and the oscilloscope, there was a potential risk of damage in the event of breakdown. Therefore, energising at lower voltages like 5 kV and 6 kV was performed. Figures 7.21 and 7.22 show

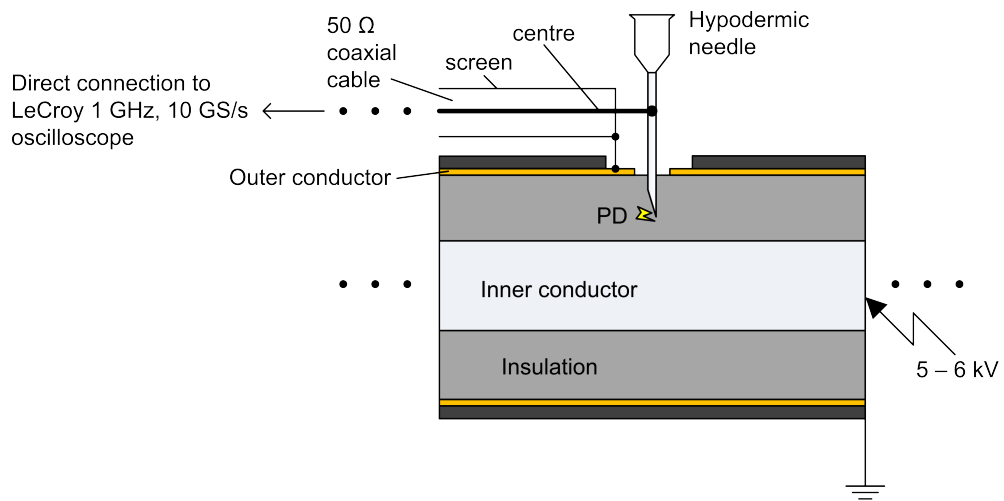


Figure 7.19: Diagram of the “direct PD measurement”. A hypodermic needle was used to create a defect within the cable insulation. Centre and outer conductors of a 50  $\Omega$  coaxial cable were connected with the needle and the cable outer conductor respectively.

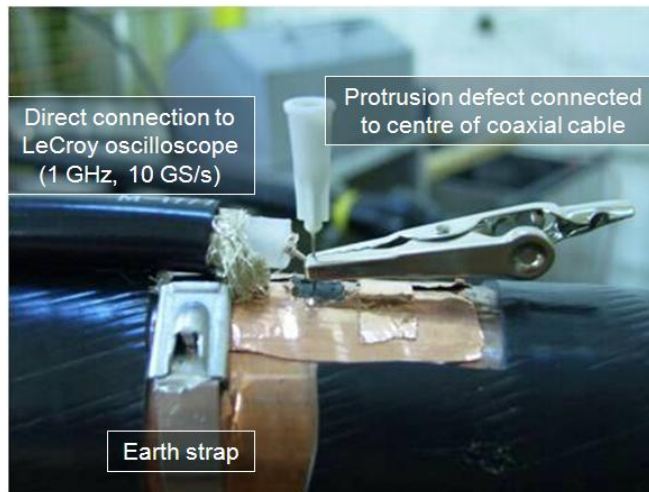


Figure 7.20: Actual connection of the “direct PD measurement”.

the recorded traces consisting of one single pulse and multiple pulses respectively. The single pulse traces can represent an individual PD event in the FDTD cable model while the multiple pulses traces can be useful in simulating multiple PD events taking place at the same time.

An FDTD cable model was created for demonstrating the proposed modelling framework. The model had dimensions which were same as those of the basic cable model shown in Figure 7.4 but some details in the model were changed. A

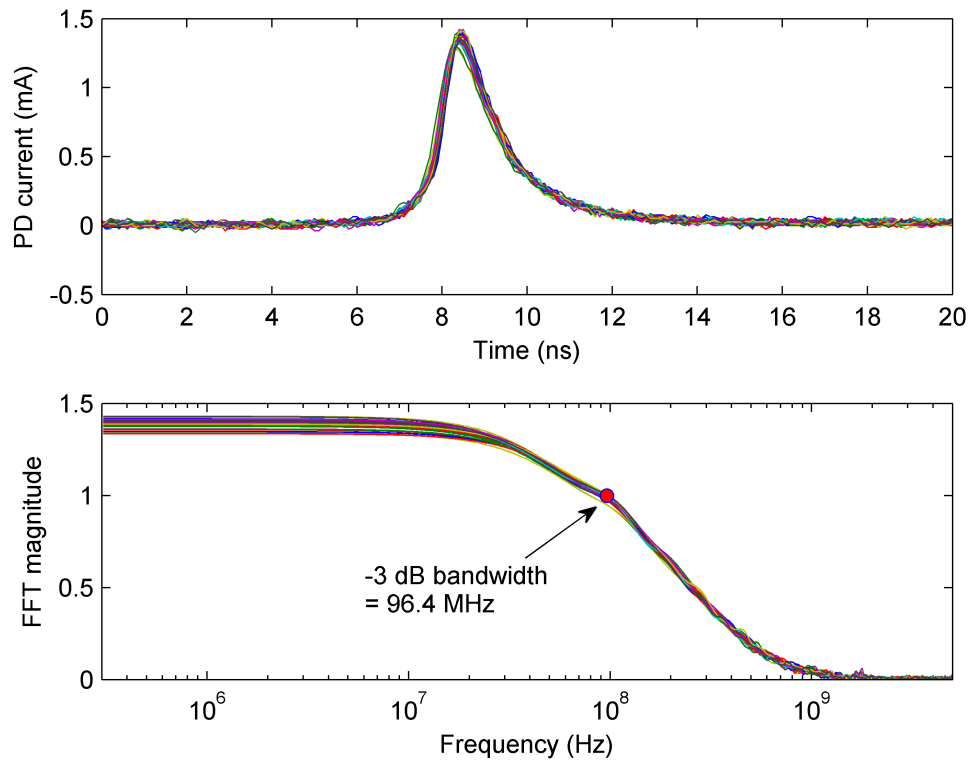


Figure 7.21: Single positive pulses recorded by “direct PD measurement” and their FFT. Average rise time of the pulses is 0.94 ns. Average full width at half magnitude (FWHM) is 1.3 ns. Average -3 dB bandwidth is 96.4 MHz.

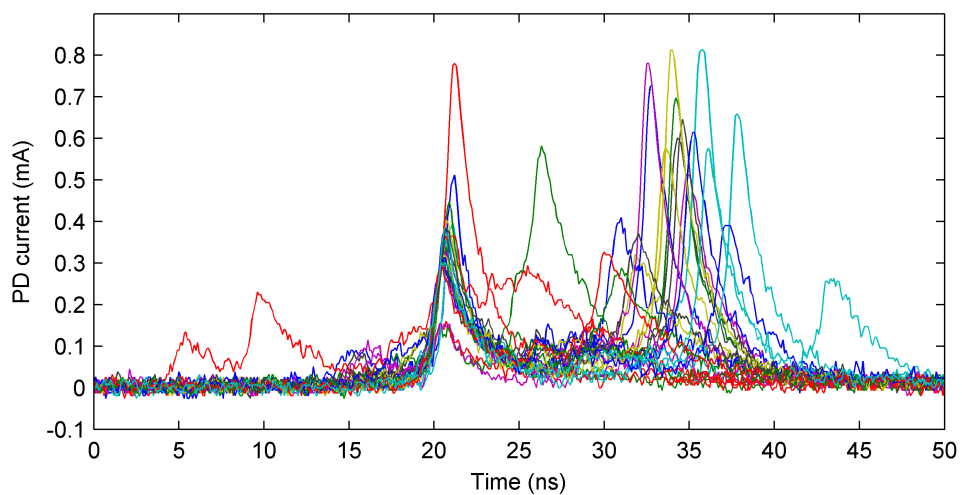


Figure 7.22: Traces consisting of multiple pulses recorded by “direct PD measurement”.

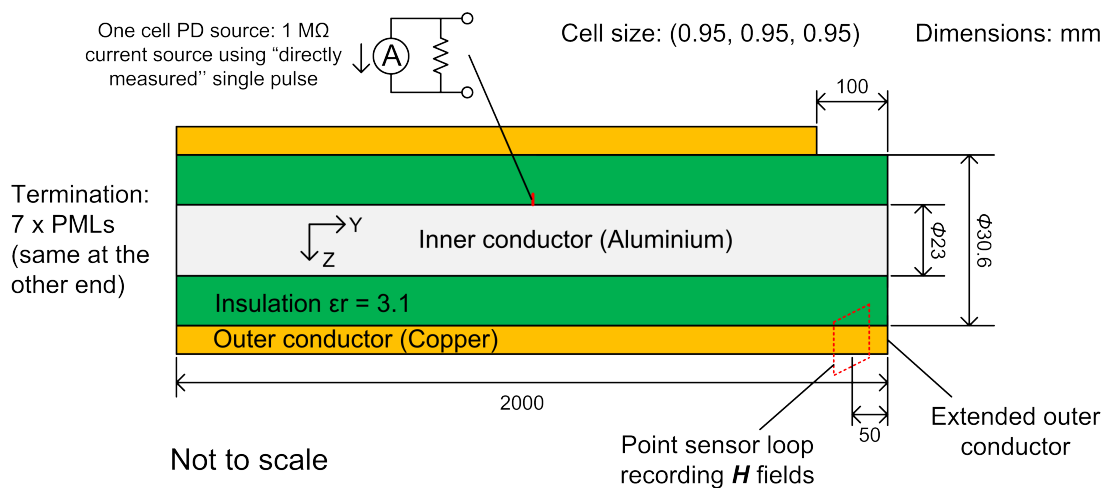


Figure 7.23: Diagram of the FDTD cable model for demonstrating the modeling framework. A sensor loop (red box around the extended outer conductor) was created to record magnetic fields. A PD source represented by a  $1\text{ M}\Omega$  current source was put on the inner conductor in the middle of the cable. Terminations at both cable ends were made using seven perfect match layers ( $7\times\text{PMLs}$ ).

diagram of the created model is shown in Figure 7.23. The inner conductor and the insulation were extended for a total cable length of 2 m while the outer conductor was curtailed by 0.1 m at one end. Instead, an extended outer conductor was made for the remaining 0.1 m. As required by the proposed method of measuring currents in XFDTD, a close loop consisting of point sensors was created on the extended outer conductor to record magnetic fields. A PD source represented by a  $1\text{ M}\Omega$  current source was defined in XFDTD on the inner conductor in the middle of the cable model. One of the single pulse traces shown in Figure 7.21 was used as the PD source current waveform. Both ends of the cable model were terminated using seven perfect match layers (PMLs). This works in XFDTD to remove reflections caused by open circuits at the cable ends. After the simulation, magnetic fields recorded by the point sensor loop were integrated to obtain the current flowing on the extended outer conductor. Using the "near the edge" HFCT 1 transfer function, converting to the HFCT's voltage output was carried out using the established transfer function model.

Piecing together the PD source current, the outer conductor current, the HFCT transfer function and the HFCT's voltage output, an illustration of the whole modeling diagram shown in Figure 7.18 was made and the various stages are illustrated in Figure 7.24.

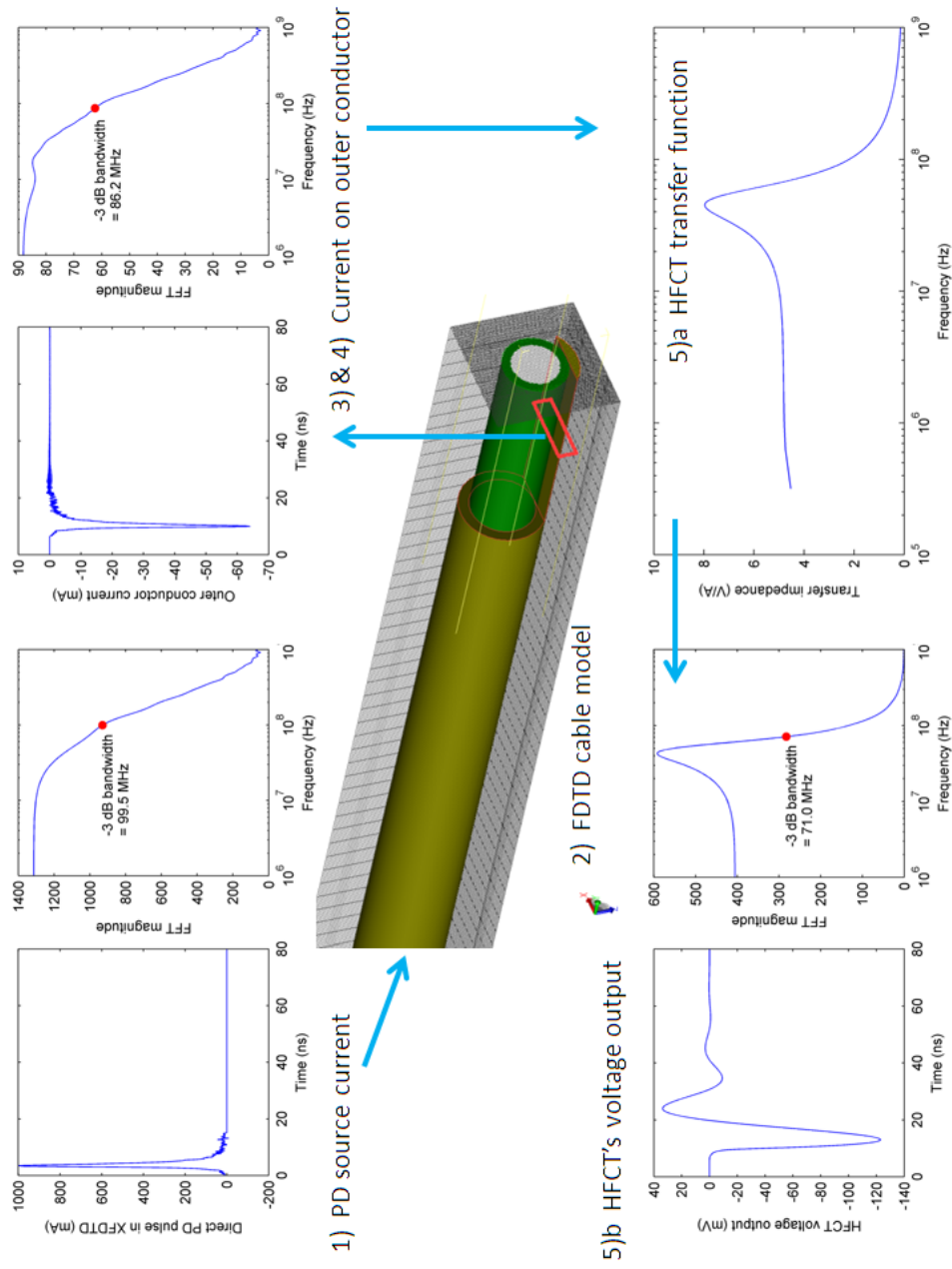


Figure 7.24: Illustration of the whole modeling process. The current pulse was derived by numeric integration of magnetic fields recorded by the closed sensor loop. The “near the edge” HFCT 1 transfer function model was used to convert the current pulse. 5)a) shows magnitude of the transfer function model. 5)b) shows the obtained HFCT’s voltage output.

Figure 7.24 shows that the derived current pulse on the extended outer conductor had a negative polarity while a positive current pulse is supposed to be flowing on the inner conductor. This was a result of (referring to Figure 7.23) the current source with the positive direction flowing into the inner conductor. The obtained HFCT's voltage output had some oscillation after the first pulse. Full width at half magnitude (FWHM) of the first pulse was widened compared to that of the current pulse on the outer conductor because of the limited HFCT bandwidth. Actually, the -3 dB bandwidth of the pulse was gradually decreasing from the PD source to the HFCT's voltage output. The frequency response of the HFCT transfer function model shown in the illustration seems including only the high frequency part of that shown in Figure 7.8a. This was because of the length of the current pulse trace being used to combine with the HFCT transfer function. The lowest frequency involved in the combination will be confined to the value calculated by (6.8), i.e., inversely proportional to the trace length (or acquisition time). Padding the trace with zeros to a longer length in the FFT processing will enable reaching lower frequencies but will require more and more PC memory. For example, the current trace was padded to  $3.1568 \mu s$  before combining with the HFCT transfer function and thus the lowest frequency involved was 316.8 kHz. The combination method using the transfer function model instead of FFT had to be used since the sampling rate used by the FDTD simulation was so high that, as discussed at end of the last section, the FFT method will not work. The time-step of the FDTD simulation was 1.5053 ps which corresponds to a sampling rate about 664 GS/s while the sampling rate used to determine the HFCT transfer functions was 10 GS/s.

The illustration has shown that how the proposed modelling framework will work on an "original" PD current pulse. The objective is to simulate the practice of HFCT-based PD detection in high voltage cables. The framework is aimed at investigating such effects like coupling of PD currents from a PD source location onto a cable outer conductor and thereafter detection by using an HFCT. To make the modelling as accurate as possible in predicting the reality, many contributions from experiments are needed, for example, "direct PD measurement" of "original" pulses, measurement of semicon properties and measurement of HFCT transfer functions. Effects resulting from PD propagation along the cable are not dealt with by the framework for the following reasons: (a) the FDTD method being a time domain method has a limited capability in simulating frequency-dependent



materials (e.g., semicon layers); (b) investigating the propagation caused effects would often require modelling of long cables, e.g., 100s to 1000s of m, which is not feasible regarding memory requirements as well as computation loads that will be involved. Nevertheless, the effects can be represented by other approaches. For example, the analytical method proposed by Oussalah et al. [26], which is based on the transmission line theory and requires measuring the cable propagation constant (5.15). By making use of the measured propagation constant, the propagation caused attenuation and distortion to the PD pulse can be calculated for any cable length. In fact, considering the cable as a two-port network, the transfer function of any length of the cable can be obtained based on the propagation constant. Applying the numerical transfer function to an input pulse will achieve the same thing as that done by the analytical method proposed by Oussalah et al. In other words, if apart from the effects from the PD coupling process and the HFCTs, the propagation caused effects on a PD pulse are to be included, provided that the cable propagation constant is obtained, either the FFT or the  $H(z)$  transfer function method discussed above can be used to account for the effects.

## 7.5 Conclusions

In order to measure currents on the conductor within an FDTD model created using XFDTD, a method based on recording magnetic fields around the conductor and applying Ampere's law to derive the currents was developed. The method was evaluated through deriving currents in two FDTD models, i.e., a basic circuit model and a basic cable model. The derived currents were checked against equivalent circuit calculation, charge conservation, and those currents recorded by a resistor component in XFDTD and the results show the efficiency of the developed method.

To the end of converting PD currents into an HFCT's voltage output, one method is by combining FFT of the currents with the HFCT transfer function and then performing an inverse FFT of the combination to find out the voltage output. An alternative approach based on the transfer function model of an LTI system was described and the procedures involved in obtaining the transfer function model  $H(z)$  according to the measured HFCT transfer function were presented. By applying the HFCT transfer functions via both the FFT and the

$H(z)$  methods to Gaussian pulses of various pulse widths, the results suggest that both methods produce similar output for those current input that has a pulse width  $\geq 2$  ns (or a -3 dB bandwidth  $< 156.2$  MHz).

The FFT method is easy to use and is regarded as being more accurate. However, its effectiveness is limited to those cases where the current input was sampled with a sampling rate not higher than the sampling rate used to obtain the HFCT transfer functions. The  $H(z)$  method did not seem to have this limitation and works on any current input. While different sampling rates may not be a problem in laboratory where both the HFCT transfer function and the currents can be measured using the same equipment with the same sampling rate, it is indeed a problem if the measured HFCT transfer function is to be combined with those simulated currents from FDTD modelling. The time-step (reciprocal of the sampling rate) of FDTD modelling is determined by the FDTD cell size. For the FDTD cable models in this work, the time-step is frequently a few ps or even shorter (i.e., sampling rate of 100s of GS/s or higher), which is far higher than those commonly used sampling rates in laboratory. In this case, only the  $H(z)$  method was found being able to produce the voltage output and the FFT method would fail to give out any output.

A hybrid framework for modelling of HFCT-based PD detection in cables has been proposed. Details of each step in the framework were discussed and, furthermore, an FDTD cable model with a PD source within the insulation was created to demonstrate effectiveness of the framework. Although the processes like PD excitation, propagation and detection are all included in the modelling framework, it was summarised that the framework is more likely to be used to investigate how PD currents are coupled onto a cable outer conductor and subsequently the effect of an HFCT in coupling with the PD currents. The reason is that the FDTD cable model is usually limited to a few meters in length by commonly available PC resources, whereas the propagation caused effects may be significant only if the propagated distance becomes 100 meters or longer. FDTD modelling of such a long cable is not currently practical. Instead, the propagation caused effect can be better dealt with by using, for example, the cable propagation constant and transmission line equations.

# Chapter 8

## Parametric Study of PD Measurement for 11 kV Cables

### 8.1 Overview of the Study

Two cable models were created in XFDTD according to the cable properties defined in Chapter 5 and by following the practical implementation guidance summarised in Chapter 3. Modelling of TDR measurement was carried out to obtain the transfer function of each cable model. By comparing the simulated transfer function to that obtained through the analytical method, the accuracy of each cable model in characterising high frequency properties of the cable was evaluated. Using the same cable models, a parametric study was then carried out to investigate induced current pulses on each cable's outer conductor for different PD sources. Two scenarios were evaluated, in which PD source sizes and cross-sectional positions were varied. Simulations were carried out for each PD source specification. Current pulses induced on the cable outer conductor were recorded and magnitudes of the pulses were plotted against the source variations to suggest how the variations caused effects on the outer conductor (or cable earth conductor) currents. The parametric study shows potential for determining coupling sensitivity between PD source currents and the corresponding PD currents on a cable earth conductor.

## 8.2 Modelling of TDR Measurement

FDTD cable models were created following the same procedures outlined in Chapter 3. For example, Figure 8.1 shows an axial cross-sectional diagram of the FDTD model for cable sample 2 (XLPE). The inner and outer conductors of the model were respectively assigned with conductivities of aluminium and copper, i.e.,  $3.54 \times 10^7$  S/m and  $5.8 \times 10^7$  S/m. The skin effect was not able to be considered (refer to Section 3.5 for explanation). The XLPE insulation was assigned a relative dielectric constant of 2.3 and 0 S/m conductivity. The loss caused by the insulation being non-ideal dielectric was unable to be included (refer to Section 3.5 for explanation). The semicon layers were created using the Debye medium in XFDTD. A 3 pole Debye medium was used with parameter values taken from Table 4.1. The parameter values of  $\sigma_{dc}$ ,  $\epsilon_{\infty}$ ,  $\epsilon_{s1}$ ,  $\epsilon_{s2}$  and  $\epsilon_{s3}$  were all multiplied by 2 for the inner semicon and 0.65 for the outer semicon. This was aimed at getting the model transfer function to fit the cable transfer function obtained from the TDR measurement. Actually, the same changes had to be made in order to make the cable attenuation calculated using the analytical method fit better with the

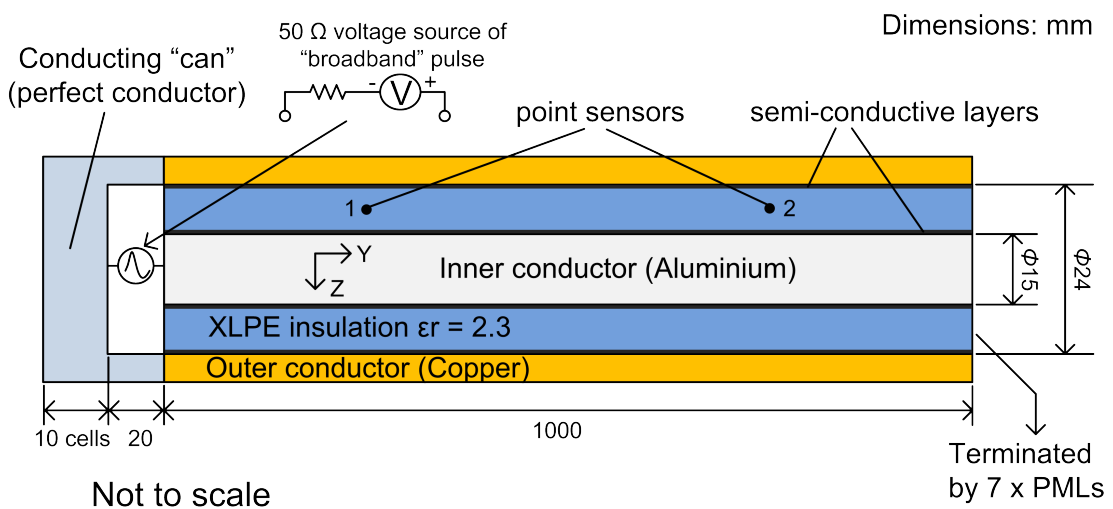


Figure 8.1: Axial cross-section of the FDTD model of cable sample 2 (XLPE). Both inner and outer semicon layers were defined by the 3 pole Debye medium in XFDTD. Two point sensors 1 and 2 axially spaced for some distance were put within the insulation to record electromagnetic fields at the corresponding point. The boundary conditions were made by 7xPMLs. In order to carry out modelling of the TDR measurement, one end of the cable was made the TDR input module. The other end of the cable and was terminated by 7xPMLs.

measurement observations (Figures 5.20 and 5.21). The same procedures were followed to create an FDTD cable model of cable sample 1 (EPR).

To evaluate the accuracy of the created FDTD cable models and the convergence of the selected FDTD parameters, modelling of the TDR measurement on the cables were performed. Figure 8.1 shows that the “conducting can” was used as the TDR input module in the model. The TDR source was simulated using a  $50 \Omega$  voltage source with the waveform of the “broadband” pulse. The “broadband” pulse is a specific waveform definition in XFDTD that is a Gaussian pulse with a bandwidth able to cover the highest frequency content possible for the specific FDTD space [107]. The highest possible frequency is subject to the maximum cell dimension  $L_{max}$  in meters. For example, a cell size of  $(\Delta x, \Delta y, \Delta z) = (0.1, 1.0, 0.1)$  mm has  $L_{max} = \Delta y = 1.0 \times 10^{-3}$  m. The highest possible frequency can be calculated by  $f_{max} = c/(10 \times L_{max})$  where  $c$  is the speed of light in free space, i.e.,  $3 \times 10^8$  m/s, and thus  $f_{max} = 30$  GHz. The frequency response of the “broadband” pulse has less than 10 dB attenuation at the highest frequency  $f_{max}$ . Therefore, with electromagnetic fields recorded by both point sensors, it is possible to work out the cable model’s predicted propagation constant  $\gamma_c(\omega)$  up to  $f_{max}$ . The electromagnetic fields at the two points,  $EM_1$  and  $EM_2$ , are related by

$$\text{FFT}[EM_2] = \text{FFT}[EM_1] \times e^{-\gamma_c(\omega)(L_2-L_1)} \quad (8.1)$$

where  $L_1$  and  $L_2$  are axial distances from the sensors 1 and 2 to the TDR input respectively. In both the created cable models, values of  $L_1 = 0.1$  m and  $L_2 = 0.9$  m were used.

Non-uniform cell sizes were applied to the cable models by following the summaries of selecting FDTD parameters in Chapter 3. For both cable models, the cross-sectional cell size was made  $\Delta x = \Delta z$ . The largest possible cross-sectional size was subject to the thinnest layer on the cable cross-section. Referring to the cable dimensions in Table 5.1, 0.3 mm and 0.4 mm were the largest possible cross-sectional cell sizes for cable samples 1 and 2 respectively. The axial cell size  $\Delta y$  was selected relatively independently of the cross-sectional size. Various cell sizes were applied to both the cable models in this way: 1) various cross-sectional cell sizes while keeping the axial cell size the same, starting from the largest possible cross-sectional cell size and then halving the size consecutively; 2) various axial cell sizes while keeping the cross-sectional cell size the same, starting from

a selected size and then halving the size consecutively.

For each cell size, the FDTD simulation was carried out requesting a result of a sufficient length of time so that both point sensors would capture the complete TDR input pulse. Radial direction components of electric fields recorded by the two sensors were used to calculate the cable model with the cell size produced cable propagation constant. For example, Figure 8.2 shows, for the XLPE cable model, the electric fields recorded by both the point sensors in one of the simulations. In either electric field trace, the first pulse was followed by a few smaller pulses, which was caused by impedance mismatch between the TDR input module and the cable model. There was resonance starting from about 5 ns in the trace recorded by sensor 1. This was a result of the frequency components of the “broadband” pulse interacting with the FDTD mesh. An FFT analysis has shown that the resonance frequency was centred at 10 GHz, which is well above the frequency range of interest here and, therefore, the resonance shall not be a problem of concern.

With the electric fields recorded by both the point sensors, and using (8.1), the propagation constant of the cable model was calculated for each applied cell size. Figure 8.3 shows attenuation results of the XLPE cable model, i.e., the real part of the propagation constant  $\gamma_c(\omega)$ . The attenuation results varied, in particular with cell size in the cross-sectional plane. Similar variations appeared

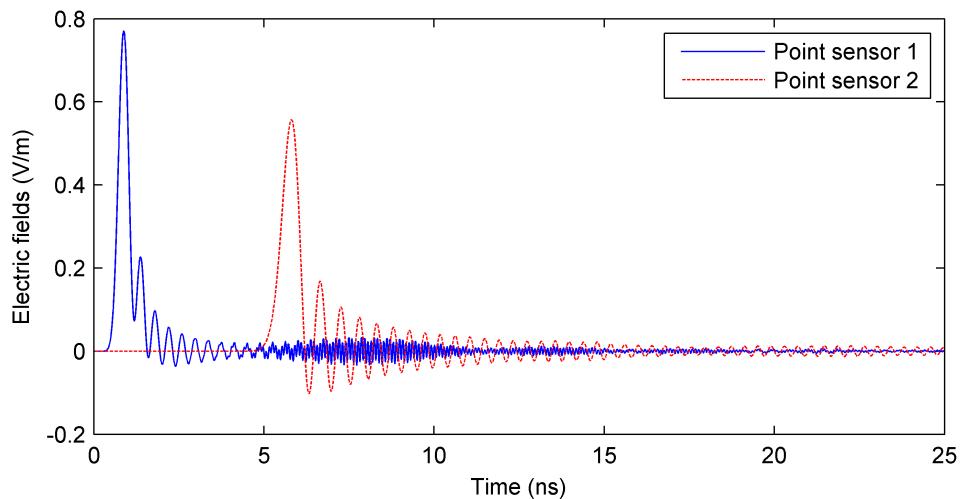
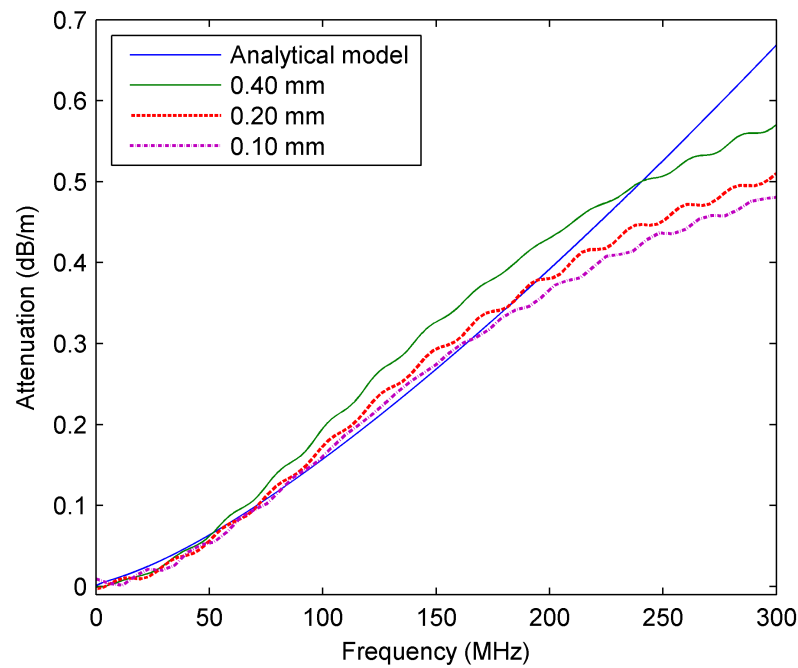
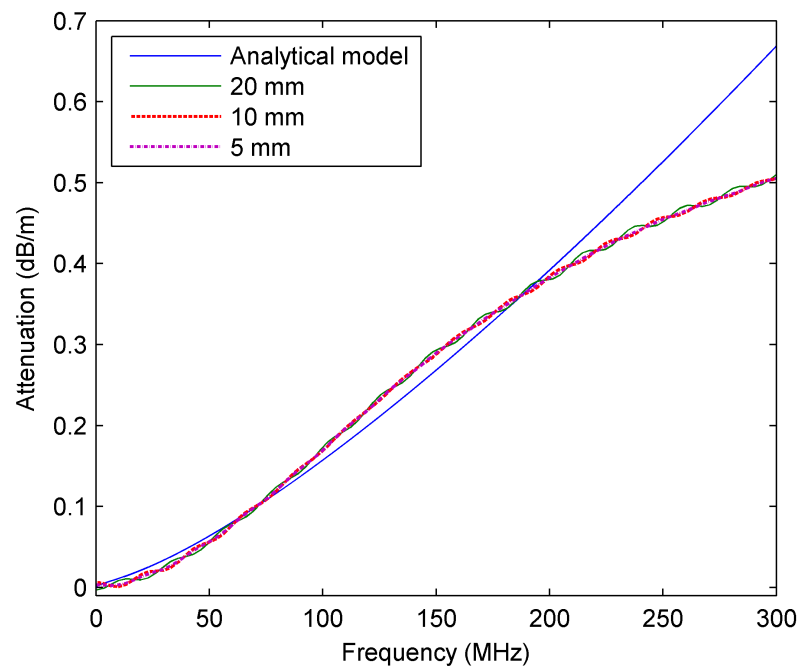


Figure 8.2: Electric fields recorded by point sensors 1 and 2. The simulation was carried out for the cable model of cable sample 2 (XLPE) with the cell size  $(\Delta x, \Delta y, \Delta z)$  set to  $(0.2, 20, 0.2)$  mm.



(a) Various cross-sectional cell sizes.



(b) Various axial cell sizes.

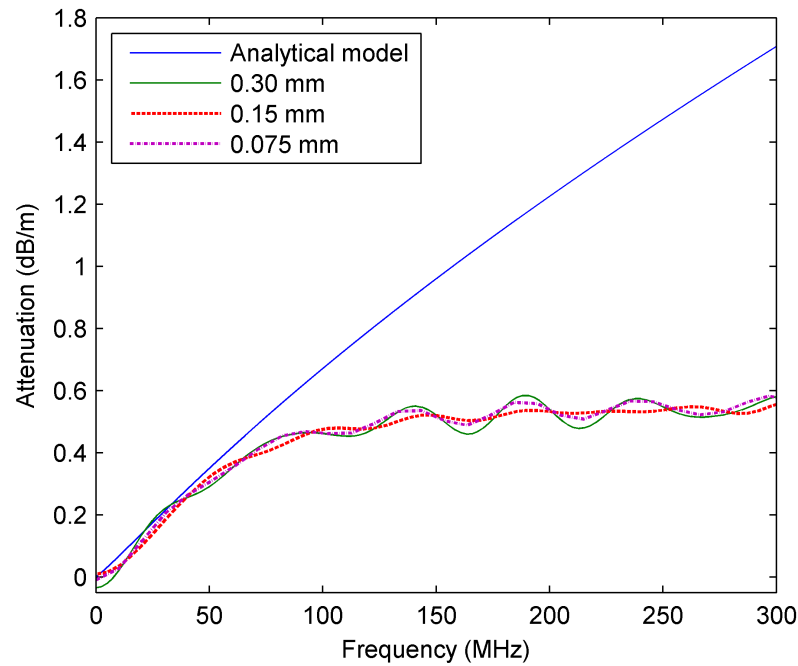
Figure 8.3: Attenuation for the cable model of cable sample 2 (XLPE). For the cross-sectional cell sizes,  $\Delta x = \Delta z = 0.40$  mm,  $\Delta x = \Delta z = 0.20$  mm and  $\Delta x = \Delta z = 0.10$  mm were respectively used while the axial cell size was kept at  $\Delta y = 20$  mm. For the axial cell sizes,  $\Delta y = 20$  mm,  $\Delta y = 10$  mm and  $\Delta y = 5$  mm were respectively used while the cross-sectional cell size was kept at  $\Delta x = \Delta z = 0.20$  mm.

in the attenuation results obtained for the EPR cable model which are shown in Figure 8.4. The attenuation varied more with the cross-sectional cell size while it looked less sensitive to the axial cell size. In terms of the convergence of the cell size, according to Figure 8.3a, it can be concluded that the cross-sectional cell size of  $\Delta x = \Delta z = 0.20$  mm was becoming convergent. Although half the cell size which is  $\Delta x = \Delta z = 0.10$  mm did make some differences in the attenuation, it was not like those significant changes which have been seen while going from 0.40 mm to 0.20 mm. At the same time, Figure 8.3b suggests that the axial cell size of  $\Delta y = 20$  mm can be considered convergent for the XLPE cable model. Similarly, for the EPR cable model,  $\Delta x = \Delta z = 0.15$  mm and  $\Delta y = 20$  mm were concluded as sufficiently convergent cell sizes.

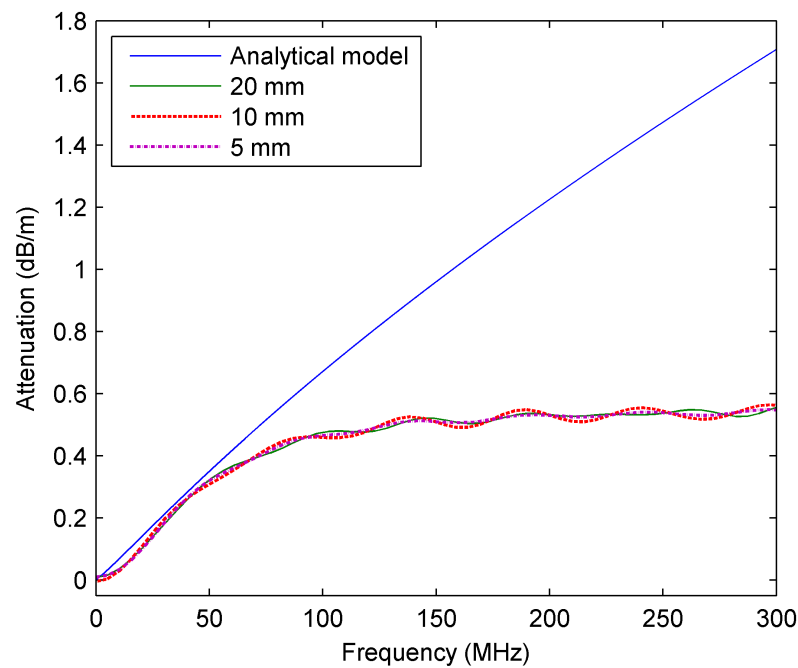
Figures 8.3 and 8.4 also show attenuation results from the analytical models. The results can be used as references for evaluating the accuracy of the cable models. Generally, for either cable, the analytical result was approximately increasing linearly with frequency while the results of the cable model were increasing with frequency but began to level out after certain frequencies. The frequencies were about 200 MHz for cable sample 2 (XLPE) and 50 MHz for cable sample 1 (EPR). Comparing with Figures 5.21 and 5.20 where the attenuation results from the analytical models agreed with those from the TDR measurement in 300 MHz and 100 MHz ranges for cable samples 2 and 1 respectively, this suggests that the FDTD models are not as good as the analytical models in characterising high frequency losses of the cables.

Both the FDTD method and the analytical method should be equally applicable in theory. In practice, existing analytical models for different types of cable are able to account for the three main causes of the cable high frequency loss which are the skin effect losses, insulation loss and semicon losses. While the skin effect is usually not feasible to include in an FDTD model, subject to available material definitions provided by the software package used in this study, the insulation loss was also not accounted for. In other words, the semicon losses have been the sole cause of high frequency losses in the created FDTD cable models. Therefore, differences between the attenuation results from the FDTD models and the analytical models are inevitable. Furthermore, for the FDTD method and the analytical method, the semicon properties used in calculation were obtained from the Debye model and the Cole-Cole model respectively. Referring to Figures 4.9 and 4.10, the Debye model had “poorer” fits to the measured semicon





(a) Various cross-sectional cell sizes.



(b) Various axial cell sizes.

Figure 8.4: Attenuation for the cable model of cable sample 1 (EPR). For the cross-sectional cell sizes,  $\Delta x = \Delta z = 0.30$  mm,  $\Delta x = \Delta z = 0.15$  mm and  $\Delta x = \Delta z = 0.075$  mm were respectively used while the axial cell size was kept at  $\Delta y = 20$  mm. For the axial cell sizes,  $\Delta y = 20$  mm,  $\Delta y = 10$  mm and  $\Delta y = 5$  mm were respectively used while the cross-sectional cell size was kept at  $\Delta x = \Delta z = 0.15$  mm.

properties than the Cole-Cole model did, which is why the FDTD models had attenuation leveled out after the certain frequencies. These factors also make it likely that the analytical method will produce attenuation results which are in better agreements with those from the TDR measurement.

However, the FDTD cable models can be accurate enough considering that the cables were only a few meters long and the source waveform had a -3 dB bandwidth of 96.4 MHz (Figure 7.21). For the EPR cable model, Figure 8.4 shows that the difference between the FDTD model and the analytical model was about 0.2 dB at 100 MHz. For a cable of length 1 m, by injecting a 100 MHz signal from one end of the cable, at the other end, the attenuation difference will result in the output a magnitude difference of 2.3 %.

Table 8.1 shows differences between the attenuation results from the FDTD cable models and the analytical models that were calculated at 50 MHz. The differences indicate that, at least at 50 MHz, a smaller cell size does not always achieve a better accuracy (less difference). For the XLPE cable model, the largest cross-sectional cell size of 0.40 mm actually had the least difference, but Figure 8.3a also shows that after 70 MHz, the result of the 0.40 mm cell size is going to have greater differences than those of the smaller ones. Nevertheless, it can be summarised that the chosen convergent cell sizes which are (0.15, 20, 0.15) mm and (0.20, 20, 0.20) mm for the EPR and the XLPE cable models respectively present a good balance between the accuracy and the calculation requirement.

It can be noticed that the attenuation traces in both Figures 8.3 and 8.4 had some apparently periodic variations. This was due to the fact that the output lengths of time requested in the simulations were not sufficiently long so that the

Table 8.1: Difference between simulated and analytical attenuation at 50 MHz.

Cable sample	Cell size (mm)	Difference (%)	Calculation time
1-(EPR)	(0.30, 20, 0.30)	19.2	32 m
	(0.075, 20, 0.075)	15.7	26 hrs, 38 m
	(0.15, 10, 0.15)	14.6	5 hrs, 57 m
	(0.15, 5, 0.15)	10.2	10 hrs, 56 m
	(0.15, 20, 0.15)	9.0	3 hrs, 37 m
2-(XLPE)	(0.10, 20, 0.10)	15.9	10 hrs, 10 m
	(0.20, 20, 0.20)	12.7	1 hr, 48 m
	(0.20, 10, 0.20)	11.3	3 hrs, 2 m
	(0.20, 5, 0.20)	10.9	6 hrs, 28 m
	(0.40, 20, 0.40)	3.7	22 m

electric fields recorded by both point sensors could have properly decreased to nearly zero. For example, Figure 8.2 shows that the electric fields recorded by point sensor 2 did not decrease completely in the output length of 50 ns (displayed was the first 25 ns). Increasing the output length to 100 – 200 ns will have the electric fields decreased more sufficiently and the periodic components removed from the calculated attenuation result.

## 8.3 Parametric Study on both 11 kV Cables

### 8.3.1 Effect of PD Size on PD Signal

Using similar cable models to those in the previous section, simulations were carried out to investigate induced current pulses on the cable outer conductors for different PD sources. Two scenarios were considered and in both, PD was represented by a  $0 \Omega$  current source in XFDTD and the current was flowing in the radial direction in accordance with the radial electric field to which the insulation is subjected.

For example, Figure 8.5 shows the model of cable sample 2 (XLPE). The PD source was put within the insulation in the middle of the cable model. Using

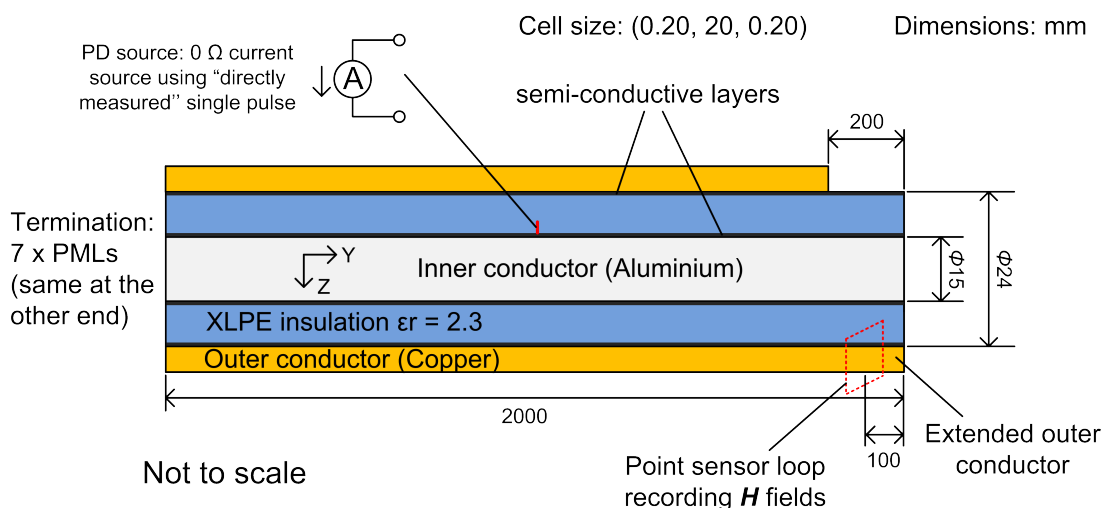


Figure 8.5: Axial cross section of the XLPE cable model for a parametric study on various PD sources within the insulation. The PD source was created as a current filament represented using a current source with  $0 \Omega$  source impedance in XFDTD. For the last 200 mm of the cable model, the outer conductor was tailored to have an extended outer conductor to allow a point sensor loop to encircle it.

the method described in Chapter 7, the PD induced current pulse on the outer conductor of the model was derived from magnetic fields recorded by the point sensor loop on the extended outer conductor. The first scenario was a PD source on the inner conductor extending in length step by step until short-circuiting the inner and outer conductors. Figure 8.6 shows a diagram of the scenario. Using

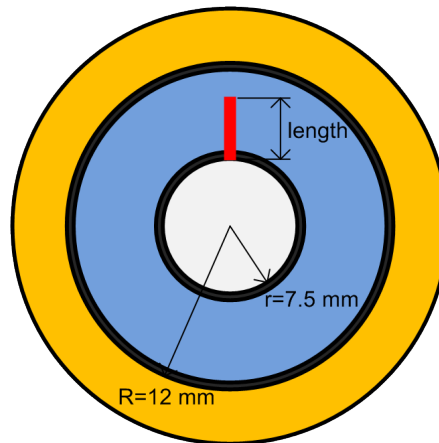
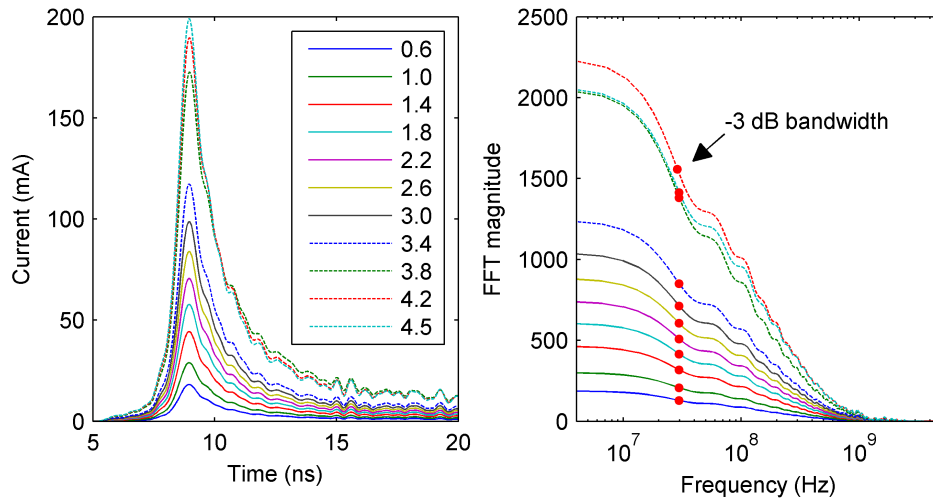


Figure 8.6: Cross section of the XLPE cable model containing an extending PD source. The length of the PD source was increased gradually from 0.6 mm to 4.5 mm which short-circuited the inner and outer conductors.

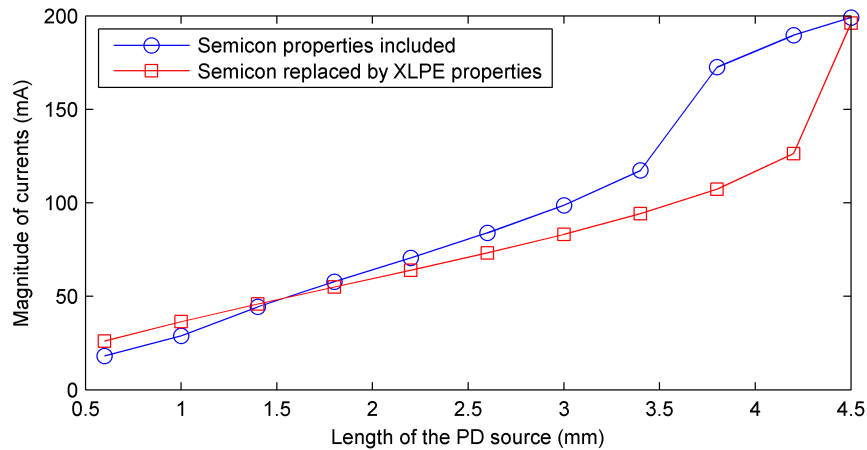
one of the “directly measured” pulses shown in Figure 7.21 as the PD source waveform, simulations were carried out for each PD source specification. Current pulses induced on the cable outer conductor were recorded and plotted in Figure 8.7a. The magnitudes of these pulses are plotted in Figure 8.7b against the PD source length.

Figure 8.7a shows that the current pulse magnitude increases with increasing length of the PD source. It can also be noticed that the shape of the pulses showed little variation, which is further confirmed by the FFT results which indicate that the -3 dB bandwidths of the pulses were all around 30 MHz. While the source pulse had a -3 dB bandwidth of 96.4 MHz (referring to Figure 7.21), the significant decrease in the pulse bandwidth was believed to be caused by the introduction of the semicon layers in the cable model. This was tested by replacing properties of both semicon layers with the XLPE insulation properties and repeating the simulations. Figure 8.8 shows that no significant bandwidth decrease in the current pulses on the cable outer conductor was observed.

Figure 8.7b shows the maximum pulse magnitudes for both cases, i.e., the



(a) Waveform and FFT of the current pulses.



(b) Maximum magnitudes of the current pulses.

Figure 8.7: Extending PD source induced current pulses on the extended outer conductor of the XLPE cable model and maximum magnitudes of the pulses. FFT analysis was performed for each current pulse and the -3 dB point was labelled with a red dot in (a).

semicon layers using the semicon properties and being replaced by the insulation properties respectively. In the XLPE case, the magnitude was increasing almost linearly until the source length was just shorter than 4.5 mm, and then, there was a jump in the pulse magnitude for the 4.5 mm, short circuit. In the semicon case, the jump came a bit earlier at 3.8 mm, which was when the PD source touched the outer semicon layer. This was because the outer semicon layer has a dc conductivity of 0.14 S/m, which makes it look more like a conductor, and therefore, resulted in the jump in pulse magnitude. Similar extending PD source

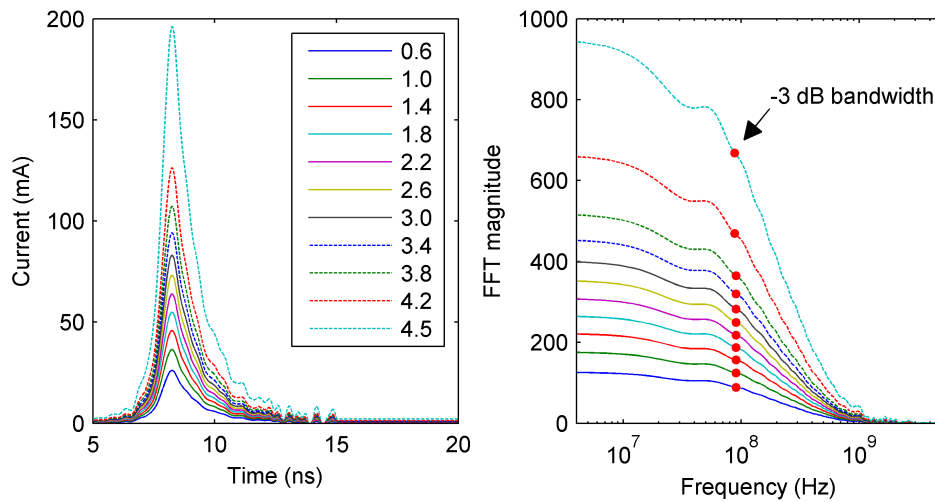


Figure 8.8: Extending PD source induced current pulses from the XLPE cable model with both semicon layers properties replaced by XLPE insulation properties.

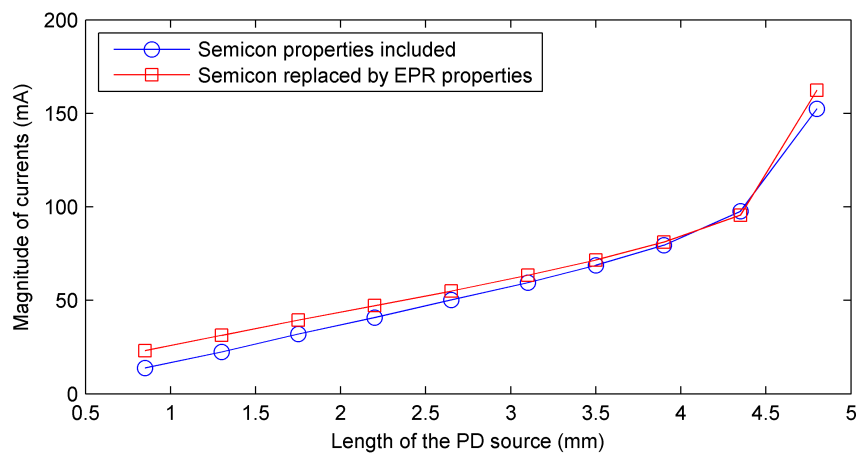


Figure 8.9: Maximum magnitudes of the current pulses on the extended outer conductor of the EPR cable model.

simulations were also carried out on the EPR cable model. Figure 8.9 shows the maximum magnitudes of the current pulses measured. Replacing properties of both semicon layers with those of the EPR insulation did not have obvious effects on the results. This can be explained by the fact that the outer semicon layer of the EPR cable model had a dc conductivity of  $6.77 \times 10^{-6}$  S/m which makes it more like an insulator, and therefore, by changing to using the EPR insulation properties, not much difference was expected.

### 8.3.2 Effect of PD Cross-sectional Position on PD Signal

The second scenario was a fixed length (1 mm) PD source moving radially from an initial position touching the inner conductor to the outer conductor. Figure 8.10 shows that the radial position of the PD source is measured by the distance from one end of the PD source to the centre axis of the cable. The same “directly

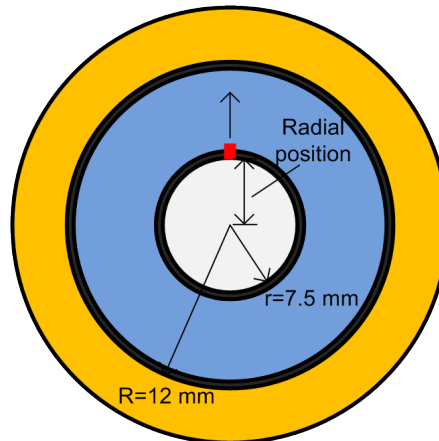
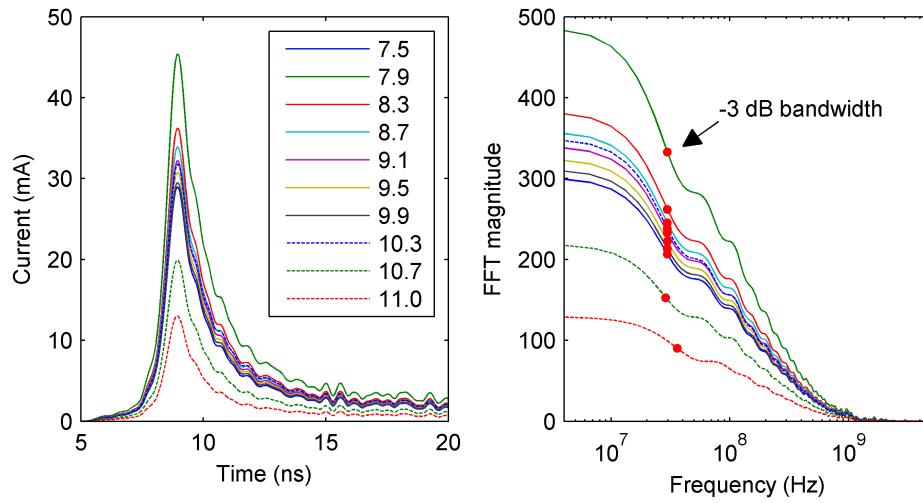


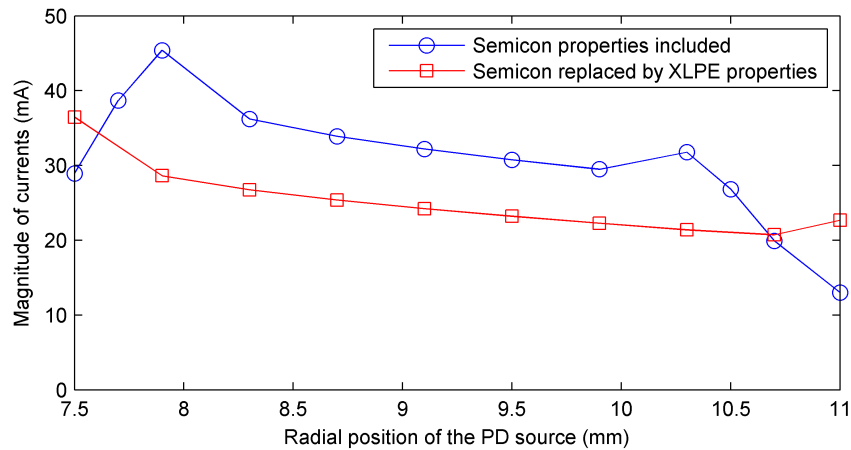
Figure 8.10: Cross section of the XLPE cable model containing a moving PD source. The length of the PD source was 1 mm. The PD was moved gradually from on the inner conductor (7.5 mm to the cable centre) to on the outer conductor (11.0 mm to the cable centre).

measured” PD pulse used for the extending PD simulations was used as the PD source waveform and simulations were carried out for each radial position of the PD source.

Current pulses were measured on the extended outer conductor of the cable model and plotted in Figure 8.11a. The maximum magnitudes of the pulses are plotted against the radial positions in Figure 8.11b. FFT analysis results in Figure 8.11a indicate that -3 dB bandwidths of the current pulses varied from 28 – 36 MHz. Figure 8.11b shows that, within the insulation layer, i.e., from the radial position of 7.9 mm to 10.3 mm, the magnitude of the current pulse on the outer conductor was generally decreasing with the PD source moving from the inner conductor towards the outer conductor. This result agreed with that reported in [109], which showed that, for excitation of TEM mode, a PD source with constant path length would excite less propagating signal as it moved from the inner to the outer conductor within a coaxial structure. Although [109] was concerned with PD in GIS, the results are related since both a cable and the



(a) Waveform and FFT of the current pulses.



(b) Maximum magnitudes of the current pulses.

Figure 8.11: Moving PD source induced current pulses on the extended outer conductor of the XLPE cable model and maximum magnitudes of the pulses.

GIS have a coaxial conductor arrangement. Similar trends have also been found in calculating theoretical PD magnitude resulting from a cavity discharge in a coaxial structure [16; 35].

Figure 8.11b also shows that the relation between the radial position and the current pulse magnitude was different while the radial position was close to either the inner or the outer conductor. Referring to the dimensions on the XLPE cable cross section reveals that these positions all have part of the PD source being within the semicon layers. The inner and outer semicon layers of the XLPE cable model had dc conductivities of 0.11 S/m and 0.14 S/m respectively. Both look



like conductors to the PD source. Being in contact with either semicon layer will result in an increase in the magnitude of the induced current pulse, the effect of which has already been seen in the study of the extending PD source. When the PD source is close to the inner conductor, another effect is that while it is moving towards the outer conductor, more length of the PD source will come out of the inner semicon, which further contributes to the magnitude increase of the induced current. This is the case for the radial positions from 7.5 mm to 7.9 mm. When the PD source is close to the outer conductor, in contrast, moving towards the outer conductor will have more length of the PD source being within the outer semicon. Therefore, a magnitude decrease in the induced current is expected, which proves to be the case for positions from 10.3 mm to 11.0 mm.

Variations in the induced current magnitude, appearing when the PD source is close to the inner and outer conductors, were not so apparent in the results of the EPR cable model which is shown in Figure 8.12. This is explained by the fact that, compared to the XLPE cable model, The inner and outer semicon layers of the EPR cable model had lower dc conductivities ( $0.024 \text{ S/m}$  and  $6.77 \times 10^{-6} \text{ S/m}$  respectively) and thus made less difference to the PD source compared to the XLPE cable model.

Further evidence of the semicon's influence is that by replacing it with the insulation properties and repeating the simulations for each PD source position, variations at both ends of the curves are no longer seen in Figures 8.11b and 8.12. The results also suggest that generally lower current magnitudes were ob-

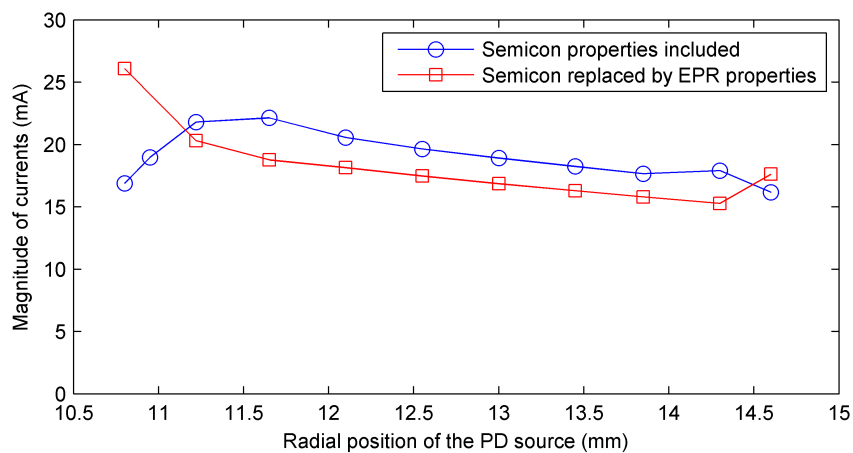


Figure 8.12: Maximum magnitudes of the current pulses on the extended outer conductor of the EPR cable model.

served while the semicon was set to using the insulation properties. This can be explained by the sensitivity function of TEM mode in a coaxial waveguide proposed by Judd et al. [109]. For a small PD source of constant path length  $\Delta r$ , the relative sensitivity of TEM mode to PD excitation can be calculated as a function of the radial position  $r$  of the PD source by

$$S_{TEM}(r) = \frac{Z_0}{4\pi b \ln(b/a)} \ln\left(\frac{r + \Delta r/2}{r - \Delta r/2}\right) \quad (8.2)$$

where  $Z_0 = \sqrt{\mu_0/\epsilon_0}$  is the free space impedance and  $a, b$  are the inner and outer radii of the coaxial conductors respectively. The presence of the semicon layers had a potential effect to increase the inner radius  $a$  by the inner semicon layer thickness and decrease the outer radius  $b$  by the outer semicon layer thickness. The effect caused a decrease of the denominator in (8.2), which resulted in higher sensitivity values for TEM mode, and therefore, higher induced current magnitudes could be expected.

It can be summarised that the parametric study shows the potential of determining coupling sensitivity between PD source currents and the corresponding PD currents on the cable earth conductor (outer conductor). Referring to the PD modelling framework in Figure 7.18, the induced currents on the earth conductor, in combination with an HFCT transfer function, can be used to predict the output response of the HFCT. Furthermore, it should allow the model to be used to infer a transfer function from the PD source to the HFCT. The converse should also be feasible, namely, that measurement of the sensor output may allow the model to infer the time domain waveform of an otherwise inaccessible measurand by using the computed reverse transfer function.

## 8.4 Conclusions

Two FDTD cable models were created for the 11 kV EPR and XLPE cables respectively. Modelling the cable geometries and defining the material properties were conducted by referring to the experience and results summarised in Chapters 3 to 5. Using the created cable models, simulations of TDR measurement were firstly carried out to evaluate the accuracy of the created FDTD cable models. By comparing the cable high frequency attenuation produced from the simulations with that calculated using the analytical model, it was found that the FDTD cable

models were able to agree reasonably with the analytical model up to 50 MHz for EPR and 200 MHz for XLPE cables. Above these frequencies, attenuation predicted by the analytical model kept increasing with frequency, while that from the FDTD simulations tended to level off with frequency. A few factors are thought to cause this difference. Among them, different dielectric models being used to represent the cable semicon properties should have a significant effect. However, considering the problem under investigation, i.e, a few meters of cable and a PD source with a bandwidth below 100 MHz, even the FDTD model of the EPR cable which can only reproduce the cable high frequency attenuation up to 50 MHz can be sufficiently accurate.

Two scenarios of varying the parameters of a PD source were considered, i.e., the extending PD source length and moving PD source of fixed length. Simulations were carried out using both the FDTD cable models to find out the induced PD currents on the cable outer conductors. Magnitudes of these currents from both the cable models have shown similar changes according to the PD source variations. Generally, for the extending PD source, increasing the PD length caused the induced current on the outer conductor to increase. For the moving PD source, moving towards the outer conductor, the induced current on the outer conductor would decrease.

The simulations presented in this Chapter have demonstrated the capabilities of FDTD modelling to study PD in cables. The simulations of TDR measurement show one way to evaluate the accuracy of the created FDTD cable models. The parametric study of the PD source variations offer the potential of determining coupling sensitivity between PD source currents and those currents induced on the cable outer conductor.

# Chapter 9

## Conclusions

### 9.1 The Modelling Framework

A hybrid modelling framework (Figure 7.18) based on combining FDTD modelling and transfer function theory has been proposed and successfully applied to investigate the PD excitation, propagation and detection processes involved in HFCT-based PD detection in HV cables. Parameters required to conduct the modelling framework are the PD source waveform, cable geometries, cable material properties, currents on the conductors within FDTD models and HFCT transfer functions. For two types of 11 kV cable (EPR-insulated and XLPE-insulated), methods to obtain these parameters have been described or developed. FDTD modelling was carried out by using a commercial software package XFDTD, while data post-processing, e.g., converting currents to HFCTs' voltage output, was performed in MATLAB. The created FDTD cable models were found to be able to reproduce high frequency losses of the cables in certain frequency ranges, depending on the accuracy of those obtained modelling parameters.

#### 9.1.1 Advantages of the Modelling Framework

In terms of modelling of HFCT-based PD detection in cables, some potential advantages of the proposed hybrid modelling framework are as follows:

1. By creating a three-dimensional model of a cable, both cross-sectional and axial details of the cable are able to be characterised. For example, modelling earth connections, terminations, joints and various defects are all possible.
2. By exciting a PD pulse anywhere in the cable model, the PD-induced

currents on the cable's inner and outer conductors some distance away from the PD launching site can be predicted. This permits variations in physical parameters of the PD that would not be possible in practical experiments.

3. By considering the effect of an HFCT on the currents flowing through the HFCT based on wideband characterisation of the HFCT's complex frequency response and transfer function theory, the HFCT's voltage output can be worked out.

4. Instead of physically modelling an HFCT in an FDTD model, implementing the effect of the HFCT using the transfer function method is more practical and makes it easier to compare different HFCTs.

### 9.1.2 Challenges

There are inevitably some limitations for the modelling framework.

Firstly, it is not convenient to work with a cable's semi-conductive (semicon) layers in an FDTD model. For modelling the semicon layers, the most suitable material definition provided by XFDTD is the Debye medium which is based on the expression of the Debye dielectric model. However, this model cannot fit the obtained semicon properties particularly well, although an approximate fit is possible within certain frequency ranges, e.g., up to 100 MHz. This can put some limits on the achievable accuracy of the created FDTD cable models. These limits are essentially caused by the FDTD technique being a time domain method which means it has a limited capability in dealing with frequency-dependent materials like the cable semicon layers.

Secondly, the created cable models are usually a few meters long, which is subject to affordable computer resources as well as required computation time. However, those effects resulting from PD propagation along a cable may only be significant when the propagated distance becomes tens or hundreds of meters. The fact would mean that it is not practical/advantageous to consider the propagation caused effects using an FDTD cable model. Considering these effects using analytical methods [26] is more efficient.

Thirdly, applying HFCT transfer functions based on the numerically calculated FFT and IFFT can fail under certain circumstances. An alternative approach has been presented that involves establishing analytical transfer function models of the measured HFCT transfer functions. Some expertise is required in

establishing the transfer function models.

## 9.2 HFCT Transfer Function Measurement

A method for measuring complex transfer functions of HFCTs has been developed and used to obtain transfer functions of both HFCTs used in this work. The method involves two measurements to record the step and the impulse responses of an HFCT respectively. The step response is used to obtain the transfer function at relative low frequencies  $< 1$  MHz, while the pulse response is used to obtain it at relative high frequencies  $> 10$  MHz. The low frequency part and the high frequency part are joined at a certain frequency (in the range 1 MHz to 10 MHz) to produce the complete HFCT transfer function. Using this method, the transfer functions of HFCT 1 and HFCT 2 were characterised in the frequency ranges of 20 kHz–500 MHz and 1 kHz–1 GHz respectively. The achievable frequency range depends on bandwidths of the step and the pulse sources, the oscilloscope used and the HFCT under test. Furthermore, the test configuration has been shown to make some differences. For example, a metal enclosure was used to centralise the conductor position in the HFCT and feed magnetic fields as evenly as possible into the HFCT.

## 9.3 Modelling Using Published Semicon Data

One of the challenges faced while trying to model a polymeric-insulated cable is that dielectric properties of the cable's inner and outer semicon layers have to be known. To measure them can involve sophisticated test cells and devices, and furthermore, it is difficult to remove suitable semicon samples from a cable if the semicon layers are bonded to the cable insulation, which is quite normal for modern polymeric-insulated cables.

Instead of practical measurement, the results presented in this work may indicate a possible solution based on using published semicon data. For example, it was not possible to remove the semicon layers of cable sample 2 (XLPE) from the cable for measurement. Therefore, published semicon data were used instead in the analytical cable model, which proved sufficient to represent the cable attenuation. By comparing the attenuation with that obtained from TDR mea-

surement and modifying the semicon properties in a “trial and error” manner, the calculated attenuation from the analytical model was shown to achieve a better agreement with the measured attenuation. The modified semicon properties were later used in creating the FDTD cable model. The attenuation produced by the FDTD cable model achieved expected agreement with that calculated by the analytical model. In this way, the cable semicon properties do not have to be measured.

## 9.4 Implementing FDTD Modelling of PD in Cables

Experience gained in efforts to create an FDTD model as accurate as possible in reproducing the cable high frequency loss has been summarised. The summary covers creating cable geometries, assigning material definitions to the components of the created cable model, setting FDTD parameters (such as cell sizes and boundary conditions), configuring a proper PD excitation source and some suggestion for FDTD modelling of TDR measurement. In particular, for assigning material definitions to the components, the effect of each component on the accuracy of the resulting cable model was discussed against the capability of the FDTD technique for characterising the effect, as well as available options provided by a practical software package. Although all the modelling work in this study was carried out using XFdtd, the summarised experience should be applicable across different FDTD software packages.

## 9.5 Applications of the Technique

FDTD models were created for both the 11 kV cables used in this study. Each of the created cable models was used to investigate induced current pulses on the cable outer conductor for different PD sources, which shows the potential of determining the coupling sensitivity between the PD source currents and the induced currents on the cable outer conductor. Modelling of TDR measurement was used to evaluate the accuracy of the created cable models. In practice, TDR measurement is a long-established method for fault location in cables. Modelling

of TDR measurement can also be used to predict what kinds of mechanical defect sizes could be measurable [150]. While only FDTD modelling of cables was carried out in this study, modelling of cable joints and terminations with more varied structures is possible and this will be of interest in future studies. Cable joints and terminations are usually weak points in a cable system, where most of electrical failures occur. PD sensors like HFCTs are often installed close to these joints and terminations, which means modelling of very long cables is not involved. The proposed hybrid modelling framework is applicable to modelling of HFCT-based PD detection in joints and terminations by simply exchanging the cable in the framework for a joint or a termination.

## 9.6 Recommendations for Future Work

### 9.6.1 Parallel Experiments and FDTD Modelling

For further validation of the effectiveness of the proposed modelling framework, parallel experimental and modelling work should be carried out and the results from them should be comparable. This is possible under laboratory circumstances with either simulated PD current sources or real PD measurement. For example, if a needle is inserted into cable insulation, a simulated PD pulse could be injected to the cable through the needle, and then by using an HFCT to detect the PD currents on the cable earth connection, it should make the involved processes very like those considered by the modelling framework. The same simulated PD pulse can be digitized and used as the excitation source waveform in an FDTD cable model created for the cable under test. If results from the test with the simulated PD pulse were found comparable with those obtained from the FDTD cable model, the test would move on to energise the cable to detect real PD from the needle defect. To make sure that the PD is from the needle defect, it would be necessary to check that, before the needle is inserted, the cable is PD-free at the actual test voltage.

For the real PD test, an ideal situation is that the “direct PD measurement” (Figure 7.20) and detection using an HFCT can be carried out simultaneously. In this case, both the PD source current and the HFCT’s voltage output are available so that the FDTD cable model has the excitation source waveform and the modelling result can be compared with the experimental result.



Towards parallel experimental and modelling work, some tests aiming to detect PD from an artificial defect introduced in an pre-moulded cable joint have already been attempted in this study. Unfortunately, the tests failed prematurely due to instantaneous breakdown caused by the introduced artificial defect which was a sharp needle fixed on the conductor connection of the produced cable joint. Some experience gained is that it might be better to put a needle on the outer conductor instead of the inner (HV) conductor, where breakdown is more likely to occur.

### 9.6.2 Converse of the Modelling Framework

Unlike the experimental tests mentioned above, in on-site tests, only the detection using HFCTs is possible. With the HFCTs' voltage output, it can be of interest to know the current input of the HFCTs and use this to estimate the original PD pulse shapes at their remote site. In that case, provided an HFCT's voltage output is available, it is potentially feasible to follow the converse of the proposed modelling framework to infer the PD source current which was the input of the framework, i.e., the current pulse used as the excitation source of an FDTD cable model. A general idea of realising the converse of the modelling framework is that instead of FDTD simulations, reversing the steps contained in the framework will be carried out by using the computed inverse transfer function of each step. For example, the HFCT inverse transfer function can be used to convert the HFCT voltage output to the current input, i.e, the current on the cable earth conductor. A transfer function can be worked out between the source current of the FDTD model and the current on the cable earth conductor. The inverse of this transfer function can be used to infer the source current of the FDTD model from the cable earth current which has been obtained by using the the HFCT inverse transfer function.

One of the final objectives of this study was to improve interpretation of the PD measurement results from on-line PD monitoring of cables. Assuming a measurement result is obtained using an HFCT, the converse principle described above can potentially be used to find out the initial PD pulse waveform at its original site. Knowing the initial PD pulse will be helpful in PD result analysis to identify the severity and type of the PD.

# References

- [1] G. F. Moore and BICC Cables Ltd. *Electric Cables Handbook*. Blackwell Science, Oxford, 1997.
- [2] BSI. LV and MV polymeric insulated cables for use by distribution and generation utilities. Part 1: General. Technical report, British Standards Institution, 2011.
- [3] O. I. Gilbertson. *Electrical Cables for Power and Signal Transmission*. John Wiley & Sons, New York, 2000.
- [4] R. Bartnikas and K. D. Srivastava. *Power and Communication Cables: Theory and Applications*. John Wiley & Sons, New Jersey, 2000.
- [5] G. C. Stone. Partial discharge diagnostics and electrical equipment insulation condition assessment. *IEEE Transactions on Dielectrics and Electrical Insulation*, 12(5):891–904, Oct. 2005.
- [6] W. Vahlstrom. Strategies for field testing medium voltage cables. *IEEE Electrical Insulation Magazine*, 25(5):7–17, Sep. 2009.
- [7] G. Hartshorn, B. Lanz, and B. Broussard. Assuring cable reliability. *IEEE Industry Applications Magazine*, 15(5):66–74, Sep. 2009.
- [8] IEEE. IEEE guide for field testing and evaluation of the insulation of shielded power cable systems rated 5 kV and above. Technical report, Institute of Electrical and Electronics Engineers, 2012.
- [9] IEEE. IEEE guide for partial discharge testing of shielded power cable systems in a field environment. Technical report, Institute of Electrical and Electronics Engineers, 2006.

- 
- [10] CIGRE SC B1. Maintenance for HV cables and accessories. Technical report, International Conference on Large Electric Systems (CIGRE), 2005.
- [11] L. Renforth, R. Mackinlay, and M. Michel. MV cable diagnostics - applying online PD testing and monitoring. In *Asia Pacific Conference on MV Power Cable Technologies*, pages 1–4, Kuala Lumpur, Malaysia, Sep. 2005.
- [12] IEC. High-voltage test techniques partial discharge measurements. Technical report, International Electrotechnical Commission, 2000.
- [13] F. H. Kreuger. *Partial Discharge Detection in High-Voltage Equipment*. Butterworths, London, 1989.
- [14] S. A. Boggs. Partial discharge: overview and signal generation. *IEEE Electrical Insulation Magazine*, 6(4):33–39, July-Aug. 1990.
- [15] S. A. Boggs and G. C. Stone. Fundamental limitations in the measurement of corona and partial discharge. *IEEE Transactions on Electrical Insulation*, EI-17(2):143–150, Apr. 1982.
- [16] S. A. Boggs. Partial discharge - Part III: cavity-induced pd in solid dielectrics. *IEEE Electrical Insulation Magazine*, 6(6):11–16, Nov. 1990.
- [17] A. J. Reid. *A New Approach to Partial Discharge Measurements for Testing Electrical Insulation Systems*. PhD thesis, Department of Electronic and Electrical Engineering, University of Strathclyde, 2007.
- [18] W. Vahlstrom. Investigation of insulation deterioration in 15 kV and 22 kV polyethylene cables removed from service. *IEEE Transactions on Power Apparatus and Systems*, PAS-91(3):1023–1035, May 1972.
- [19] R. Baumgartner, B. Fruth, W. Lanz, and K. Pettersson. Partial discharge. IX. PD in gas-insulated substations-fundamental considerations. *IEEE Electrical Insulation Magazine*, 7(6):5–13, Nov. 1991.
- [20] John Densley. Ageing mechanisms and diagnostics for power cables - an overview. *IEEE Electrical Insulation Magazine*, 17(1):14–22, Jan.-Feb. 2001.

- [21] M. S. Mashikian. Preventive maintenance testing of shielded power cable systems. In *Conference Record of the 2001 Pulp and Paper Industry Technical Conference*, pages 59–66, Portland, OR, June 2001.
- [22] M. S. Mashikian and A. Szarkowski. Medium voltage cable defects revealed by off-line partial discharge testing at power frequency. *IEEE Electrical Insulation Magazine*, 22(4):24–32, July-Aug. 2006.
- [23] F. H. Kreuger, M. G. Wezelenburg, A. G. Wiemer, and W. A. Sonneveld. Partial discharge. XVIII. Errors in the location of partial discharges in high voltage solid dielectric cables. *IEEE Electrical Insulation Magazine*, 9(6):15–22, Nov.-Dec. 1993.
- [24] M. D. Judd. Contact discharges as a source of sub-nanosecond high voltage pulses. *Journal of Physics D: Applied Physics*, 34(18):2883–2893, Sep. 2001.
- [25] A. J. Reid, M. D. Judd, B. G. Stewart, and R. A. Fouracre. Partial discharge current pulses in SF<sub>6</sub> and the effect of superposition of their radiometric measurement. *Journal of Physics D: Applied Physics*, 39(19):4167–4177, Sep. 2006.
- [26] N. Oussalah, Y. Zebboudj, and S. A. Boggs. Analytic solutions for pulse propagation in shielded power cable for symmetric and asymmetric PD pulses. *IEEE Transactions on Dielectrics and Electrical Insulation*, 14(5):1264–1270, May 2007.
- [27] E. W. Shu and S. Boggs. Dispersion and pd detection in shielded power cable. *IEEE Electrical Insulation Magazine*, 24(1):25–29, Jan.-Feb. 2008.
- [28] E. Lemke, T. Strehl, W. Weissenberg, and J. Herron. Practical experiences in on-site PD diagnosis tests of HV power cable accessories in service. In *Conference Record of the 2006 IEEE International Symposium on Electrical Insulation*, pages 498–501, Toronto, ON, June 2006.
- [29] Chunchuan Xu, Liming Zhou, J. Y. Zhou, and S. A. Boggs. High frequency properties of shielded power cable part 1: overview of mechanisms. *IEEE Electrical Insulation Magazine*, 21(6):24–28, Nov.-Dec. 2005.

- 
- [30] G. C. Stone and S. A. Boggs. Propagation of partial discharge pulses in shielded power cable. In *1982 Annual Report of the Conference on Electrical Insulation and Dielectric Phenomena*, pages 275–280, Washington, DC, Oct. 1982. National Academy of Sciences.
- [31] S. Boggs, A. Pathak, and P. Walker. Partial discharge. XXII. High frequency attenuation in shielded solid dielectric power cable and implications thereof for PD location. *IEEE Electrical Insulation Magazine*, 12(1):9–16, Jan.-Feb. 1996.
- [32] Chunchuan Xu and S. A. Boggs. High frequency properties of shielded power cable part 3: loss from neutral wire-shield interaction. *IEEE Electrical Insulation Magazine*, 23(2):12–16, Mar.-Apr. 2007.
- [33] Jim Jun Guo and S. A. Boggs. High frequency signal propagation in solid dielectric tape shielded power cables. *IEEE Transactions on Power Delivery*, 26(3):1793–1802, July 2011.
- [34] Chunchuan Xu and S. A. Boggs. High-frequency loss in unjacketed distribution cable and its effect on PD measurement. *IEEE Transactions on Power Delivery*, 24(2):495–500, Apr. 2009.
- [35] S. Boggs and J. Densley. Fundamentals of partial discharge in the context of field cable testing. *IEEE Electrical Insulation Magazine*, 16(5):13–18, Sep.-Oct. 2000.
- [36] S. A. Boggs, J. M. Braun, and G. C. Stone. Attenuating voltage surges in power cable by modifying the semiconductive shields. In *Conference Record of the 1992 IEEE International Symposium on Electrical Insulation*, pages 491–494, Baltimore, MD, June 1992.
- [37] Li-Ming Zhou and S. Boggs. Effect of shielded distribution cable on very fast transients. *IEEE Transactions on Power Delivery*, 15(3):857–863, July 2000.
- [38] IEEE. IEEE guide for field testing of shielded power cable systems using very low frequency (VLF) (less than 1 Hz). Technical report, Institute of Electrical and Electronics Engineers, 2013.

- [39] E. Gulski, F. J. Wester, J. J. Smit, P. N. Seitz, and M. Turner. Advanced partial discharge diagnostic of MV power cable system using oscillating wave test system. *IEEE Electrical Insulation Magazine*, 16(2):17–25, Mar. 2000.
- [40] K. Kurahashi, K. Asari, K. Yatsuka, M. Watanabe, K. Kishi, and H. Inoue. Development of failure prediction method for accessories of XLPE cable lines. In *Proceedings of the 3rd International Conference on Properties and Applications of Dielectric Materials*, volume 2, pages 699–702, Tokyo, Japan, July 1991.
- [41] C. G. Henningsen, K. Polster, B. A. Fruth, and D. W. Gross. Experience with an on-line monitoring system for 400 kV XLPE cables. In *Proceedings of the 1996 IEEE Transmission and Distribution Conference*, pages 515–520, Los Angeles, CA, Sep. 1996.
- [42] Chang-Young Lee, Seok-Hyun Nam, Su-Gil Lee, Dong-Wook Kim, and Myung-Kyu Choi. High frequency partial discharge measurement by capacitive sensor for underground power cable system. In *Proceedings of the 2000 International Conference on Power System Technology*, volume 3, pages 1517–1520, Perth, WA, Dec. 2000.
- [43] L. Zhong, Y. Xu, G. Chen, A. E. Davies, Z. Richardson, and S. G. Swingler. Use of capacitive couplers for partial discharge measurements in power cables and joints. In *Proceedings of the 2001 IEEE 7th International Conference on Solid Dielectrics*, pages 412–415, Eindhoven, Netherlands, June 2001.
- [44] D. Pommerenke, T. Strehl, R. Heinrich, W. Kalkner, F. Schmidt, and W. Weissenberg. Discrimination between internal PD and other pulses using directional coupling sensors on HV cable systems. *IEEE Transactions on Dielectrics and Electrical Insulation*, 6(6):814–824, Dec. 1999.
- [45] E. Pultrum. On-site testing of cable systems after laying, monitoring with HF partial discharge detection. In *IEE Two Day Colloquium on Supertension*, pages 21/1–21/4, London, UK, Nov. 1995.
- [46] N. H. Ahmed and N. N. Srinivas. On-line partial discharge detection in

- cables. *IEEE Transactions on Dielectrics and Electrical Insulation*, 5(2): 181–188, Apr. 1998.
- [47] Y. Tian, P. L. Lewin, and A. E. Davies. Comparison of on-line partial discharge detection methods for HV cable joints. *IEEE Transactions on Dielectrics and Electrical Insulation*, 9(4):604–615, Aug. 2002.
- [48] R. Morin, R. Bartnikas, and G. Lessard. In-service location of partial discharge sites in polymeric distribution cables using capacitive and inductive probes. In *1999 IEEE Transmission and Distribution Conference*, volume 1, pages 120–127, New Orleans, LA, Apr. 1999.
- [49] L. E. Lundgaard and W. Hansen. Acoustic method for quality control and in-service periodic monitoring of medium voltage cable terminations. In *Conference Record of the 1998 IEEE International Symposium on Electrical Insulation*, volume 1, pages 130–133, Arlington, VA, June 1998.
- [50] Y. Tian, P.L. Lewin, A. E. Davies, and Z. Richardson. Acoustic emission detection of partial discharges in polymeric insulation. In *1999 Eleventh International Symposium on High Voltage Engineering*, volume 1, pages 82–85, London, UK, Aug. 1999.
- [51] D. C. Smith. *High Frequency Measurements and Noise in Electronic Circuits*. Van Nostrand Reinhold, New York, 1993.
- [52] B. T. Phung, T. R. Blackburn, and R. E. James. On-line partial discharge measurement on high voltage power cables. In *1999 Eleventh International Symposium on High Voltage Engineering*, volume 4, pages 328–332, London, UK, Aug. 1999.
- [53] B. R. Hamerling, F. J. Wester, E. Gulski, J. J. Smit, and E. R. S. Groot. Fundamental aspects of on-line PD measurements on distribution power cables. In *Proceedings of the 2001 IEEE 7th International Conference on Solid Dielectrics*, pages 408–411, Eindhoven, Netherlands, June 2001.
- [54] C. Zhou, X. Song, M. Michel, and D. M. Hepburn. On-line partial discharge monitoring in medium voltage underground cables. *IET Science, Measurement Technology*, 3(5):354–363, Sep. 2009.

- [55] L. Renforth, M. Seltzer-Grant, R. MacKinlay, S. Goodfellow, D. Clark, and R. Shuttleworth. Experiences from over 15 years of on-line partial discharge (OLPD) testing of in-service MV and HV cables, switchgear, transformers and rotating machines. In *2011 IEEE IX Latin American Robotics Symposium and IEEE Colombian Conference on Automatic Control*, pages 1–7, Bogota, Colombia, Oct. 2011.
- [56] M. S. Mashikian, Rajeev Bansal, and R. B. Northrop. Location and characterization of partial discharge sites in shielded power cables. *IEEE Transactions on Power Delivery*, 5(2):833–839, Apr. 1990.
- [57] F. Puletti, M. Olivieri, A. Cavallini, and G. C. Montanari. Localization of partial discharge sources along HV and MV cable routes. In *The 7th International Power Engineering Conference*, pages 1–199, Singapore, Nov. 2005.
- [58] Z. S. Zhang, D. M. Xiao, and Y. Li. Rogowski air coil sensor technique for on-line partial discharge measurement of power cables. *IET Science, Measurement Technology*, 3(3):187–196, May 2009.
- [59] S. A. Dyer. *Wiley Survey of Instrumentation and Measurement*. John Wiley & Sons, New York, 2004.
- [60] U. Schichler. A sensitive method for on-site partial discharge detection on XLPE cable joints. In *Proceedings of the 5th International Conference on Properties and Applications of Dielectric Materials*, volume 2, pages 1099–1102, Seoul, South Korea, May 1997.
- [61] Junhua Luo, Jiang Feng, Jian Yuan, Cuijiao Ma, and Yuchang Qiu. Partial discharge detection in XLPE power cable with CT sensor. In *Proceedings of the 2001 IEEE 7th International Conference on Solid Dielectrics*, pages 400–403, Eindhoven, Netherlands, June 2001.
- [62] P. van der Wielen, J. Veen, P. A. A. F. Wouters, and E. F. Steennis. Sensors for on-line PD detection in MV power cables and their locations in substations. In *Proceedings of the 7th International Conference on Properties and Applications of Dielectric Materials*, volume 1, pages 215–219, Nagoya, Japan, June 2003.



- [63] K. S. Yee. Numerical solution of initial boundary value problems involving Maxwells equations in isotropic media. *IEEE Transactions on Antennas and Propagation*, AP14(3):302–307, May 1966.
- [64] M. D. Judd. Using finite difference time domain techniques to model electrical discharge phenomena. In *2000 Annual Report Conference on Electrical Insulation and Dielectric Phenomena*, volume 2, pages 518 – 521, Victoria, BC, Canada, Oct. 2000.
- [65] D. Pommerenke and S. Sakaguchi. Application of Maxwell solvers to PD propagation. I. Concepts and codes. *IEEE Electrical Insulation Magazine*, 18(5):15–21, Sep.-Oct. 2002.
- [66] S. Okabe, S. Yuasa, S. Kaneko, M. Yoshimura, H. Muto, H. Yoshiyasu, C. Nishida, and M. Kamei. Simulation of propagation characteristics of higher order mode electromagnetic waves in GIS. *IEEE Transactions on Dielectrics and Electrical Insulation*, 13(4):855–861, Aug. 2006.
- [67] M. Hikita, S. Ohtsuka, T. Teshima, S. Okabe, and S. Kaneko. Examination of electromagnetic mode propagation characteristics in straight and L-section GIS model using FD-TD analysis. *IEEE Transactions on Dielectrics and Electrical Insulation*, 14(6):1477–1483, Dec. 2007.
- [68] M. Hikita, S. Ohtsuka, J. Wada, S. Okabe, T. Hoshino, and S. Maruyama. Propagation properties of PD-induced electromagnetic wave in 66 kV GIS model tank with L branch structure. *IEEE Transactions on Dielectrics and Electrical Insulation*, 18(5):1678–1685, Oct. 2011.
- [69] M. Hikita, S. Ohtsuka, J. Wada, S. Okabe, T. Hoshino, and S. Maruyama. Study of partial discharge radiated electromagnetic wave propagation characteristics in an actual 154 kV model GIS. *IEEE Transactions on Dielectrics and Electrical Insulation*, 19(1):8–17, Feb. 2012.
- [70] M. Hikita, S. Ohtsuka, T. Teshima, S. Okabe, and S. Kaneko. Electromagnetic (EM) wave characteristics in GIS and measuring the EM wave leakage at the spacer aperture for partial discharge diagnosis. *IEEE Transactions on Dielectrics and Electrical Insulation*, 14(2):453–460, Apr. 2007.
- [71] M. Yoshimura, H. Muto, C. Nishida, M. Kamei, S. Okabe, and S. Kaneko. Propagation properties of electromagnetic wave through T-branch in GIS.

- IEEE Transactions on Dielectrics and Electrical Insulation*, 14(2):328–333, Apr. 2007.
- [72] T. Hoshino, S. Maruyama, and T. Sakakibara. Simulation of propagating electromagnetic wave due to partial discharge in GIS using FDTD. *IEEE Transactions on Power Delivery*, 24(1):153–159, Jan. 2009.
- [73] M. Hikita, S. Ohtsuka, S. Okabe, J. Wada, T. Hoshino, and S. Maruyama. Influence of disconnecting part on propagation properties of PD-induced electromagnetic wave in model GIS. *IEEE Transactions on Dielectrics and Electrical Insulation*, 17(6):1731–1737, Dec. 2010.
- [74] X. Hu, M. D. Judd, and W. H. Siew. A study of PD location issues in GIS using FDTD simulation. In *2010 45th International Universities Power Engineering Conference (UPEC)*, pages 1–5, Cardiff, Wales, Aug.-Sept. 2010.
- [75] M. D. Judd, L. Yang, and I. B. B. Hunter. Partial discharge monitoring of power transformers using UHF sensors. Part I: sensors and signal interpretation. *IEEE Electrical Insulation Magazine*, 21(2):5–14, Mar.-Apr. 2005.
- [76] L. Yang, M. D. Judd, and G. Costa. Simulating propagation of UHF signals for PD monitoring in transformers using the finite difference time domain technique [power transformers]. In *2004 Annual Report Conference on Electrical Insulation and Dielectric Phenomena (CEIDP)*, pages 410–413, Boulder, CO, Oct. 2004.
- [77] Zhiguo Tang, Chengrong Li, Wei Wang, Hui Wang, Li Wang, and Yansheng Ding. The propagation characteristics of electromagnetic wave generated from partial discharges in power transformer by FDTD simulation. In *2007 Annual Report Conference on Electrical Insulation and Dielectric Phenomena (CEIDP)*, pages 200–203, Vancouver, BC, Oct. 2007.
- [78] A. M. Ishak, M. D. Judd, and W. H. Siew. A study of UHF partial discharge signal propagation in power transformers using FDTD modelling. In *2010 45th International Universities Power Engineering Conference (UPEC)*, pages 1–5, Cardiff, Wales, Aug.-Sep. 2010.
- [79] Peng Wang, Jian Li, Linjie Zhao, Tianyan Jiang, and Zhiman He. Investigation on the propagation characteristic of electromagnetic waves in

- converter transformers. In *2012 International Conference on High Voltage Engineering and Application (ICHVE)*, pages 353–357, Shanghai, Sep. 2012.
- [80] Xu Zhao, Yonghong Cheng, Yongpeng Meng, Kai Wu, and Yuhan Niu. The propagation characteristics of UHF partial discharge in power transformers with complex winding structure. In *2012 Annual Report Conference on Electrical Insulation and Dielectric Phenomena (CEIDP)*, pages 60–63, Montreal, QC, Oct. 2012.
- [81] M. D. Judd. Radiometric partial discharge detection. In *2008 International Conference on Condition Monitoring and Diagnosis (CMD)*, pages 1025–1030, Beijing, Apr. 2008.
- [82] A. J. Reid, M. Stewart, and M. D. Judd. FDTD modeling of UHF partial discharge sensor response. In *2009 International Conference on Sustainable Power Generation and Supply (SUPERGEN)*, pages 1–4, Nanjing, China, Apr. 2009.
- [83] A. M. Ishak, M. D. Judd, W. H. Siew, and P. C. Baker. Evaluation of FDTD modelling as a tool for predicting the response of UHF partial discharge sensors. In *Conference Record of the 2012 IEEE International Symposium on Electrical Insulation (ISEI)*, pages 502–506, San Juan, PR, June 2012.
- [84] R. Heinrich, R. Jobava, W. Kalkner, and A. Gheonjian. Investigation and optimization of a sensor for partial discharge detection on high voltage XLPE cables. In *Proceedings of III International Seminar/Workshop on Direct and Inverse Problems of Electromagnetic and Acoustic Wave Theory*, pages 134–137, Tbilisi, Nov. 1998.
- [85] R. Heinrich, R. Jobava, W. Kalkner, and A. Gheonjian. Numerical modelling for investigation and optimization of a sensor for sensitive partial discharge detection on high-voltage XLPE cables. *European Transactions on Electrical Power*, 10(3):161–166, May-June 2000.
- [86] D. Pommerenke, R. Jobava, and R. Heinrich. Electromagnetic finite differences time domain (FDTD) modeling of partial discharge coupling applied to high voltage cables and cable joints. In *Eighth International Conference*

- on Dielectric Materials, Measurements and Applications*, pages 497–502, Edinburgh, Sep. 2000.
- [87] D. Pommerenke, R. Jobava, and R. Heinrich. Numerical simulation of partial discharge propagation in cable joints using the finite difference time domain method. *IEEE Electrical Insulation Magazine*, 18(6):6–11, Nov.-Dec. 2002.
- [88] R. Jobava, D. Pommerenke, R. Heinrich, W. Kalkner, and A. Gheonjian. Calculation of pulse propagation in coaxial cables with multi-layered insulation system. In *Proceedings of the 5th International Seminar/Workshop on Direct and Inverse Problems of Electromagnetic and Acoustic Wave Theory*, pages 35–40, Tbilisi, Oct. 2000.
- [89] Y. Baba, N. Tanabe, N. Nagaoka, and A. Ametam. Transient analysis of a cable with low-conducting layers by a finite-difference time-domain method. *IEEE Transactions on Electromagnetic Compatibility*, 46(3):488–493, Aug. 2004.
- [90] R. Jobava, R. Heinrich, D. Pommerenke, W. Kalkner, and A. Gheonjian. Efficient FDTD simulation of fields in coaxial cables with multi-layered insulation partially formed by dispersive layers of extremely high permittivity. In *Proceedings of the 7th International Seminar/Workshop on Direct and Inverse Problems of Electromagnetic and Acoustic Wave Theory*, pages 91–94, Tbilisi, Oct. 2002.
- [91] R. Papazyan, D. Pommerenke, and R. Eriksson. Modeling the wave propagation properties of power cables using numerical simulations. In *2004 Conference on Precision Electromagnetic Measurements Digest*, pages 412–413, London, June 2004.
- [92] R. Papazyan, P. Pettersson, and D. Pommerenke. Wave propagation on power cables with special regard to metallic screen design. *IEEE Transactions on Dielectrics and Electrical Insulation*, 14(2):409–416, Apr. 2007.
- [93] Kai Wang, D. Pommerenke, R. Chundru, T. Van Doren, J.L. Drewniak, and A. Shashindranath. Numerical modeling of electrostatic discharge generators. *IEEE Transactions on Electromagnetic Compatibility*, 45(2):258–271, May 2003.

- [94] B. U. Musa, W. H. Siew, and M. D. Judd. Computation of transient electromagnetic fields due to switching in high-voltage substations. *IEEE Transactions on Power Delivery*, 25(2):1154–1161, Apr. 2010.
- [95] K. Yamamoto, S. Yanagawa, K. Yamabuki, S. Sekioka, and S. Yokoyama. Analytical surveys of transient and frequency-dependent grounding characteristics of a wind turbine generator system on the basis of field tests. *IEEE Transactions on Power Delivery*, 25(4):3035–3043, Oct. 2010.
- [96] A. Taflove and M. E. Brodwin. Numerical-solution of steady-state electromagnetic scattering problems using time-dependent Maxwells equations. *IEEE Transactions on Microwave Theory and Techniques*, 23(8):623–630, Aug. 1975.
- [97] A. Taflove. Application of the finite-difference time-domain method to sinusoidal steady-state electromagnetic-penetration problems. *IEEE Transactions on Electromagnetic Compatibility*, 22(3):191–202, Aug. 1980.
- [98] K. S. Kunz and R. J. Luebbers. *The Finite Diference Time Domain Method for Electromagnetics*. CRC PressINC, Boca Raton, 1993.
- [99] G. Mur. Absorbing boundary-conditions for the finite-difference approximation of the time-domain electromagnetic-field equations. *IEEE Transactions on Electromagnetic Compatibility*, 23(4):377–382, Nov. 1981.
- [100] J. P. Berenger. A perfectly matched layer for the absorption of electromagnetic-waves. *Journal of Computational Physics*, 114(2):185–200, Oct. 1994.
- [101] Z. S. Sacks, D. M. Kingsland, R. Lee, and J. F. Lee. A perfectly matched anisotropic absorber for use as an absorbing boundary condition. *IEEE Transactions on Antennas and Propagation*, 43(12):1460–1463, Dec. 1995.
- [102] S. D. Gedney. An anisotropic perfectly matched layer-absorbing medium for the truncation of FDTD lattices. *IEEE Transactions on Antennas and Propagation*, 44(12):1630–1639, Dec. 1996.
- [103] Z. P. Liao, H. L. Wong, B. Yang, and Y. Yuan. A transmitting boundary for transient wave analyses. *Scientia Sinica Series a-Mathematical Physical Astronomical & Technical Sciences*, 27(10):1063–1076, 1984.

- 
- [104] R. Luebbers, F. P. Hunsberger, K. S. Kunz, R. B. Standler, and M. Schneider. A frequency-dependent finite-difference time-domain formulation for dispersive materials. *IEEE Transactions on Electromagnetic Compatibility*, 32(3):222–227, Aug. 1990.
- [105] D. M. Sullivan. *Electromagnetic Simulation Using the FDTD Method*. John Wiley & Sons, New York, 2000.
- [106] A. Taflov and S. C. Hagness. *Computational Electrodynamics: The Finite-Difference Time-Domain Method*. Artech House, Norwood, MA, 2000.
- [107] Remcom Inc. *XFDTD Reference Manual*. PA, USA, 7.1 edition, 2010.
- [108] Lumerical Solutions Inc. FDTD solutions, Version 8.0. URL <http://www.lumerical.com>.
- [109] M. D. Judd, O. Farish, and B. F. Hampton. The excitation of UHF signals by partial discharges in GIS. *IEEE Transactions on Dielectrics and Electrical Insulation*, 3(2):213–228, April 1996.
- [110] W. L. Weeks and Y. M. Diao. Wave propagation characteristics in underground power cable. *IEEE Transactions on Power Apparatus and Systems*, PAS-103(10):2816–2826, Oct. 1984.
- [111] A. Ametani, Y. Miyamoto, and N. Nagaoka. Semiconducting layer impedance and its effect on cable wave-propagation and transient characteristics. *IEEE Transactions on Power Delivery*, 19(4):1523–1531, Oct. 2004.
- [112] G. Mugala, R. Eriksson, and P. Pettersson. Dependence of XLPE insulated power cable wave propagation characteristics on design parameters. *IEEE Transactions on Dielectrics and Electrical Insulation*, 14(2):393–399, Apr. 2007.
- [113] F. T. Ulaby. *Fundamentals of Applied Electromagnetics*. Pearson Prentice Hall, New Jersey, 2004.
- [114] F. Kremer and A. Schonhals. *Broadband Dielectric Spectroscopy*. Springer, Berlin Heidelberg, 2003.

- 
- [115] A. K. Jonscher. *Dielectric Relaxation in Solids*. Chelsea Dielectrics Press, London, 1983.
- [116] G. Mugala, R. Eriksson, and P. Pettersson. Comparing two measurement techniques for high frequency characterization of power cable semiconducting and insulating materials. *IEEE Transactions on Dielectrics and Electrical Insulation*, 13(4):712–716, Aug. 2006.
- [117] Zhifang Du, P. K. Willett, and M. S. Mashikian. Performance limits of PD location based on time-domain reflectometry. *IEEE Transactions on Dielectrics and Electrical Insulation*, 4(2):182–188, Apr. 1997.
- [118] A. R. Blythe and D. Bloor. *Electrical Properties of Polymers*. Cambridge University Press, Cambridge, 2005.
- [119] E. Bogatin. *Signal and Power Integrity - Simplified*. Pearson Education, Boston, 2009.
- [120] W. S. Zaengl. Dielectric spectroscopy in time and frequency domain for HV power equipment. I. Theoretical considerations. *IEEE Electrical Insulation Magazine*, 19(5):5–19, Sep.-Oct. 2003.
- [121] E. Tanabe and W. T. Joines. A nondestructive method for measuring the complex permittivity of dielectric materials at microwave frequencies using an open transmission line resonator. *IEEE Transactions on Instrumentation and Measurement*, IM-25(3):222–226, Sep. 1976.
- [122] T. W. Athey, M. A. Stuchly, and S. S. Stuchly. Measurement of radio frequency permittivity of biological tissues with an open-ended coaxial line: Part I. *IEEE Transactions on Microwave Theory and Techniques*, 30(1):82–86, Jan. 1982.
- [123] M. A. Stuchly, T. W. Athey, G. M. Samaras, and G. E. Taylor. Measurement of radio frequency permittivity of biological tissues with an open-ended coaxial line: Part II - experimental results. *IEEE Transactions on Microwave Theory and Techniques*, 30(1):87–92, Jan. 1982.
- [124] D. Berube, F. M. Ghannouchi, and P. Savard. A comparative study of four open-ended coaxial probe models for permittivity measurements of lossy

- dielectric/biological materials at microwave frequencies. *IEEE Transactions on Microwave Theory and Techniques*, 44(10):1928–1934, Oct. 1996.
- [125] C. L. Pournaropoulos and D. K. Misra. The co-axial aperture electromagnetic sensor and its application in material characterization. *Measurement Science & Technology*, 8(11):1191–1202, Nov. 1997.
- [126] E. Ritz and M. Dressel. Analysis of broadband microwave conductivity and permittivity measurements of semiconducting materials. *Journal of Applied Physics*, 103(084902):1–8, Apr. 2008.
- [127] U. Kaatze and Y. Feldman. Broadband dielectric spectrometry of liquids and biosystems. *Measurement Science & Technology*, 17(2):R17–R35, Feb. 2006.
- [128] A. P. Gregory and R. N. Clarke. A review of RF and microwave techniques for dielectric measurements on polar liquids. *IEEE Transactions on Dielectrics and Electrical Insulation*, 13(4):727–743, Aug. 2006.
- [129] J. Krupka. Frequency domain complex permittivity measurements at microwave frequencies. *Measurement Science & Technology*, 17(6):R55–R70, June 2006.
- [130] Chunchuan Xu and S. A. Boggs. High frequency properties of shielded power cable part 2: sources of error in measuring shield dielectric properties. *IEEE Electrical Insulation Magazine*, 22(1):7–13, Jan.-Feb. 2006.
- [131] R. Heinrich, S. Bonisch, D. Pommerenke, R. Jobava, and W. Kalkner. Broadband measurement of the conductivity and the permittivity of semiconducting materials in high voltage XLPE cables. In *2000 Eighth International Conference on Dielectric Materials, Measurements and Applications*, pages 212–217, Edinburgh, Sep. 2000. The Institution of Electrical Engineers, London.
- [132] G. Mugala, R. Eriksson, U. Gafvert, and P. Petterson. Measurement technique for high frequency characterization of semiconducting materials in extruded cables. *IEEE Transactions on Dielectrics and Electrical Insulation*, 11(3):471–480, June 2004.



- [133] R. Papazyan, P. Pettersson, H. Edin, R. Eriksson, and U. Gafvert. Extraction of high frequency power cable characteristics from S-parameter measurements. *IEEE Transactions on Dielectrics and Electrical Insulation*, 11(3):461–470, June 2004.
- [134] M. Tozzi, A. Cavallini, G. C. Montanari, and G. L. G. Burbui. Pd detection in extruded power cables: an approximate propagation model. *IEEE Transactions on Dielectrics and Electrical Insulation*, 15(3):832–840, June 2008.
- [135] A. J. Reid, X. Hu, M. D. Judd, and W. H. Siew. Defect location and characterisation in an EPR MV cable using TDOA and thermal techniques. In *Proceedings of XVII International Symposium on High Voltage Engineering*, pages 1094–1098, Hannover, Germany, Aug. 2011.
- [136] *HP 8712C and HP 8714C RF Network Analyzers User Guide*. Hewlett-Packard Company, 1998.
- [137] P. Wagenaars, P. A. A. F. Wouters, P. C. J. M. van der Wielen, and E. F. Steennis. Approximation of transmission line parameters of single-core and three-core XLPE cables. *IEEE Transactions on Dielectrics and Electrical Insulation*, 17(1):106–115, Feb. 2010.
- [138] Third Party Engineering Consultancy. Confidential report provided to british energy. Technical report, British Energy, 2008.
- [139] R. Papazyan and R. Eriksson. Calibration for time domain propagation constant measurements on power cables. *IEEE Transactions on Instrumentation and Measurement*, 52(2):415–418, Apr. 2003.
- [140] C. W. T. McLyman. *Transformer and Inductor Design Handbook*. Marcel Dekker, New York, 2004.
- [141] S. A. Boggs. Partial discharge - Part II: detection sensitivity. *IEEE Electrical Insulation Magazine*, 6(5):35–42, Sep.-Oct. 1990.
- [142] A. J. Reid and M. D. Judd. Ultra-wide bandwidth measurement of partial discharge current pulses in SF<sub>6</sub>. *Journal of Physics D: Applied Physics*, 45(16):5203, Apr. 2012.

- 
- [143] C. L. Phillips, J. Parr, and E. Riskin. *Signals, Systems, and Transforms*. Pearson Education, New Jersey, 2008.
- [144] J. S. Chitode. *Digital Signal Processing*. Technical Publications Pune, Pune, India, 2008.
- [145] S. Engelberg. *Digital Signal Processing: an Experimental Approach*. Springer, London, 2008.
- [146] D. J. Griffiths. *Introduction to Electrodynamics*. Prentice Hall, New Jersey, 1999.
- [147] F. Haghjoo, M. Sarlak, and S. M. Shahrtash. Implementation of an on-line PD measurement system using HFCT. *World Academy of Science, Engineering and Technology*, 25(168):945–951, Jan. 2009.
- [148] K. J. strm and B. Wittenmark. *Computer-controlled Systems: Theory and Design*. Prentice Hall, New Jersey, 1997.
- [149] M. Hassul and B. Shahian. Frequency domain identification for undergraduates. *IEEE Transactions on Education*, 35(4):368–375, Nov. 1992.
- [150] X. Hu, A. J. Reid, W. H. Siew, and M. D. Judd. FDTD modeling of fast transient currents in high voltage cables. In *2012 IEEE International Power Modulator and High Voltage Conference (IPMHVC)*, pages 256–259, San Diego, CA, June 2012.

# Appendix A

This Appendix demonstrates the derivation of the formulation (5.10) used to find out the cable propagation constant  $\gamma_c$  from the corresponding TDR measurement results. The TDR measurement described in Chapter 5 was using the measurement and calibration procedures proposed in [139]. The measurement setup used (Figure 5.13) can be represented by a physical model shown in Figure 1. The index numbers in Figure 1 specify the points where the voltages are calculated. The index number 3 indicates the measuring point. All variable values in the following discussion are going to be expressed with reference to this point.

Firstly, for the forward travelling waves, their voltage amplitudes at the points

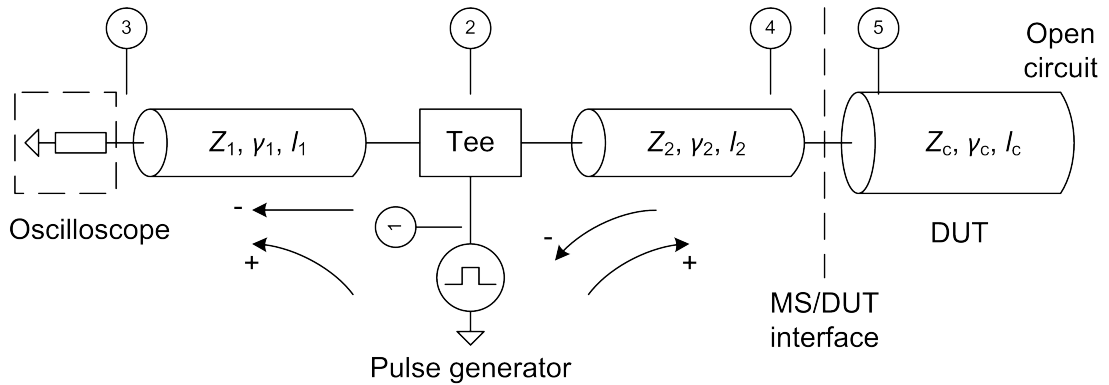


Figure 1: A physical model of the TDR measurement setup, where  $Z$ ,  $\gamma$  and  $l$  are the characteristic impedance, propagation constant and length of the corresponding cable respectively. “MS” is measurement system and “DUT” is device under test. “+” and “-” represent directions of the forward (incident) and backward (reflection) travelling waves respectively.

specified by the index numbers can be related as,

$$V_{+2} = V_{+1} \quad (1)$$

$$V_{+3} = V_{+2}T_t e^{-\gamma_1 l_1} \quad (2)$$

$$V_{+4} = V_{+2}T_t e^{-\gamma_2 l_2} \quad (3)$$

$$V_{+5} = V_{+4}T_+ = V_{+4}(1 + \Gamma_+) \quad (4)$$

where  $V_{+1}$  is the voltage amplitude of the pulse generator,  $T_t$  is the transmission coefficient of the “Tee”, and  $T_+/\Gamma_+$  is the transmission/reflection coefficient at the MS/DUT interface in the “+” direction. A perfect match is assumed at the “Tee”, i.e., no reflection from the “Tee” is considered. It is also assumed that  $Z_1 = Z_2$ .

Secondly, for the backward travelling waves, there are the following equations,

$$V_{-4} = V_{-5}T_- = V_{-5}(1 + \Gamma_-) \quad (5)$$

$$V_{-3} = V_{-4}e^{-\gamma_2 l_2}T_t e^{-\gamma_1 l_1} \quad (6)$$

where  $T_-/\Gamma_-$  is the transmission/reflection coefficient at the MS/DUT interface in the “-” direction.

Considering an ideal open circuit at the other end of DUT, there is

$$e^{-\gamma_2 l} = \frac{V_{-5}}{V_{+5}}. \quad (7)$$

Submitting (1)–(6) into (7) gives

$$e^{-\gamma_2 l} = \frac{V_{-5}}{V_{+5}} = \frac{V_{-3}}{V_{+3}} \cdot \frac{e^{\gamma_2 2l_2}}{T_t(1 + \Gamma_+)(1 + \Gamma_-)}. \quad (8)$$

Since  $\Gamma_- = -\Gamma_+$ , the remaining unknowns in (8) are  $\Gamma_+$ ,  $T_t$  and those of DUT.

The reflection coefficient  $\Gamma_+$  is calculated by

$$\Gamma_+ = \frac{Z_c - Z_2}{Z_c + Z_2} = \frac{V_{-4}^m}{V_{+4}}. \quad (9)$$

where  $V_{-4}^m$  is the signal reflected at the MS/DUT interface and can be written

with reference to the measuring point 3 as

$$V_{-4}^m = \frac{V_{-3}^m}{T_t e^{-\gamma_2 l_2} e^{-\gamma_1 l_1}}. \quad (10)$$

Substituting (10), (2) and (3) into (9) can have

$$\Gamma_+ = \frac{V_{-3}^m}{V_{+3}} \cdot \frac{1}{T_t e^{-\gamma_2 2l_2}}. \quad (11)$$

If a separate measurement is carried out with one end of coaxial cable 2 short-circuited, then

$$V_{-3}^{short} = -V_{+2} T_t^2 e^{-\gamma_2 2l_2} e^{-\gamma_1 l_1}. \quad (12)$$

where  $V_{-3}^{short}$  is the measured signal reflected at the short-circuited end of coaxial cable 2. Using (12), (2) and (11) gives

$$V_{+3} = -\frac{V_{-3}^{short}}{T_t e^{-\gamma_2 2l_2}} \quad (13)$$

$$\Gamma_+ = -\frac{V_{-3}^m}{V_{-3}^{short}}. \quad (14)$$

and by substituting into (8), it finally produces

$$e^{-\gamma 2l} = \frac{V_{-3} V_{-3}^{short}}{(V_{-3}^m)^2 - (V_{-3}^{short})^2}. \quad (15)$$

To obtain the variable values of (15) so as to calculate the propagation constant of DUT, two TDR measurements are required: one with coaxial cable 2 short-circuited and one with DUT connected. Comparing (15) with (5.10),  $V_{-3}$ ,  $V_{-3}^m$  and  $V_{-3}^{short}$  are corresponding to  $V_{cable}$ ,  $V_{adapter}$  and  $V_{short}$  respectively.

# Appendix B

This Appendix outlines the steps involved in fitting the transfer function model (7.5) to those measured HFCT transfer functions so that unknown coefficients in (7.5) can be determined.

The fitting was carried out using the transfer function synthesising method presented in [149]. The method starts from replacing  $s$  in (7.5) with  $j\omega$ , which produces

$$H(j\omega) = \frac{b_m(j\omega)^m + b_{m-1}(j\omega)^{m-1} + \dots + b_1(j\omega) + b_0}{a_n(j\omega)^n + a_{n-1}(j\omega)^{n-1} + \dots + a_1(j\omega) + 1} \quad (16)$$

where  $a_0$  is predefined as 1 and  $H(j\omega) = R + jX$ .  $R$  and  $X$  are, at the angular frequency  $\omega$ , the real and imaginary parts of the measured transfer function respectively.

Rewriting (16) as

$$b_m(j\omega)^m + b_{m-1}(j\omega)^{m-1} + \dots + b_1(j\omega) + b_0 = (a_n(j\omega)^n + a_{n-1}(j\omega)^{n-1} + \dots + a_1(j\omega) + 1)(R + jX). \quad (17)$$

and by moving the unknowns to the left side of the equation and writing more compactly, there is

$$\sum_{i=0}^m b_i(j\omega)^i - \left( \sum_{i=1}^n a_i(j\omega)^i \right) (R + jX) = R + jX. \quad (18)$$

Solving (18) requires to equate all the real terms on the left side to  $R$  on the right side and all the imaginary terms to  $X$ . To that end, some indexes are introduced

to make  $m$  and  $n$  either even or odd

$$\begin{aligned} p &= [m/2] \\ q &= [(m-1)/2] \\ r &= [n/2] \\ s &= [(n-1)/2] \end{aligned}$$

where  $[\cdot]$  returns the integer value of the number within it. By using the new indexes, the terms on the left side of (18) is rewritten as

$$\sum_{i=0}^m b_i(j\omega)^i = \sum_{h=0}^p b_{2h}(-1)^h\omega^{2h} + j \sum_{l=0}^q b_{2l+1}(-1)^l\omega^{2l+1} \quad (19)$$

and

$$\begin{aligned} \left( \sum_{i=1}^n a_i(j\omega)^i \right) (R + jX) = \\ \left( \sum_{u=1}^r a_{2u}(-1)^u\omega^{2u} + j \sum_{v=0}^s a_{2v+1}(-1)^v\omega^{2v+1} \right) \cdot (R + jX). \end{aligned} \quad (20)$$

With (19) and (20), separating the real and imaginary parts of (18) is done as follows,

$$\sum_{h=0}^p b_{2h}(-1)^h\omega^{2h} - R \sum_{u=1}^r a_{2u}(-1)^u\omega^{2u} + X \sum_{v=0}^s a_{2v+1}(-1)^v\omega^{2v+1} = R \quad (21)$$

and

$$\sum_{l=0}^q b_{2l+1}(-1)^l\omega^{2l+1} - X \sum_{u=1}^r a_{2u}(-1)^u\omega^{2u} - R \sum_{v=0}^s a_{2v+1}(-1)^v\omega^{2v+1} = X. \quad (22)$$

Evaluating (21) and (22) at various measurement frequencies will generate a set of equations with  $b_i$  and  $a_i$  as unknown parameters. These equations can be

represented in a matrix form as

$$\begin{pmatrix} \Omega_1 & 0 & \Omega_2 & \Omega_3 \\ 0 & \Omega_4 & \Omega_5 & \Omega_5 \end{pmatrix} \begin{pmatrix} b_0 \\ \cdot \\ b_{2p} \\ b_1 \\ \cdot \\ b_{2q+1} \\ a_2 \\ \cdot \\ a_{2r} \\ a_1 \\ \cdot \\ a_{2s+1} \end{pmatrix} = \begin{pmatrix} \mathbf{R} \\ \mathbf{X} \end{pmatrix} \quad (23)$$

where the coefficients  $b_i$  and  $a_i$  are partitioned by even and odd indexes to have simplified representations of the submatrices  $\Omega_1 \cdots \Omega_6$ . In practical calculation, the columns of  $\Omega$  would be interchanged to make the coefficients appear consecutively, i.e.,  $P = [b_0, b_1 \cdots b_m, a_1, a_2 \cdots a_n]^T$ . The submatrices are given by

$$\Omega_1 = \begin{pmatrix} 1 & -\omega_1^2 & \omega_1^4 & \cdot & \cdot & (-1)^p \omega_1^{2p} \\ 1 & -\omega_2^2 & \omega_2^4 & \cdot & \cdot & (-1)^p \omega_2^{2p} \\ \cdot & \cdot & \cdot & \cdot & \cdot & \cdot \\ \cdot & \cdot & \cdot & \cdot & \cdot & \cdot \end{pmatrix} \quad (24)$$

$$\Omega_2 = \begin{pmatrix} \omega_1^2 R_1 & -\omega_1^4 R_1 & \omega_1^6 R_1 & \cdot & \cdot & (-1)^{r+1} \omega_1^{2r} R_1 \\ \omega_2^2 R_2 & -\omega_2^4 R_2 & \omega_2^6 R_2 & \cdot & \cdot & (-1)^{r+1} \omega_2^{2r} R_2 \\ \cdot & \cdot & \cdot & \cdot & \cdot & \cdot \\ \cdot & \cdot & \cdot & \cdot & \cdot & \cdot \end{pmatrix} \quad (25)$$



$$\Omega_3 = \begin{pmatrix} \omega_1 X_1 & -\omega_1^3 X_1 & \omega_1^5 X_1 & \cdot & \cdot & (-1)^s \omega_1^{2s+1} X_1 \\ \omega_2 X_2 & -\omega_2^3 X_2 & \omega_2^5 X_2 & \cdot & \cdot & (-1)^s \omega_2^{2s+1} X_2 \\ \cdot & \cdot & \cdot & \cdot & \cdot & \cdot \\ \cdot & \cdot & \cdot & \cdot & \cdot & \cdot \end{pmatrix} \quad (26)$$

$$\Omega_4 = \begin{pmatrix} \omega_1 & -\omega_1^3 & \omega_1^5 & \cdot & \cdot & (-1)^q \omega_1^{2q+1} \\ \omega_2 & -\omega_2^3 & \omega_2^5 & \cdot & \cdot & (-1)^q \omega_2^{2q+1} \\ \cdot & \cdot & \cdot & \cdot & \cdot & \cdot \\ \cdot & \cdot & \cdot & \cdot & \cdot & \cdot \end{pmatrix} \quad (27)$$

$$\Omega_5 = \begin{pmatrix} \omega_1^2 X_1 & -\omega_1^4 X_1 & \omega_1^6 X_1 & \cdot & \cdot & (-1)^{r+1} \omega_1^{2r} X_1 \\ \omega_2^2 X_2 & -\omega_2^4 X_2 & \omega_2^6 X_2 & \cdot & \cdot & (-1)^{r+1} \omega_2^{2r} X_2 \\ \cdot & \cdot & \cdot & \cdot & \cdot & \cdot \\ \cdot & \cdot & \cdot & \cdot & \cdot & \cdot \end{pmatrix} \quad (28)$$

$$\Omega_6 = \begin{pmatrix} -\omega_1 R_1 & \omega_1^3 R_1 & -\omega_1^5 R_1 & \cdot & \cdot & (-1)^{s+1} \omega_1^{2s+1} R_1 \\ -\omega_2 R_2 & \omega_2^3 R_2 & -\omega_2^5 R_2 & \cdot & \cdot & (-1)^{s+1} \omega_2^{2s+1} R_2 \\ \cdot & \cdot & \cdot & \cdot & \cdot & \cdot \\ \cdot & \cdot & \cdot & \cdot & \cdot & \cdot \end{pmatrix}. \quad (29)$$

The matrix form (23) can be expressed by

$$\Omega P = V \quad (30)$$

where  $P$  is the coefficient vector and  $V$  is the vector of the measured transfer functions. The coefficient vector is solved out by

$$P = \Omega^{-1} V \quad (31)$$

provided that  $\Omega$  is a square matrix, which means the total number of the measurement frequencies equals to the number of the unknown coefficients. However,

in practice, there have to be many more measurement frequencies so as to make use of averaging to reduce measurement errors that will effect the obtained coefficients. In this case,  $\Omega$  will have more rows than columns and is not square and as a result (31) is not valid. One possible solution is to multiply both sides of (30) by  $\Omega^T$

$$\Omega^T \Omega P = \Omega^T V. \quad (32)$$

The matrix  $\Omega^T \Omega$  is square. Assuming it invertible, the solution is

$$P = (\Omega^T \Omega)^{-1} \Omega^T V. \quad (33)$$

It is well known that (32) is actually doing a least-squares fit of the coefficients to the measured data.  $\Omega^T \Omega$  is said to be a pseudo-inverse which can be numerically unstable. Alternatively, QR transformation can also be used to solve (32) [149]. By solving out the unknown parameters  $b_i$  and  $a_i$ , the transfer function model  $H(s)$  in (7.5) is established.

# Appendix C

## Published conference papers

[1] X. Hu, A. J. Reid, W. H. Siew, and M. D. Judd. FDTD Modeling of Fast Transient Currents in High Voltage Cables. In 2012 IEEE International Power Modulator and High Voltage Conference (IPMHVC), pages 256-259, San Diego, CA, June 2012.

[2] X. Hu, W. H. Siew and M. D. Judd. Implementing HFCTs in FDTD Modelling of Partial Discharge Detection in Power Distribution Cables, 5th Universities High Voltage Network (UHVnet) Colloquium (Leicester, UK), January 2012.

[3] A. J. Reid, X. Hu, M. D. Judd, and W. H. Siew. Defect Location and Characterization in an EPR MV Cable Using TDOA and Thermal Techniques. In Proceedings of XVII International Symposium on High Voltage Engineering, pages 1094-1098, Hannover, Germany, Aug. 2011.

[4] A. J. Reid, X. Peng, X. Hu, M. D. Judd, W. H. Siew, C. Zhou and D. M. Hepburn. Comparison of Partial Discharge Characteristics from Insulation Defects in 11kV EPR Cable. In Proceedings of XVII International Symposium on High Voltage Engineering, pages 866-871, Hannover, Germany, Aug. 2011.

[5] X. Hu, A. J. Reid, M. D. Judd and W. H. Siew. FDTD Modelling of Partial Discharge Detection in Power Distribution Cables using HFCTs, 4th Universities High Voltage Network (UHVnet) Colloquium (Winchester, UK), January 2011.

[6] X. Hu, M. D. Judd, and W. H. Siew. A Study of PD Location Issues in GIS

Using FDTD Simulation. In 2010 45th International Universities Power Engineering Conference (UPEC), pages 1-5, Cardiff, Wales, Aug.-Sept. 2010.

[7] A. J. Reid, X. Hu, M. D. Judd and W. H. Siew. FDTD Modelling of Partial Discharge in Shielded Power Cables, 3th Universities High Voltage Network (UHVnet) Colloquium (Manchester, UK), January 2010.